A Portable CCD Array Detector for In-situ Analysis of Powder Samples using Combined X-ray Diffraction/X-ray Fluorescence Techniques

Thesis submitted for the degree of Doctor of Philosophy at Brunel University

by

Amir Intisar

Imaging for Space and Terrestrial Applications Group

School of Engineering and Design

Brunel University, Uxbridge

29th May 2009

A Portable CCD Array Detector for In-situ Analysis of Powder Samples using Combined X-ray Diffraction/X-ray Fluorescence Techniques

Amir Intisar

Abstract

This work describes the design, development and testing of a portable charge-coupled device detector system to be used for the simultaneous collection of X-ray diffraction and X-ray fluorescence data from powdered samples. The detector was designed for both terrestrial and extra-terrestrial applications that require in-situ analysis of samples, where access to a laboratory instrument is restricted. The detector system incorporates 4 e2v technologies CCD30-11 devices, employing multi-phase pinned technology for low noise operation. Geometrical calculations and thermal studies concerning the design of the detector are presented, with particular emphasis on motivations for the chosen geometry. Initial characterisation and calibration of the detector was performed in a laboratory environment using a purpose built test facility. The test facility included a high brightness X-ray micro-source from Bede Scientific Instruments, coupled with an XOS polycapillary collimating optic, which was used to deliver a focused beam of low divergent X-rays to the sample. The design of the test facility is discussed and the spectra and flux produced by the X-ray micro-source are investigated. The operational performance of the detector is highlighted and the use of the instrument in different applications is described, namely the planetary sciences and pharmaceuticals sector. Finally, based on the knowledge gained from initial testing of the instrument, improvements to the detector design are outlined, which greatly enhance the combined X-ray diffraction/X-ray fluorescence performance of the instrument.

Declaration

I hereby declare that no part of this thesis has been previously submitted to this or any other university as part of the requirement for a higher degree. The work described herein was conducted solely by the undersigned except for those colleagues and other workers acknowledged in the text.

Amir Intisar

29th May 2009

Dedication

For Mum and Dad

Acknowledgements

Firstly, I would like to thank my supervisor Ian Hutchinson for his guidance, help and support over the past 4 years. His friendly attitude and experience made the PhD a pleasant and rewarding experience. I would also like to thank all the group members of ISTA for their contribution towards my PhD.

I would particularly like to acknowledge the following people for their involvement in my PhD. Thanks go to David Simpson, Andrew Holland, Richard Ingley, Neil Murray, Gopal Jeyasundra, John Osmond, Jason Gow, Thomas Greig, Peter Pool, Dave Burt, Gordon Cressey, Javier Cuadros, Chris Castelli, David Hall, Jordi Callafel, Asim Sultan, Rajiv Bose, Tom Walker and Adrian Martin. A special thanks goes to David Smith for reading my thesis and teaching me basic English spelling and grammar. Thanks also to my mum, dad, sister, friends and family for encouraging me for the past 4 years.

Finally, I would like to acknowledge the financial support received from the Engineering and Physical Sciences Research Council and e2v technologies during my research studentship.

Contents

Chapter 1 : Introduction

1.1 X-ray Spectroscopy using Charge Coupled Devices

The use of the charge-coupled device (CCD) for X-ray spectroscopy applications has become very widespread in recent years. Although CCDs were initially designed to perform in the optical range, technological advances have allowed CCDs to be used for detecting soft X-rays in the 0.1 keV − 10 keV range. Combined with high quantum efficiency (QE), low noise and high energy resolution, CCDs are well established as one of the most popular X-ray detector technologies of the modern day. Relatively small pixel sizes (e.g. 13 µm)^2 have also enhanced the spatial resolution of CCDs, drawing interest from the astronomy field [Lumb et al. 1991]. CCDs are also attractive to the X-ray imaging/spectroscopy detector market due to their small size (~ 400 mm^2) and low power consumption (< 1 W). The advent of advanced inverted mode operation (AIMO) has allowed CCDs to operate with dark current values of less than 1 e^- per/pixel/second (p/p/s) at ~ -20 °C [e2v technologies 2007]. AIMO CCDs can be cooled using thermo electric coolers (TECs) enabling a new generation of portable CCD instruments for planetary and scientific applications. Recent years have seen a rapid increase in the number of CCDs being used on planetary exploration rovers [Bell et al. 2004] and space based telescopes [Bruijne 2007]. The production of back illuminated (BI) CCDs has led to further improvements in the low energy X-ray response ranging from 0.1 – 3 keV [Castelli 1991]. The key to using CCDs for X-ray spectroscopy applications is collecting isolated X-ray events or events that are contained within a single pixel. Deep depletion CCDs allow an increase in isolated events for higher X-ray energies ranging from 3 – 10 keV. The production of BI CCDs fabricated on high resistivity silicon (Si) has ensured that CCDs are one of the most popular detectors for X-ray spectroscopy applications in the modern day.

The study presented in this thesis is related to the design of a CCD-based detector system [Intisar et al. 2008]. The purpose of the detector is to simultaneously collect X-ray diffraction (XRD) and X-ray fluorescence (XRF) data from powdered samples. The ability of the CCD to determine the energy of single photons and discriminate the spatial position of X-ray photons makes it an ideal detector for XRF and XRD respectively [Cornaby et al. 2000]. CCDs can offer spatial resolutions of 6.5 µm and energy resolutions of < 130 eV at 5898 eV. The use of CCD detectors for XRD

analysis allows the entire powder diffraction pattern to be collected at once and read-out quickly, which greatly reduces data collection times in comparison to traditional scanning point detectors. The detector designed for this work uses 4 CCDs tiled in a curved geometry. The CCDs are tiled along the curvature of a 120 mm circle, where the point of sample irradiation represents the centre point. A reflective XRD geometry is used with a 4° angle of incidence to achieve a higher signal to noise ratio (SNR) in comparison to transmission geometries. Using a large sample to detector distance results in very high spatial resolution (0.012°) and the use of 4 CCDs provides large angular coverage from approximately 4 − 64°. Figure 1.1 depicts the concept of the detector, from here on referred to as the 'CCD-Array', intercepting diffracted and characteristic X-rays from a powder sample. The intended use of the CCD-Array is in the planetary sciences sector where unknown rock samples can be classified based on their mineralogical and chemical content using XRD and XRF respectively [Vaniman et al. 2000]. The CCD-Array can also be utilised in many terrestrial markets for phase identification and the analysis of contaminants.

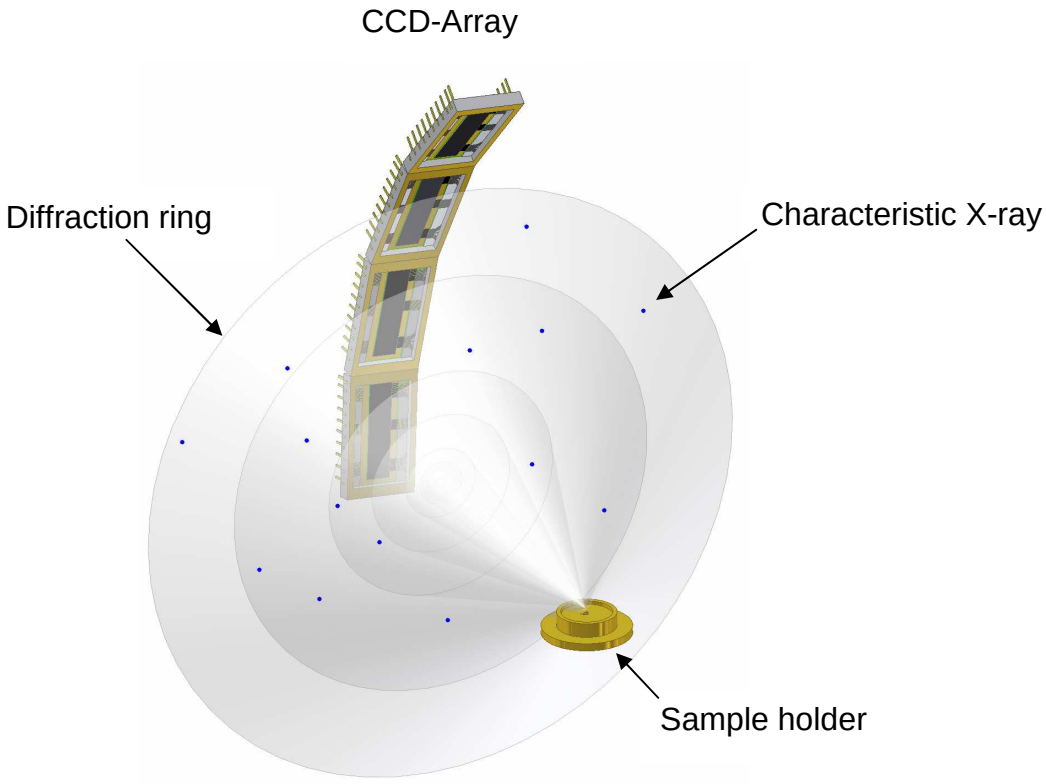

Figure 1.1: Detector concept – XRD/XRF data being emitted from a powder sample and simultaneously collected by the CCD-Array

1.2 X-ray Diffraction

X-ray diffraction (XRD) is one of the most widely used material characterisation methods in the world [Cullity 1978]. It is a non-destructive technique that can reveal the composition and crystallographic structure of natural and manufactured materials. XRD is applicable to many fields such as pharmaceuticals, forensics, crystallography, geology and material sciences. However, the focus of this thesis is the use of XRD for the mineralogical analysis of powdered rock samples. XRD can be used for the qualitative analysis of these minerals as well as for determining the mineral abundances of multi-phase mixtures (i.e. quantitative analysis).

Almost 95% of solid matter can be classified as being crystalline. Atoms inside these crystals are arranged in a periodic structure in 3 dimensions, located on repeating planes. Figure 1.2 shows a cross section of a crystal lattice.

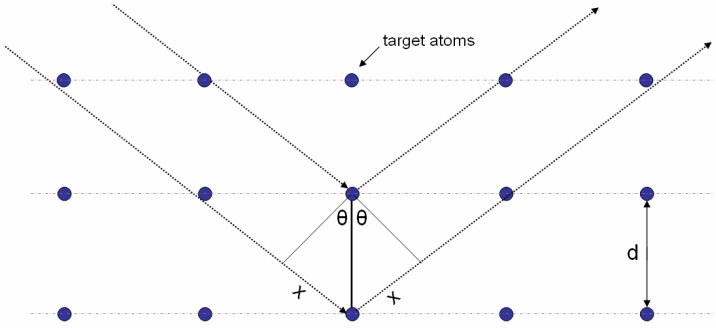

Figure 1.2: Geometry of Bragg's law required for XRD

When X-rays interact with such crystals, they can either be partly transmitted, absorbed, scattered or diffracted. The diffraction of X-rays from a crystal lattice occurs because the distance between lattice planes *d*, is comparable in size to the wavelength of X-rays (1×10^{-10} m). The lattice acts as a diffraction grating with peaks located at specific angles, known as Bragg angles. These Bragg angles are detected when the following condition is met:

$$n\lambda = 2dSin(\theta), \tag{1.1}$$

where λ is the wavelength of the incident X-rays and θ is the angle of incidence of the incoming X-ray beam with respect to the lattice plane. The condition states that the extra distance travelled by the diffracted beam ($2x$), must be an integral (n) multiple of

wavelengths (λ) for the beams to be in phase. Under such conditions, coherent scattering of the beam takes place, resulting in a Bragg peak. XRD can be used for the classification of rocks because the *d*-spacing for every sample is unique. Each sample therefore has its own unique fingerprint. Currently, over 600,000 (including over 10,000 minerals) diffraction patterns have been collected and stored as reference materials in the International Centre for Diffraction Data (ICDD) Powder Diffraction Files (PDFs). Diffraction data can be collected and then compared to ICDD PDFs for qualitative analysis, by comparing the 2θ positions of the 3 largest peaks.

This thesis is concerned with the X-ray powder diffraction (XRPD) technique. XRPD involves grinding samples into fine grained powders (usually less than 10 µm grains) and exposing these grains to a monochromatic beam of collimated X-rays. When the sample has been ground to a fine powder, all possible planes of reflection are present, revealing all the possible diffraction peaks. An example XRPD pattern of aragonite ($CaCO_3$) taken by a CCD detector is shown in figure 1.3, clearly displaying multiple Bragg peaks located at various 2θ positions.

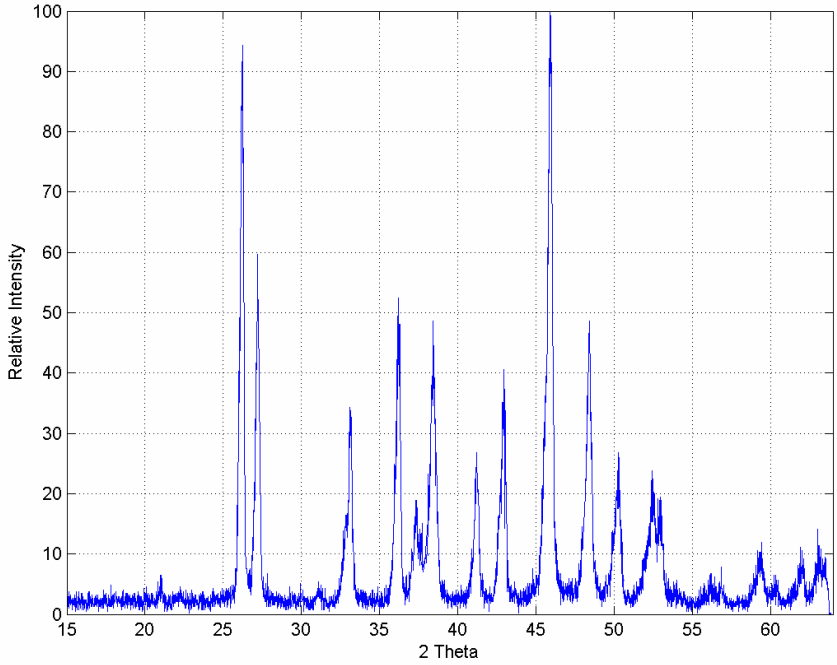

Figure 1.3: XRPD pattern of $CaCO_3$ taken with a CCD detector

This is the major advantage of using powder diffraction as opposed to single crystal methods, which involves varying the angle of incidence manually for each 2θ step. The major disadvantage of XRPD, in comparison to single crystal methods, is peak

overlapping, which is caused from the overcrowding of peaks in the XRD pattern. This can cause complications in the peak identification process and hence, qualitative analysis.

The main features of the XRPD technique are listed below:

- qualitative analysis - identification of minerals, rocks and soils,
- quantitative analysis - identification of mineral abundances in a multi-phase sample,
- determination of the crystal structure and unit cell dimensions for crystalline samples,
- determination of crystallite size from peak broadening,
- determination of crystallite shape from peak symmetry, and
- ideally suited to applications where only small quantities of the samples are available for analysis (e.g. < 10 mg).

The simplicity of grinding a rock into fine grains and exposing them to a monochromatic beam of collimated X-rays has enabled X-ray powder diffraction to become one of the most widespread tools for the identification of rocks and minerals. With constant improvements in X-ray detectors and analysis techniques, XRPD is becoming more attractive to many different industries for material characterisation.

1.3 X-ray Fluorescence

X-ray Fluorescence (XRF) is another non-destructive technique that is used in determining the elemental (i.e. chemical) composition of a sample. XRF is a more versatile technique than XRD as it can be applied to solids and liquids as well as powdered grains and has gained much interest from applications that need to identify impurities or contaminants. Example applications include forensics, printed circuit board quality control and gold karat analysis (jewellery industry).

The process of XRF is based on the photoelectric effect. The photoelectric effect takes place when an incident X-ray photon imparts all of its energy to an electron in the

atom of the target material [Hall 1936]. If the incoming photon has sufficient energy to release a bound electron, a photoelectron is ejected from the atom and a vacancy is created. To create a vacancy, the incoming X-ray photon must have an energy greater than the absorption edge of the given shell, also known as the electron binding energy E_B. The energy of the emitted photoelectron E, has a magnitude given by:

$$E = hf - E_B, \tag{1.2}$$

where h is Planck's constant and f is the frequency of the incoming photon (Hz). For example, the K shell binding energy of the copper (Cu) atom is 8979 eV [Fuggle & Martensson 1980], therefore any incident X-ray photon with an energy less than 8979 eV, cannot produce a K sell vacancy in the Cu atom. Once the vacancy is created, the atom de-excites by allowing an electron from a higher energy shell to fill the vacancy and release a characteristic photon. The energy of the photon emitted by an atom depends on the electron energy configuration within the atom. The energy levels which electrons occupy within an atom can be described using the Bohr model. In 1913 Niels Bohr suggested variations to the classical theory of mechanics in order to explain how radiation emitted from different atoms was unique [Beiser 1995]. Similar to previous principles, Bohr's model states that electrons rotate in a circular orbit around the nucleus, bound by Coulomb attraction (between electron and nucleus). However, Bohr's model states that electrons exist on discrete energy levels known as K, L, M and N shells. Electrons that are orbiting the nucleus do not give rise to any radiating energy as they remain on the same energy level. Radiation is emitted from the atom when electrons from a higher energy state fill vacancies in lower energy states (e.g. L shell electron fills a K shell vacancy).

Electron shells are composed of subshells labelled as s, p, d and f. The s, p, d and f subshells can hold 2, 6, 10 and 14 electrons respectively. The first shell, K, contains one subshell and can hold 2 electrons ($1s^2$). The second shell, L, contains 2 subshells and can hold 8 electrons ($2s^2$, $2p^6$). For example, the electron configuration of the Cu atom, which contains 29 electrons, can be expressed as:

$$1s^2\ 2s^2\ 2p^6\ 3s^2\ 3p^6\ 3d^{10}\ 4s^1$$

The energy of characteristic photons produced by an atom depends on which one of these shells, the electron filling the vacancy has originated from. Figure 1.4 shows the names of different types of photons produced based on the interacting electron shells.

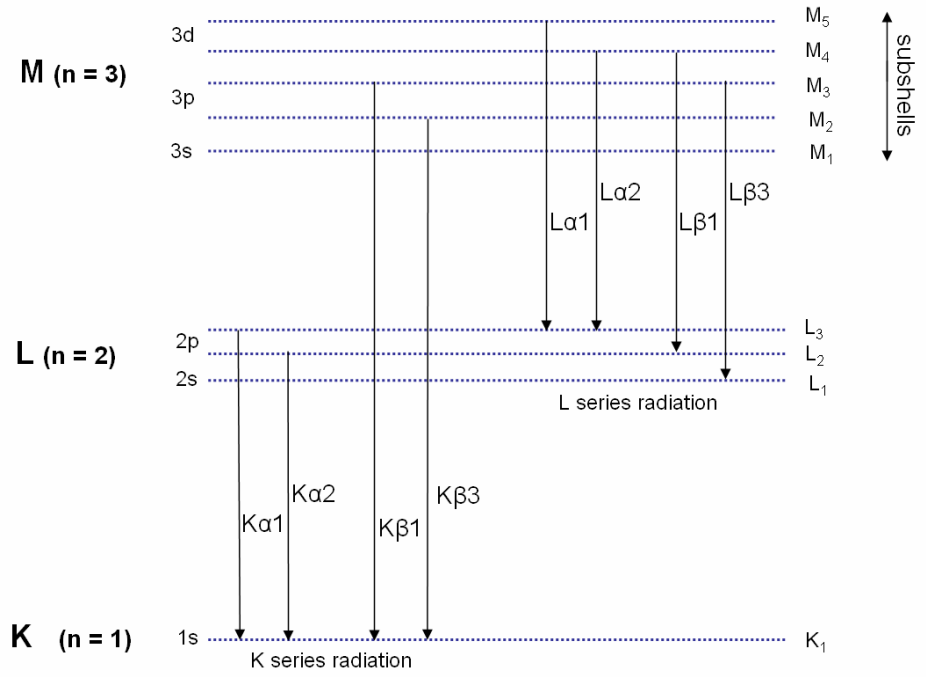

Figure 1.4: Characteristic X-rays produced from different electron shell interactions

The energy released by a characteristic X-ray is equal to the difference between the 2 energy levels. For example, the energy of a Cu $K\alpha_1$ X-ray is the difference between the K shell binding energy (8979 eV) and L_3 shell binding energy (932 eV), which results in the emission of an 8047 eV photon [Bearden 1967][Krause & Oliver 1979].

The relationship between the frequency of a particular characteristic X-ray emission f_c, and the atomic number Z, can be expressed using Moseley's Law as [Moseley 1913, 1914]:

$$\sqrt{f_c} = C(Z - \sigma_s), \tag{1.3}$$

where C is a constant depending on the type of shell (K, L, M, N) and σ_s is the shielding constant which also depends on the type of shell (σ_s has a value of 1 for the K shell and a value of 7.4 for the L shell). Figure 1.5 shows the relationship between

the energy of characteristic X-rays and atomic number *Z*, ranging from 1 − 10 keV. The work in this thesis is concerned with the core elements found in rocks/minerals, which produce characteristic X-rays with energies found in the soft X-ray range from 0.1 – 10 keV (Z < 30). The only emissions with any measurable probability in this range originate from K shells, namely Kα and Kβ. The separation in eV between the $K\alpha_1$ and $K\alpha_2$ characteristic X-rays from elements in the soft X-ray range is too small to be distinguished by CCD detectors.

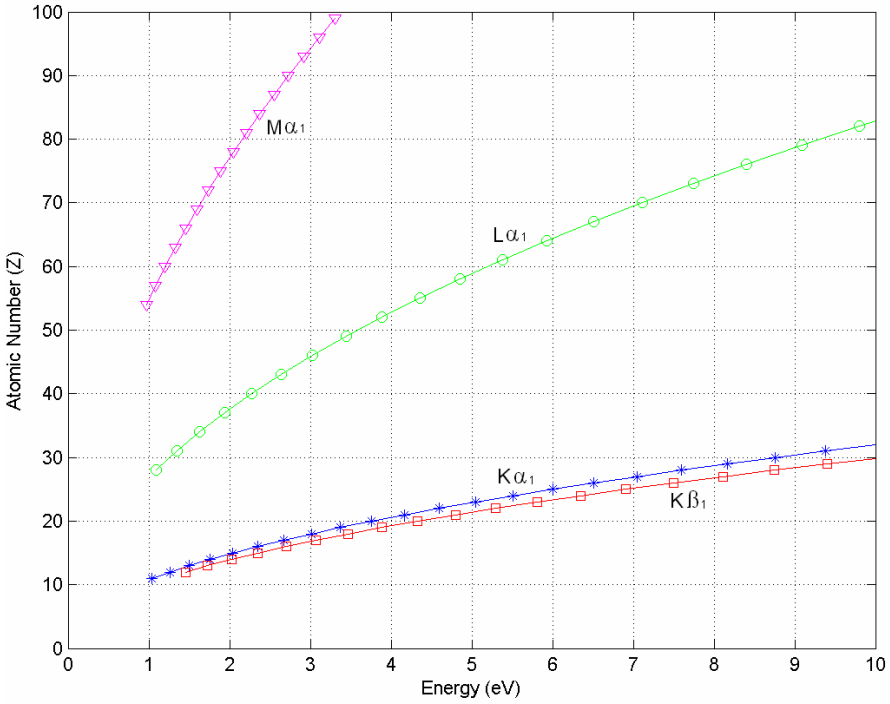

Figure 1.5: Relationship between energy and atomic number of characteristic X-rays

Once a K shell electron has been filled by an electron from a higher energy shell, 2 processes can occur. Either the de-excitation of the atom causes the release of a characteristic X-ray photon, or the energy is emitted as an Auger electron. The fluorescence yield w_i, can be approximated using the expression [Krause 1979]:

$$w_i = \frac{Z^4}{A_i + Z^4} \quad , \tag{1.4}$$

where A_i is a constant with a value of ~ 10^6 for the K shell and 10^8 for the L shell. The yield of Auger electrons for a given shell is 1 minus the fluorescence yield and is shown in figure 1.6.

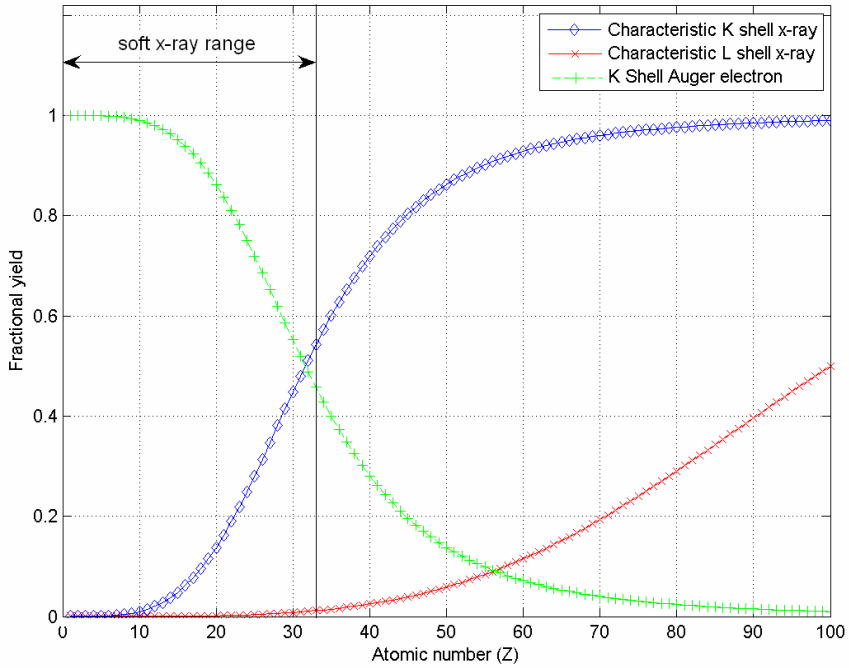

Figure 1.6: Fractional yield of characteristic X-ray photons and Auger electrons

At lower Z elements, K shell Auger electrons are more predominant than K shell characteristic photons. By exciting atoms in powder grains with high energy X-rays, the emission of characteristic photons can be detected by the CCD and XRF analysis can be performed [Lumb & Holland 1998]. Figure 1.7 shows the detection of multiple characteristic X-rays from elements in peridotite collected with a CCD.

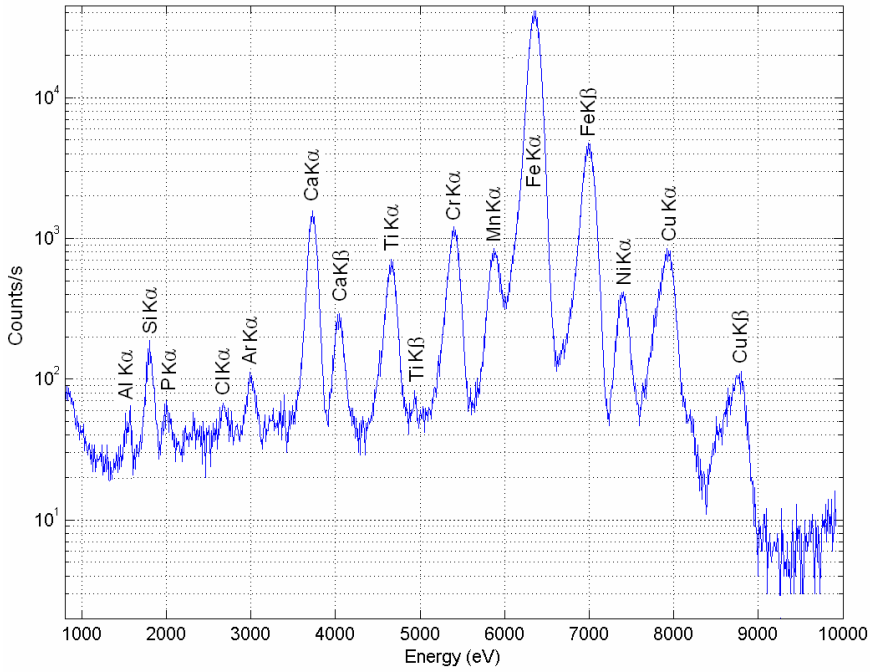

Figure 1.7: XRF spectrum of peridotite powder collected with a CCD

1.4 Combined XRD/XRF

In recent years there has been an increase in demand for instruments that can collect both XRD and XRF information simultaneously, especially in the planetary sciences sector [Blake et al. 1992, 2000] [Cornaby et al. 2001]. The difficulty in spatial calibration of XRD equipment as well as a need for high X-ray flux and intensive sample preparation has prevented the use of XRD for planetary science. To date, an XRD instrument has never been deployed for any planetary mission. However, research into combined XRD/XRF instruments has been widespread in recent years especially in Europe [Marinangeli et al. 2007] and the USA [Sarrazin et al. 2005]. The National Aeronautics and Space Administration (NASA) has announced the presence of a combined XRD/XRF instrument called Chemin (see Section 1.6), on the 2011 Mars Science Laboratory (MSL). The European Space Agency (ESA) has also announced a combined XRD/XRF instrument to be used on the 2016 ExoMars rover. Both of these missions aim to identify the mineralogy and chemical composition of the Martian surface, which may indicate the presence of past or present life. Both instruments will include CCD detectors, which further highlights the recognition of CCDs as X-ray spectroscopy detectors.

Various in-situ XRF instruments have been successfully deployed on Mars missions (Viking 1 and 2, Mars Pathfinder). These instruments revealed vast amounts of chemical information regarding the measured samples. Aided by less critical equipment geometry (compared to XRD) and lower X-ray excitation flux, XRF has always prevailed a more conducive technique for the classification of rocks than XRD.

XRF only reveals the chemical composition of the sample and does not yield a definitive mineralogical solution. For example, calcium carbonate ($CaCO_3$) exists in many different forms such as aragonite, limestone and chalk. Bombarding these samples with X-rays and measuring the energy of characteristic X-rays would simply reveal calcium (Ca), carbon (C) and oxygen (O) for all 3 samples. The chemical data provides multiple possibilities for the mineralogy and cannot definitively identify the analysed sample.

For this reason, combining XRD is important to clarify any uncertainties from XRF data. Both techniques should complement each other in their findings and reveal both chemical and mineralogical information regarding the sample under investigation. Using the example of $CaCO_3$, XRD techniques can find the position of the 3 largest diffraction peaks to be that of aragonite, with the use of the ICCD PDFs. Applying XRF analysis would reveal the presence of Ca, C and O characteristic X-rays which would compliment the data obtained from the XRD observations. All future references to $CaCO_3$ refer to aragonite powder samples.

1.5 In-situ X-ray Spectroscopy on Mars

The first attempts of Mars exploration began in the 1960's when several USSR probes failed to reach the red planet such as Marsinik 1, 2 and Sputnik 22, 24. The first successful mission to Mars occurred on July 14th 1965 when NASA's Mariner 4 returned 22 images of the Martian surface revealing distinct crater formations. These images suggested that water played a significant role in shaping the Martian landscape [Kargel 2004]. Since water is the key ingredient in determining if life ever arose on the red planet [McKay 1986], the exploration of Mars is easily justified [Harland 2005]. Applying X-ray spectroscopy on the Martian surface is vital in detecting the presence of rocks and minerals that contain, or have been altered by water.

XRF chemical data has been collected by various surface landers on Mars. XRF instruments have been used on 2 Viking landers, the Mars Pathfinder and the Mars Exploration Rover (MER). XRD techniques have never been used for planetary exploration, however an XRD instrument was proposed for analysis of the Lunar surface [Blake 2000] in the late 1960s. Combined XRD/XRF will be attempted for the first time in 2011 on Mars with the use of Chemin [Blake et al. 1992b]. This instrument is similar to the CCD-Array as both instruments use CCD detectors. The next section briefly describes the XRF instruments that have been mentioned above, with particular emphasis on their detector capabilities.

1.5.1 Viking XRF Spectrometer

In 1976, 2 Viking landers reached Mars landing 6500 km apart. Both landers contained an XRF spectrometer (XRFS) which became the first instruments to

perform in-situ chemical analysis of the Martian surface [Clark et al. 1977]. X-ray generation was achieved using 2 radioactive Fe^{55} and Cd^{109} sources, which produced characteristic X-rays at 5.9, 22.2 and 87.7 keV. The use of Cd^{109} allowed the majority of elements to be analysed. The characteristic X-rays were detected using 4 gas proportional counters (GPCs) with a FWHM capability of 1.2 keV at 5.9 keV. Although solid-state detectors provided much higher energy resolution, GPCs were used because they required no cooling and could operate at ambient Martian temperatures.

Due to window sensitivity and detector properties, the low energy detection limit of the instrument was limited to Na Kα X-rays (1041 eV). Due to the poor energy resolution of GPCs, accurate quantitative results were difficult to achieve, however computer modelling of the data suggested the main composition of the surface consisted of SiO_2 (45%), Fe_2O_3 (18%), Al_2O_3 (5%), MgO (8%), CaO (5%) and SO_3 (8%) [Clark et al. 1982].

1.5.2 Mars Pathfinder – APXS

The Alpha Proton X-ray Spectrometer (APXS) was one of 3 instruments on board the Mars Pathfinder Rover, called Sojourner, which landed on July 4th, 1997. The APXS operated in 3 modes using alpha particles, protons and X-rays to excite Martian rocks and soils [Rieder et al. 1997]. Three solid-state detectors were used for each mode of operation. The characteristic X-rays emitted from the sample in XRF mode were detected using a Si PIN detector (Amptek XR-100T). The detector operated at ambient Martian temperatures, achieving a resolution of ~ 250 eV at 6403 eV [Redus et al. 2001].

Data in XRF mode was collected at night for periods of 10 hours. Due to poor energy resolution, many X-ray peaks overlapped such as Na Kα, Mg Kα, Al Kα and Si Kα and peak fitting algorithms were required for quantitative results. The APXS sensor analysed 6 soils and 5 rocks, however the data obtained in the alpha and proton mode was corrupted due to high levels of CO_2 in the Martian atmosphere. The data obtained in XRF mode provided the most credible results, portraying the Martian landscape to be richer in Silica (SiO_2) than measurements made by the Viking XRFS. A summary of elemental abundances from 3 soils and 2 rocks are shown in table 1.1

Elements	Symbol	A - 2 soil	A - 4 soil	A - 5 soil	"Barnicle Bill" - rock	"Yogi" - rock
carbon	*C*	-	-	-	-	-
oxygen	*O*	42.5	43.9	43.2	45	44.6
sodium	*Na*	3.2	3.8	2.6	3.1	1.9
magnesium	*Mg*	5.3	5.5	5.2	1.9	3.8
aluminium	*Al*	4.2	5.5	5.4	6.6	6
silicon	*Si*	21.6	20.2	20.5	25.7	23.8
phosphorus	*P*	-	1.5	1	0.9	0.9
sulphur	*S*	1.7	2.5	2.2	0.9	1.7
chlorine	*Cl*	-	0.6	0.6	0.5	0.6
potassium	*K*	0.5	0.6	0.6	1.2	0.9
calcium	*Ca*	4.5	3.4	3.8	3.3	4.2
titanium	*Ti*	0.6	0.7	0.4	0.4	0.5
chromium	*Cr*	0.2	0.3	0.3	0.1	0
manganese	*Mn*	0.4	0.4	0.5	0.7	0.4
iron	*Fe*	15.2	11.2	13.6	9.9	10.7
nickel	*Ni*	-	-	0.1	-	-
Sum		100	100	100	100	100

Table 1.1: Preliminary results of elemental abundances of 3 soils and 2 rocks measured by the Pathfinder APXS on Mars

1.5.3 MER – APXS

In 2004, 2 rovers named Spirit and Opportunity successfully landed on Mars. Since a proton mode was not included in the new APXS sensor, the sensor was known as the Alpha Particle X-ray Spectrometer [Rieder et al. 2003]. The major improvement in the sensor was the detector, which was now a Si drift detector [Lechner et al. 2004]. This detector achieved a 160 eV FWHM at 5898 eV, which was a significant improvement on the pathfinder APXS. Due to this increased resolution, elements between 1 − 2 keV were uniquely identified without the need for complex peak fitting algorithms. X-ray excitation was provided using a radioactive Cm^{244} source and data was collected for periods of 2 − 4 hours in the Martian night. The Si drift detector has provided the highest energy resolution of any XRF detector on Mars to date.

1.6 Chemin

Chemin is named after its ability to collect both chemical (“chem”) and mineralogical (“min”) information from powder samples simultaneously. Chemin is a miniaturised XRD/XRF instrument [Bish et al. 1998, 2007], which will be part of NASA’s MSL, planned for launch in 2011. During MSL’s 1 Martian year lifetime (687 Earth days), Chemin will analyse up to 74 samples, with data collection times of up to 10 hours for each sample. Data will be transferred back to Earth for further processing and analysis.

The purpose of the CCD-Array built for this thesis and the Chemin instrument are identical. The aim of both instruments is to simultaneously collect both XRD and XRF information from powder samples using CCDs. The original Chemin geometry was in reflective mode, which was more suited to XRF analysis. However, Chemin now employs the transmission geometry, which is not conducive to XRF analysis since the incident beam is highly absorbed at the detector side of the sample and therefore, the flux of characteristic X-rays produced on the detector side is very low. XRF analysis with the Chemin instrument is now performed on a 'best efforts' basis. Figure 1.8 shows the geometry of the Chemin instrument.

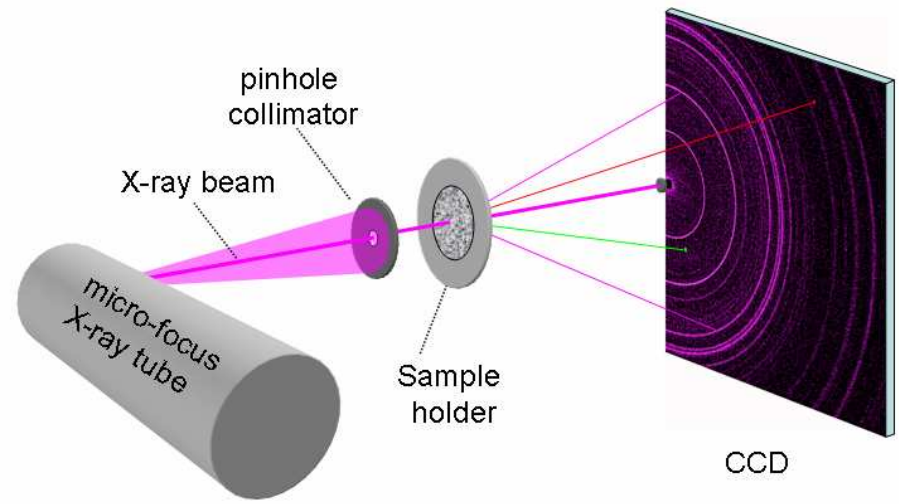

Figure 1.8: Transmission geometry of the Chemin instrument (image courtesy of NASA)

The X-ray source is Oxford Instruments Apogee^{TM} micro-focus tube with a Cobalt (Co) anode and 50 µm spot size. As shown in figure 1.8, a 30 µm spot of the sample is irradiated using a pinhole to improve the resolution of the diffracted beams. The X-rays produced by the source are characteristic Co Kα (6903 eV), Co Kβ (7649 eV) and continuous X-rays with a maximum energy dependant on the applied voltage (usually operated at 40 kV resulting in 40 keV photons). The CCD used is e2v technologies CCD224, which is a deep depletion, frame transfer device with a 600 × 582 imaging area and $(40\ \mu m)^2$ pixels. This device produces a 50 µm depletion depth which increases the amount of isolated events detected by the CCD in comparison to a standard device. The use of larger pixels also increases the detection

of isolated events as fewer X-ray ionise in between pixel boundaries resulting in split events. To eliminate dark current the CCD is cooled between -60 °C and -100 °C using a cryocooler. The top electrode structure of the device has also been thinned over portions of the pixel area, to increase the QE at lower X-ray energies. To increase the detectors opacity to light, a 0.15 µm Al film supported by a 0.2 µm polyimide film is placed in front of the CCD.

Samples are delivered to the Chemin instrument from the Sample Acquisition/Sample Handling and Processing (SA/SPaH) system, through a funnel. Powder samples are placed in a sample wheel which contains 27 reusable 'cells', and 5 cells pre loaded with standard reference materials (SRMs) for calibration. The funnel contains a 1 mm mesh, although powder grains will be pre sorted to < 150 µm by the SP/SPAH, prior to entering the Chemin funnel. If grains with a diameter between 1 mm and 150 µm pass through the funnel, they will remain in the upper reservoir section of the sample cell until the cell is rotated 180° clockwise, where the sample will be dumped into the sump. The funnel receives 65 mm^3 of sample, 10 mm^3 of which is required to fill the sample cell. Each sample cell is a circular disc with an 8 mm diameter and 175 µm thickness. During the filling of the sample cells, piezoelectric actuators are used to ensure the sample cell is tightly filled with grains and during emptying of the sample cells, the actuators ensure any grains stuck to any part of the cell are removed. The piezoelectric actuators are also used during analysis to vibrate the sample and increase the random orientation of powder grains. The sides of the sample cells (where the incident beam enters and diffracted X-rays depart) contain either 6 µm of Mylar or Kapton to hold the samples in place. Mylar contains a very low diffraction background in comparison to Kapton, which contains a diffraction peak at $6° - 7°$ 2θ. This can be problematic when analysing clay minerals, which contains low angle peaks in this range. Kapton is however more durable than Mylar, which is important when analysing acidic samples, therefore 14 sample cells are equipped with Mylar windows, and 13 cells contains Kapton. Once the sample has been loaded, the incident X-ray beam irradiates the centre of the 8 mm disc. Once all exposures have been collected, data is transmitted back to Earth and once a satisfactory analysis has taken place, the sample wheel is rotated 180° and the analysed sample is dumped.

By applying the single photon counting technique, the Chemin CCD detector can distinguish the energy of incident X-rays (energy resolution of 240 eV at 6.4 keV) as well as determine the spatial position of diffracted X-rays (40 µm spatial resolution). This technique requires an exposure time which does not allow the CCD to become saturated with charge, and thereby prevent > 1 photon being detected by a single pixel. By determining the position of all isolated Co Kα X-rays detected in all exposures, a 2-dimensional diffraction pattern can be generated, as shown in figure 1.9. This image is a 600 × 582 array, where each pixel contains a number N_{diff}, which represents the number of diffracted photons collected in that pixel over all exposures. Figure 1.9 shows the XRD pattern of non-purified silver behenate collected by the Chemin instrument.

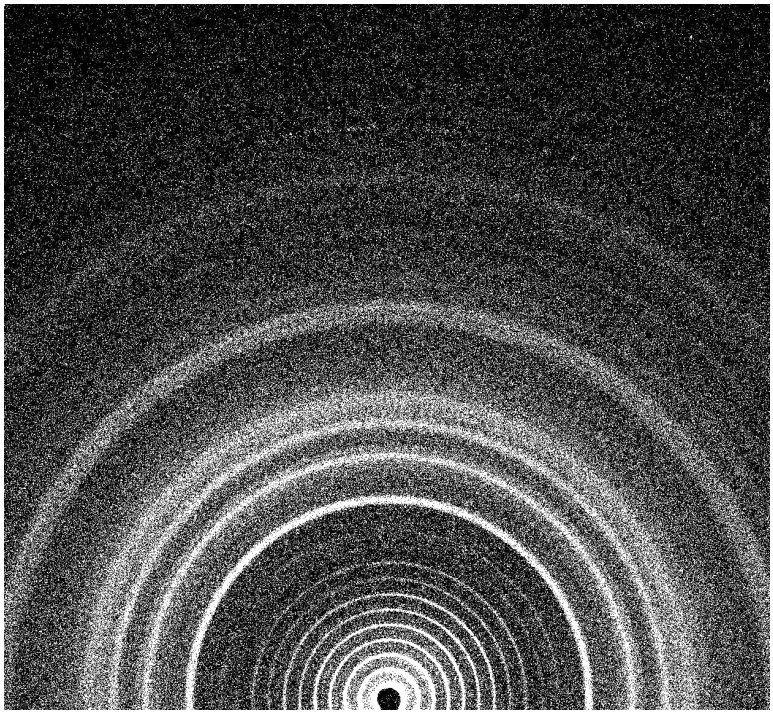

Figure 1.9: XRPD pattern of non-purified silver behenate collected by the Chemin instrument (image courtesy of NASA)

Once the 2-dimensional image has been generated, the diffraction rings are radially integrated to produce the 2θ vs. intensity diffractogram. Both qualitative and quantitative analysis can then be performed. A beam stop is used to prevent the incident beam from being detected by the CCD. Its location is at the bottom centre of the CCD and can be seen in figure 1.9.

By accumulating all isolated events collected in all exposures, a histogram is generated which contains the elemental/chemical information. Due to the 6 µm sample cell window and Al film covering the detector, the low energy detection limit are elements with an atomic number > 11 (> Na Kα (1041 eV)). The higher energy detection limit is dependant on the operating voltage of the 40 kV X-ray source, however even when operated at 10 kV, all elements with a K shell emission in the soft X-ray range can be detected. A summary of the Chemin instruments specifications are given in table 1.2.

Parameter	Information
X-ray source	Microfocus source, Co anode
Sample irradiation spot size	30 µm
XRD/XRF geometry	Transmission
2θ angular range	5 - 55º
2θ FWHM resolution	0.26º
Spatial resolution	40 µm
CCD	CCD224
CCD Format	FI, deep depletion, frame transfer
CCD Operating temperature	(- 60 ºC) - (- 100 ºC)
CCD imaging area	600 × 582 pixels
XRF energy resolution (at 6.4 keV)	240 eV FWHM
CCD energy range	1 - 15 keV
Single exposure times	5 - 30 s
Typical number of exposures	60 - 10,000
Typical data collection time	10 hours

Table 1.2: Summary of Chemin specifications

Chemin will be the first in-situ X-ray diffractometer ever used for planetary exploration and will attempt to unequivocally determine the Martian mineralogy. The Chemin instrument was successfully tested in Badwaters Flat, Death Valley, California in May 2004 [Sarrazin et al. 2005].

1.7 Terra

Terra is a commercial model of the Chemin instrument, designed by inXitu. Terra is the first portable XRD/XRF analyser, which can be used for in-situ analysis on the field. The entire assembly including battery, X-ray source, sample holder and CCD detector is held within a briefcase weighing less than 15 kg. The geometry of the Terra instrument is similar to the Chemin flight model, however samples are loaded manually into a removable sample holder. Sample are ground to < 150 µm grains and

then loaded into the single sample cell, which is vibrated during data collection using piezoelectric actuators to vary orientations of particles within the incident X-ray beam. The sample holder is then refitted into the instrument and locked in place.

The Co X-ray source is operated at 30 kV, 300 µA and allows the detection of characteristic X-rays from Ca (Z = 20) to Uranium (Z = 92). The low energy detection limit of the instrument is currently not optimised [Chipera et al. 2009], since some of the key elements found in rocks ranging from 1 − 2 keV are too highly absorbed to be detected. The background spectrum also contains characteristic X-ray peaks from Cu, Fe and Zn due to the components within the instrument, which must be subtracted from the XRF spectrum. The device can be powered using an AC adapter, or can be operated for ~ 4 hours with the use of 4 Lithium-ion batteries that are contained within the 15 kg instrument. The data collection process is initiated through the digital display, which can be accessed wirelessly using any 802.11b compliant device. Some of the key properties of the Terra device are listed in table 1.3.

Parameter	Information
Wieght	14.5 kg, with 4 batteries
Size	48.5 cm × 39.2 cm × 19.2 cm
XRD FWHM resolution	0.26º
XRD angular range	5 - 55º 2θ
Detector	Peltier cooled CCD
Detector image area	1024 × 256 pixels
XRF energy resolution	230 eV at 5898 eV
XRF energy range	3 - 25 keV
Sample grain size	150 µm grains
Sample quantity	< 15 mg
X-ray target material	Cobalt
X-ray tube voltage	30 kV
X-ray tube power	10 W
Battery lifetime	~ 4 hours
Power consumption	85 - 90 W
Data storage	40 Gb internal hard drive
Wireless connectivity	802.11 b
Operating temperature	(-20º C) - (+35º C)
Enclosure	Rugged case

Table 1.3: Summary of Terra instrument specifications

Terra is geared towards applications that require on site analysis, such as pharmaceuticals, forensics, archaeology, geology and material sciences. Data is

collected in a similar manner to the Chemin flight model and qualitative XRD analysis can be performed in seconds [Chipera et al. 2009]. Quantitative analysis can be performed on the 2θ vs. intensity pattern after data collection using programs such as GSAS [Larson & Von Dreele 1994].

1.8 Research Goals

The main aim of the project was to design and develop a novel CCD array detector, capable of simultaneously collecting combined XRD/XRF data from powder samples. A test facility was designed for initial testing of the portable detector. Particular emphasis was based on optimising the geometry of the CCDs in relation to the sample, which determined the resolution and angular range achieved by the detector for XRD applications. Based on the lessons learned from testing the CCD-Array in a laboratory environment, recommendations for a 2nd generation CCD-Array would be suggested.

The second goal of the project was based on characterisation and testing. Accurate qualitative analysis required spatial calibration of the CCD-Array and intensity calibration of the CCDs was required for accurate quantitative analysis. Thermal characterisation of the detector was also required to determine the TECs performance in cooling the CCDs. The operational performance of the CCD30-11 was also investigated which included characterisation of the dark current, readout noise, energy/angular resolution, depletion depth and QE performance. The temperature and power requirements of the CCD-Array to perform combined XRD/XRF analysis were also investigated.

The final aim of the project was to determine the ability of the CCD-Array to meet the science requirements of different applications, namely in the planetary sciences and pharmaceuticals sector. The use of the CCD-Array in such applications is discussed and optimisation of the geometry is suggested.

The work carried out for this thesis was funded by a Co-operative Award in Science and Engineering (CASE) studentship from the Engineering and Physical Sciences Research Council (EPSRC) in collaboration with e2v technologies (formerly Marconi, formerly EEV) of Chelmsford, Essex, UK.

1.9 Thesis Organisation

This thesis is organised into 6 further chapters. Chapter 2 discusses the geometry options available for XRD analysis, namely the parallel beam and Bragg-Brentano geometry. The options are compared in terms of resolution and flux and the geometries most suited to portability and testing are outlined.

Chapter 3 describes the structure and operation of CCDs and the different noise sources that limit their performance for X-ray spectroscopy applications. The ability of the CCD to detect X-rays in the soft X-ray range is also discussed, which includes features such as energy resolution, charge transfer efficiency, charge diffusion and QE. Chapter 3 also presents theory governing the production of X-rays. A model of a typical X-ray spectrum is generated using relevant theory and compared to actual spectra collected with the Bede micro-source. It is shown the X-ray spectra produced from the source without X-ray optics, resembles a blackbody curve with intense Cu Kα and Cu Kβ characteristic X-rays. The advantages of using X-ray polycapillary optics for XRPD applications are highlighted. The flux produced by the Bede micro-source with respect to tube voltage and current is also calibrated, and the background spectra produced in XRD and XRF patterns are presented.

Chapter 4 discusses the design of the CCD-Array and test facility. Each of the individual components of the detector are described, including the on-board headboard electronics and X-ray window. A thermal study is also presented, which calculates the different heat loads (passive/active) within the CCD-Array during cooling and confirms these calculations through thermal measurements. The ability of the test facility to absorb and dissipate heat using a circulating coolant is discussed. The designed geometry of the CCD-Array is presented and confirmed with the use of SRMs. The main components of the test facility are reviewed with particular emphasis on the collimation and monochromation process.

Chapter 5 describes the data collection, analysis and modelling of combined XRD/XRF data using CCDs. Since XRD analysis using CCD detectors is a relatively new technique, the majority of this chapter focuses on XRD. Since the key to collecting XRD/XRF data is detecting isolated X-ray events, the initial section of this chapter confirms the depletion depth of the CCD30-11 devices using X-ray spread

event analysis and comparative measurements with devices of known resistivity. The data collection process is investigated and methods of reducing XRD noise in CCD images are presented. The advantages and disadvantages of different CCD architectures for XRD analysis are also discussed. The final section presents results from a novel modelling program, designed to simulate the collection of XRPD data using CCDs. The results are shown to be in very good agreement with the experimental data. The model allows users to pre-calculate optimised CCD integration times, calculate total diffracted events, determine pixel event statistics and understand the effect of CCD binning during data collection.

Chapter 6 is concerned with the operational performance of the CCD-Array. Problems that may be encountered by a portable instrument are discussed, which include sample preparation issues, power consumption and the CCD operating temperature required to perform combined XRD/XRF analysis. The application of the CCD-Array in the planetary sciences sector and the pharmaceuticals industry is also discussed.

Chapter 7 outlines the main conclusions of this thesis and describes possible future work.

A table containing information about the test samples mentioned in this thesis can be found in Appendix A.

1.10 Publications

The following publications feature work presented in this thesis:

Intisar, A., Hutchinson, I., Holland, A., Simpson, D.J., Pool, P., 2008. Development of a CCD-Array detector for combined XRD/XRF applications. Proc. SPIE, Vol. 7021.

Chapter 2 : XRD Geometry Design

This chapter presents the different geometries available for the CCD-Array to perform XRD analysis. The advantages and disadvantages of the different geometries are presented and the optimum arrangement for testing the CCD-Array is determined. For a portable instrument, the main factor dictating the type of XRD geometry used is the X-ray source. Traditionally, radioactive sources have been utilised by portable spectrometers, due to their small size, low mass and the fact that they can operate without any power consumption or external electronics. The fluorescence yield of elements from 1 − 10 keV ranges from approximately 0.01 − 0.54 [Krause 1979], which is a reasonably efficient process. However, XRD efficiencies range from 10^{-6} − 10^{-3}. XRD experiments therefore require a higher flux of incident X-rays to achieve a similar throughput to XRF experiments. For this reason, research into low power X-ray tubes for in-situ combined XRD/XRF analysis has been widespread in recent years [Cornaby 2002], however, this requires increased instrument volume, mass and power consumption. Divergent X-rays produced from a radioactive source or miniature X-ray tube can be used to provide a geometry known as Bragg-Brentano (BB). If a miniature X-ray tube with special X-ray optics is used (usually a polycapillary collimating optic for XRD applications), then an alternative geometry known as parallel beam (PB) can be used. Both options are considered and a comparison in terms of flux and resolution is presented.

2.1 XRD Geometries

2.1.1 Bragg-Brentano

The most popular arrangement used in the majority of laboratory diffractometers is the reflective BB geometry and is shown in figure 2.1. In BB geometry, X-rays diverge from the source, irradiate the sample and are diffracted back onto the focusing circle, with a radius denoted by R_{fc}. In traditional BB diffractometers, the X-ray source and point detector are moved along the measuring circle and as the angle of incidence of the X-ray source θ_{inc}, increases at a given step size (e.g. 0.02°), the resulting diffraction peak at an angle θ (in relation to the sample holder and 2θ in relation to the incident beam axis), is captured by the detector. The resolution achieved in this geometry is determined by the size of the receiving slits at the

detector. This geometry requires very precise and correlated movement of the X-ray source and detector along the measuring circle. It is therefore critical that the X-ray source to sample distance R_{ss}, and the sample to detector distance R_{sd}, are identical. The sample must also be aligned exactly along the curvature of the focusing circle, which requires high precision alignment to prevent common sample related errors such as flat specimen and sample displacement error.

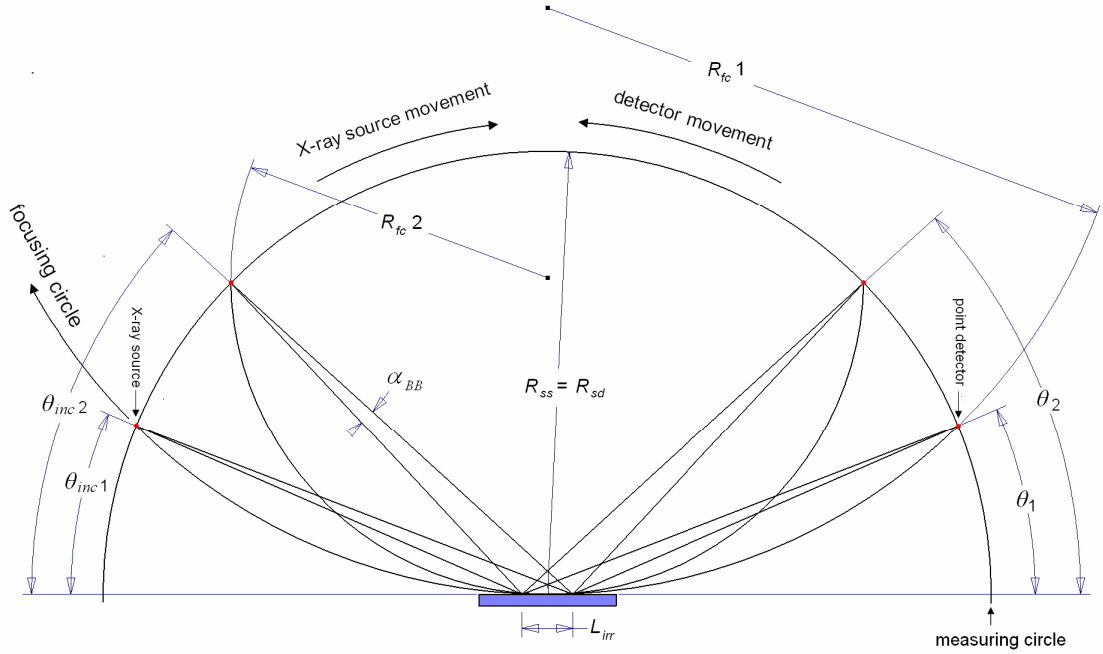

Figure 2.1: Traditional BB reflective geometry ($R_{ss} = R_{sd}$)

For a portable instrument, precise movement of the X-ray source and detector along the measuring circle is very difficult to implement and requires extra components and complexity. For portability, the X-ray source and detector positions are fixed and the diffracted X-rays are detected either along the focusing circle or on the measuring circle, without any variation in θ_{inc}.

Due to difficulties in placing CCDs along the focusing circle (for reasons discussed in Section 2.3), arranging the CCDs along the measuring circle is most suited to a portable instrument. As shown in figure 2.4, this geometry results in a decrease in resolution of the diffracted X-ray peaks, since the X-rays are no longer detected on the focusing circle. Since the X-rays are detected by an array of CCDs, receiving slits cannot be used to limit the size of the diffracted beams. Although this geometry results in decreased resolution, a major advantage is that R_{ss} is not required to be the

same as R_{sd}, which results in less alignment errors and easier sample preparation. Data collection times are also greatly reduced since the entire XRD pattern is collected at once using an area detector as opposed to a scanning point detector. The 3 variations to the BB geometry are from this point forward referred to in the format listed in table 2.1.

Geometry	Alignment	Detector location	θ_{inc}
BB_1	$R_{ss} \neq R_{sd}$	Focusing circle	Fixed
BB_2	$R_{ss} \neq R_{sd}$	Measuring circle	Fixed
BB_3	$R_{ss} = R_{sd}$	Measuring circle	Varied

Table 2.1: Summary of BB geometries and labelling format

The use of the BB_2 geometry is most suited to portability, however, applications of the BB_1 geometry are discussed in Section 2.3. The majority of laboratory diffractometers use the BB_3 arrangement and achieve the highest resolution of the 3 geometries but require increased size, precision and sample alignment.

The divergence of the incident X-rays and the length of sample irradiated (L_{irr}) are limited using a collimator. Assuming a collimator of length L_{coll}, is placed between an X-ray source producing divergent X-rays and a sample, with a pinhole size P_{ob}, the angular divergence α_{BB}, can be calculated using the expression:

$$\alpha_{BB} = 2 \times \tan^{-1}\left(\frac{P_{ob} \times 0.5}{L_{coll}}\right). \qquad (2.1)$$

For example, a collimator of ~ 60 mm length, with a 100 µm pinhole, will reduce the divergence of X-rays to < 0.1° (1.7 mrad). Figure 2.2 shows the sample irradiation process in the reflective XRD geometry, which can be used to calculate the sample irradiation length in both BB_2 and PB geometries. The only difference between the two geometries is α_{div}, the angular divergence of the incident beam, which is α_{BB} in the BB_2 geometry (depends on equation 2.1) and α_{PB} in the parallel beam geometry (usually ~ 0.2° at 8 keV). By increasing L_{coll}, α_{BB} can be reduced to the desired divergence, whereas α_{PB} remains fixed by the critical angle of the incident X-rays. This usually means that more sample is irradiated in PB geometry since $\alpha_{PB} > \alpha_{BB}$. However, if the pinhole to sample distance L_{ps}, is small (< 5 mm), then L_{irr} is approximately equal in both BB_2 and PB geometry.

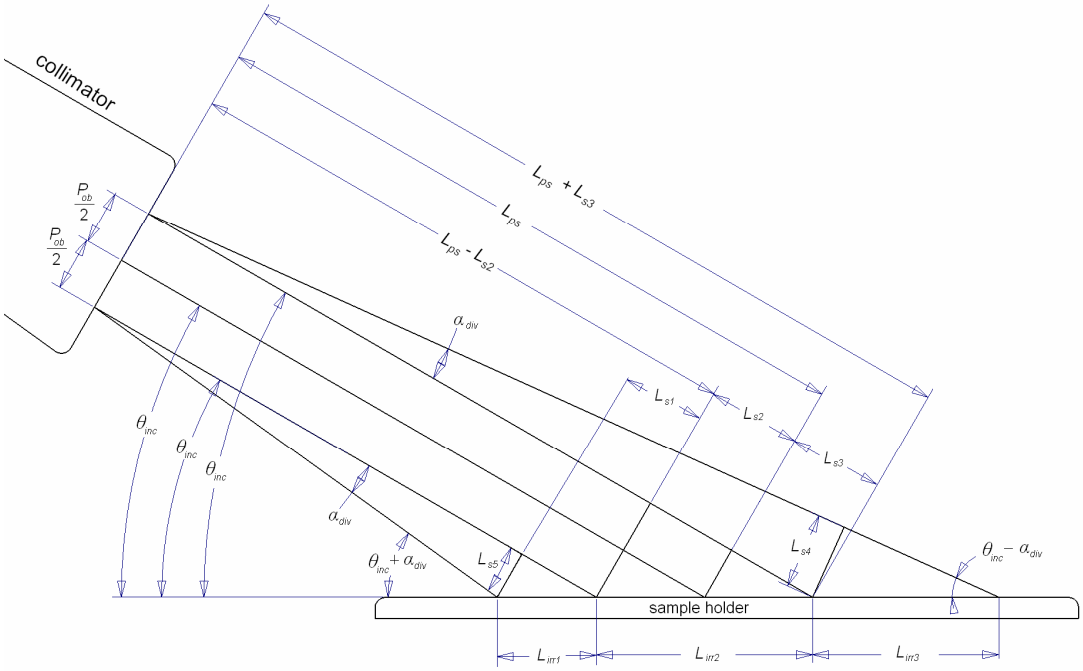

Figure 2.2: Geometry of sample irradiation process in reflective XRD geometry

In figure 2.2, L_{irr2} can be calculated using the expression:

$$L_{irr2} = \frac{P_{ob}}{\sin(\theta_{inc})}, \tag{2.2}$$

and L_{s3} can be calculated as:

$$L_{s3} = \frac{P_{ob}}{2\tan(\theta_{inc})}, \tag{2.3}$$

and L_{s4} can be expressed as:

$$L_{s4} = (L_{ps} + L_{s3}) \times \sin(\alpha_{div}). \tag{2.4}$$

The sample irradiated to the right of the sample centre L_{irr3}, can then be calculated as:

$$L_{irr3} = \frac{L_{s4}}{\sin(\theta_{inc} - \alpha_{div})}. \tag{2.5}$$

Since the sample area located to the right of the sample holder centre is further away from the pinhole than the sample area at the left, L_{irr3} will be much greater than L_{irr1}, especially at low angles of incidence.

Since L_{s1} is approximately equal to L_{s2} and L_{s3}, L_{s5} can be expressed as:

$$L_{s5} = (L_{ps} - 2L_{s3}) \times \sin(\alpha_{div}), \tag{2.6}$$

and L_{irr1} can then be calculated as:

$$L_{irr1} = \frac{L_{s5}}{\sin(\theta_{inc})}. \tag{2.7}$$

Finally, the overall sample irradiation length can be determined as:

$$L_{irr} = L_{irr1} + L_{irr2} + L_{irr3}. \tag{2.8}$$

For high resolution applications, P_{ob} is minimised to reduce L_{irr}, however this reduces the flux incident on the sample and results in increased data collection times. Assuming P_{ob} is minimised to increase resolution, the main factor dictating the resolution of the diffracted beam is θ_{inc}. Figure 2.3 shows the variation in the overall sample irradiation length L_{irr}, with increasing angles of incidence. To minimise L_{irr}, the pinhole should be placed as close as possible to the sample holder. Figure 2.3 also shows the increase in L_{irr} when L_{ps} is increased by 10 mm.

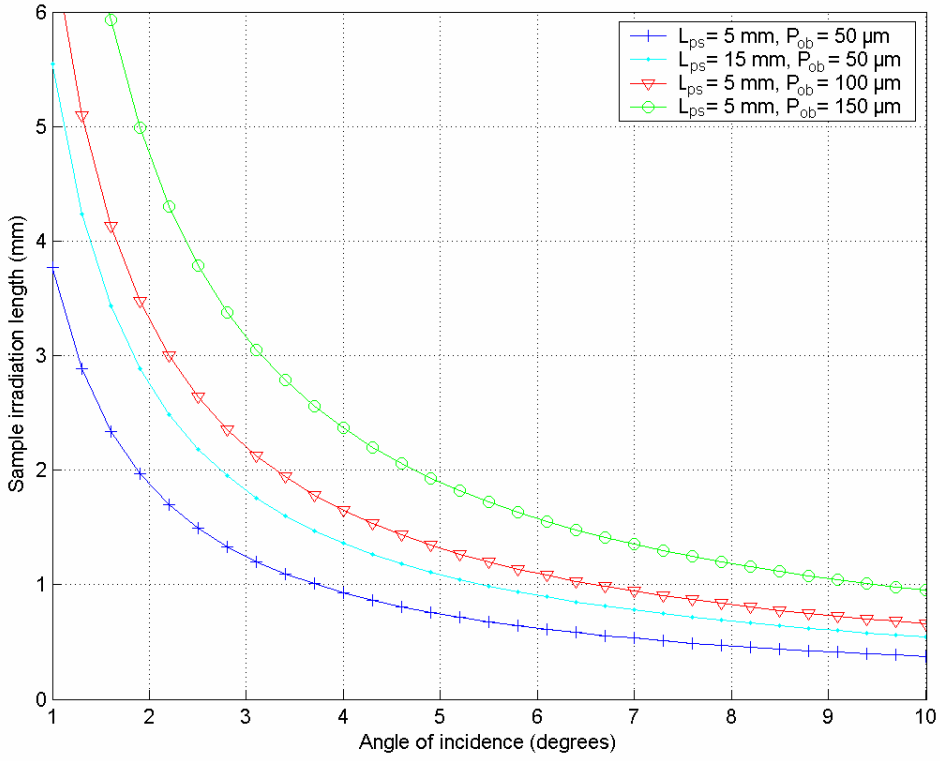

Figure 2.3: Variation in L_{irr} with increasing θ_{inc}

Figure 2.3 emphasises the trade-off between low angle coverage and L_{irr} in the reflective geometry. As θ_{inc} is reduced, L_{irr} increases, thereby increasing the size of the diffracted X-ray beams. Figure 2.4 shows the variation in resolution achieved in BB_2 geometry on different measuring circles.

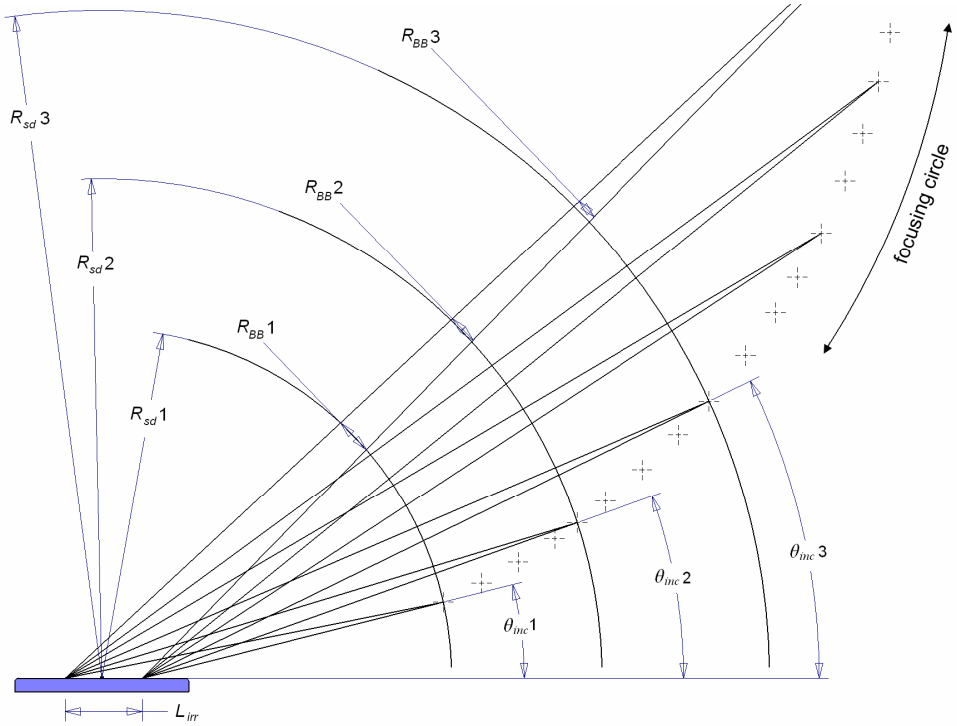

Figure 2.4: Resolution achieved with increasing R_{sd} in BB_2 geometry ($R_{ss} \neq R_{sd}$)

The key features of the BB_2 geometry can be summarised as follows:

- $R_{ss} \neq R_{sd,}$ therefore sample alignment is much easier,
- a decrease in θ_{inc} and increase in P_{ob}, L_{ps} or α_{BB}, results in an increase in L_{irr}. An increase in L_{irr} will increase the size of the diffracted beams and thereby reduce the resolution, R_{BB}, and
- increasing R_{sd} will improve the resolution achieved across the detector (the measuring circle 'R_{sd} 3' in figure 2.4 provides the best resolution, 'R_{BB} 3'), but will subsequently degrade the low angle detection limit (θ_{inc} 3 > θ_{inc} 2 > θ_{inc} 1). The resolution in BB_2 geometry is therefore limited by the angle of incidence. The angle of incidence should always be equal to the half the angle of lowest required 2θ peak.

Figure 2.5 summarises the resolution achieved (FWHM) on a 120 mm measuring circle for different angles of incidence in the BB_2 geometry. These resolutions do not include any broadening effects from the sample.

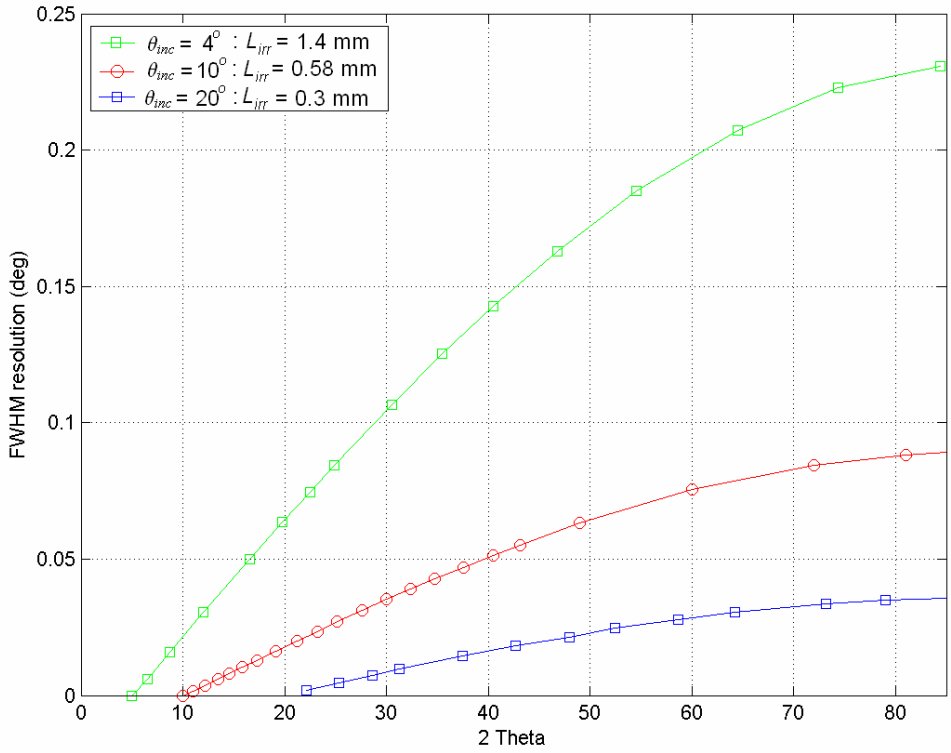

Figure 2.5: Resolution achieved in BB_2 geometry on a 120 mm measuring circle with varying θ_{inc}. P_{ob} = 100 µm

2.1.2 Parallel Beam

An alternative geometry to BB_2 can be achieved with the use of X-ray pollycapillary collimating optics, known as parallel beam (PB) geometry. For example, if a polycapillary collimating optic was fitted to a miniature X-ray tube, the divergent X-rays could be collected over a large solid angle and focused to produce a low divergent beam of quasi-parallel X-rays. This would result in a very large intensity gain and reduce data collection times. Since the X-ray beam is self-focused, there are no focusing circles in this geometry, therefore R_{ss} is not required to be the same as R_{sd}, which results in less precise sample alignment requirements. This eliminates the common sample transparency and flat specimen errors caused in BB_3 geometry. In PB geometry, the angle of incidence is fixed and the CCDs are aligned on the measuring circle, so that they are orthogonal to the diffracted beams. Figure 2.6 shows the arrangement of the PB geometry.

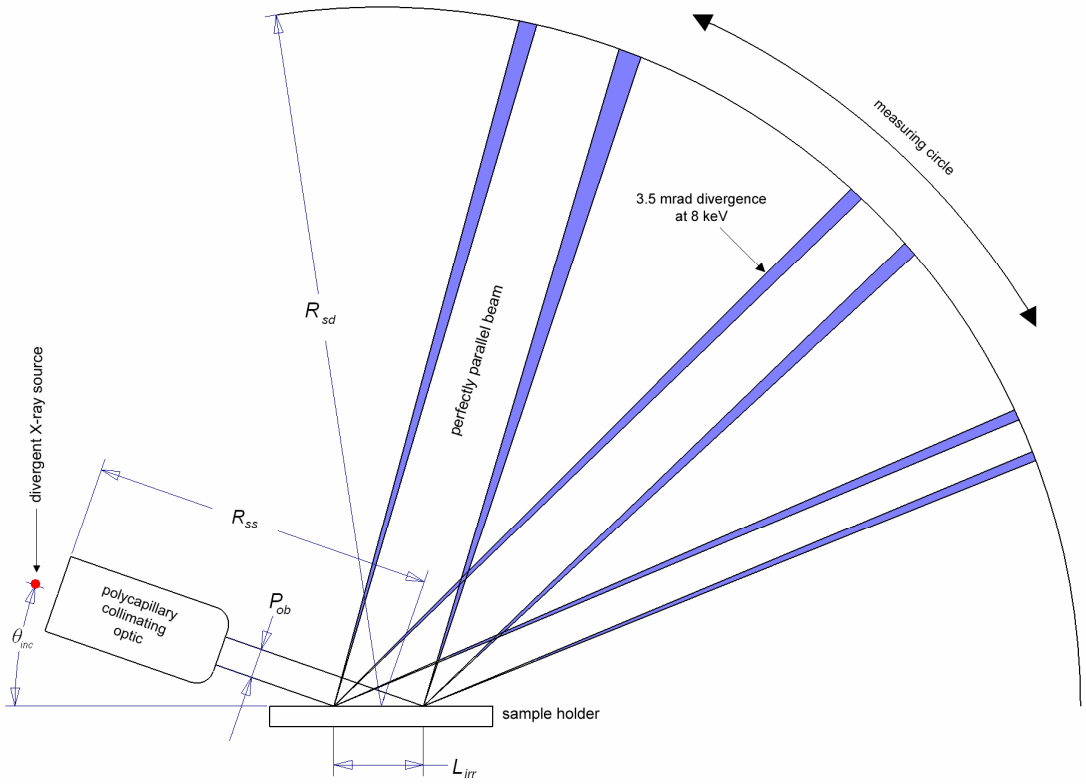

Figure 2.6: Parallel beam geometry ($R_{ss} \neq R_{sd}$)

The geometry of the diffracted beam is shown in figure 2.7.

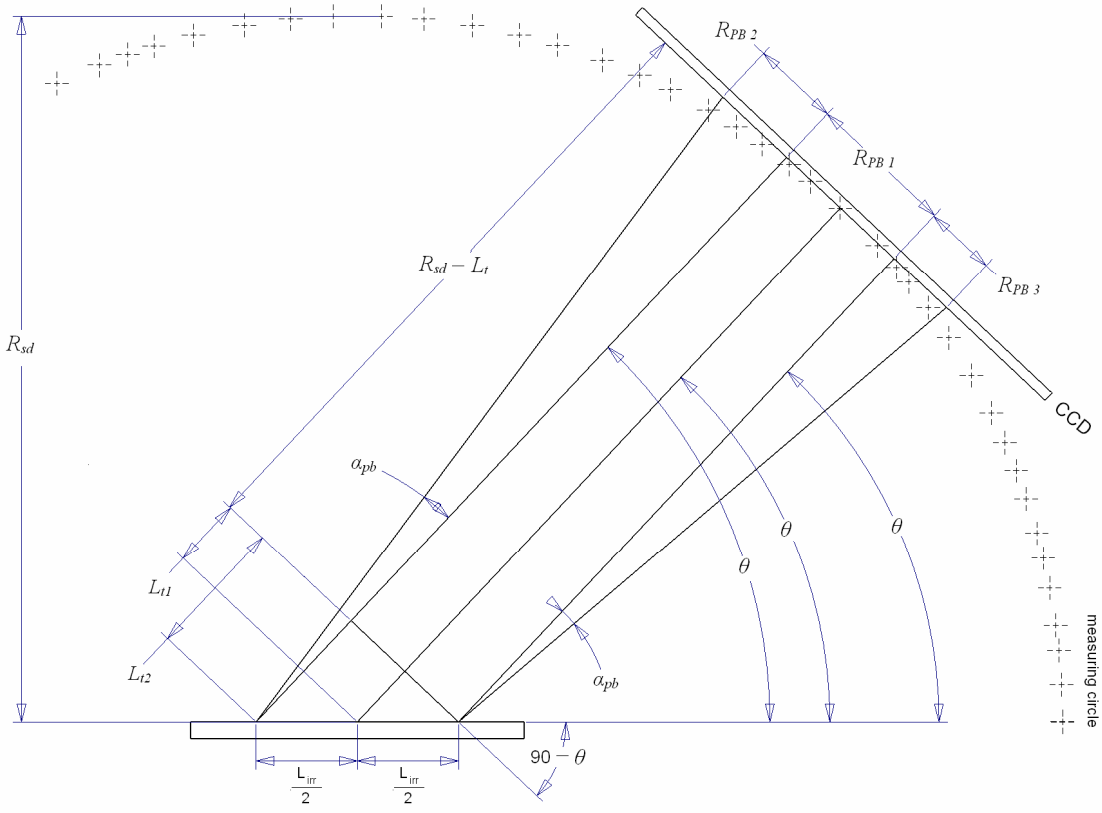

Figure 2.7: Geometry of diffracted beam in PB arrangement

Similar to BB_2 geometry, the resolution in PB geometry is directly related to L_{irr} (L_{irr} is related to θ_{inc} and P_{ob}). The length of sample irradiated in PB geometry can be calculated using equation 2.8.

R_{PB1} is related to L_{irr} and the diffraction angle θ, through the expression:

$$R_{PB1} = L_{irr} \times \cos(90 - \theta). \tag{2.9}$$

X-rays diffracted from the right of the sample holder centre (as shown in figure 2.7) travel a shorter path to reach the measuring circle in comparison to X-rays diffracted from the left , therefore $R_{PB2} > R_{PB3}$. L_{t1} can be calculated using the expression:

$$L_{t1} = \frac{L_{irr} \sin(90 - \theta)}{2}, \tag{2.10}$$

and R_{PB3} can then be calculated using the expression:

$$R_{PB3} = \tan(\alpha_{PB}) \times (R_{sd} - L_{t1}), \tag{2.11}$$

and L_{t2} can be evaluated as:

$$L_{t2} = \sin(90 - \theta) \times L_{irr}, \tag{2.12}$$

and R_{PB2} can then be calculated using the expression:

$$R_{PB2} = \tan(\alpha_{PB}) \times (R_{sd} - L_{t2}). \tag{2.13}$$

Finally, the overall resolution of the diffracted beam R_{PB}, can be expressed as:

$$R_{PB} = R_{PB1} + R_{PB2} + R_{PB3}. \tag{2.14}$$

The typical FWHM divergence of X-rays from a polycapillary optic is ~ 3.5 mrad (~ 0.2°) at Cu Kα (8047 eV).

Figure 2.8 summarises the FWHM resolution achieved in PB geometry with increasing P_{ob}. These resolutions do not include any broadening effects from the sample.

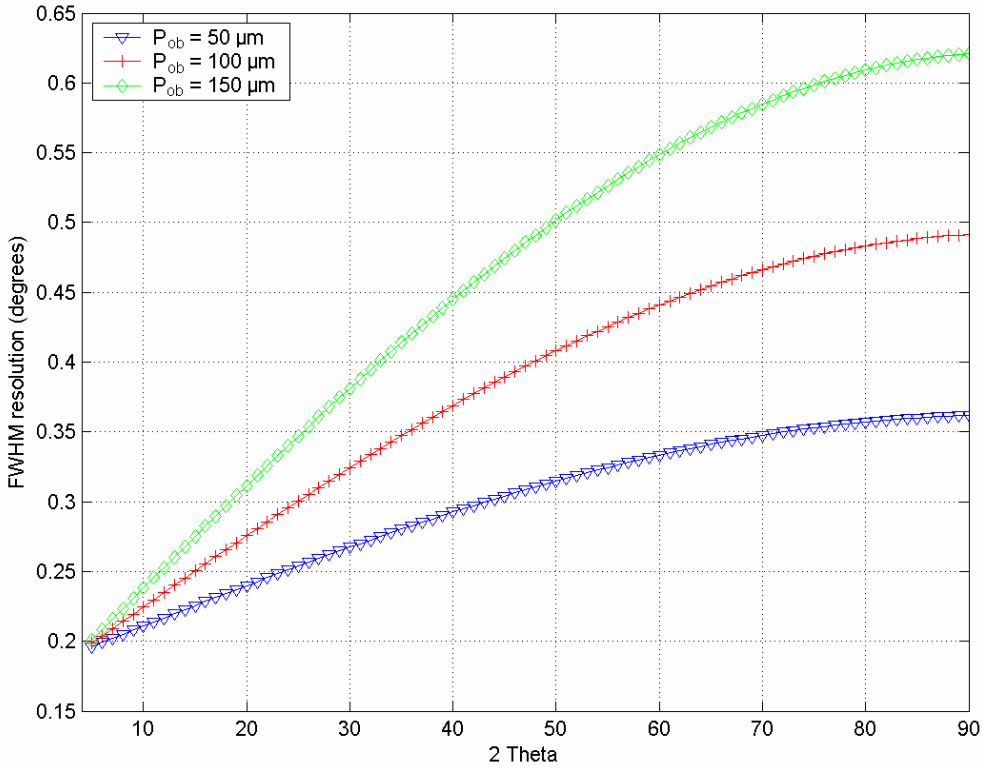

Figure 2.8: Variation in resolution with increasing P_{ob} in PB geometry. α_{PB} = 0.2°, θ_{inc} = 4° and R_{sd} = 120 mm

The key features of the PB geometry can be summarised as follows:

- $R_{ss} \neq R_{sd}$, therefore sample alignment is much easier,
- by using X-ray polycapillary collimating optics, a highly divergent beam of X-rays can be focused into a quasi-parallel beam (the X-rays are termed 'quasi-parallel' since the emission angle of X-rays is not perfectly parallel to the optic, but at very small angles (2 − 3.5 mrad)) and results in an increased gain in intensity of the diffracted X-rays, and
- a decrease in θ_{inc} results in an increase in L_{irr}. R_{PB} is proportional to L_{irr}, therefore for low angle coverage, the resolution achieved across the detector decreases, as shown in figure 2.9. Larger beam sizes increase the incident flux irradiating the sample, but cause an increase in L_{irr}, and hence, a reduction in resolution.

Figure 2.9 shows the trade-off between low angle coverage and resolution in the PB geometry, with a beam diameter of 50 µm.

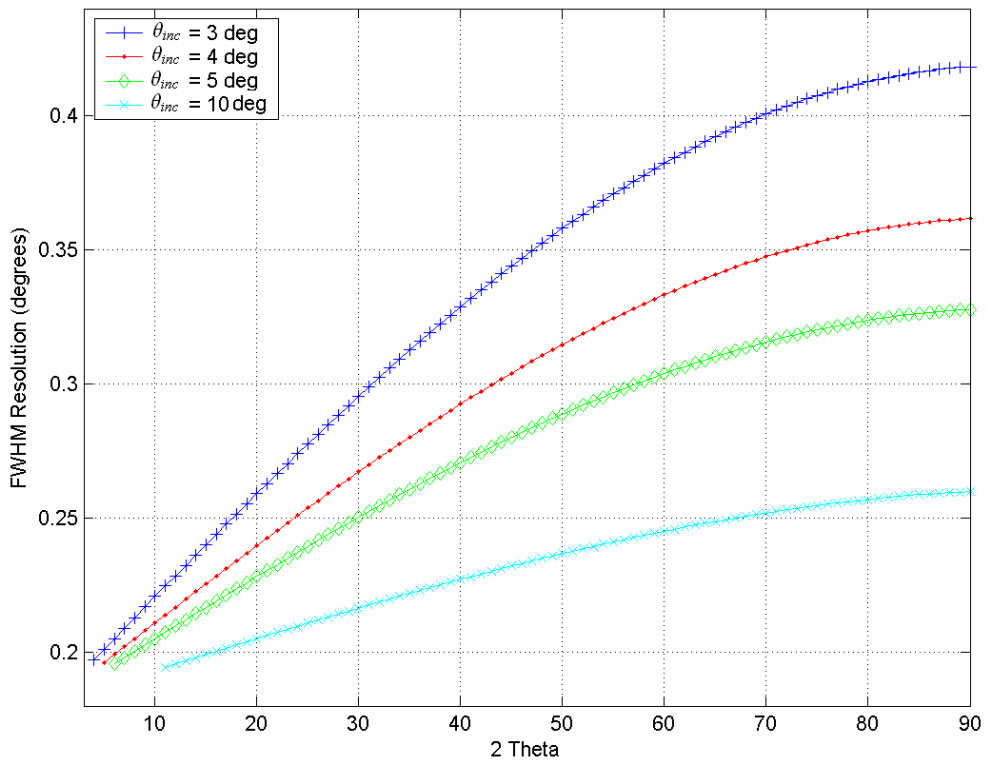

Figure 2.9: Variation in resolution with increasing angle of incidence in PB geometry

2.2 Portable X-ray sources

As previously mentioned, the main factor dictating the XRD geometry for a portable instrument is the X-ray source. Three main sources can be considered, which consist of a radioactive source, a miniature source producing divergent X-rays and a miniature source with X-ray optics producing collimated focused X-rays. Ideally, a miniature X-ray tube would be utilised on a portable diffractometer. This would produce higher flux than a radioactive source and could also be used with or without X-ray optics to provide PB or BB_2 geometry respectively, dependant on the application requirements. However, volume, mass and power consumption are crucial considerations for a portable instrument. Radioactive sources are small, lightweight and consume no power, but produce low flux for XRD applications resulting in longer data collection times. A flux comparison is made between the 3 sources by estimating the flux in a 100 µm diameter spot, 40 mm from the X-ray source output.

2.2.1 Radioactive Source

Fe^{55} radioactive sources can produce 3.7×10^9 becquerels (Bq) of radioactivity at full life. These sources have a half life (the time after which the flux is reduced to half of

the original flux) of 2.7 years. Radioactive sources are usually replaced between their 2nd and 3rd half life, which means Fe^{55} sources can be used for 5 − 6 years. One Bq represents a single spontaneous nuclear disintegration per second. For an Fe^{55} radioactive source, 0.28 photons are emitted [Grieken & Markowicz 2001] per disintegration, resulting in a total flux of ~ 1×10^9 photons/s. Two characteristic manganese (Mn) K shell emissions are produced each disintegration, namely Mn Kα (5898 eV) and Mn Kβ (6490 eV), which have an intensity ratio of 1:0.17 respectively [Krause 1979]. Assuming this flux is isotropic and emitted in a sphere, the flux produced with respect to R_{ss} is shown in figure 2.10.

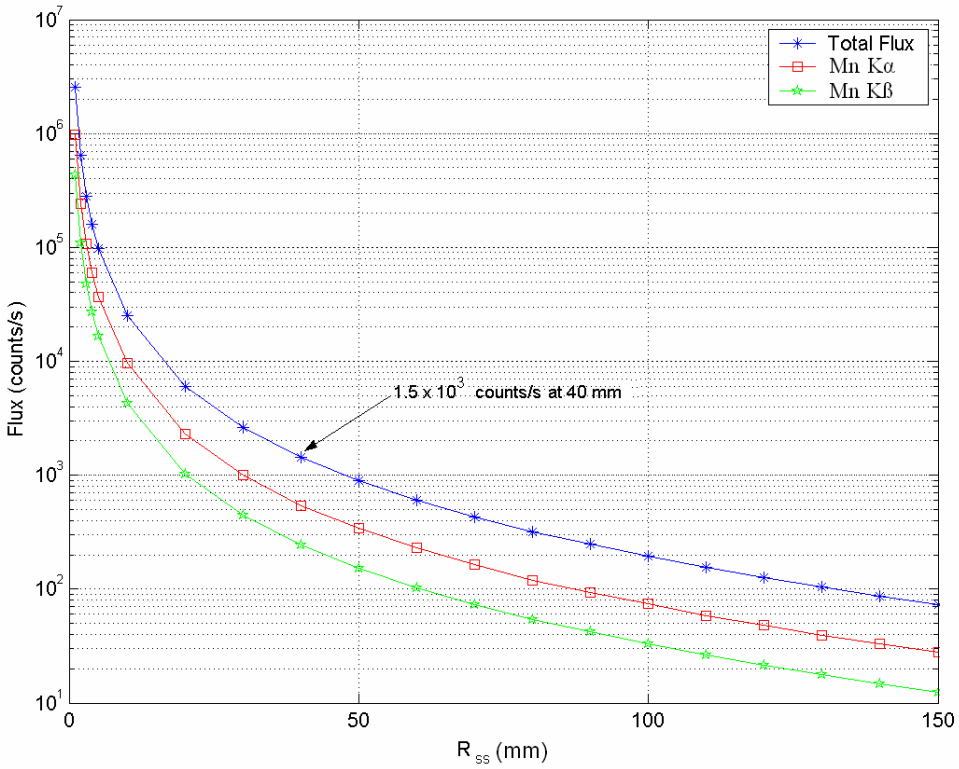

Figure 2.10: Reduction in flux from a radioactive source in a 100 µm spot with increasing X-ray source to sample distance

2.2.2 Miniature X-ray Tubes

In recent years, miniature X-ray tubes (produced by companies such as Oxford Instrument, Moxtek and Amptek) have slowly replaced radioactive sources on portable XRF instrument to reduce data collection times. The flux produced by these types of X-ray tubes is now calculated by considering the 'Mini-X' source manufactured by Amptek. The source produces 1×10^6 counts/s in a 1 mm diameter spot, 40 cm from the X-ray output [Amptek 2008]. The Mini-X operates at a

maximum of 40 kV, 100 µA and emits X-rays in a 120° output cone. The flux is reasonably isotropic across the output cone angles of +20° and -20° [Amptek 2008]. At a distance of 40 cm, the 120° output cone has a diameter of 138 cm. The flux contained within ± 20° is isotropic and at a distance of 40 cm, this covers ~ 30 mm. The flux within a 100 µm spot can therefore be calculated as ~ 10% of the flux contained within the 1 mm spot. The X-ray spectrum at 40 kV, 100 µA, contains 3 tungsten characteristic X-ray lines (W $L\alpha_1$ (8397 eV), W $L\beta_1$ (9672 eV) and W $L\gamma_1$ (11,285 eV)) and continuous X-rays up to 40 kV, as shown in figure 2.11. The flux includes absorption by a 500 µm Be window and 40 cm of air. The unfiltered spectrum would greatly reduce data collection times for XRF analysis, however, it is not ideal for XRD analysis since a monochromatic spectrum is required. This can be achieved by using a 25 µm Cu filter, which contains an absorption edge (8979 eV) between the W Lα and W Lβ/W Lγ X-ray lines. This isolates the W Lα X-rays and produces a more monochromatic X-ray spectrum for XRD analysis, but greatly reduces the flux of the W Lα line, as shown in figure 2.11.

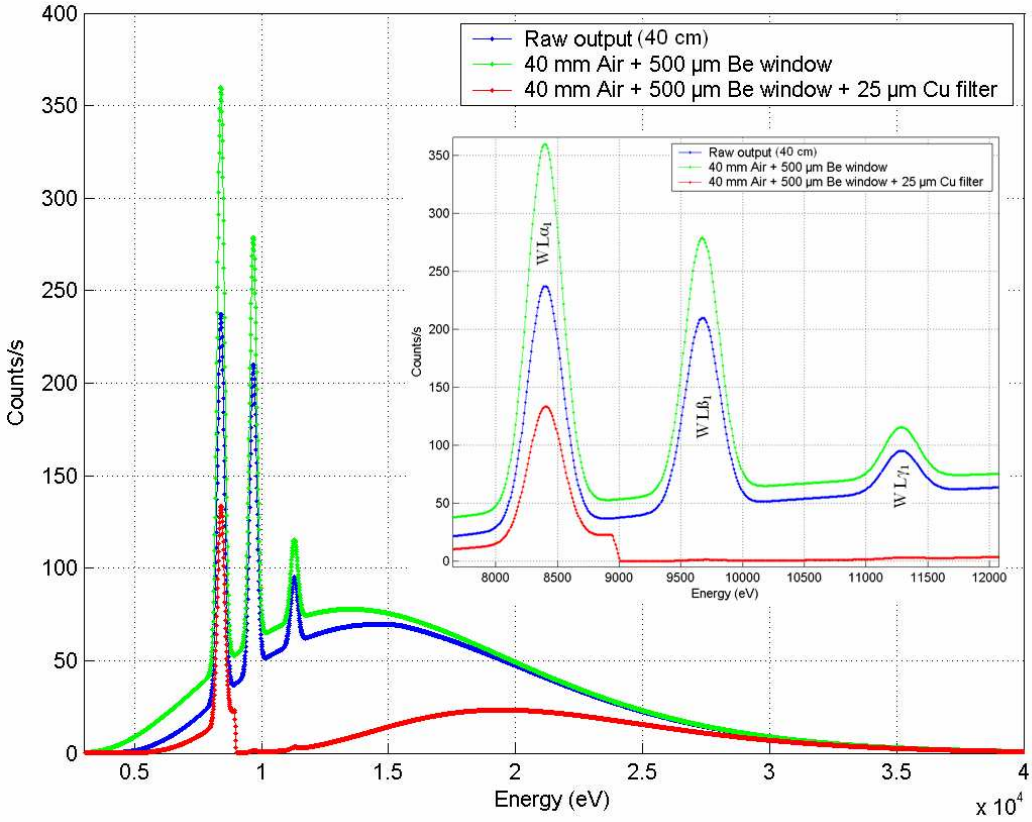

Figure 2.11: Approximate spectrum produced by Mini-X at 40 kV, 100 µA (through a 100 µm diameter spot)

A summary of the estimated flux produced by the Mini-X is outlined in table 2.2.

	Total Flux	W $L\alpha_1$	W $L\beta_1$	W $L\gamma_1$
Unfiltered (40 mm air, 500 µm Be)	1.36×10^5	1.4×10^4	1.24×10^4	5.8×10^3
Filtered (40 mm air, 500 µm Be, 25 µm Cu)	3.9×10^4	7.1×10^3	53	154

Table 2.2: Estimated flux produced by the Mini-X portable X-ray source at 40 kV, 100 µA, at a distance of 40 mm in a 100 µm spot (all fluxes in counts/s)

Currently, no portable X-ray tubes containing polycapillary collimating optics are commercially available. Estimating the flux that would be contained within a 100 µm spot, 40 mm from the X-ray source, is therefore difficult to estimate. However, if coupled to the Mini-X tube, the divergent X-rays could be collected over a large solid angle and transformed into a low divergent beam of focused X-rays, thereby increasing the flux of incident X-rays. It is estimated that the flux produced within the 100 µm spot would be at least 1 order of magnitude larger than flux produced by the Mini-X divergent source, although increased gains of 100 have been reported [Yiming & Gibson 2002]. Another advantage of polycapillary optics (see Section 3.15) is the ability to reduce high energy continuous X-rays [McDonald 1996]. If an optic was coupled to the Mini-X source and a 25 µm Cu filter was used to eliminate the unwanted characteristic X-rays, the spectrum produced would be almost entirely monochromatic (W $L\alpha_1$). Table 2.3 summarises the estimated flux produced by the 3 X-ray sources.

	Total flux	Main characteristic line flux
Radioactive Fe^{55} source	1.4×10^3	1.18×10^3
Portable X-ray source (unfiltered)	1.36×10^5	1.4×10^4
Portable X-ray source (filtered)	3.9×10^4	7.1×10^3
Portable source with X-ray optic (filtered)	9×10^4	7.1×10^4

Table 2.3: Summary of flux produced by a radioactive Fe^{55} source, a portable X-ray tube producing divergent X-rays (Mini-X) and a portable tube coupled with an X-ray polycapillary collimating optic. Flux values represent the counts/s contained within a 100 µm spot, 40 mm from the sample

The data collection times of the 3 sources can be compared as follows. The number of diffracted photons incident on the detector during each exposure N_{diff}, has a Poissonian distribution with an error E_{rr}, given by the expression:

$$E_{rr} = \sqrt{N_{diff}}\,. \tag{2.15}$$

In order to reduce the error to 1%, at a 68% confidence level, 1×10^4 diffracted photons must be collected. If the sample has an efficiency of 0.001 (every 1×10^3 incident photons produces 1 diffracted photon), the data collection times required by the 3 portable X-ray sources to reduce the Poissonian errors on the X-ray peak to 1%, can be summarised as shown in table 2.4.

	Incident flux	N_{diff}	E_{rr}	Exposure required
Radioactive Fe^{55} source	1.18×10^3	1.2	1.10	8,333 (2 hrs,18 min)
Portable X-ray source (filtered)	$7.1. \times 10^3$	7.1	2.66	1,851 (30 min)
Portable source with X-ray optic (filtered)	7.1×10^4	71	8.43	185 (3 min)

Table 2.4: Summary of the data collection times required by the 3 portable sources to achieve a counting error of 1% (all fluxes in counts/s)

The major advantage of the X-ray polycapillary optic is evident from table 2.4, as an intensity error of 1% can be achieved in less than 3 minutes. The PB configuration is ideal for 'quick' analysis, as qualitative results can be achieved in minutes. For portability with power and instrument volume restrictions, the radioactive source is ideal, however much longer exposures times are required to reduce intensity errors.

2.3 Optimised Geometry

The optimum geometry for XRD analysis is entirely dependant on the application. Both BB and PB geometries have advantages and disadvantages based on the requirements of the analysis. This section compares the different geometries discussed in this chapter in relation to resolution, flux and angular range, and determines which geometry is more suited to portability and which is suited to testing.

For optimum resolution, the CCDs should be placed along the focusing circle in the BB_1 geometry to detect the focused X-rays, but this is restricted by two main issues. Since $R_{fc} >> R_{sd}$, an impractical number of CCDs are required to cover a similar angular range to the BB_2 geometry. Figure 2.12 shows the number of 26 µm pixels

required to cover an angular range from 5 − 65°, with varying angles of incidence, for a measuring circle radius of 50 mm and 120 mm.

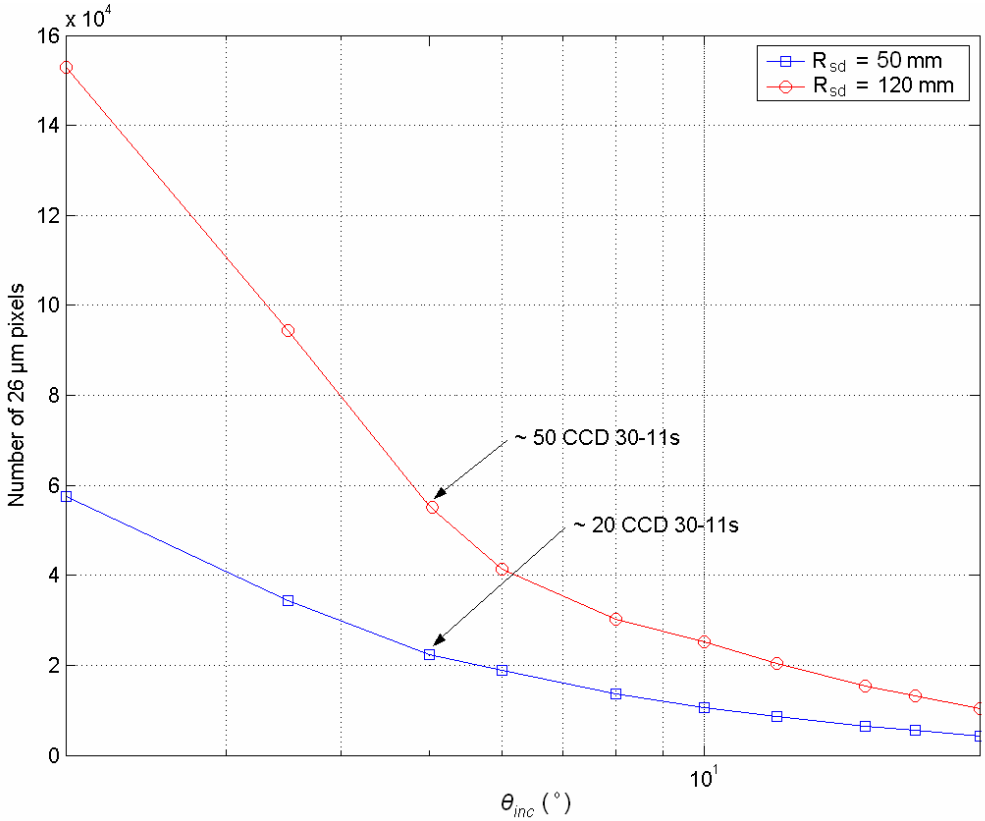

Figure 2.12: Number of (26 µm)^2 CCD pixels required to cover an angular range from 5 − 65° 2θ in BB_1 geometry

As shown in figure 2.12, when R_{sd} is 120 mm, ~ 50 CCD30-11s are required to cover an angular range from 5 − 65° on the focusing circle, whereas only 4 CCDs would be required on a 120 mm measuring circle. Even when reducing R_{sd} to 50 mm, ~ 20 CCDs are required, however, the BB_1 geometry can be used for certain applications. For example, an application may require a angular coverage ranging from 12 − 68° but need the best possible resolution between 12 − 20°. The designed geometry has no size restrictions. Figure 2.13 shows a possible solution using the both BB_1 and BB_2 geometries.

By placing two CCDs in BB_1 geometry between 12 − 20°, higher resolution is achieved in comparison to placing the CCDs on the measuring circle. Since the resolution requirements are less crucial from 20 − 68°, the CCDs can be placed in BB_2 geometry to reduce the volume of the detector. Intensity corrections would be

required with the CCDs in BB_1 geometry, since the sample to detector distance is larger. This geometry requires an additional 56 mm length in comparison to a geometry in which all the CCDs are located on the measuring circle, and also requires an additional CCD.

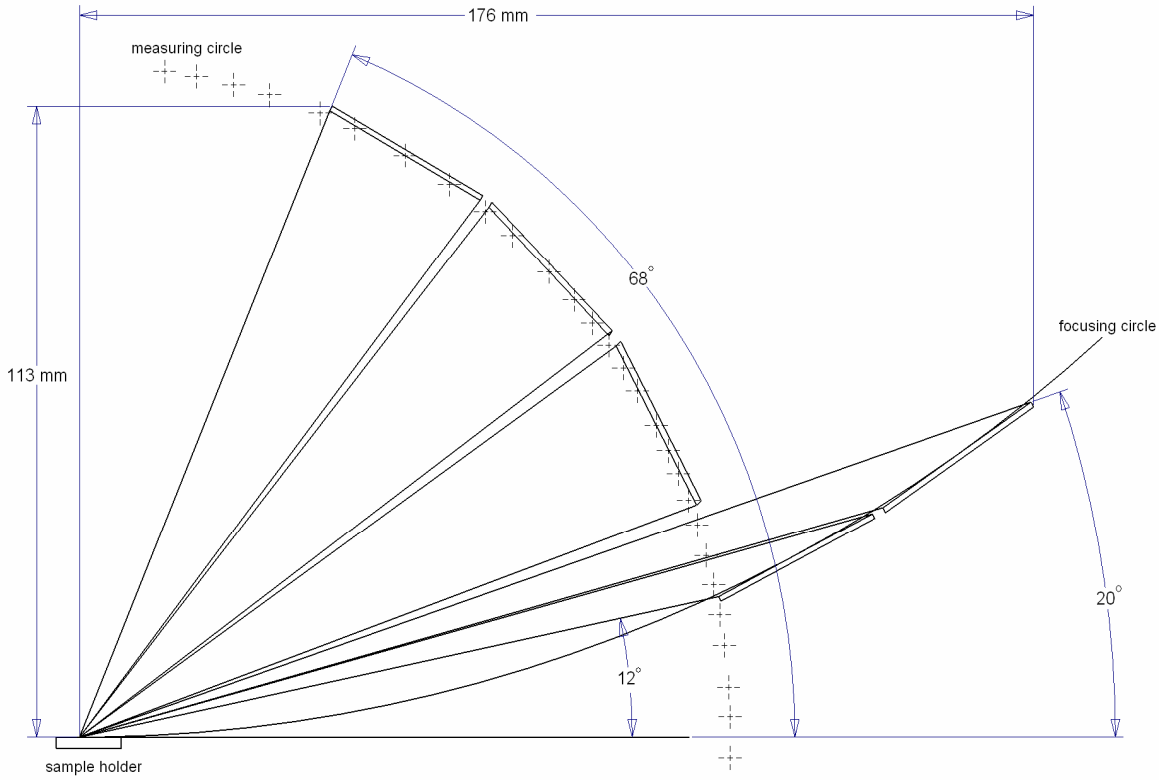

Figure 2.13: Ideal geometry to provide angular coverage from 12 − 68° θ, with the highest possible resolution between 12 − 20°, using both BB_1 and BB_2 geometries. CCD length is 26.6 mm (CCD30-11)

Another problem in BB_1 geometry is shown in figure 2.14. In BB_2 geometry, the imaging areas of the CCDs are almost entirely orthogonal to the diffracted X-rays. In BB_1 geometry, diffracted X-rays are detected by the CCDs at very sharp angles. This is particularly true at low 2θ angles, as shown in figure 2.14. For example, consider two peaks of identical intensities, one located at the centre of CCD 1 and the other at the centre of CCD 3. Assume the depletion depth of the devices x_p, is 12 µm. If 100 Cu Kα X-rays (~ 8 keV) are detected orthogonally to the CCDs, ~ 16 will be absorbed in the CCD's depletion region. However, if these X-rays are detected at a θ angle of

7° (CCD 1), then the effective depletion depth will increase to 98 µm (12 µm/sin(7°)). Similarly, for CCD 3, the effective depletion depth will increase to 46 µm. The two identical peaks located on CCD 1 and CCD 3 will therefore differ by ~ 35%. These errors can be accounted for in the XRD pattern and reduced, however this requires additional processing. This variation in QE and the impractical number of CCDs required to cover a reasonable angular range, restricts the use of BB_1 geometry for the majority of applications.

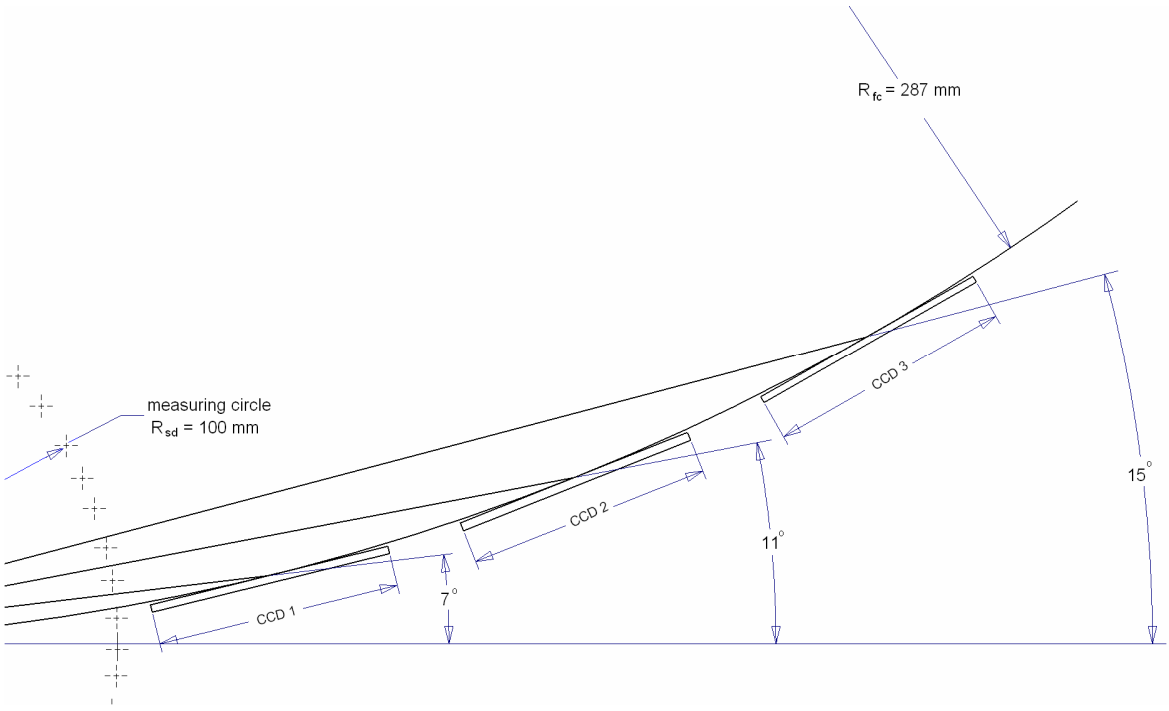

Figure 2.14: Geometry of 3 CCDs on a focusing circle with a radius of 287 mm. R_{sd} = 100 mm and θ_{inc} = 5°

As outlined in Section 2.1, the resolutions achieved in PB and BB_2 geometries are limited by the same factors, namely the angle of incidence, size of the irradiating beam and the radius of the measuring circle. Figure 2.15 compares the resolution achieved in both geometries with a 4° incident angle and 120 mm measuring circle.

For a beam size of 100 µm, it is clear that BB_2 geometry provides better resolution. Even when P_{ob} is reduced to 25 µm in the PB geometry, the BB_2 arrangement provides better resolution at angles < 78°. However, the PB geometry can greatly reduce data collection times (see table 2.4) and provide higher SNR for a given

exposure time. The major advantage of both geometries is R_{ss} does not equal R_{sd}, therefore sample alignment is easier in comparison to the BB_3 geometry.

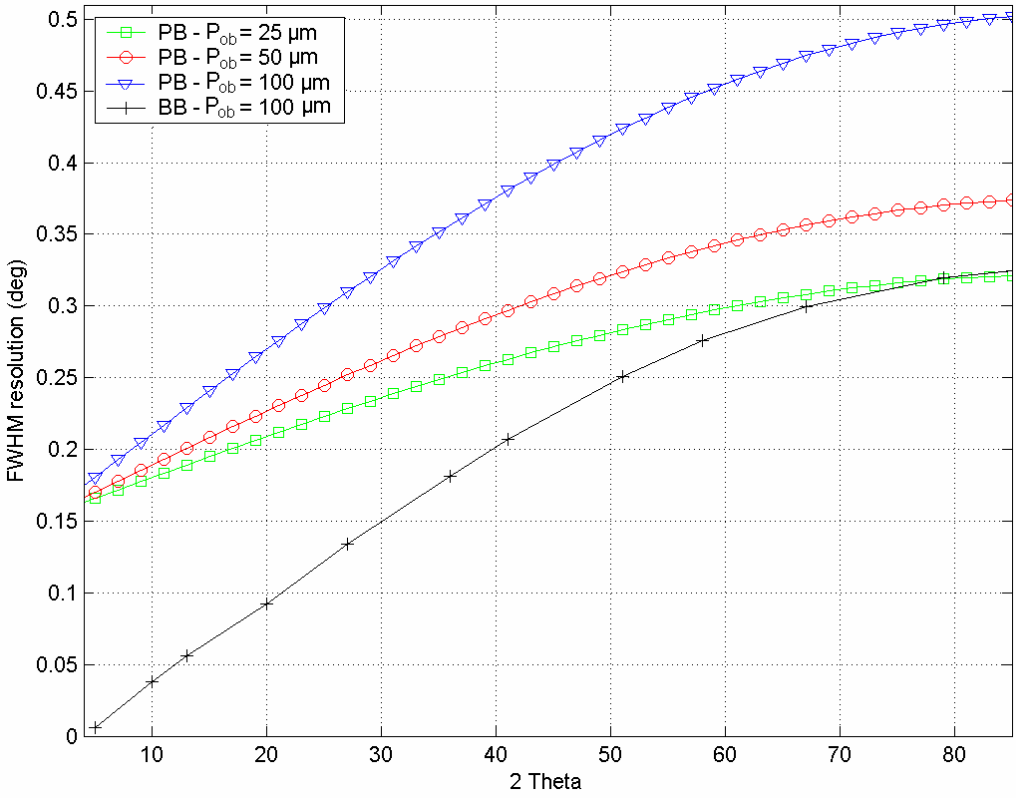

Figure 2.15: Comparison of resolution achieved in PB and BB_2 geometry

Table 2.5 summarises the performance of the geometries discussed in this chapter (excluding BB_3), by a simple marking system out of 10 for the performance parameters of resolution, flux, angular range, data collection times, sample preparation and portability.

	Resolution	Flux	Angular Range	Data collection time	Sample preperation	Portability
BB_2 - RS	8	3	10	2	6	10
BB_2 - PXT	8	5	10	6	6	3
PB - PXT	4	10	10	10	10	3
BB_1 - RS	10	3	1	2	6	1
BB_1 - PXT	10	5	1	6	6	1

Table 2.5: Summary of XRD geometry scores (out of 10) based on resolution, flux angular range, data collection times, sample preparation and portability. '*RS*' represents a radioactive source and '*PXT*' represents a portable X-ray tube

2.4 CCD-Array Testing Geometry

The geometry used in testing the CCD-Array was determined as follows. In order to cover a reasonable angular range (~ 60°), which is required for the majority of applications, with a practical number of CCDs, the BB_1 geometry can be eliminated. Since the initial focus of the work was based on testing and calibrating the CCD-Array, reducing data collection times was given priority over achieving the best resolution, therefore PB geometry was selected over BB_2 geometry. Another consideration was the radius of the measuring circle. Figure 2.16 shows the increase in spatial resolution achieved by a CCD (with 26 µm pixels) with increasing R_{sd}, and the resulting decrease in resolution of the diffracted beam in PB geometry.

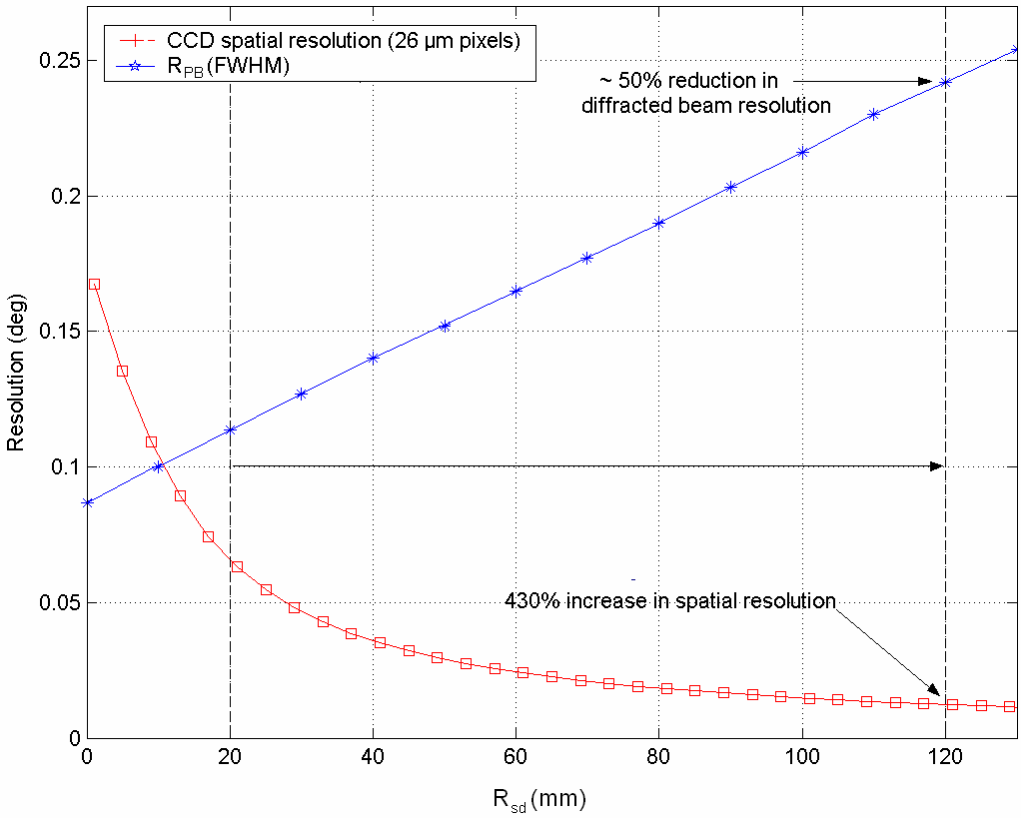

Figure 2.16: Increase in spatial resolution (assuming 26 µm pixels) and reduction in R_{PB} with increasing sample to detector distance

Figure 2.16 shows that when R_{sd} is increased from 20 mm to 120 mm, a 430% increase in spatial resolution can be achieved, whilst the reduction in R_{PB} is ~ 50%. This measuring circle radius was expected to provide excellent spatial resolution (0.012°) for XRD analysis, similar to that achieved by laboratory instruments

(typically 0.01°). By taking a survey of samples relevant to various fields of research (geology, pharmaceuticals, etc.), an angular range from 4 − 64° was expected to cover the major peaks in the majority of samples [Cressey 2006]. A summary of the designed CCD-Array geometry for testing is summarised in table 2.6.

Parameter	Information
Geometry	Parallel Beam
P_{ob}	50 - 150 μm
Angular coverage	4 - 64º 2θ
Number of CCDs	4
R_{sd}	120 mm
Spatial resolution	0.012º
R_{PB} at 10º, 30º, 60º 2θ (P_{ob} = 50 μm)	0.18º, 0.26º, 0.34º
θ_{inc}	4º
Sampe irradiation length (50 μm beam)	0.91 mm
L_{ps} (typical)	5 mm
α_{PB} (at Cu Kα)	0.2º FWHM

Table 2.6: Summary of geometry designed for testing of the CCD-Array

2.5 Discussion

This chapter has compared the different geometries available to the CCD-Array for performing XRD analysis. The geometries have been compared in terms of flux and resolution and the advantages and disadvantages of different portable X-ray sources have been highlighted. It was found that aligning the CCDs along the focusing circle in BB_1 geometry provided the highest resolution but this required an impractical number of CCDs to cover a large angular range. By comparing the BB_2 and PB geometry, it was found that for a given beam size, the BB_2 arrangement provided higher resolution. The resolution achieved in both geometries was limited by the angle of incidence and diameter of the irradiating beam. The main trade-off in both geometries was between the angle of incidence and resolution. The major advantage of the PB geometry was the increase in flux that can be achieved with the use of polycapillary collimating optics. However, unlike the BB_3 geometry, which controls the resolution of the diffracted beams using receiving slits, both BB_2 and PB geometries result in defocusing of the diffracted X-rays. For testing, it was concluded that the PB geometry would provide an ideal arrangement, as data collection times would be greatly reduced.

Chapter 3 : The Charge-Coupled Device / X-ray Generation

3.1 Introduction

This chapter describes the principles behind the semiconductor imaging device used for this project, the CCD. The structure and operation of the CCD is discussed in detail as well as the fundamental building block of the CCD, the metal oxide semiconductor (MOS) capacitor. The operational and readout procedures are also explained, including the different noise sources that limit the performance of the detector for scientific applications. The physical processes involved in the detection of X-ray photons by the CCD are also investigated and the different CCD architectures available for increased quantum efficiency in the soft X-ray range (0.1 − 10 keV) are reviewed. The characteristics of the Bede micro-source (spectra and flux) are described and the advantages of using polycapillary optics for XRD applications are highlighted.

3.2 The Charge-Coupled Device

The CCD was invented in Bell Laboratories in 1969 by G. Smith and W. Boyle [Boyle & Smith 1970]. The CCD is a photon sensitive device that produces charge when exposed to light. The charge generated is proportional to the energy of the incoming photon. Initially the CCD was designed as a memory device, but its ability to convert light to electrons with such high linearity made it ideally suited to the commercial imaging market. Over the last decade, the CCD has been at the forefront of digital camera technologies and digital video recording. Commercial CCDs consume little power, offer very high resolution, and are relatively inexpensive. The focus of this work however, is the use of CCDs for scientific applications. Scientific CCDs are designed for much lower noise performance, increased quantum efficiency and are almost completely free of cosmetic defects. The operation and performance of such scientific CCDs is now discussed.

3.3 Device Structure

The CCD is composed of a 2-dimensional array of closely spaced MOS capacitors. Figure 3.1 shows the structure of the MOS capacitor, which represents a single CCD pixel. The MOS capacitor is so called as it contains a metal contact (electrode), an oxide (SiO_2) and a semiconductor (p-type Si). The active region of the CCD is known

as the epitaxial region and is made by doping the Si with boron, thereby forming a p-type semiconductor. The doping concentration of the p-type layer is expressed as N_a, and is usually between $1 \times 10^{13} - 1 \times 10^{16}$ cm^{-3}. Modern day CCDs are based on the buried channel MOS capacitor, which involves implanting an n-type layer (Si doped with phosphorus) into the epitaxial region. The reason for the implementation of this additional n-type layer is discussed in Section 3.4.2. The standard thickness of the buried channel for e2v devices is approximately 1 µm. The doping of the n-type layer is expressed as N_d, and has a value of 1×10^{16} cm^{-3} for e2v devices [Burt 2006]. Figure 3.1 shows a cross section view of a standard p-type CCD.

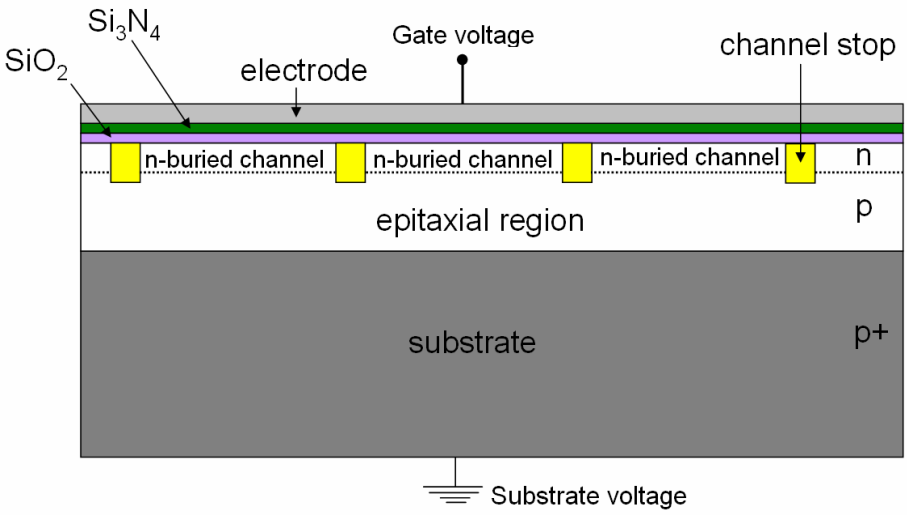

Figure 3.1: Structure of a buried channel CCD – Cross section

The epitaxial layer is grown on top of a highly doped p-type material which forms the substrate. An oxide layer (SiO_2) lies directly beneath the electrode structure and acts as an insulator between the electrode and the underlying Si. A layer of Si nitride (Si_3N_4) is also added to prevent further non-uniform growth of the oxide and improve the electrical insulation between the electrodes and underlying Si. Although not shown in figure 3.1, an additional layer of SiO_2 is located around the electrodes to insulate them from particle contamination.

Bias voltages are applied to the electrode structure, which is usually constructed from strips of overlapping polysilicon. Most devices constructed by e2v are 3-phase devices (i.e. 3 electrodes per pixel). All electrodes lie parallel to one another, where the width of 3 of these electrodes defines the size of each pixel (as illustrated in figure

3.2). Standard device pixel sizes include (13.5 µm)² and (26 µm)², with a standard electrode thickness of approximately 0.085 µm.

The electrode structure lies orthogonally on top of p^+ potential barriers known as channel stops. The channel stops are implanted into the epitaxial region and are held at 0 V potential to confine charge in the lateral direction. During the integration of the image the second electrode *Iø2* is usually held at the biasing voltage, whilst *Iø1* and *Iø3* are held at 0 V. This resembles the behaviour of the channel stops but in the orthogonal direction to form potential barriers, known as barrier phases. These 2 features prevent the leakage of signal electrons to neighbouring pixels during integration.

Once the charge has been integrated, the charge packets are transferred from electrode to electrode until the charge from each column is passed into the readout register. This is the final clocking stage of the signal electrons, which are transferred sequentially to an output amplifier located on the CCD. The headboard circuit provides additional gain to the output signal, which is then digitised by an ADC (analogue to digital converter) and displayed as a 2-dimensional image on the computer screen. The process of charge measurement is discussed in Section 3.6.

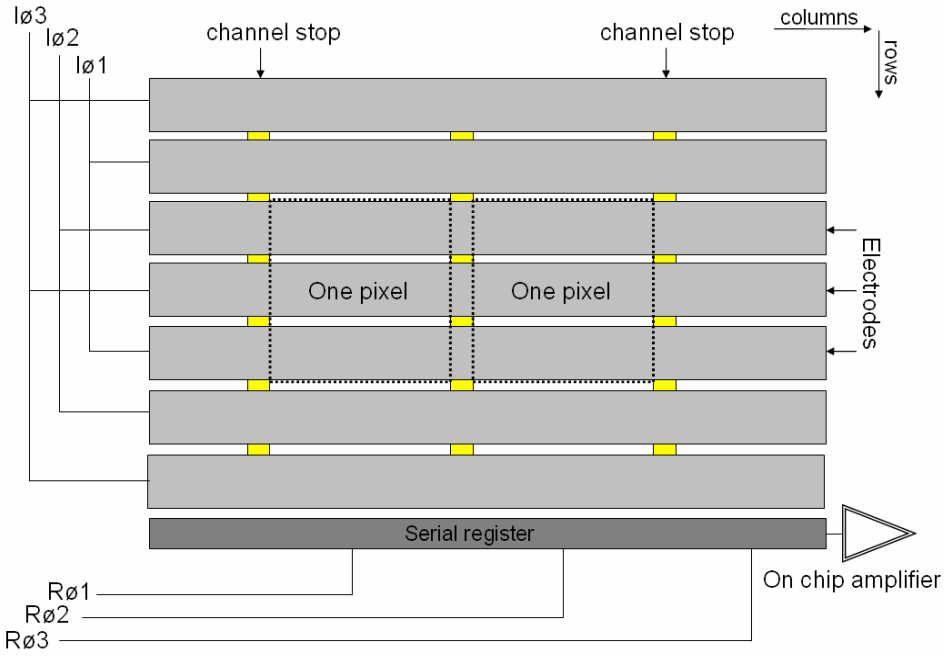

Figure 3.2: Structure of a standard 3-phase CCD – top view

3.4 Potentials in Silicon

The MOS capacitor is the main building block of the CCD and performs the 2 vital procedures of collecting and transferring charge. The potentials of the surface channel and buried channel MOS capacitors are now discussed.

3.4.1 Surface Channel Structure

The structure of the surface channel MOS capacitor is the same as the buried channel capacitor shown in figure 3.1, but without the n-type layer located between the electrode and epitaxial layer. The epitaxial layer of the device is fabricated on p-type Si in which the majority carriers are holes. When a positive voltage is applied to the electrode, the majority carriers in the epitaxial layer are repelled from the surface and a depletion region forms. When an X-ray ionises in the Si and produces electron hole pairs, the electrons are attracted to the surface and the holes are repelled towards the back substrate. This type of MOS capacitor is known as surface channel because the electrons are stored at the surface.

The potential profile through the depletion region of p-type Si can be expressed using Poisson's equation as:

$$\frac{d^2V}{dx^2} = \frac{qN_a}{\varepsilon_{SI}}, \tag{3.1}$$

where q is the charge of an electron (1.6×10^{-19} C) and ε_{SI} is the permittivity of Si (1.04×10^{-12} F/cm). By integrating equation 3.1 with the boundary condition that the electric field is zero at the depletion depth x_p, equation 3.2 gives an expression for the electric field through the device:

$$\frac{dV}{dx} = \frac{qN_a}{\varepsilon_{SI}}(x - x_p). \tag{3.2}$$

Integrating equation 3.2 with respect to x, gives an expression for the change in potential through the Si, at a given distance x, from the surface:

$$V = \frac{qN_a}{2\varepsilon_{SI}}(x - x_p)^2. \tag{3.3}$$

At the surface of the device ($x = 0$), the applied voltage V, equals the surface voltage, V_S. Using equation 3.3, the relationship between the surface voltage and depletion depth can be expressed as:

$$V_S = \frac{qN_a x_p^{\,2}}{2\varepsilon_{SI}}. \tag{3.4}$$

In the surface channel MOS capacitor, signal electrons generated by incident X-rays are stored and transferred at the Si-SiO_2 interface. Some signal electrons become trapped at the Si-SiO_2 interface and are left behind during the clocking process, which severely degrades charge transfer efficiency. This problem was solved with the integration of buried channel MOS capacitors into the CCD architecture.

3.4.2 Buried Channel Structure

Buried channel CCDs introduce an extra layer of n-type material 'buried' underneath the Si-SiO_2 interface. The introduction of this layer changes the shape of the potential curve seen in a surface channel device. A potential well is produced just below the Si-SiO_2 interface, where signal electrons collect and this eliminates trapping at the surface.

The buried channel structure forms a pn junction which is reverse biased by applying a positive voltage on the gate electrode (V_G) and a negative voltage on the back substrate [Bertolini & Coche 1968]. Before the junction is reverse biased, mobile holes from the p side diffuse across the junction to the n side. Similarly, mobile electrons from the n side diffuse onto the p side. This process continues until enough fixed lattice charges build up to repel the migration of charge carriers across the junction. The application of a positive gate voltage and lower substrate voltage (V_{SS}) increases the width of the naturally formed depletion region. Mobile electrons in the buried channel are attracted to the positive charges at the gate electrode and mobile holes are repelled and pushed down to the more negative substrate. The resulting area is depleted of majority carriers and defines the region where signal electrons are generated and collected. The n-type buried channel on e2v devices is usually ~ 1 µm thick and allows the storage of signal electrons approximately 0.5 µm beneath the Si-SiO_2 interface. During the read out process this prevents any charge trapping at the Si-SiO_2 interface. Standard e2v devices are fabricated on 100 Ω.cm resistivity Si

which corresponds to a doping concentration N_a, of approximately 1×10^{14} cm^{-3}. The doping concentration of the n-buried layer is approximately 1×10^{16} cm^{-3}. The resistivity R_s, of the Si (Ω.cm) and doping concentration are related through the expression [Castelli 1991]:

$$R_s = \frac{1.25 \times 10^{16}}{N_a}. \tag{3.5}$$

Figure 3.3 shows the potential gradient of a standard buried channel CCD. The thickness of the buried channel t, is 1 µm and the values of N_a and N_d are 1×10^{15} cm^{-3} and 1×10^{16} cm^{-3} respectively. The oxide thickness d_{ox}, has a value of 0.1 µm. The potential gradient of the buried channel structure can be calculated in 3 stages which describe the electric field through the oxide, n-channel and p-channel respectively. The potential through the oxide V_{OX}, at a given distance x, between the oxide surface and n-buried channel is given as [Janesick 2001]:

$$V_{OX} = V_G - V_{FB} - E_{OX}(x + d_{ox}), \tag{3.6}$$

where V_{FB} is the flatband voltage, E_{OX} is the electric field through the oxide (V/cm) and V_G is the voltage applied to the gate electrode. The potential through the n-buried channel V_n, at a distance x can be expressed as [Janesick 2001]:

$$V_n = V_{\max} - \frac{qN_d}{2\varepsilon_{SI}}(x - x_n)^2, \tag{3.7}$$

where x_n is location of the potential maxima and V_{max} is the maximum channel potential. The potential through the p channel at a given distance x, can be expressed as [Janesick 2001]:

$$V_p = \frac{qN_a}{2\varepsilon_{SI}}(x - t - x_p)^2. \tag{3.8}$$

The potential at the np junction V_J, without the application of a positive voltage at the gate electrode has a value of approximately 11 V for e2v CCDs.

The maximum channel potential V_{max}, can be calculated as [Janesick 2001]:

$$V_{\max} = V_J\left(1+\frac{N_a}{N_d}\right). \tag{3.9}$$

The location of the potential maxima x_n, can be expressed as [Janesick 2001]:

$$x_n = t - x_p\left(\frac{N_a}{N_d}\right). \tag{3.10}$$

The maximum depletion depth in the p channel x_p, is given by:

$$x_p = \sqrt{\frac{2\varepsilon_{si}\left(V_G - V_{SS}\right)}{qN_a}}\,. \tag{3.11}$$

Figure 3.3 shows the potential profile of a typical buried channel CCD for 4 different gate voltages, outlining the location of the potential maxima x_n, and the width of the depletion region ($x_p + t$).

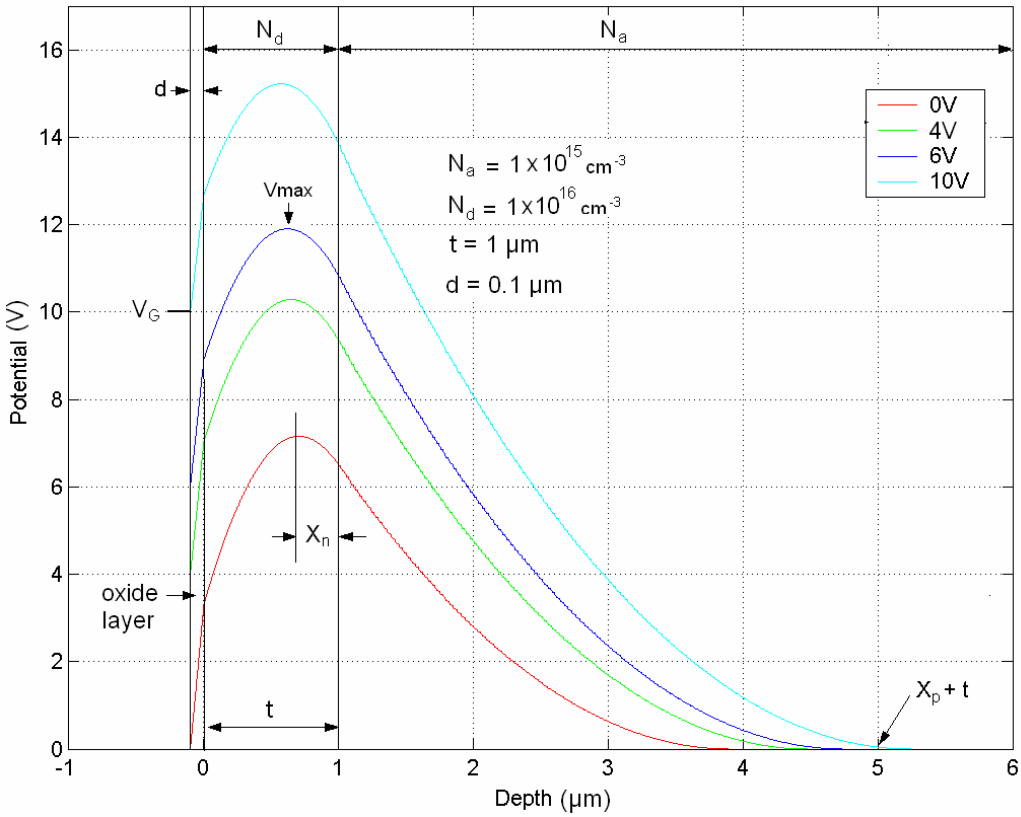

Figure 3.3: Potential profile in a buried channel CCD with varying gate potential (curves generated using equations 3.6 − 3.11)

3.5 Charge Transfer

Once charge is collected in the potential wells of the CCD, it is then 'coupled' from one pixel to another. Figure 3.4 shows the transfer process for a 3-phase CCD with a biasing voltage of 12 V. Once the image has been integrated, signal electrons collect in the nearest potential well, which is usually located underneath *Iø2* and the readout process begins. Charge is moved by manipulating the voltages applied to the 3 different electrodes in each pixel. The complete transfer of one pixel is illustrated in figure 3.4. During the serial readout process, occurring at t1, *Iø2* is maintained at 12 V to hold the charge for each pixel. At t2, 12 V is applied to *Iø3* in conjunction with *Iø2*, which results in electrons diffusing into the common potential well formed by both electrodes. At t3, the applied voltage is removed from *Iø2* so all the signal electrons can be collected by the strong electric field produced by *Iø3*. At t4, *Iø1* is biased high allowing charge to be shared from *Iø3*. At t5 *Iø3* is biased low allowing all the signal charge to be transferred to *Iø1*. At t6, *Iø2* is biased high and charge is coupled from *Iø*1 to *Iø2*. At t7, the charge is completely transferred to *Iø2* and the transfer of charge through 3 electrodes (1 pixel) is complete. Another column has now been transferred to the serial register for amplification. This process continues N_R times, where N_R is the number of rows in the CCD image.

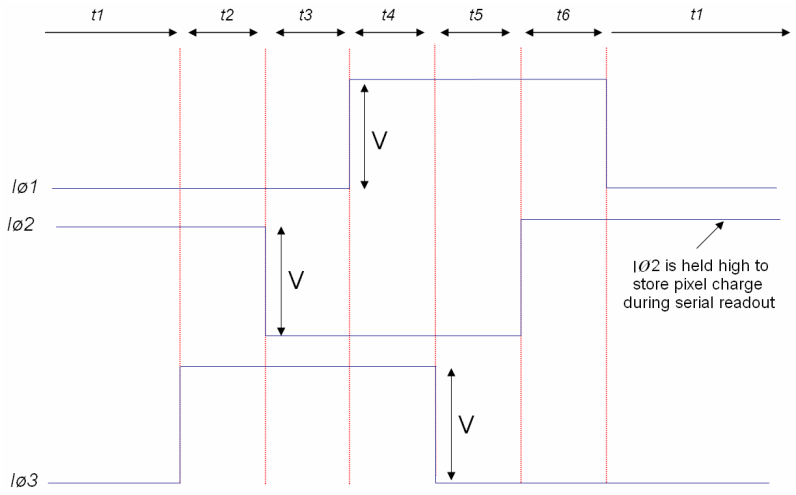

Figure 3.4: Parallel charge transfer process for a 3 phase device

3.6 Charge Measurement

The final stage in the CCDs operation is the amplification and conversion of charge packets which is achieved with an on-chip amplification circuit. This conversion of

signal electrons to a voltage can introduce unwanted noise in the signal which is discussed in Section 3.8. Figure 3.5 shows the typical output circuit for a CCD, which consists of an output field effect transistor (FET) and a reset FET.

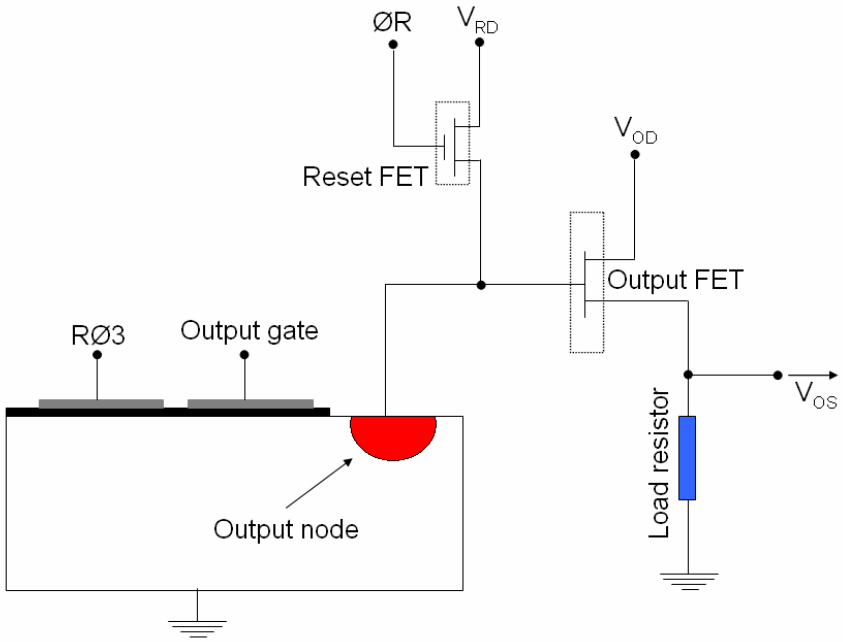

Figure 3.5: Typical output circuit of a standard CCD

The output gate in the serial register is connected to an output node, which is made of n-type Si. The output node is biased to form a deep potential well for signal electrons prior to their measurement by the output FET. The signal packets in the output node are sequentially either converted to an output voltage by the output FET, or drained away. This sequence is controlled by the reset clock, *ØR*. When the reset FET is biased low, the signal electrons from the output node cause a change in voltage at the gate of the output FET, V_{FET}. This change in voltage is proportional to the charge stored in the output node which is vital in maintaining the CCD's linearity (photon → electrons → voltage). Assuming the output FET is operated in its linear region, the change in voltage at the output FET ΔV_{FET}, can be expressed as:

$$\Delta V_{FET} = \frac{Q_{ON}}{C_{FET}} G_{FET}, \tag{3.12}$$

where Q_{ON} is the charge contained in the output node, C_{FET} is the capacitance of the output FET (~ 10 pF) and G_{FET} is the gain of the output FET (~ 0.7 V). This change in

voltage controls the flow of current between the source and drain of the output FET (~ 5 mA). The output voltage is a measure of the voltage across an external load (5 − 10 kΩ) between source and drain, which is usually located off-chip on the headboard.

Once the signal charge from the output node has been converted into an output voltage, the reset FET is biased high, so the charge in the output node is drained away by V_{RD} and the output node is set to a reference voltage. The next group of signal electrons from the neighbouring pixel are then transferred from the last serial register pixel to the output node and the process is repeated until the entire CCD image has been converted to a voltage and amplified. The output gate is biased high during amplification of the signal packet to prevent electrons from the output node spilling back into the last serial register pixel. The sensitivity of a CCD output amplifier is measured in terms of the number of Volts assigned to each electron. Standard CCD sensitivities range from of 1 – 5 μV/e^-. For example, a single Fe^{55} X-ray will generate a voltage of approximately 4.8 mV for an output amplifier sensitivity of 3 μV/e^-.

3.7 CCD Architectures

Two main architectures exist for CCD applications known as full frame and frame transfer CCDs. Full frame CCDs only contain an image section which is connected to the serial register. During the readout process, the CCD continues to accumulate charge since the image area is still exposed to incoming signal, which causes image smear. One way of preventing this image smearing is the use of frame transfer devices.

In a frame transfer CCD, half of the CCD is covered using an opaque shield (usually aluminium), forming a ‘store’ section. Once the image has been integrated, it is quickly transferred to the store section by manipulating the parallel clocks (through the process described in Section 3.5). The image is then read out from the store section whilst a new image is integrated in the image section. This can allow much quicker integration of images and a large reduction in smearing. However, twice as much Si is needed to fabricate a frame transfer device. Section 5.5 demonstrates the effect of image smear when collecting XRPD data and the benefits of operating a full frame CCD in frame transfer mode.

3.8 Noise Sources in a CCD

There are various sources for the generation of noise in a CCD, which limit the performance of the detector [Burt 1991]. These noise sources can originate from on-chip noise such as dark current, transfer noise and photon shot noise. The output amplifier on the CCD also generates noise such as transistor noise and pixel reset noise. External sources can also produce noise in the image such as electromagnetic interference (EMI) from nearby equipment and the leakage of light onto the CCD imaging area. The main constituents of CCD noise are now discussed.

3.8.1 Dark Current

Dark current is so called due to the ability of the CCD to produce current (charge) in the dark. Electrons in the Si atom require energy to bridge the gap between from valence band to the conduction band (1.11 eV). Upon receiving energy in the form of a photon or in the case of dark current, thermal energy, the electrons gain enough energy to move into the conduction band. Here they are able to move around and contribute to the signal collected by the CCD's potential wells. Dark current forms part of the detected signal packet and constitutes as noise. Dark current is entirely dependant on the temperature of the Si. The dark current detected in each pixel of the CCD originates from 3 main sources, which are the depletion region, the field free region and the Si-SiO_2 interface. The dark current at the buried channel I_d, can be expressed as [Holland 1990]:

$$I_d = \left(\frac{qn_i}{2\tau}\right)x_p + \left(\frac{qD_n}{L_n N_a}\right)n_i^2 + \frac{qs_{rv}n_i}{2}. \qquad (3.13)$$

The first term is the dark current generated in the depletion region, where n_i is the intrinsic carrier concentration and τ is the effective lifetime in the depletion region. The second term is the leakage current in the field free region where D_n is the diffusion constant, L_n is the diffusion length (equation 5.7). The dark current generated in the field free region is approximately equal to the length of the epitaxial layer of the device and is expressed in pA/cm². The final term in the expression constitutes the majority of the dark current, which is at the Si-SiO_2 interface. The symbol s_{rv}, represents the surface recombination velocity. The dark current

experienced in each pixel of the CCD has a Poissonian distribution with an error σ_{DC}, given by the square root of I_d.

Figure 6.19 shows the reduction in dark current achieved by AIMO CCDs. AIMO CCDs contain boron implants located underneath certain electrodes to form potential barriers. By applying 0 V gate voltage and ~ 8 − 9 V substrate voltage, holes accumulate at the Si-SiO_2 interface and combine with the electrons. These holes effectively change the surface of the CCD from an n-type to p-type material, hence the term 'inverted'. This practically eliminates the dark current generation at the surface of the device, resulting in a typical leakage current of ~ 10 pA/cm² at 20 °C for e2v devices. The disadvantage of this architecture is a reduced full well capacity and a smaller depletion depth since V_G is 0 V during integration.

3.8.2 Transfer Noise

During the charge transfer process, no electrons should be left behind during the transfer of electrons between neighbouring pixels. This must be performed N_R times, where N_R is the number of rows in the CCD imaging area. When the charge packet reaches the output amplifier, the number of electrons at the output node should be the same as the number of electrons in the original potential well. This represents 100% charge transfer efficiency (CTE). This would ensure the output signal produced for the charge packet would be exactly proportional to the energy of the X-ray event that took place in the target pixel.

Modern day scientific CCDs can achieve a CTE very close to 100%. All modern CCDs are based on the buried channel MOS capacitor device, which typically provides CTE in the region of 0.99999. This means that if 1×10^6 electrons are moved from one pixel to another, only 10 electrons will be left behind. Transfer noise is therefore the average number of electrons removed from a charge packet during the transfer of the charge between pixels. If n_{cp} is the number of electrons in the charge packet, the average number of electrons lost σ_{loss}, during an entire readout of the CCD image can be expressed as:

$$\sigma_{loss} = \sqrt{N_R n_{cp} CTI} \ , \tag{3.14}$$

where *CTI* is the charge transfer inefficiency (1 – CTE).

3.8.3 Photon Shot Noise

The absorption of an X-ray photon in the CCD results in the generation of electron hole pairs. There exists a statistical variation in the number of electron hole pairs produced which was characterised by U.Fano in 1947 and is known as the fano factor. Fano determined that some of the energy of the photon was lost to the Si lattice, resulting in a variation in the number of electron hole pairs produced. The mean number of electron hole pairs $n_{e\text{-}h}$, produced by an X-ray of energy E, is described as:

$$n_{e-h} = \frac{E}{\omega}, \tag{3.15}$$

where ω is ~ 3.67 eV at ~ +20 °C and varies with temperature (see Section 3.9) and represents the average energy required to produce a single electron hole pair in Si [Groom 2004]. With the introduction of the statistical variance, the error associated with the number of electron hole pairs generated can be expressed as:

$$\sigma_{SN} = \sqrt{\frac{FE}{\omega}}, \tag{3.16}$$

where F is the fano factor [Fano 1947] and has a value of approximately 0.115 [Alig et al. 1980].

3.8.4 Transistor Noise

The noise induced from the output circuit has 2 main sources, flicker noise and Johnson noise. Flicker noise or '1/f' noise arises from the trapping and releasing of signal charge in the drain to source channel in the output FET. Flicker noise is removed by the same process as removing pixel reset noise, which is known as correlated double sampling (CDS) [Hopkinson & Lumb 1982]. Flicker noise dominates at readout frequencies < 100 kHz.

Johnson noise is caused by the random thermal motion of charge carriers in the conducting channel of the output FET. Readout frequencies higher than 100 kHz are dominated by Johnson noise. Typical readout noise values for e2v CCDs are in the range of 4 – 8 e^- r.m.s.

3.8.5 Pixel Reset Noise

Pixel reset noise is generated from the sequential resetting of the output node to a reference voltage V_{RD}. This noise source induces a small variation in the applied reference voltage from pixel to pixel. The reset noise σ_{reset}, for a given Si temperature T_{si}, is given by:

$$\sigma_{reset} = \sqrt{\frac{kT_{si}C_N}{q}}, \tag{3.17}$$

where σ_{reset} is the r.m.s. reset noise in electrons, C_N is the capacitance of the output node and k is the Boltzmann constant. Pixel reset noise can however be eliminated by the use of CDS. As mentioned previously, prior to signal electrons from a new pixel being transferred to the output node, the output node is set to a reference voltage V_{RD}. This charge is then measured. The reset FET is then biased low and charge from last readout register is transferred to the output node. The new signal charge in the output node is measured which is a combination of the signal charge and the reference level. The actual signal is then computed as the difference between the 2 measurements. Using the CDS method, the fluctuations in the applied reference voltage are greatly reduced.

The expression for the overall CCD noise can be expressed as:

$$\sigma_{total} = \sqrt{\sigma_{RN}{}^2 + \sigma_{DC}{}^2 + \sigma_{SN}{}^2}, \tag{3.18}$$

where σ_{RN} is the readout noise of the CCD in e^- r.m.s., which can be measured using the serial-overscan pixels in the CCD image.

3.9 Variation in electron-hole pair production in Si

The value of ω, which represents the energy required to create a single electron hole pair, is dependant on the temperature of the CCD. The value of ω at lower temperatures, where CCDs are operated to eliminate dark current, vary from source to source. The indirect bandgap energy of Si for a given temperature $E_g\ (T_{si})$, can be expressed as [Varshni 1967]:

$$E_g(T_{si}) = E_g(0) - \frac{\beta T_{si}^{\,2}}{T_{si} + \gamma}, \tag{3.19}$$

where $E_g(0)$ has a value of 1.1557 eV for Si, β has a value of 7.021×10^{-4} eV/K and γ has a value of 1108 K. At room temperature, $E_g(300K)$ equates to 1.1108 eV. The variation in ω as a function of temperature can be expressed as [Groom 2004]:

$$\Delta\omega(T_{si}) = a[E_g(T_{si}) - E_g(300K)], \tag{3.20}$$

where a is a constant that has been measured by various sources [Groom 2004] and ranges from 2.12 − 2.87. Figure 3.6 shows the variation in ω for a given temperature T_{si}, using 3 sources for the value of a. A good agreement of ~ 3.67 is seen at room temperature (+23 °C). The devices used for this work operate at an average temperature of -37.5 °C, therefore a value of 3.7 is used to approximate ω.

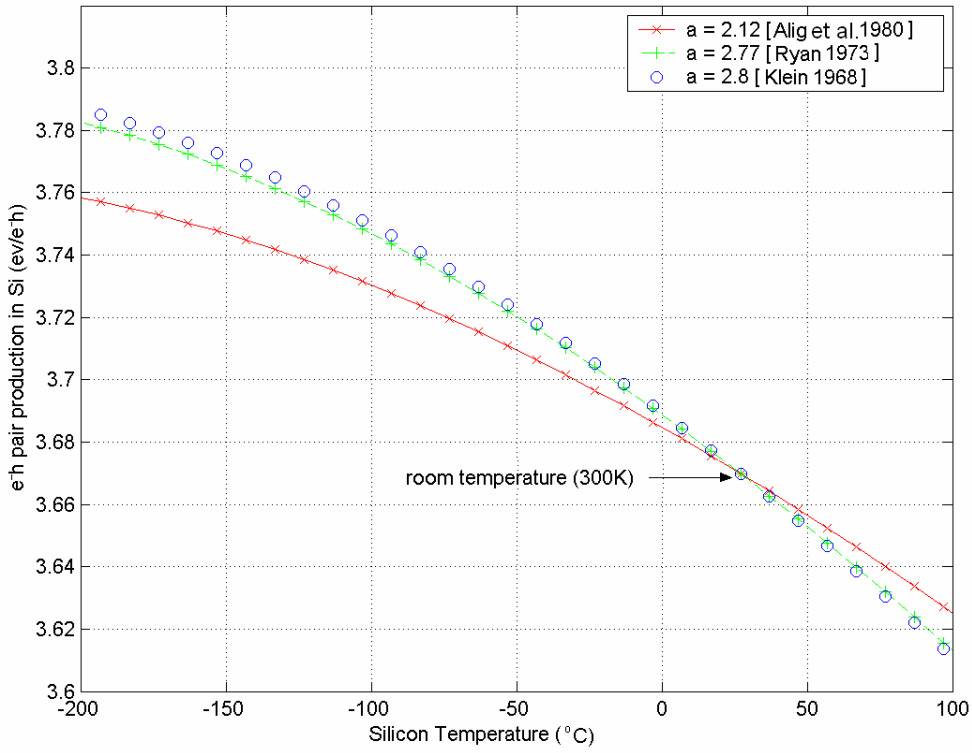

Figure 3.6: Variation in ω as a function of Si temperature

3.10 X-ray Absorption in Silicon

In terms of CCD applications, 2 regions of the electromagnetic spectrum are of interest, light which ranges from $400 \times 10^{-9} - 700 \times 10^{-9}$ m and X-rays which range

from $10 \times 10^{-8} - 10 \times 10^{-10}$ m. Light photons create single electron hole pairs with a very small cloud diameter whereas X-rays create multiple electron hole pairs (100 − 1000) with larger charge clouds. The transmission of electromagnetic radiation through a material can be expressed as [Cullity 1976]:

$$I_I = I_o e^{\left(-\frac{\mu}{\rho} x \rho\right)}, \tag{3.21}$$

where I_I is the intensity of the beam at a depth x into the material, I_o the intensity of the beam at the surface, ρ is the density of the absorbing material (g/cm^3) and μ/ρ is the mass attenuation coefficient [Hubbell & Seltzer 1995]. The product of the mass attenuation coefficient and the density of the material is the linear attenuation coefficient μ. The absorption length represents the depth at which 1/e (68%) of X-rays have been absorbed. The absorption length of X-rays ranging from 30 − 12,000 eV in Si is shown in figure 3.7 [Henke et al. 1993]. For X-ray spectroscopy applications, the important region to maximise the CCDs performance is between ~ 0.5 − 10 keV. Standard CCDs can detect X-rays up to ~ 15 keV and deep depletion sensors extend this limit to ~ 20 keV (QE of ~ 1%)

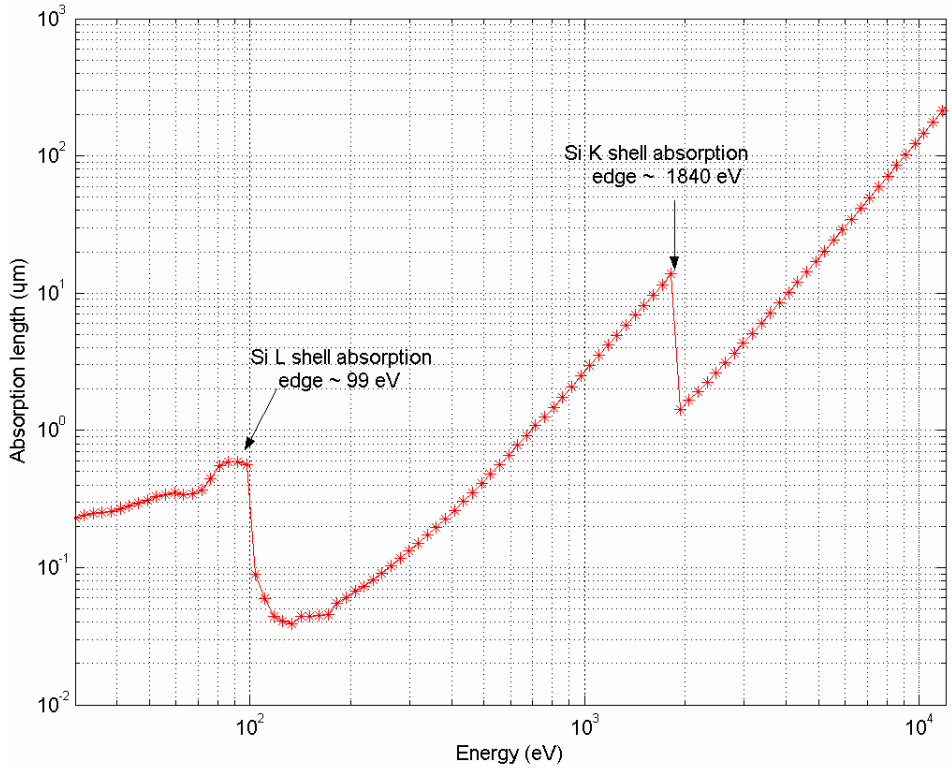

Figure 3.7: Absorption length of 30 – 12,000 eV X-rays in Si

3.10.1 X-ray Detection in Silicon

X-rays detected in the CCD interact with the inner K shell electrons in the Si atom [Kane 1962]. The incoming X-ray dislodges the K shell electron and produces a photo-electron with a kinetic energy equal to:

$$E_{Electron} = E_{X-ray} - E_{Kshell} \ , \tag{3.22}$$

where E_{Kshell} is the K shell binding energy of Si and has a value of 1.84 keV. If the incoming X-ray has an energy less than E_{Kshell}, then it interacts with an L shell electron. The ejected photo-electron produces a trail of ionising electron hole pairs through inelastic collisions. The number of electron hole pairs produced can be calculated using equation 3.15. For example, a Cu Kα X-ray which has an energy of 8047 eV creates approximately 2192 electron hole pairs at room temperature. The X-ray forms an initial cloud of electrons and then travels to the potential wells with further spreading of the cloud based on where the X-ray ionised. The spreading of charge clouds based on X-ray interaction depths is explained in Section 3.11.

The original atom where the X-ray interaction took place is left in an excited state (ionised). The de-excitation of this atom also contributes to the signal charge. The total number of electrons produced by the X-ray signal is therefore equal to:

$$E_{Electron} = (E_{X-ray} - E_{Kshell}) + E_{L\rightarrow K} \ , \tag{3.23}$$

where the third term in the equation $E_{L\rightarrow K}$, represents the energy released during the de-excitation of the original atom where the X-ray interaction took place. This de-excitation can release energy in 2 main forms which are summarised below.

3.10.1.1 Auger Electrons

Once a K shell electron has been removed, the atom relaxes by allowing an L shell electron to fill the vacancy. This can result in the emission of a neighbouring L shell electron which will have an energy equal to $E_{Kshell} - E_{Lshell}$. For Si, E_{Lshell} has a value of ~ 99 eV, which results in the value of $E_{L\rightarrow K}$ to equal 1.740 keV. For the Si atom, the probability of producing Auger electrons is very high (~ 95.3%), as shown in figure 1.6.

3.10.1.2 Fluorescent Si X-rays

The transition of an L shell electron to the K shell can also release energy in the form of a fluorescent Si Kα X-ray, which will have the same energy as a K shell Auger electron. The probability of producing the Si Kα photon is low (~ 4.7%). Si Kα X-rays have a 1/e absorption length of approximately 10 µm [Henke et al. 1993] in Si. This usually results in the ionisation of the X-ray within the same pixel, however if absorbed in a different pixel, this would result in the third term in equation 3.23, $E_{L\to K}$ to equal 0. The X-ray would therefore produce less signal charge and would appear on the spectrum with an energy 1.740 keV less than the actual X-ray energy. These spectral features are known as 'escape peaks'. The fluorescence of all elements within the CCD architecture such as O and nitrogen (N) is also possible. However, the fluorescence yield of these elements is very low and therefore very difficult to measure. This also includes the L shell emissions in the Si atom.

3.10.2 Energy Resolution

Normal operating mode for a CCD involves cooling the detector to practically eliminate dark current. AIMO devices provide leakage current of less than 1 e^- p/p/s at -20 °C. NIMO devices must be cooled to ~ -100 °C to provide comparable dark current. Assuming the CCD is operating with negligible dark current, the energy resolution of the detector is simply limited by the readout noise and can be expressed as:

$$FWHM\,(eV) = 2.35\omega\sqrt{{\sigma_{RN}}^2 + \frac{FE}{\omega}}\,. \qquad (3.24)$$

From equation 3.24, the energy resolution of the detector varies depending on the readout noise of the CCD (assuming dark current has been practically eliminated through cooling) and the X-ray energy. The energy resolution is fano limited, which is the statistical uncertainty in the number of electron hole pairs produced by an X-ray of energy *E*.

Figure 3.8 shows the variation in FWHM for 3, 6 and 9 e^- r.m.s. noise as a function of X-ray energy. The readout noise can be improved by reducing the readout speed of each pixel but this causes an increase in the total readout time of the device.

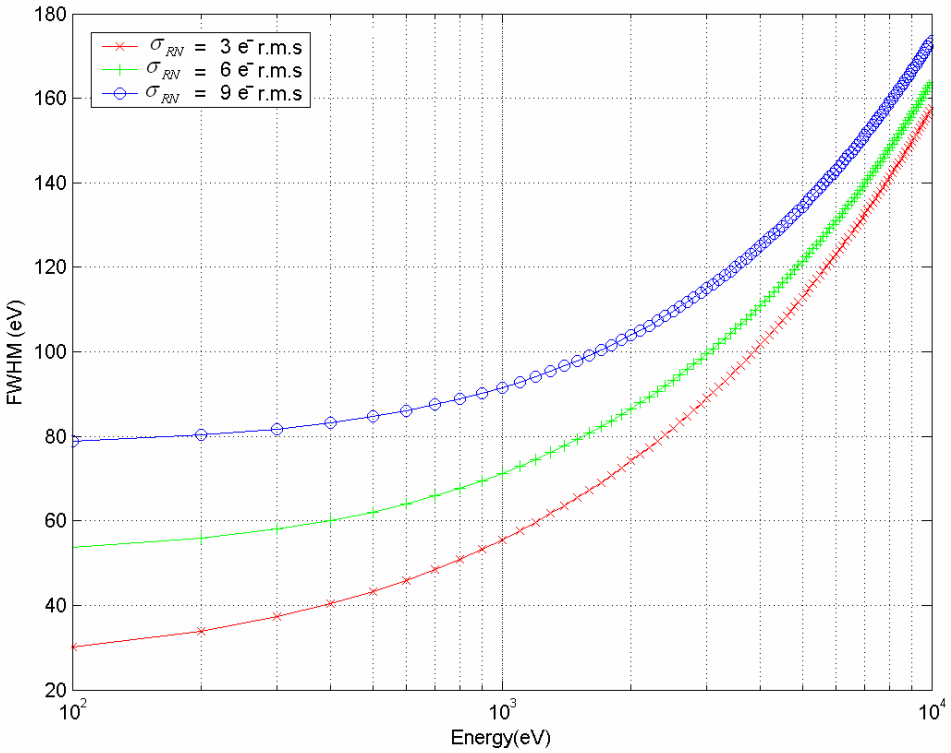

Figure 3.8: Variation in FWHM with X-ray energy for 3, 6 and 9 e^- r.m.s. readout noise

3.10.3 Quantum Efficiency

The QE of a CCD represents its efficiency at collecting X-rays of different energies. The QE of standard front illuminated (FI) CCDs (such as the CCD30-11s used for this project) can be calculated in 2 stages. The first stage involves calculating the absorption of X-rays through the dead layer of the CCD T_{DL}, which consists of the electrode structure, SiO_2 and Si_3N_4 layers. This dead layer effects lower energy X-rays, which struggle to penetrate the initial layers of the CCD and reach the active depletion region. The second factor in the QE calculation is the percentage of X-rays collected in the depletion region of the CCD. Once X-rays penetrate the dead layer, some are collected in the CCD's depletion region, which depends on the extent of the depletion region and the X-ray energy. The expression for QE is given by:

$$QE = T_{DL}\left(1 - e^{-\lambda_E \times Z_d}\right), \tag{3.25}$$

where λ_E is the linear attenuation coefficient in Si at X-ray energy E, and Z_d is the thickness of the CCD's depletion region. For a standard FI CCD, the transmission through the dead layer can be expressed as:

$$T_{DL} = \prod_{L=1}^{n_{dl}} e^{-\lambda_L \times t_L} \ , \tag{3.26}$$

where n_{dl} is the number of dead layers on the surface of the device, λ_L is the linear attenuation coefficient and t_L is the thickness of layer L. Standard e2v devices are fabricated on 100 Ω.cm epitaxial Si with a thickness of 20 − 25 µm. Depending on biasing conditions, such device construction yields a depletion depth in the region of 6 − 12 µm. Standard CCDs display a good QE in the 1– 5 keV range but a much lower response to X-rays ranging from 5 – 10 keV. Due to the surface layers of the device, X-rays less than ~ 1 keV experience severe attenuation that results in poor QE at low energies. These problems with QE have been greatly improved with the advent of deep depletion/high-rho and BI devices. These are now discussed.

3.10.3.1 Deep Depletion and High-Rho CCDs

A much higher response to X-rays in the 5 – 10 keV range can be achieved by the use of deep depletion CCDs. Deep depletion e2v CCDs are fabricated on 1000 − 1500 Ω.cm Si with an increased epitaxial layer thickness of ~ 50 µm [Pool 2005]. Deep depletion devices provide depletion depths of approximately 20 – 33 µm, providing much higher QE than standard devices between 5 – 10 keV. These devices still suffer from poor low energy QE response due to the dead layer structure. Figure 3.9 shows the QE response of a deep depleted device in comparison to a standard FI and BI device.

The highest response to soft X-rays can be achieved using e2v's 'high-rho' CCDs [Murray et al. 2008]. These CCDs are fabricated using 8 kΩ.cm epitaxial Si, achieving a depletion depth of ~ 300 µm when biased at ~ 110 V. High-rho CCDs can achieve a QE of 80% at 10 keV.

3.10.3.2 Back Illuminated CCDs

In BI CCDs, the back substrate material is thinned and X-rays are detected from the rear of the CCD. This prevents lower energy X-rays from being absorbed by the electrode structure and greatly improves the QE at lower energies. A small oxide layer forms naturally on the back surface but its effects are minimal. X-rays therefore directly interact with the epitaxial layer. The QE of a BI CCD can be calculated using

equation 3.25, where T_{DL} equates to the transmission through the SiO_2 layer. Figure 3.9 shows the increased QE achieved with a BI CCD in comparison to a FI CCD. Increased transmission of low energy X-rays can also be achieved through open electrode and electrode thinning techniques, but the response of BI CCDs shows the best improvement.

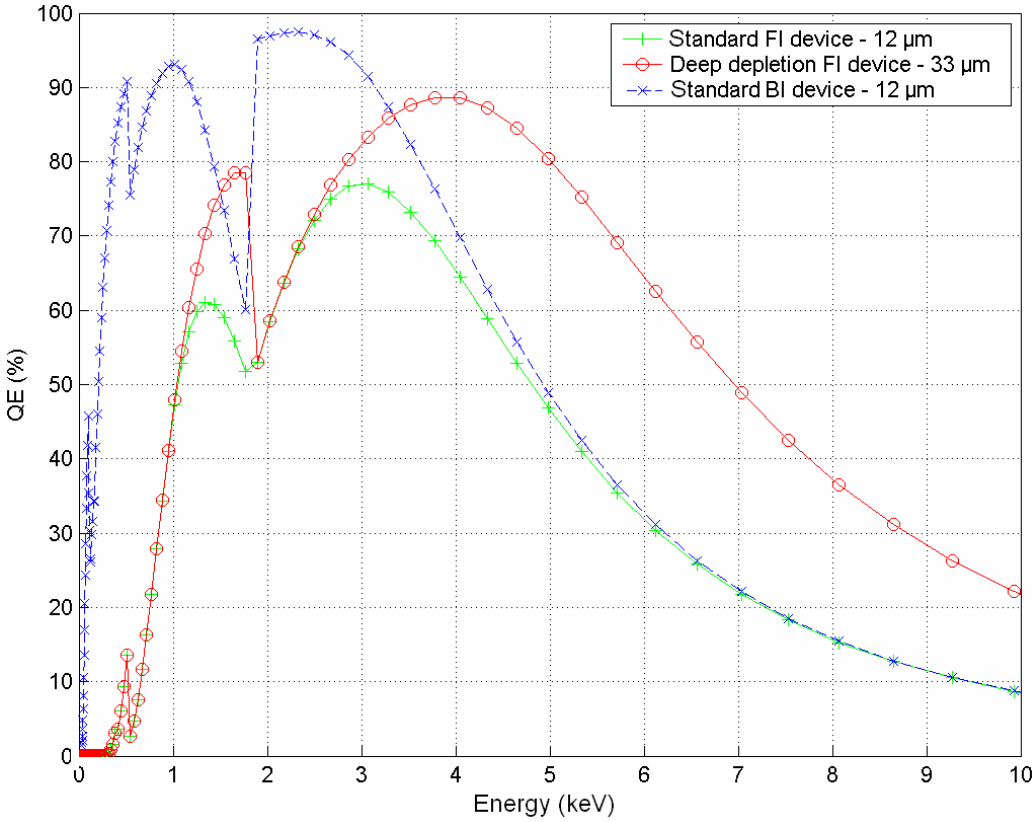

Figure 3.9: QE of a standard FI, deep depleted and standard BI CCD

X-ray spectroscopy is one of the many fields which has made use of the combination of BI CCDs fabricated on high resistivity Si [Jorden et al. 2006]. Such CCDs provide very high QE over the entire soft X-ray range 0.1 − 10 keV.

3.11 Charge Diffusion in CCD Detectors

The depth of the depletion region varies based on the voltage across the CCD and the doping concentration. Underneath the depletion layer lies a region where the electric field does not exist and results in charge diffusion [Pavlov & Nousek 1999]. The next section describes the process in calculating the charge cloud formed by an X-ray based on the interaction depth, *z*. The CCD is divided into the depletion region with a

depth represented by Z_d, the field free region Z_{ffr} and Z_s, which represents the depth of the CCD substrate.

3.11.1 Initial Charge Cloud

The process of X-ray interaction begins with the ionisation of the X-ray photon at a given depth in the CCD. An initial charge cloud forms, the size of which is related to the X-ray energy of the photon, but not related to where the interaction took place. The 1σ initial cloud radius (µm) is given by [Castelli 1991]:

$$R_i = 0.0171 E_{electron}^{1.75}, \tag{3.27}$$

where $E_{electron}$ is the X-ray photon energy in keV minus the K shell binding energy of Si (1.84 keV). The size of the initial charge cloud for soft X-rays is very small in comparison to the pixel size. A 10 keV X-ray generates an initial charge cloud of approximately 0.17 µm. The growth of the initial charge cloud based on interaction depth is now discussed.

3.11.2 Diffusion in the Depletion Region

The effects of radial diffusion in the depletion region are minimal as the electrons are quickly swept away by the electric field to the buried channel. If the X-ray interaction takes place at $0 > z < Z_d$, the 1σ radius of the charge cloud at the buried channel can be expressed as [Holland 1990]:

$$R_d = \left(\left(\frac{2 D_n \varepsilon_{SI}}{\mu_{si} q N_a} \right) * \left(\ln \left(\frac{Z_d}{Z_d - z} \right) \right) \right)^{0.5}, \tag{3.28}$$

where D_n is the diffusion coefficient and is given by [Janesick 2001]:

$$D_n = \frac{\mu_{si} k T_{si}}{q}, \tag{3.29}$$

where μ_{si} is the mobility of electrons in the Si and is related to the doping concentration (1500 $cm^2\ V^{-1}\ s^{-1}$ for 100 Ω.cm device). The 1σ cloud radius of X-rays reaching the buried channel is a combination of the initial cloud radius and the radial diffusion in the depletion region and is given by the expression:

$$R = \sqrt{R_i^{\,2} + R_d^{\,2}} \,. \tag{3.30}$$

Figure 3.10 shows the variation in 1σ cloud radius for X-rays interacting in a 12 µm and 33 µm depletion region. This represents a 100 Ω.cm and 1000 Ω.cm resistivity device biased with 12 V gate voltage and 0 V substrate voltage respectively. The size of the initial cloud radius formed by a K Kα (3313 eV) photons is also shown.

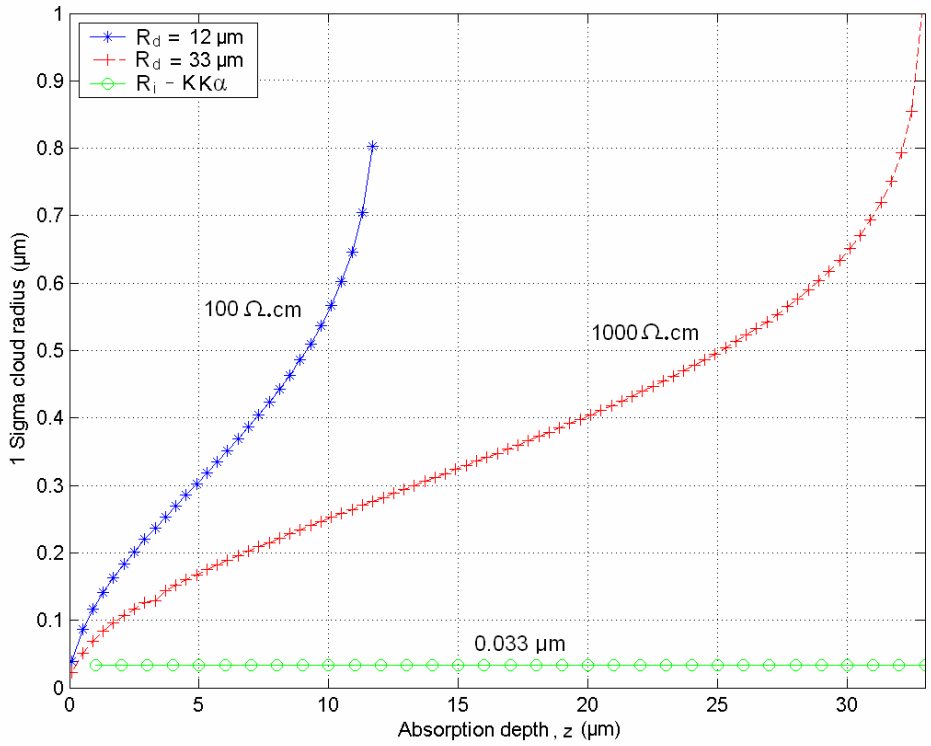

Figure 3.10: 1σ cloud radius as a function of absorption depth for 100 and 1000 Ω.cm CCDs

Since a 1000 Ω.cm device will have a stronger electric field than a 100 Ω.cm device under similar biasing, the charge cloud will be swept away quicker with a reduction in spreading, which will results in an increase in isolated X-ray events.

3.11.3 Diffusion in the Field Free Region

If the X-ray interacts in the field free region ($Z_{ffr} > z > Z_d$), the charge cloud radially diffuses until it reaches the depletion boundary [Hopkinson 1983]. Once at the depletion boundary, the charge cloud is influenced by the electric field and quickly swept away to the nearest potential well. By this time however, the charge cloud will have a very large radius (in comparison to charge clouds generated in the depletion

region) and will produce more split events than isolated events. The 1σ cloud radius at the depletion boundary is given by [Holland 1990]:

$$R_{ffr} = \frac{Z_{ffr}}{2}\sqrt{1-\left(\frac{z-Z_d}{Z_{ffr}}\right)}. \tag{3.31}$$

Due to the radial diffusion of X-rays in the field free region, R_{ffr} is much larger than R_d. The 1σ cloud radius at the buried channel is a combination of the initial cloud radius, the spreading in the field free region and the further spreading in the depletion region and is expressed as:

$$R = \sqrt{R_i^{\,2} + R_d^{\,2} + R_{ffr}^{\,2}}\,. \tag{3.32}$$

If the X-rays interact in the p^+ substrate, then charge loss through recombination is experienced as well as charge diffusion. Unlike events generated in the field free region, events that originate from the substrate cannot be summed to form the original X-ray event. The modelling of X-rays interacting in the substrate is further discussed in Section 5.6.1.

3.12 Bede micro-source X-ray generator

To characterise the CCD-Array with reasonable data collection times, a powerful X-ray source was required. Ideally, the X-ray source should irradiate a small spot on a powder sample with a high flux of high brightness and monochromatic X-rays. Without the presence of focusing optics, conventional X-ray tubes produce highly divergent X-rays with an intensity distribution spread across a large angular range. Using X-ray optics, small surfaces of the sample can be stimulated with an increased intensity gain. This project makes use of a Bede Scientific Instruments micro-source [Bede Scientific Instruments 2004], which consists of a conventional X-ray source coupled with an X-ray Optical Systems (XOS) polycapillary collimating optic. The process of X-ray generation within the micro-source is now discussed.

3.13 X-ray Production

In an X-ray tube, the initial stage of X-ray generation is the emission of electrons from the cathode. Through thermionic emission, electrons are emitted from the

electrically heated filament and if a large potential difference is applied between the cathode and anode, electrons are rapidly accelerated towards the anode. It is the bombardment of the electrons with the target material that generates the X-rays at the point of impact. The efficiency of X-ray generation during the electron and anode interaction is very low (~ 1%) and the generated X-rays radiate in all directions. Approximately 99% of the kinetic energy of the impacting electrons is converted to heat, so the anode in an X-ray tube must be constantly cooled to prevent the target melting. The dissipation of heat produced from the Bede micro-source is discussed in Section 4.3.3. Two types of X-rays are generated from the interaction of electrons with the anode, continuous and characteristic X-rays. These are now discussed.

3.13.1 Continuous X-rays

Continuous X-rays (also known as 'bremsstrahlung') are produced when electrons of sufficient kinetic energy are rapidly decelerated, resulting in the release of energy. The name bremsstrahlung is a German word meaning, "braking radiation". As the incoming electron approaches the highly positively charged nucleus of the anode material, the electron is deflected and decelerates ('brakes') due to its smaller negative charge. Some electrons are stopped immediately and give up all their kinetic energy in the form of an X-ray photon. Some electrons are deflected from nucleus to nucleus and release their kinetic energy in stages. The kinetic energy (KE) of an electron, in Joules, at the point of impact is given as:

$$KE = eV\,, \tag{3.33}$$

where e is the charge of the electron and V is the potential difference across the anode and cathode. This is the maximum possible energy of any X-ray produced in the interaction of the electrons with the anode and defines the upper limit of the spectrum in eV.

A model of continuous X-rays can be generated using Planck's blackbody theory. Planck's theory describes the intensity of radiation emitted by a blackbody as a function of wavelength for a given temperature. Planck's law applies to all parts of the electromagnetic spectrum and can be used to describe the variation in continuous X-rays generated from an X-ray tube as a function of increasing tube voltage. As the tube voltage increases, the kinetic energy of the electrons accelerated towards the

anode increases. Since 99% of the interactions of the electrons with the anode are converted to heat, increasing the tube voltage causes an increase in the temperature of the anode (or radiating blackbody). Planck's blackbody law is expressed as:

$$I(\lambda,T)=\frac{2hc^2}{\lambda^5}\frac{1}{e^{\left(\frac{hc}{\lambda kT}\right)}-1}, \tag{3.34}$$

where I is the intensity of radiation as a function of wavelength λ (m) and blackbody temperature, T (K), h is Planck's constant (4.13×10^{-15} eV s), c is the speed of light (3×10^8 m/s) and k is the Boltzmann constant (8.617×10^{-5} eV K^{-1}). The temperature of a blackbody emitting X-rays ranges from $3 \times 10^6 - 3 \times 10^8$ K. Using equation 3.34, the shape of the continuous spectrum for a given tube voltage can be generated and is shown in figure 3.11 (the spectra are shown as a function of photon energy (eV) as opposed to wavelength). The wavelength of electromagnetic radiation can expressed as a quantum of energy as:

$$E(eV)=\frac{hc}{\lambda(m)}. \tag{3.35}$$

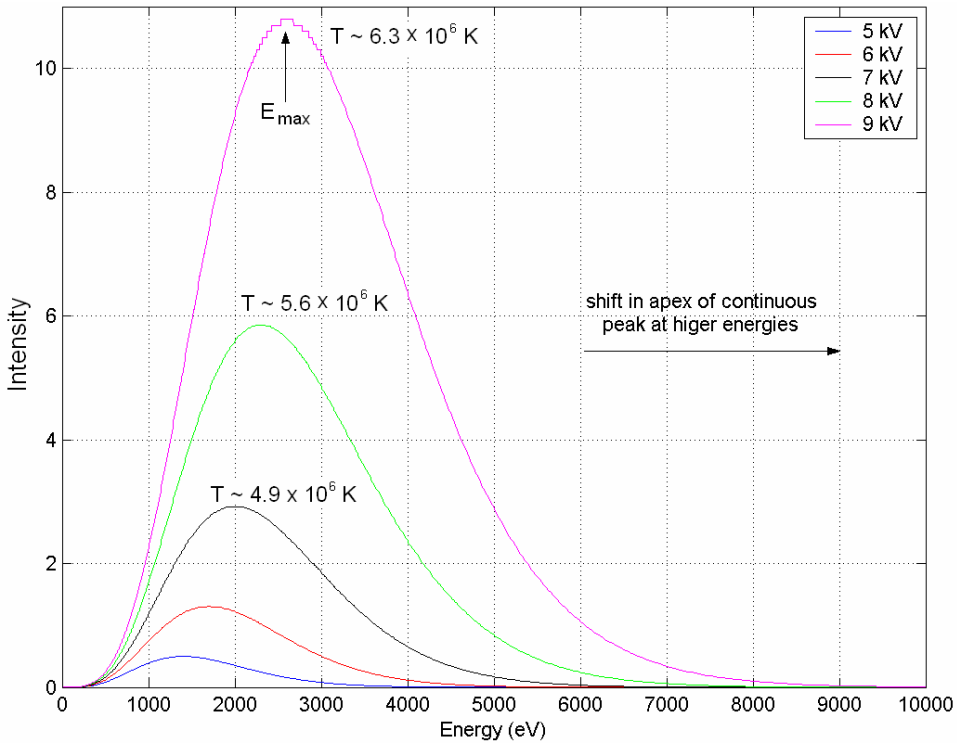

Figure 3.11: Intensity of continuous X-ray spectra as a function of X-ray tube voltage

As outlined in equation 3.33, the maximum energy of a photon produced by an X-ray source will equal the maximum kinetic energy of the electrons being accelerated by the cathode. This maximum energy represents the tube voltage expressed in eV. Another feature of the continuous spectra is the shift of the peak at higher tube voltages. The apex of each of the spectra increases for higher values of tube voltage. The position of these peaks can be calculated using Wien's law. This law describes the energy of the peak intensity distribution for a given blackbody temperature and can be expressed as as:

$$E_{\max} = \frac{hcT}{3\times10^{-3}}, \tag{3.36}$$

where E_{max} represents the energy location of peak intensity of the continuous peak, as indicated in figure 3.11.

3.13.2 Characteristic X-rays

The intensity of characteristic X-rays can be hundreds of times stronger than the neighbouring continuous spectrum and it is the presence of these strong characteristic emissions in the incident spectrum that makes XRD analysis possible. The wavelength of the characteristic lines is dependant on the material of the anode. When the accelerating electrons have sufficient energy to dislodge an electron from the atom of the anode material, a photoelectron is produced. The characteristic X-rays produced by the Cu anode are Cu Kα at 8047 eV (1.54×10^{-10} m) and Cu Kβ at 8904 eV (1.39×10^{-10} m). The intensity of the characteristic K line I_{Kline}, produced by an X-ray source can be calculated using the expression [Cullity 1976]:

$$I_{Kline} = Bi\left(V - V_K\right)^n, \tag{3.37}$$

where B is a constant dependant on the X-ray source, i is the X-ray tube current, V is the X-ray tube voltage, V_K is the K shell excitation voltage and n is a constant ranging from 1 − 2. Equation 3.37 dictates that the characteristic K shell X-rays of copper are only excited after the tube voltage exceeds the X-ray binding energy of the Cu K shell. The value of V/V_K determines the increase in intensity of the characteristic X-rays. The maximum increase in intensity occurs when $V/V_K = \sim 6$. For example, an X-ray tube containing a Cu anode should be operated at a maximum of 50 kV to

exploit the maximum possible intensity of the characteristic peaks. Exceeding the voltage beyond 50 kV (V/V_K = ~ 6) allows the electrons bombarding the target to penetrate too far into the anode and internal absorption of the X-rays occurs.

3.14 Bede Spectrum Without XOS Optic

This section compares the spectra obtained from the Bede micro-source (without the focussing optic) to Planck's blackbody distribution. The aim is to show the continuous spectra from the X-ray source can be reproduced by varying the temperature of the radiating blackbody in the region of 10^7 K [Kawaii & Ishii 2005]. Figure 3.12 shows the spectrum collected from the Bede micro-source operated at 40 kV, 0.01 mA using a Si Lithium (SiLi) detector. Due to the high flux, a 50 µm aluminium (Al) foil was used to attenuate the X-rays and reduce the 'dead time' of the detector. Using equation 3.34, the temperature parameter *T*, was set to approximately 3×10^7 K (~ 40 kV) as a starting point to the fit. The 2 characteristic X-rays were modelled using Gaussian models with 3 degrees of freedom (intensity, FWHM and energy). The ratio of Cu Kα:Cu Kβ X-rays was expected to be 1:0.17 [Krause 1979].

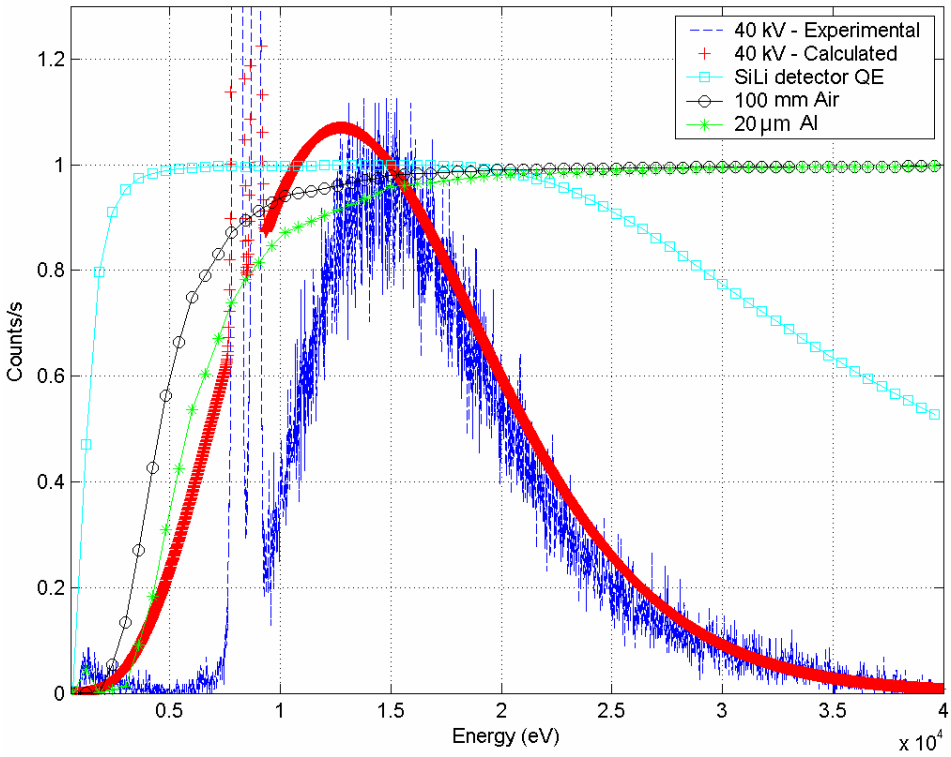

Figure 3.12: Comparison of calculated and observed spectra at 40 kV operating voltage, accompanied with experimental attenuation factors

The model is in good agreement with the experimental data from 15 − 40 keV. However, the attenuation at lower energies is significant and all 3 attenuation factors must be taken into account to reach a reasonable agreement. A least squares fit was applied to the calculated model and the experimental data with refineable parameters of air gap between sample and detector (± 5 mm), aluminium thickness (± 1 µm) and the temperature of the blackbody, T (± 0.1 × 10^7 K). Figure 3.13 shows the final fit between the calculated and experimental data, considering all attenuation factors. A poor agreement was still noticed at lower X-ray energies. It was expected that some of the generated X-rays were absorbed within the anode itself, resulting in higher attenuation at lower energies. Nevertheless, the results show that Planck's blackbody distribution can be used to reproduce the continuous X-ray spectra.

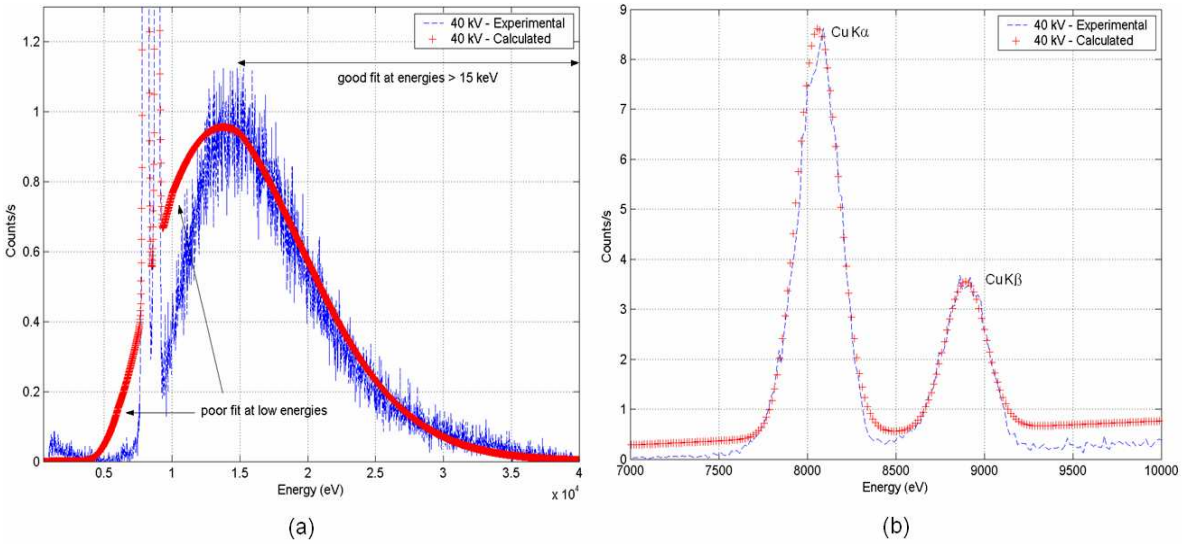

Figure 3.13: Comparison of calculated and observed spectra at 40 kV for (a) continuous X-rays and (b) characteristic X-rays

3.15 X-ray Polycapillary Optic

This section presents a brief overview of the main principles of polycapillary optics. Various types of polycapillary optics exist for use in different applications [McDonald 1996]. This section describes the principles of optics designed for XRD applications, the polycapillary collimating optic. Polycapillary optics consists of thousands of hollow glass capillary tubes. The highly divergent X-rays produced from the X-ray source are collected by the entrance window of the optic and guided down the capillary tube by total external reflection (similar to how fibre optics transmit

light). The X-ray photons are reflected due to the difference in refractive indices of the 2 materials (glass and air). When an X-ray photon enters the optic with an angle of incidence (θ_i) smaller than the critical angle (θ_c) of the reflecting material (glass in the XOS optic), it undergoes total external reflection. X-rays satisfying this condition are effectively transported down the tube undergoing multiple reflections in order to exit the optic. X-rays leaving the output are transformed into a quasi-parallel beam of low divergent X-rays focused into a small spot. The critical angle is energy dependant and for glass capillary tubes is given by the expression:

$$\theta_c\,(mrad) = \frac{32}{Energy(keV)}\,. \tag{3.38}$$

The divergence of the output beam is determined by two factors. The maximum angle at which an X-ray of a given energy can exit the optic is θ_c. However, this assumes the capillary that has transported the X-ray is perfectly straight. Minor defects in the capillary axis can also increase or decrease the angle of the emitted X-ray [Padiyar et al. 2000]. For polycapillary X-ray optics, the divergence at Cu Kα energies is usually ~ 3.5 mrad [Misture & Hailer 2000], as shown in figure 3.14.

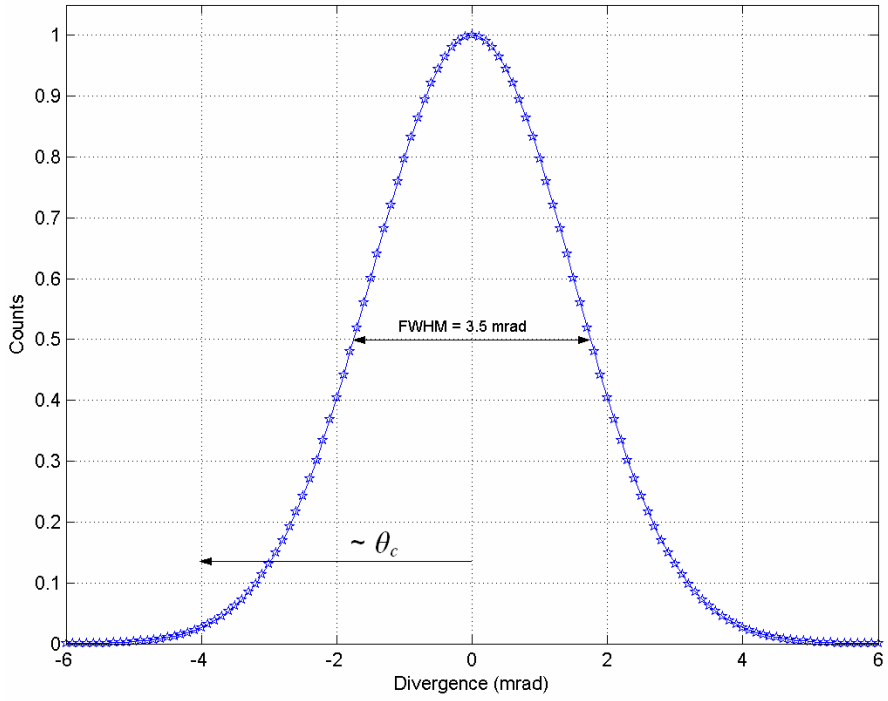

Figure 3.14: Divergence of Cu Kα X-rays from a polycapillary collimating optic, which resembles a Gaussian distribution with a FWHM of 3.5 mrad

The advantages of X-ray polycapillary collimating optics are:

- Increased intensity gain over sample (× 10 − 100) area resulting in reduced data collection times [Yiming & Gibson 2002],
- sample is irradiated with a quasi-parallel beam,
- X-rays are captured over large collection angle (~ 20°),
- transmission efficiency is as high as 30% at Cu Kα energies (~ 8 keV),
- low divergence (< 4 mrad), and
- suppression of high energy continuous X-rays resulting in a more monochromatic beam.

3.15.1 XOS Polycapillary Optic

Figure 3.15 shows an image of the X-ray beam produced by the XOS polycapillary optic coupled with the Bede micro-source. The image was taken using a dental CCD 38-10 (e2v technologies).

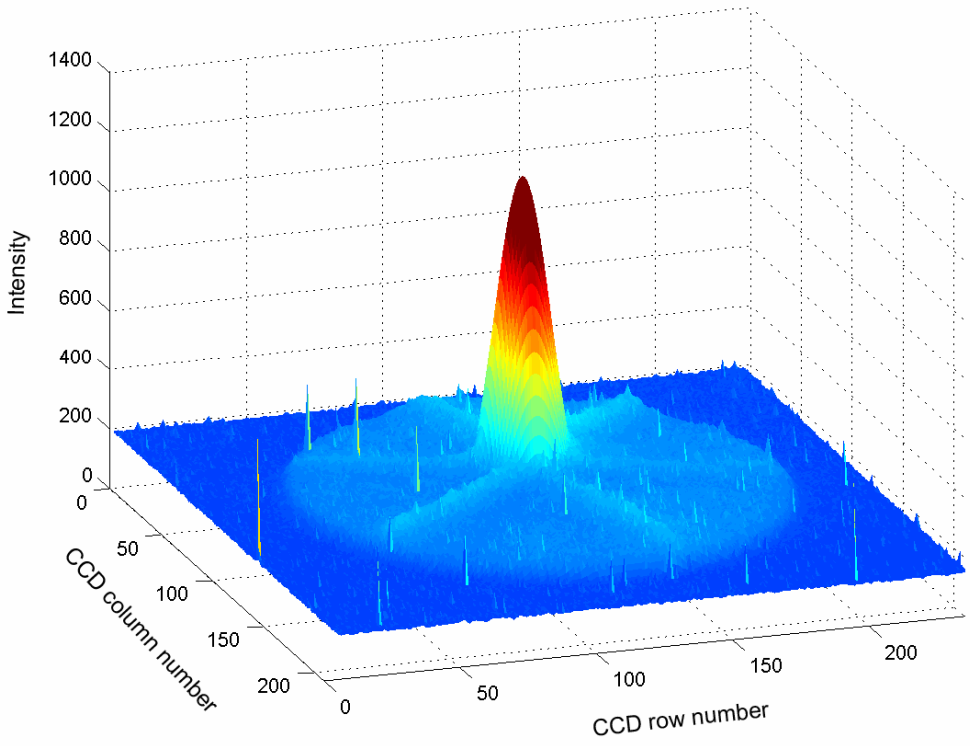

Figure 3.15: Energy distribution of X-ray beam produced from XOS optic

The energy distribution of the focused beam resembles a 3-dimensional Gaussian shape. The apex of the focussed beam represents the area of highest intensity and was utilised for sample irradiation. The alignment of the X-ray beam with the pinhole and sample is discussed in Section 4.9. The focussed beam was approximately 1 mm in diameter at a distance of 10 cm from the optic output, with a FWHM divergence of 3.5 mrad. The application of the optic yields a very different spectrum to that presented in Section 3.14, which is now discussed.

3.15.2 X-ray Optic Spectra

In Section 3.14 the continuous spectrum from the Bede micro-source was shown to resemble a blackbody curve with the tube voltage corresponding to the temperature of the radiating blackbody. This was taken without the presence of the XOS polycapillary focusing optic. The optic was vital to the project as it allowed a high flux of X-rays to be focused onto a small surface area of the sample with very low divergence. The optic not only focused the highly divergent beam of X-rays produced from the source but also modified the spectrum in favour of XRD applications [Misture & Hailer 2000]. Spectra from the source were collected using a SiLi detector and are shown in figure 3.16 for varying tube voltages. All spectra were collected at 0.01 mA using a 50 µm beam.

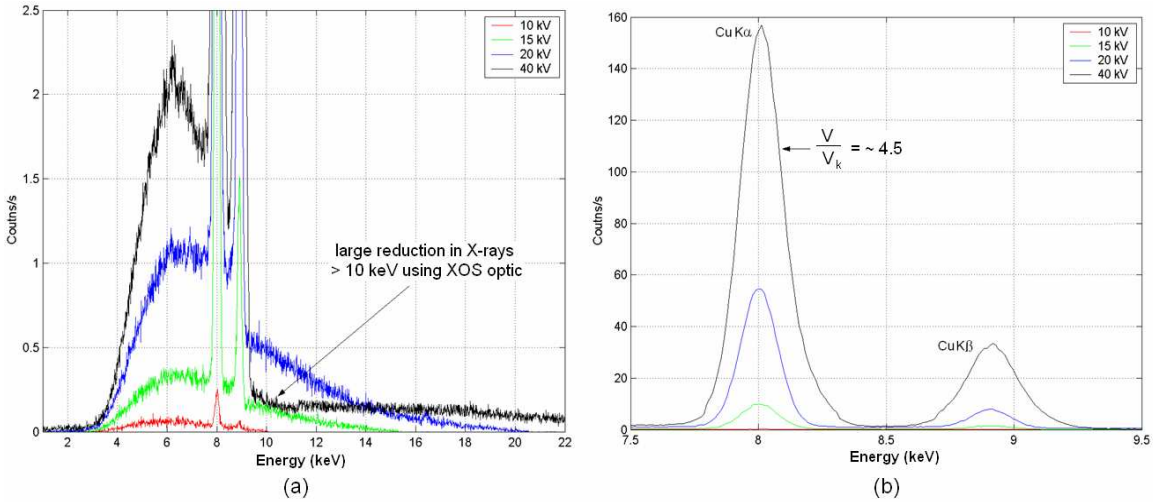

Figure 3.16: (a) Continuous and (b) characteristic X-ray spectra produced by XOS polycapillary optic with increasing tube voltage

One main alteration is seen in the spectra with the X-ray optic in comparison to the normal blackbody spectrum. X-rays greater than approximately 10 keV are highly

attenuated by the optic. As shown in equation 3.38, the critical angle for total external reflection decreases with increasing X-ray energy. The probability of an X-ray being successfully guided through the optic is much higher for lower energy X-rays, which results in another advantage of using polycapillary collimating optics for XRD applications. One source of noise in a diffraction pattern is related to the ratio of characteristic X-rays to continuous X-rays. With the use of polycapillary focusing optics, applying a high voltage to the X-ray source can increase the intensity of the characteristic radiation whilst reducing the number of high energy bremsstrahlung X-rays generated. This feature of the optic proves very useful for XRD.

Similar to the spectra without the optic, the intensity of the characteristic X-rays is directly related to $V/V_{K.}$ Since V/V_K is less than 5 at maximum tube voltage, the intensity of the characteristic X-rays is strongest at 40 kV. A summary of fluxes produced by the optic at different tube voltages is summarised in table 3.1.

3.15.3 Monochromated X-ray Spectra

As shown in figure 3.16, when operated at 40 kV the XOS optic almost completely suppressed higher energy bremsstrahlung photons greater than 10 keV. The perfect spectrum for XRD experiments would simply contain Cu Kα X-rays without Cu Kβ and continuous X-rays. A 15 µm sheet of nickel (Ni) was used to reduce the Cu Kβ to Cu Kα ratio and also reduce lower energy bremsstrahlung X-rays. The use of a filter would also reduce the flux of Cu Kα X-rays, however as the flux produced from the source was so high, the reduction of noise through incomplete monochromation was more important.

The absorption of the Cu Kα and Cu Kβ characteristic X-rays through the 15 µm Ni filter is calculated in Section 4.7. Figure 3.17 shows the resulting spectrum with the use of the Ni filter. With the application of the XOS optic and the Ni filter, almost all continuous X-rays have been eliminated from the spectrum. Without the filter, the continuous X-rays accounted for 16% of the total spectrum flux. With the Ni filter, this was reduced to less than 6%. The Cu Kβ X-rays have been successfully eliminated to 1% of the total spectrum allowing the Cu Kα X-rays to dominate the spectrum at 93%. A summary of all fluxes is given in table 3.1.

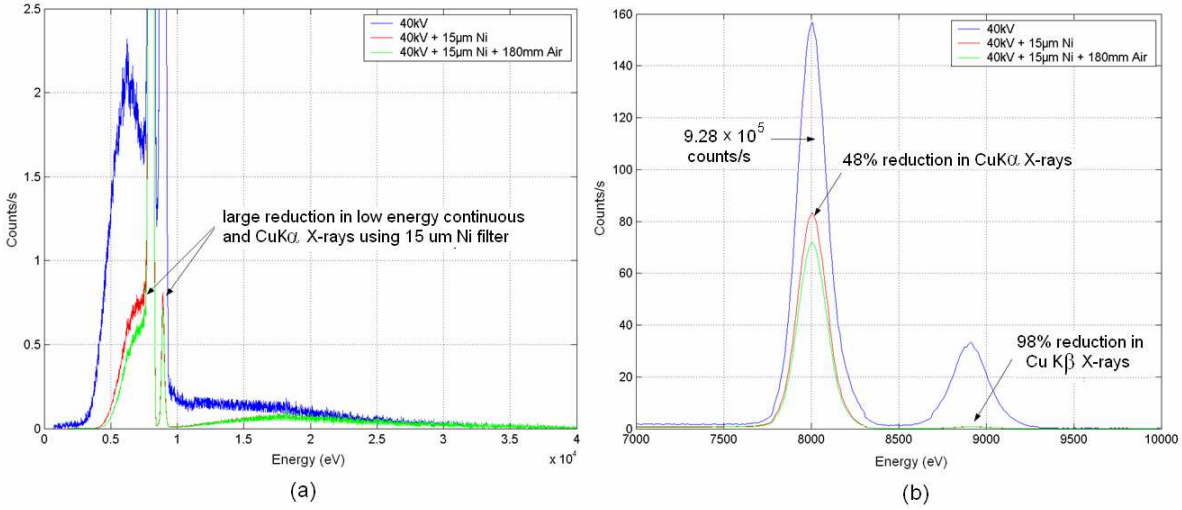

Figure 3.17: Reduction of (a) continuous and (b) characteristic X-ray flux by 15 µm Ni filter and 180 mm air gap between optic and sample at 40 kV, 2 mA

The calculations shown in equation 3.39 and 3.40 confirm the thickness of the Ni filter to be 15 µm. The Cu Kα and Cu Kβ X-rays were expected to be reduced to 52% and 2% respectively (see Section 4.7), which agrees with the calculations.

$$CuK\alpha \frac{IntegratedIntensity(withFilter)}{IntegratedIntensity(withoutFilter)} = \frac{140828}{271968} = 51.78\% \qquad (3.39)$$

$$CuK\beta \frac{Integrated\,Intensity\,(withFilter\,)}{Integrated\,Intensity\,(withoutFil\,ter\,)} = \frac{830}{41958} = 1.97\% \qquad (3.40)$$

Assuming a linear increase in intensity with tube current, table 3.1 summarises the flux of X-rays at 2 mA for different tube voltages.

Tube Voltage (*kV*)	Spot Size (µm)	CuKα	CuKβ	Continuous	Total
10	50	1.04×10^3	3.2×10^2	3.76×10^3	5.12×10^3
15	50	3.34×10^4	5.6×10^3	2.82×10^4	6.72×10^4
20	50	1.82×10^5	2.84×10^4	1.04×10^5	3.14×10^5
30	50	5.11×10^5	8×10^4	2.23×10^5	8.14×10^5
40	50	5.92×10^5	1.54×10^5	1.82×10^5	9.28×10^5
40 + 15 µm Ni filter	50	3.35×10^5	3.6×10^3	2.1×10^4	3.6×10^5
40	100	1.18×10^6	3.08×10^5	3.64×10^5	1.86×10^6
40	150	1.78×10^6	4.62×10^5	5.46×10^5	2.78×10^6

Table 3.1: Summary of flux produced in a 50 µm spot, at 2 mA for different operating voltages. All fluxes in counts/s

The X-ray flux produced by the micro-source at 80 W with the XOS polycapillary collimating optic has been documented elsewhere [Gibson & Gibson 2002]. According to the results published in this paper, the micro-source produces a flux of 1.2×10^9 counts/s in a 1.5 mm beam. Assuming a Gaussian distribution of the beam, where 1.5 mm represents the 6σ width, the flux contained within a 50 µm spot is $\sim 8 \times 10^6$ counts/s. This is ~ 1 order of magnitude larger than the flux calculation of 9.2×10^5 counts/s shown in table 3.1. Since the results in this paper were published by the manufacturers of the optic, XOS, it was expected that the X-ray flux was not perfectly linear with respect to tube current, and errors were caused from multiplying the spectra collected at 0.01 mA by a factor of 200 (to obtain the flux at 2 mA).

3.16 Background Spectra

3.16.1 XRF

Figure 3.18 shows a background XRF spectrum collected under the normal experimental arrangement. The background spectrum represents X-rays scattered from an empty sample holder and other parts of the facility. Table 3.2 summarises the standard operating conditions used for combined XRD/XRF analysis. Unless otherwise stated, all spectra presented in this thesis were collected using the operating conditions listed in Table 3.2.

Parameter	Value	Unit
X-ray tube voltage	40	kV
X-ray tube current	2	mA
Mylar thickness	20	µm
Filtration	15 µm Ni	
R_{ss}	180	mm
R_{sd}	120	mm
θ_{inc}	4	º 2θ
P_{ob}	100	µm
CCD exposure time	1	s
Number of exposures	1000 - 2000	
CCD readout time	1.6	s
CCD operating mode	NIMO	
I_d	1	e^- p/p/s
σ_{RN}	7.4	e^- r.m.s
Image area	256 × 1040	pixels

Table 3.2: Summary of standard operating conditions used for combined XRD/XRF analysis. NIMO refers to 'non-inverted mode operation'

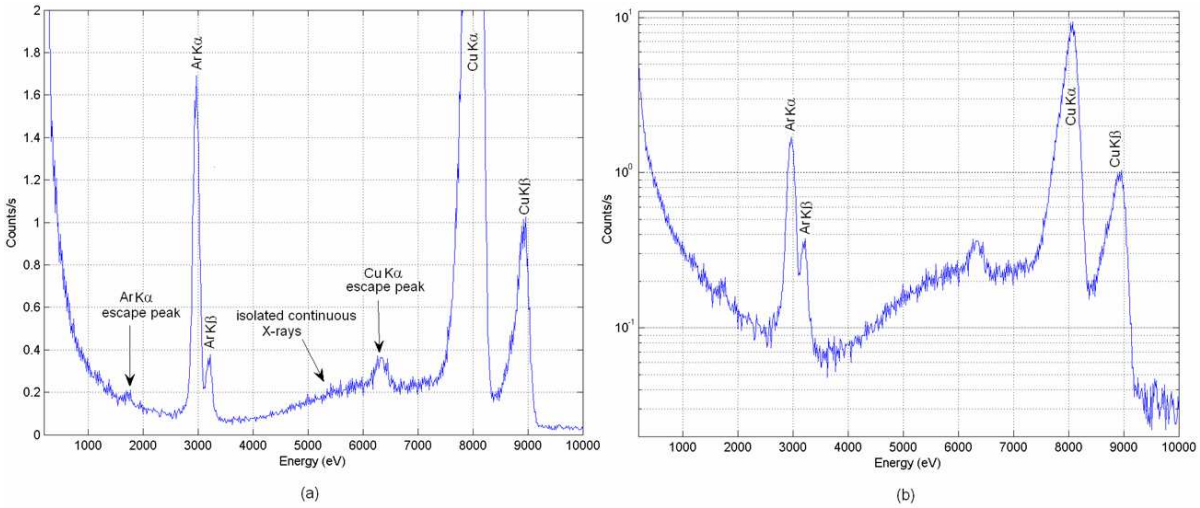

Figure 3.18: Background XRF spectrum collected at 40 kV, 2 mA in (a) linear intensity scale and (b) log intensity scale

The spectrum shows the presence of 2 strong Cu K shell emissions from the Bede micro-source. The data was collected without the presence of the Ni filter to increase the incident flux. These characteristic X-rays have been generated through elastic scattering from the sample holder, air and other parts of the test facility. The spectrum also shows a Cu Kα escape peak with an intensity of ~ 0.01 of the main Cu Kα peak.

The isolated continuous X-rays seen between 4 − 7.5 keV in the background spectrum can be seen in the incident spectrum shown in figure 3.16. Two Argon (Ar) Kα and Kβ peaks are also noticed in the background spectrum, which originate from the 108 mm of air between the sample holder and CCD-Array. Table 3.3 lists the main components of air along with the fluorescence yield of their K shell emissions.

Component	Volume (%)	Symbol	$K\alpha_1$ (eV)	$K\beta_1$ (eV)	K shell Yield
Nitrogen	78.084	N	392	-	0.004
Oxygen	20.947	O	523	-	0.006
Argon	0.934	Ar	2957	3192	0.115

Table 3.3: Elemental composition of air with corresponding characteristic K shell emission energies and fluorescence yield

The flux incident on the sample with an X-ray power of 80 W, within a 50 µm beam, was 9.28×10^5 counts/s (a 'count' represents a single X-ray event of any energy). With a fluorescent yield of 0.004 and 0.006 for N and O respectively, one would

expect a large number of characteristic X-rays to be emitted from the sample. Although this is true, these X-rays experience severe attenuation from air prior to detection by the CCD. Consequently, elements with an atomic number Z, below 13 (such as N and O) are very difficult to detect. Although the volume of Ar (Z = 18) in air is much smaller than N and O, the transmission of Ar Kα X-rays through 108 mm of air is sufficient to allow detection. Any X-rays with an energy greater than the K absorption edge of Ar (3203 eV) can cause K shell emissions in the Ar atom.

3.16.2 XRD

The background pattern produced in an XRPD pattern relates to the angular (2θ) scattering of Cu Kα X-rays. Equation 6.2 can be used to calculate the length a signal X-ray must travel to escape the sample. This equation highlights that the path length of an emitted photon is inversely proportional to the emission angle, θ (with respect to the sample holder and 2θ with respect to the incident beam axis). Therefore, signal X-rays must travel longer path lengths to escape the sample at lower 2θ angles, resulting in increased attenuation. The total attenuation depends on the energy of the signal X-rays generated in the sample and the characteristics of the sample (i.e. thickness and linear attenuation coefficient).

Section 6.2.1 outlines the attenuation of signal X-rays from 0.1 − 10 keV through a basalt powder for varying emission angles. Figure 3.19 shows the XRD scattering profile of the energy discriminated and the combined XRD/XRF data of peridotite, a common igneous rock found on Earths mantle, comprising of the minerals olivine and pyroxene. The reason why the energy discriminated diffraction pattern in figure 3.19 has a linear scattering profile is because Cu Kα (8047 eV) X-rays experience very little attenuation in the peridotite sample. If the CCD images are radially integrated without energy discriminated data (combined XRD/XRF), then the expected scattering profile is seen at lower 2θ angles. A reduction in scattering from ~ 0° − 30° is noticed due to increased attenuation of lower energy X-rays (<< 8047 eV). The energy discriminated data results in a higher SNR ratio in comparison to the raw data, which highlights the advantage of using energy discriminating detectors for XRD analysis.

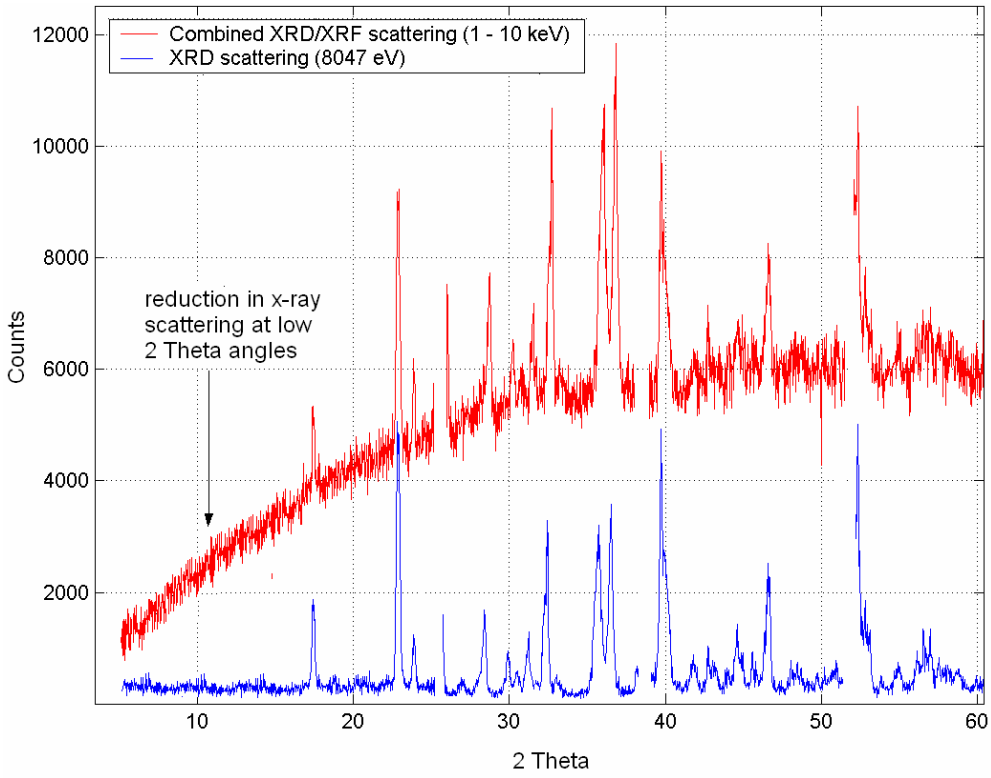

Figure 3.19: Radial integration of energy discriminated (Cu Kα events only) and raw data (combined XRD/XRF) for a peridotite powder sample

3.17 Discussion

This chapter has provided an overview of the underlying principles of scientific CCDs. The operation and structure of the CCD has been discussed as well as the processes of charge generation, collection, transfer and measurement. The noise sources, which limit the performance of the detector for X-ray spectroscopy applications, have also been presented. Different CCD architectures for increased QE in the soft X-ray range have also been reviewed.

The process of X-ray generation by the Bede micro-source has been outlined using relevant theory and spectra have been collected using a SiLi detector. This chapter also introduced the concept of polycapillary collimating optics, which focus a highly divergent beam of X-rays into a small beam of low divergent quasi-parallel X-rays. It was shown that with the use of a 15 µm Ni filter and the Bede micro-source operated at 40 kV, the spectrum incident on the sample was almost an entirely monochromatic (93%) beam of Cu Kα X-rays. The incident beam irradiating the sample was ideal for XRD applications and the large flux produced ensured a high throughput of XRF data.

Chapter 4 : The CCD-Array and Test Facility

4.1 Introduction

This chapter describes the design of the detector built for this thesis work. The initial section describes the design and main building blocks of the CCD-Array, which includes the headboard electronics and X-ray window. Thermal results are also presented which describe the cooling of the CCDs using a TEC. The heat loads inside the CCD-Array during TEC cooling are determined through calculations and confirmed with measurements. Thermal simulations are used to provide a more accurate temperature profile across the shapal and CCD assembly. The ability of the test facility to dissipate heat through liquid cooling is also presented. The layout of the CCDs inside the detector was based on a precisely calculated geometry with respect to the sample. SRMs from the National Institute of Standards and Technology (NIST) were used to confirm the spatial geometry of the CCDs. Any inaccuracies caused from misalignments were identified and corrected. The other components in the test facility are also discussed with particular emphasis on the collimation and monochromation stages.

4.2 The CCD-Array

The CCD-Array was developed to be capable of simultaneously collecting combined XRD/XRF data from powdered rock samples. Initial testing was conducted in a laboratory environment, using a specially designed test facility. The key feature of the CCD-Array was the use of 4 CCDs in a curved arrangement. The CCDs lie on the edge of a 120 mm arc, where the centre point is represented by the point of sample irradiation on the sample holder. The geometry was such that the point of tangency was the central pixel on each of the CCDs. The geometry of the CCD-Array design is discussed further in Section 4.5.

The design requirements of the CCD-Array can be summarised as follows:

- The CCDs would lie along the curvature of a 120 mm circle resulting in very high spatial resolution. For XRD applications with less intense resolution requirements, the CCD image would be binned to reduce data collection times.

- The CCD-Array would provide an angular coverage of approximately 60° 2θ, ranging from ~ 4 − 64° for Cu Kα radiation.
- A single TEC would be used to provide cooling to all 4 CCDs to reduce the size and power requirements of the detector.
- A material of very high thermal conductivity and low thermal expansion would be used to couple the CCDs to the TEC.
- AIMO CCDs would be used to relax cooling requirements at the expense of depletion depth. Reducing power requirements was crucial for portability.
- Temperature sensors would be strategically glued to the CCDs and Shapal to perform thermal tests.
- The CCD-Array would require high precision manufacturing (2 − 3 decimal places) to ensure accurate spatial calibration of the detector for qualitative XRD analysis.
- The test facility would incorporate liquid cooling to absorb heat generated by the CCD-Array, X-ray source and coolant pipes.
- Headboard electronics would form part of the detector for portability.
- The detection of characteristic X-rays from 1 − 2 keV was crucial for accurate chemical/elemental analysis of rocks, therefore the chosen X-ray window would allow a high transmission of X-rays from 1 − 2 keV.
- Ideally, the CCD-Array would be opaque to visible light. The only leakage of light into the detector would be caused from the X-ray window. The thickness of the X-ray window would be carefully selected to achieve reasonable opacity, whilst maintaining a high transmission of X-rays from 1 − 2 keV. For flexibility, a second sheet of the X-ray window material could be used to make the CCD-Array fully lightproof at the expense of X-ray transmission.

The building blocks of the detector are labelled 1 – 9 in figure 4.1 and are now described.

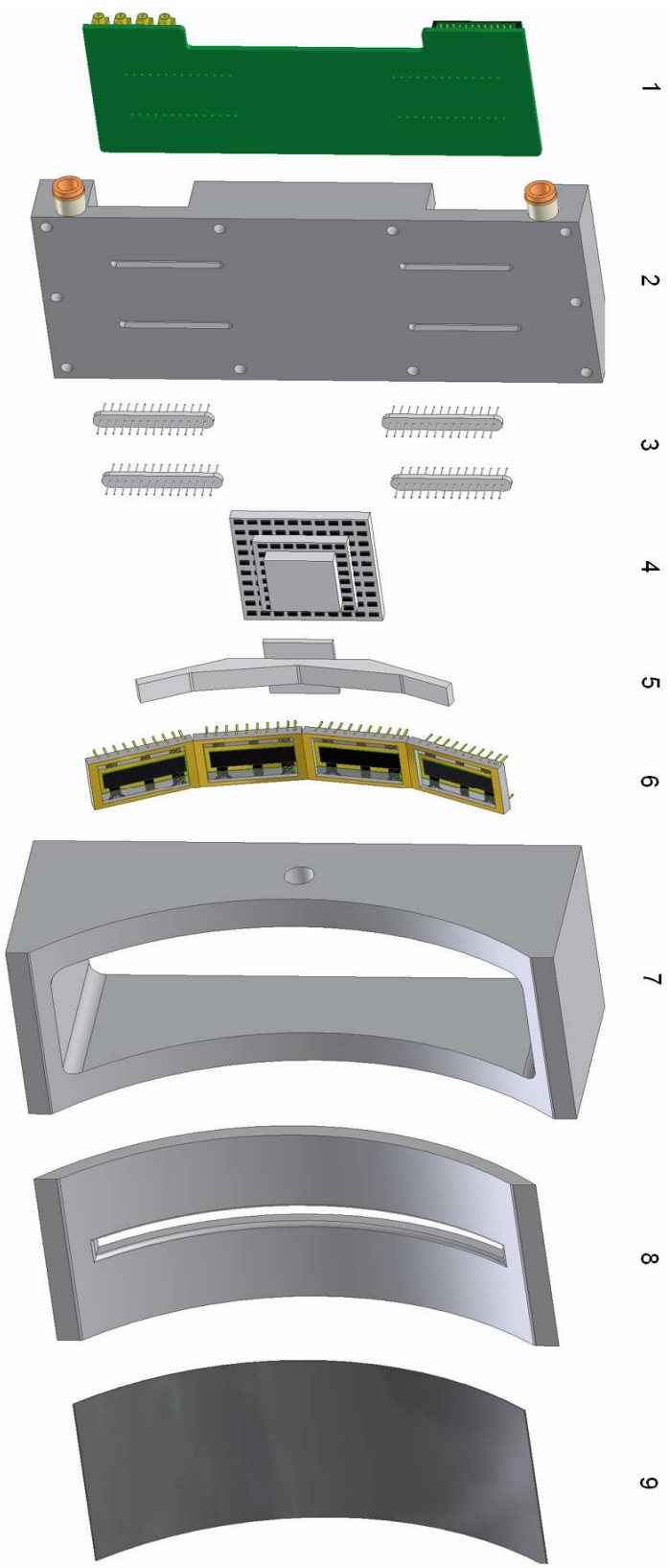

Figure 4.1: Individual components of the CCD-Array

- **Headboard Electronics (1)**

The headboard contained 4 connections to the feed through pins located on the back of the base plate (feature 2 in figure 4.1). Each of the feed through connectors comprised of 14 connections that allowed the headboard to be pushed through the feed through pins and fixed onto the base plate. Figure 4.2 shows the orientation of the CCD30-11 in relation to the headboard (rear view). The individual feed through connectors were labelled X2, X3, X4 and X5.

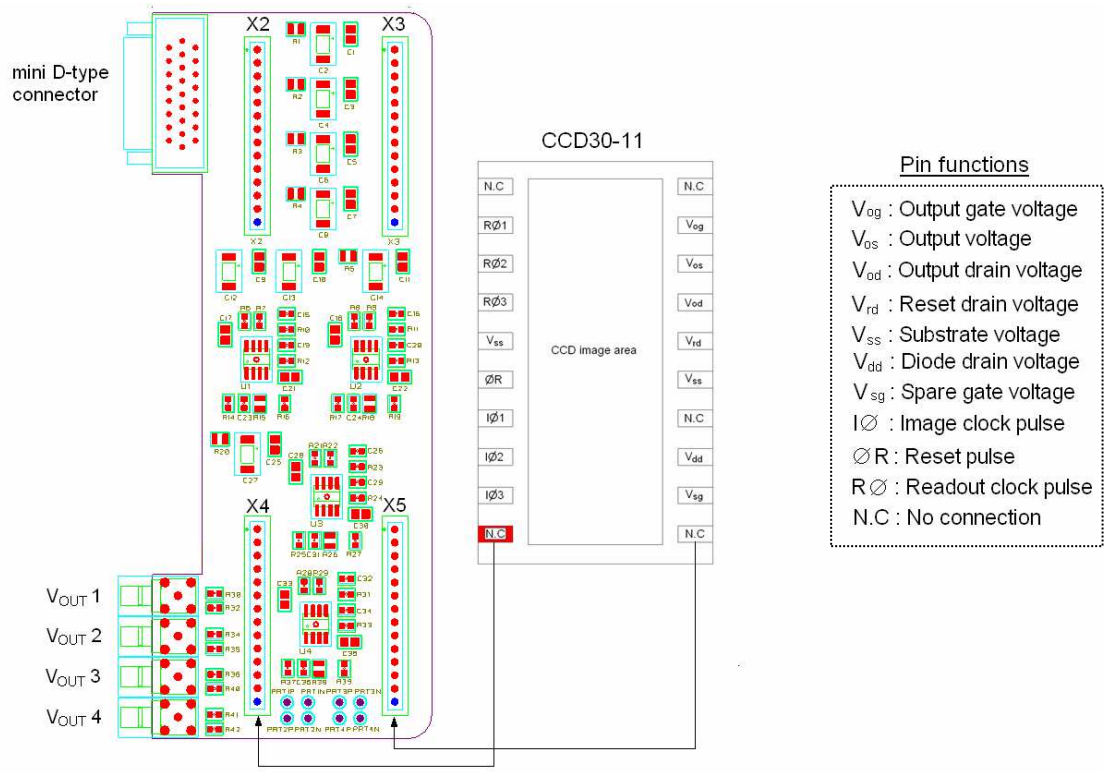

Figure 4.2: Schematic of the CCD-Array headboard electronics (rear view)

All 4 CCDs were glued to the Shapal ceramic with pin 1 (coloured red) located at the bottom left (looking from the back of the detector). The mini D-type connector provided all necessary sequencing and bias voltages, which were supplied by the CCD drive electronics. The signals in the feed through connectors were placed strategically to align with the CCD pins and minimise wiring. Table 4.1 summarises the function of each pin of the 4 feed through connectors.

X2		X3		X4		X5	
Pin #	**Function**	**Pin #**	**Function**	**Pin #**	**Function**	**Pin #**	**Function**
1	N.C	*1*	N.C	*1*	N.C	*1*	N.C
2	IØ3	*2*	Gnd	*2*	SØ3	*2*	Gnd
3	IØ2	*3*	V_{dd}	*3*	SØ2	*3*	V_{dd}
4	IØ1	*4*	V_{SS}	*4*	SØ1	*4*	V_{SS}
5	V_{SS}	*5*	V_{rd}	*5*	V_{SS}	*5*	V_{rd}
6	ØR	*6*	V_{od} 1	*6*	ØR	*6*	V_{od} 2
7	RØ3	*7*	V_{OS} 1	*7*	RØ3	*7*	V_{OS} 3
8	RØ2	*8*	V_{og}	*8*	RØ2	*8*	V_{og}
9	RØ1	*9*	V_{OS} 2	*9*	RØ1	*9*	V_{OS} 4
10	N.C	*10*	N.C	*10*	N.C	*10*	N.C
11	TEC (-)	*11*	TEC (+)	*11*	PRT 1 (+)	*11*	PRT 3 (+)
12	TEC (-)	*12*	TEC (+)	*12*	PRT 1 (-)	*12*	PRT 3 (-)
13	TEC (-)	*13*	TEC (+)	*13*	PRT 2 (+)	*13*	PRT 4 (+)
14	TEC (-)	*14*	TEC (+)	*14*	PRT 2 (-)	*14*	PRT 4 (-)

Table 4.1: Pin functions of feed through connectors

The CCDs were sequenced simultaneously but read out independently at ~ 165 kHz through 4 outputs labelled V_{OUT} 1 − 4, as shown in figure 4.2. The sensitivity of the on-chip amplifier of the CCD30-11 was 1.5 µV/e^-. The output voltage from the CCD was further amplified by the headboard by a factor of 11 to allow the charge packet to be detected by an ADC. A Cu Kα X-ray therefore produced an output voltage from the headboard of ~ 36 mV. Due to the high current required by the TEC (~ 6 A), 4 feed through pins were used for each TEC terminal. Four platinum resistive thermometers (PRTs) were used to monitor the temperature inside the CCD-Array during operation.

- **Copper Base Plate (2)**

The copper base plate was zinc plated to prevent corrosion and all other components were either glued or bolted to the base plate. The TEC was centrally glued to the base plate using Hysol, a special non out-gassing glue (out-gassing involves the release of gases that are trapped inside the pores or cracks of a material which contaminate sensitive equipment in a vacuum). In order to absorb the heat generated by the hot side of the TEC, a liquid cooling channel was introduced along the outer edges of the base plate. Figure 4.3 shows the direction of cooling at the rear of the base plate. The location of the headboard is highlighted in green and was designed to slot inside the rear of the base plate.

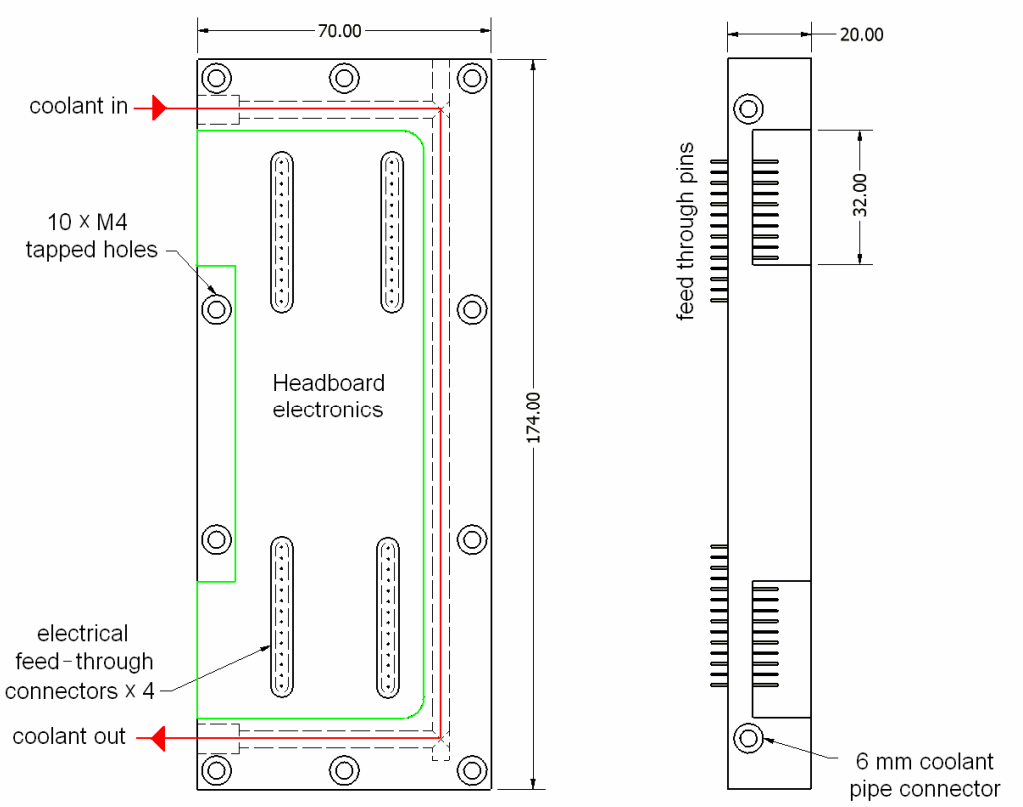

Figure 4.3: Copper base plate of the CCD-Array outlining the direction of cooling and location of headboard electronics (all dimensions in mm)

- **Feed Through Pins (3)**

Four electrical feed through pins were glued into recessed slots at the rear of the base plate. Each of the feed through connectors contained 14 pins with a 2 A rating. The feed through pins provided the interface between the CCDs inside the vacuum and the headboard electronics at standard atmospheric pressure.

- **TEC (4)**

The TEC was chosen using Melcor's Thermoelectric cooler selection software [Aztec 2005]. Since the heat sink for the TEC was a liquid cooled copper base plate, the thermal resistance of the heat sink was expected to be very low. The heat loads inside the CCD-Array chamber were predicted to be approximately 4 – 5 W and the cold side temperature T_c, was set to -30 °C. The TEC chosen for the application was a 3-stage 80 W TEC (3CP 085 065-71-31-17). The TEC was capable of a maximum temperature differential ΔT_{max} ($T_h - T_c$) of 97 °C and maximum heat pumping capacity of 15.5 W. The temperature of the hot side of the TEC (T_h) was not expected to

increase more than 5 °C above the ambient temperature (+20 °C) at full operating power. The theoretical maximum T_c was therefore ~ -70 °C with no heat loads. Detailed calculations regarding the actual heat loads incident on the cold side of the TEC (Q_c) are presented in Section 4.3.

- **Shapal Ceramic (5)**

A special ceramic known as Shapal was chosen to conduct heat from the CCDs to the TEC, due to its very high thermal conductivity (90 W/m K) and low thermal expansion (4.4 × 10^{-6}/ °C). The curvature of the 4 CCDs was defined by the geometry of the Shapal ceramic, as shown in figure 4.4. The conduction of heat is inversely proportional to length (see equation 4.6), therefore the length of the Shapal was minimised and designed to cover only half of CCD 1 and CCD 4.

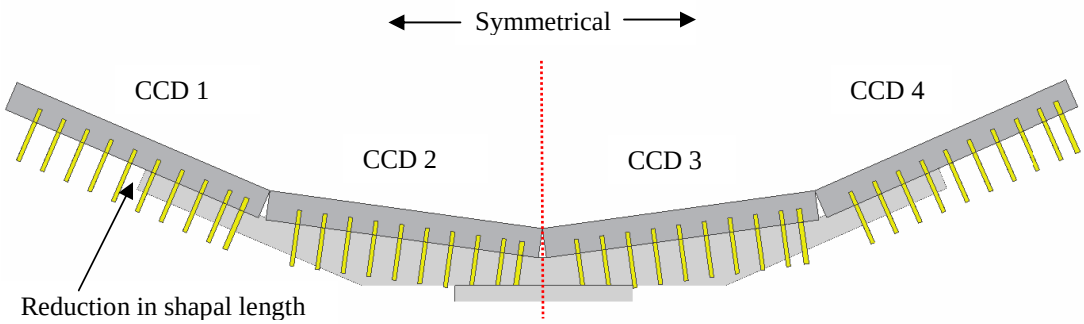

Figure 4.4: Geometry and symmetry of Shapal ceramic and 4 CCD30-11s

- **CCD30-11 (6)**

The CCDs supplied by e2v for the CCD-Array were 6 FI AIMO CCD30-11s. The CCD30-11 is an ideal X-ray spectroscopy detector [e2v technologies 2007]. Leakage current of less than 1 e^- p/p/s can be achieved at -20 °C, combined with a low readout noise of ~ 5 e^- r.m.s. at ~150 kHz readout speed. The CCD30-11 contains a 1040 (columns) × 256 (rows) image area (16 pre-scan) with (26 µm)² pixels allowing very high spatial resolution for XRD experiments.

- **Chamber Front (7)**

The front of the chamber was made from aluminium and was designed with the same 120 mm curvature as the CCDs to minimise instrument volume. The chamber front

was bolted onto the base plate with 10 M4 bolts. A 12-inch flexible vacuum pipe was glued into a 9.2 mm hole on the chamber front, which connected the CCD-Array to a vacuum pump. Approximately 30 − 45 seconds was required to create a vacuum of ~ 3×10^{-3} mbar inside the CCD-Array. A 2.3 mm deep recessed channel was also introduced around the backside of the chamber to accommodate an O-ring seal, ensuring the array was airtight.

- **Chamber Lid (8)**

The window on the chamber lid was designed with the same width as the imaging area of the CCD30-11 (6.7 mm). The edges of the window were rounded to reduce the stress imposed on the X-ray window under vacuum.

- **X-ray Window (9)**

The X-ray window consisted of a 20 µm thick sheet of aluminised Mylar (Polyethylene Terephthalate). The Mylar sheet was glued to the chamber lid and a vacuum test was performed to ensure the Mylar would sustain a vacuum in the range of 10^{-3} − 10^{-6} mbar. This test was performed prior to gluing the CCDs to the Shapal, since implosion of the X-ray window under vacuum could destroy the CCDs.

The main advantage of Mylar as an X-ray window was the high transmission of X-rays from 1 − 10 keV (see figure 6.3). This was vital in the detection of X-rays from 1 − 2 keV which are commonly found in rocks, namely Na Kα (1041 eV), Mg Kα (1254 eV), Al Kα (1487 eV) and Si Kα (1740 eV). Another important function of the Mylar was to block visible light entering the CCD-Array. One sheet of Mylar (20 µm) was unable to make the detector fully lightproof. To make the device fully portable and lightproof, 2 sheets of Mylar were required, however, this was at the expense of X-ray transmission. To prevent light leakage when testing the CCD-Array using a single 20 µm sheet, the CCD-Array was placed in a lightproof box. An initial concern with the design of the detector was implosion of the Mylar X-ray window under vacuum, which could damage the CCDs. The deflection of the Mylar window W_{df}, can be calculated as [Leonhardt & Mapes 1993]:

$$W_{df} = K_c \left(\frac{p_w {a_L}^4}{Y_m t_w} \right)^{0.33}, \qquad (4.1)$$

where K_c is a constant which has a value of 0.36 for rectangular windows, p_w is the pressure applied to the window (Pa), a_L is the length of the short side of the window (m), Y_m is Young's Modulus and t_w is the thickness of the window (m). Using equation 4.1, the length of deflection of the Mylar window under vacuum was calculated to be 0.654 mm or 654 µm. This was based on an applied pressure of 1×10^5 Pa, which represents the difference in pressure inside and outside the vacuum (~ 1 bar). The stress on the mylar *S*, can be expressed as [Timeoshenko 1959]:

$$S = G\left[Y_m \left(\frac{p_w a_L}{t_w} \right)^2 \right]^{0.33}, \tag{4.2}$$

where G is a geometric constant with a value of 0.34 for rectangular windows and 0.27 for circular windows. Mylar has as a tensile strength of 190×10^6 Pa. Using equation 4.2 it can be calculated that the minimum thickness of Mylar required to sustain a vacuum of ~ 1×10^{-6} mbar inside the CCD-Array is ~ 2.5 µm. The actual thickness used (20 µm) exceeds this calculation by a factor of 8, due to the high risk of CCD damage assuming window failure. At the time of writing this thesis, the Mylar X-ray window had survived 25 months under vacuum without any signs of material degradation or fatigue.

4.3 CCD-Array Thermal Characterisation

The CCD30-11 detectors used in constructing the CCD-Array operated using AIMO, therefore produced dark current of ~ 1 e^- p/p/s at -20 °C. The target temperature of the CCDs was therefore -20 °C, although it is shown in Section 6.4 that the CCDs can perform accurate combined XRD/XRF analysis at much higher temperatures. In order to measure temperatures, 5 PRTs were glued at specific locations inside the CCD-Array chamber. Theses locations were:

- **Copper Base plate**: A PRT was glued ~ 5 mm from the TEC on the base plate to estimate T_h.

- **Shapal Ceramic**: 2 PRTs were glued to the Shapal ceramic. One was glued to the base of the Shapal and was used to measure T_c. The second PRT was glued to the edge of the Shapal. This was to monitor the increase in temperature across the

Shapal ceramic. Since the properties of the Shapal were symmetrical, only 2 PRTs were needed for the thermal test.

- **CCDs**: Due to the symmetry of the Shapal, the properties (exposed surface area, temperature, dark current) of CCD 1 and CCD 4 were identical, as were the properties of CCD 2 and CCD 3. One PRT was glued to the ceramic of CCD 1 and a second was glued to the ceramic of CCD 2.

4.3.1 CCD Cooling: Vacuum vs. Nitrogen Gas Environment

Two environments inside the CCD chamber were considered for the cooling process. One method involved filling the CCD chamber with nitrogen gas (N_2) and the second method involved creating a vacuum (~ 10^{-3} mbar) inside the CCD chamber. Both methods ensured the removal of water vapour in the air which would freeze at low temperatures to form ice. The preferred method for cooling was to use N_2 as this would not cause any stress on the Mylar X-ray window. The main heat loads from the N_2 and vacuum experiments were convective and radiative heat loads respectively. The amount of heat transferred to an object through radiative heat transfer Q_{Rad} , can be expressed as [Young 1992]:

$$Q_{Rad}(W) = e\sigma_{sf} A\left(T_R{}^4 - T_A{}^4\right), \tag{4.3}$$

where e is the emissivity of the body emitting the radiation (0 − 1), σ_{sf} is Stefan's constant (5.67 × 10^{-8} W/m² K^4), A is the surface area of the body receiving the radiation (m²), T_A is the temperature (°C) of the body receiving the radiation and T_R is the temperature (°C) of the radiating body (a warmer object radiates heat through electromagnetic radiation to a colder object). The emissivity of the CCD ceramic was found to be 0.8 [The Engineering Toolbox 2005] and the emissivity of the Shapal was expected to be 0.85 [Precision Ceramics 2007].

The amount of heat transferred to a body through convective heat transfer Q_{cv}, can be expressed as [Young 1992]:

$$Q_{cv}(W) = h_{tc} A\left(T_{amb} - T_A\right), \tag{4.4}$$

where h_{tc} is the heat transfer coefficient and T_{amb} is the ambient temperature (°C). The value of h_{tc} is between 10 − 30 for normal convection and greater than 30 for forced

convection. The value of h_{tc} for N_2 was estimated to be ~ 10. Table 4.2 summarises the calculated radiative and convective heat loads.

	CCD1	CCD2	CCD3	CCD4	Shapal	Total
Surface area (m²)	1.6×10^{-3}	1.46×10^{-3}	1.46×10^{-3}	1.6×10^{-3}	2.07×10^{-3}	8.26×10^{-3}
Q_{Rad} (W)	0.294	0.280	0.280	0.294	0.529	**1.677**
Q_{cv} (W)	0.898	0.878	0.878	0.898	1.720	**5.272**

Table 4.2: Summary of radiative/convective heat loads on CCDs and Shapal ceramic

As shown in table 4.2, the amount of heat transfer from convection far exceeds the radiative heat transfer. The effect of radiative heat transfer was negligible in the N_2 experiment as the temperature of the N_2 and chamber walls was very similar. Based on the calculations shown in table 4.2, the performance of the TEC under vacuum was expected to be much better than with N_2. Figure 4.5 shows the response of the various PRTs with respect to increasing TEC power.

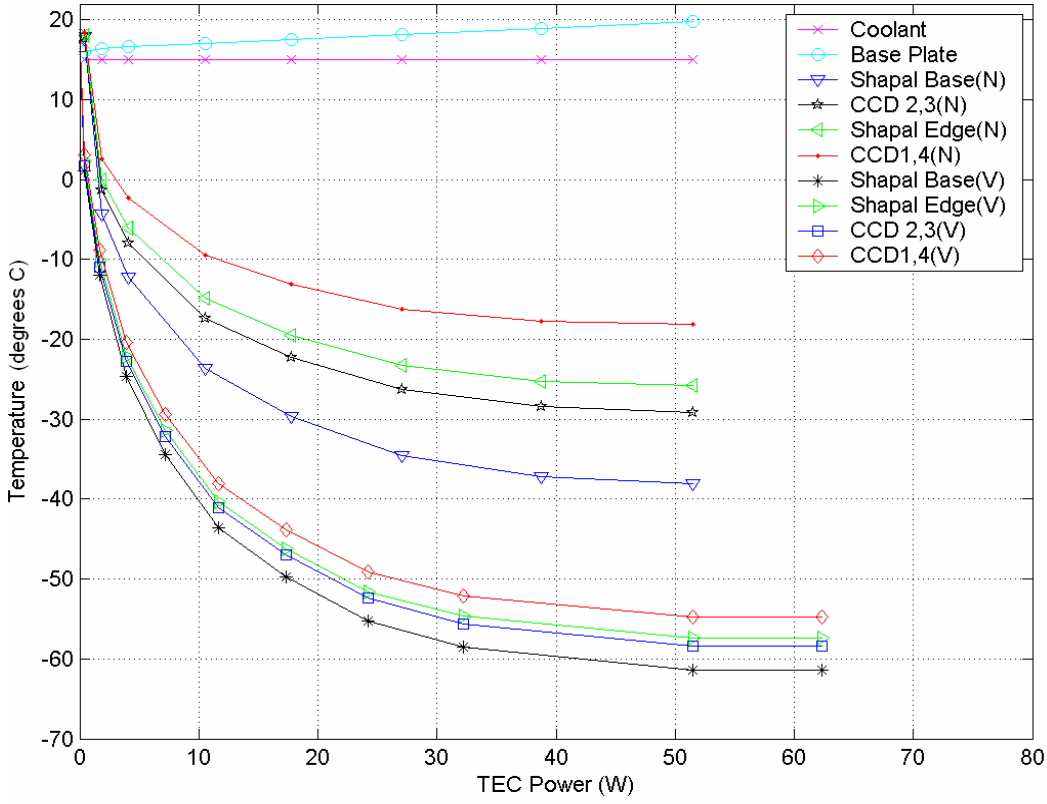

Figure 4.5: CCD-Array thermal results in N_2 and vacuum cooling environments

Both methods showed a similar increase in the temperature of the copper base which peaked at approximately 20 °C at full TEC power. Figure 4.5 highlights the increased

convective heat load on the CCDs and Shapal assembly using the N_2 cooling method. The experimental results and heat load calculations emphasised the need to operate the detector under vacuum during cooling. For portability, the CCD-Array could also be sealed once under vacuum. The results also draw attention to the high thermal conductivity of the Shapal ceramic (90 W/m K). The increase in temperature from the centre of the Shapal ceramic to the edge, was found to be only 3 °C at full operating power (when under vacuum). A similar increase in temperature was also noticed with the CCDs.

The relationship between Q_c and T_c at 6 A operating current can be approximated using the expression [Aztec 2005]:

$$Q_c(W) = (0.1598 \times T_c) + 11.507 . \quad (4.5)$$

The Q_c for the radiative and convective experiments was calculated to be 1.695 W and 5.43 W respectively, using equation 4.5. The expected values of Q_c based on T_c are in very close agreement with the calculations outlined in table 4.2. The calculations highlight that the transfer of radiative heat between chamber walls and CCDs/Shapal is close to 100%. This was to be expected since the assembly was inside a vacuum and there is no attenuation of the electromagnetic waves transferring the heat. Equation 4.5 also confirms the value of 10 for the heat transfer coefficient of N_2, was a very good approximation.

4.3.1.1 Thermal Simulations

A thermal modelling program was used to determine a more accurate temperature profile of the CCDs and Shapal, since the PRTs only provided the temperature profile at 4 distinct locations. The CCD ceramic of the CCD30-11 was constructed from alumina (Al_2O_3) as opposed to aluminium nitride (AlN), which is used by e2v for CCDs that require higher precession flatness [Pool 2005]. Table 4.3 lists the properties of the Shapal and CCD ceramic used in the simulations.

Parameter	Shapal	CCDs (Al_2O_3)
Specific heat (J/Kg K)	790	880
Density (g/cm^3)	2.9	3.69
Thermal conductivity (W/m K)	90	28

Table 4.3: Properties of Shapal and CCD ceramic used for thermal simulation

T_h was calculated to be + 25 °C [Aztec 2005] with the TEC operated at 6 A. The theoretical temperature of T_c without any heat loads was approximately – 70 °C (25 °C – ΔT_{max}). Radiative and convective heat loads were added to the CCDs and Shapal assembly and the temperature profiles were monitored in steady state (separate simulations). The resulting temperature profile of the CCD and Shapal assembly after radiative heat loads is shown in figure 4.6.

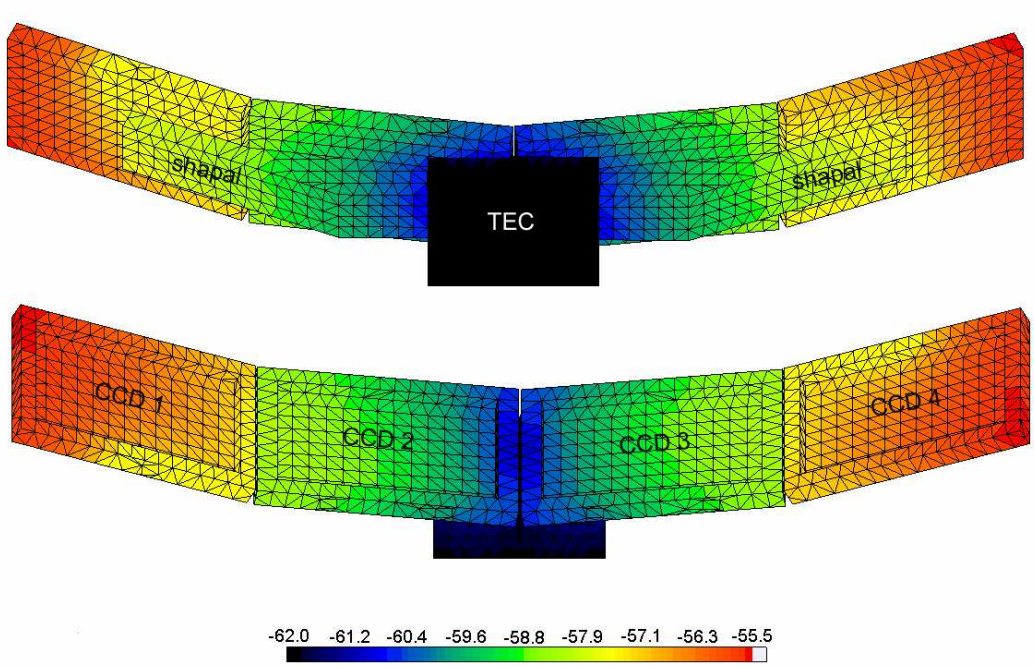

Figure 4.6: Resulting temperature profile of CCD-Array after radiative heat loads

Results from the thermal simulations are shown in table 4.4, compared with the PRT measurements shown in figure 4.5.

	Vacuum		Nitrogen	
	Expected	Simulated	Expected	Simulated
Shapal base (℃)	-61.4	-62.1	-38.0	-43.3
Shapal edge (℃)	-57.4	-58.1	-25.8	-29.8
CCD 1 (℃)	-54.7	-55.5	-18.1	-22.9
CCD 2 (℃)	-58.4	-58.0	-29.1	-34.2

Table 4.4: Comparison between simulated and experimental temperatures of shapal and CCDs at steady state

For the vacuum environment, a good agreement was seen between the PRT measurements and the simulated temperature profile with errors of < 2%. An important result obtained from the thermal simulations was the temperature of the

bottom CCD ceramic packaging, or Si temperature. Maximum temperature deviations across the Si imaging area were calculated to be < 1.2 °C for all 4 CCDs. This was not expected to cause measurable variations in dark current across the image area, as the dark current was < 1 e^- p/p/s at temperatures < -20 °C. The results also confirm the advantage in design of reducing the length of the shapal ceramic (covers only half of CCD 1 and CCD 4), as this increased the conduction of heat, whilst causing negligible effects on the dark current.

Errors of ~ 14% were recorded for the N_2 environment simulation, however both experimental measurements and calculations confirmed that creating a vacuum inside the CCD-Array was more conducive to CCD cooling. Figure 4.21 shows the T_c vs. Q_c performance of the TEC, displaying the final measurements for Q_{Rad} and Q_{cv}.

4.3.2 Thermal Performance under Normal Operation

When the CCDs were wired to the feed through connectors and the electrical headboard was connected, a very large drop in thermal performance was recorded on all PRTs. Power dissipated from the CCDs during operation also caused an increase in temperature of the CCDs. The magnitude and effect of the heat loads from electrical wiring and CCD power dissipation are now described.

4.3.2.1 Electrical Wiring

Since the temperature of the feed through pins was comparable to the temperature of the vacuum base (~ 19 °C), heat was conducted from the feed through pins to the CCDs. The amount of heat conducted through a material, Q_{cnd}, can be expressed as [Young 1992]:

$$Q_{cnd}(W) = k_t A\left(\frac{T_W - T_B}{L_m}\right), \tag{4.6}$$

where k_t is the thermal conductivity of the material (W/m K), A is the cross sectional area of the conducting material (m²), T_W is the temperature of the body where heat is being conducted from (°C), T_B is temperature of the body where heat is being conducted (°C) and L_m is the length of the conducting material (m). The electrical wiring consisted of 0.5 mm diameter copper and a PVC insulating material. The thermal conductivity of PVC (0.19 W/m K) is insignificant in comparison to that of

copper (400 W/m K) and was therefore not considered in the calculations. The average length of the wires was calculated to be approximately 62 mm by direct measurement. Using equation 4.6, the total heat load on each CCD pin was calculated to be 0.104 W and on the total array was approximately 2.9 W (0.104 W × 29 wires).

4.3.2.2 Active CCD load

During data collection, all 4 CCDs were integrated and read out continuously. Power was dissipated by all 4 CCDs during this process and converted to heat. This section estimates the heat dissipation from each CCD during operation.

- **Parallel Clocking Power Dissipation**

The time taken T_{cp}, to charge a capacitor is expressed as, $T_{cp} = R_{cp} \times C_{cp}$, where R_{cp} is the resistance (Ω) and C_{cp} is the capacitance (F) of the capacitor. Therefore, the time taken τ_p, to charge a CCD pixel is the multiplication of the electrode series resistance (R_p) and the capacitance of each 3-phase pixel (C_p). For the CCD30-11, R_p is ~ 23 Ω and C_p is ~ 8 nF [Burt 2006], therefore τ_p equates to 0.18 µs (5.4 MHz). The parallel clocking power dissipation in the CCD can be expressed as [Jorden et al. 2003]:

$$P_{PCD} = \frac{3T_P}{T_T}\left(\frac{2\tau_P}{t_r} \times C_P V^2 f_{tr}\right), \tag{4.7}$$

where V is amplitude of the clock swing (12 V), t_r is the pixel transfer time (13 µs), T_p is the time taken to transfer all rows to the serial register (256 × t_r), f_{tr} is the pixel transfer frequency and T_T is the total time between readout cycles (1.61 s). Using equation 4.7, P_{PCD} was calculated to be ~ 0.01 mW.

- **Serial Clocking Power Dissipation**

The serial clocking power dissipation can also be calculated using equation 4.7 where τ_p is 0.92 seconds, t_r is 6 µs, f_{tr} is 165 kHz, C_p is 40 pF, T_p is 1.6 seconds and T_T is 2.6 seconds. The serial clock power dissipation P_{SCD}, was calculated to be ~ 0.37 mW.

The total clocking power dissipation P_{CD}, for the CCD-Array was, 4 × (P_{PCD} + P_{SCD}) which equates to 1.52 mW. Since $t_r >> \tau_p$, the power dissipated by clocking the CCD is negligible. The effect of power dissipation through clocking is insignificant unless the CCD is being readout at TV rates (MHz).

- **Output Amplifier Power Dissipation**

The power dissipated in the load resistor can be expressed as $V_{os} \times I$, where V_{os} is the potential difference across the 10 kΩ load resistor and I is the current flow from source to drain (~ 5 mA). This results in a total power dissipation in the load resistor of ~ 25 mW. However, the load resistors for the 4 CCD30-11s were located off-chip, therefore this was not considered as a heat load. The output node FET also draws current [McFee 2000] resulting in a power dissipation P_{FET}, expressed as, $(V_{od} - V_{os}) \times I$, which equates to ~ 75 mW. For all 4 CCD30-11 outputs, P_{FET} was ~ 300 mW. The total power dissipation by the 4 CCDs Q_{CCD}, was the combination of P_{CD} and P_{FET}, which was a total of 301.52 mW.

Figure 4.7 shows the steady state temperature of all PRTs at full TEC power with all passive (radiative - chamber walls, conductive – electrical wiring) and active (CCD) heat loads.

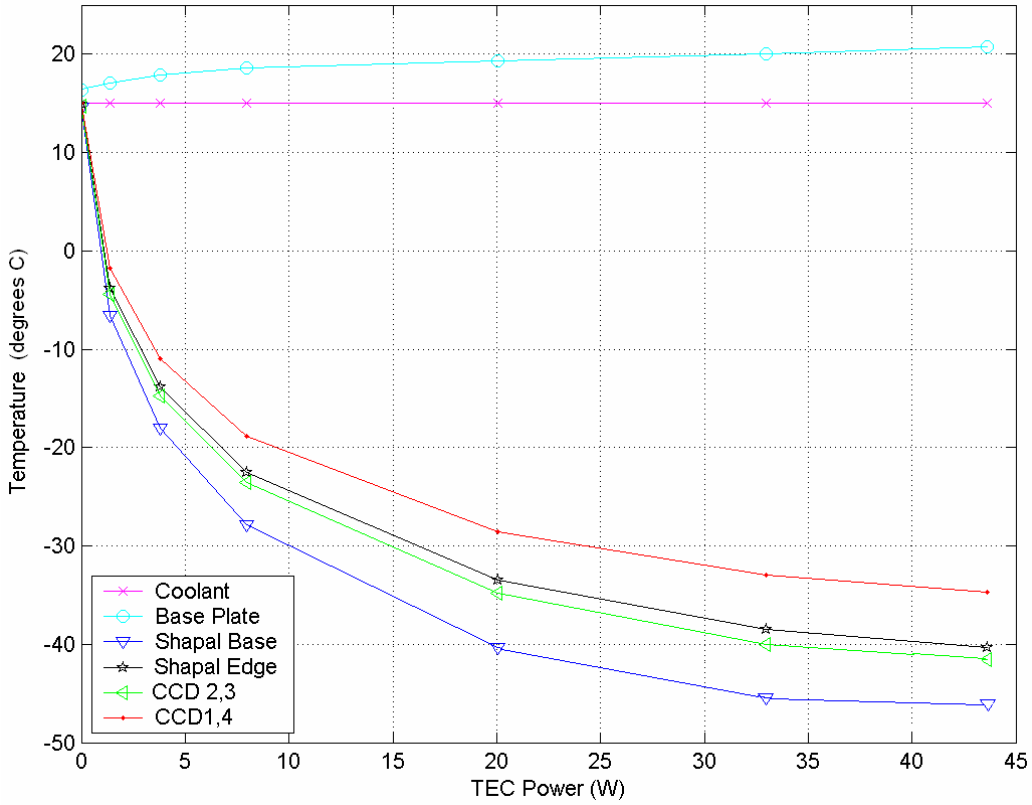

Figure 4.7: Temperature profile of CCDs and Shapal under normal operation

This represents the temperature profile of the CCD-Array under standard operating conditions. The total value of Q_c was a combination of Q_{Rad}, Q_{cnd} and Q_{CCD} which was

~ 4.8 W. This value was based on calculations using equations listed in Section 4.3.1. The final value of T_c under normal operation was ~ -47.5 °C. By using equation 4.5, the expected value of Q_c equates to 4.316 W, which is in very good agreement with the calculated value.

The difference in temperature between CCDs 1 & 4 and CCDs 2 & 3 was approximately 5 °C, however this amounts to a difference in dark current of less than 1 e^- p/p/s (see figure 6.19). Figure 4.21 summarises the performance of the TEC with the different heat loads discussed in Section 4.3. The normal operation of the CCD-Array is represented as $Q_{Rad} + Q_{cnd} + Q_{CCD}$ with T_c equal to -45 °C.

4.3.3 Heat Dissipation by Liquid Cooling

The heat generated by the CCD-Array and other features of the test facility was absorbed by a re-circulating coolant, known as Hexid. The total heat load from the backside of the TEC Q_h, can be expressed as:

$$Q_h = Q_c + V_{TEC} \times I_{TEC}\,, \tag{4.8}$$

where $V_{TEC} \times I_{TEC}$ is the operating power of the TEC. The total heat load Q_h, from the CCD-Array under normal operating conditions was ~ 55 W. The test facility consisted of 2 other heat loads, which originated from the Bede micro-source ($Q_{X\text{-}ray}$) and the coolant pipes (Q_P). The normal operating power of the Bede micro-source was 80 W, 99% of which was converted to heat. The coolant pipes were manufactured from Polyurethane, which is an exceptionally good insulator with a thermal conductivity of 0.02 W/m K [Young 1992]. Although the thermal conductivity of the polyutherane was very low, the coolant was required to flow through approximately 6.5 m to complete 1 cycle. Due to the large length of piping, the heat conducted from the ambient air (~ 22 °C) to the coolant (15 °C) was calculated over the 6.5 m coolant flow distance. Using equation 4.6, the total heat load from the pipes was calculated to be 7.5 W. The total heat from the entire facility Q_T, can be expressed as:

$$Q_T(W) = Q_h + Q_{X-ray} + Q_P\,. \tag{4.9}$$

This results in a total heat load of ~ 140 W that was absorbed by the coolant. The ability of the coolant to absorb Q_T depended on the flow rate F_C (cm^3/s), and the

specific heat capacity of the coolant, S_H (J/Kg K). The value of F_C was adjusted using a pressure gauge in the chiller, which was factory set to 650 mL/min or 10.8 cm^3/s. The heat required (ΔQ) to increase the temperature (ΔT) of a unit quantity of mass of a substance m_s, with a specific heat capacity $S_{H,}$ by 1 °C can be calculated using the expression:

$$\Delta Q = \frac{m_s \times S_H \times \Delta T}{t_{hx}} \, . \tag{4.10}$$

The Hexid solution used to absorb heat from the test facility had a specific heat capacity of 3780 J/Kg K and a density of 1.02 g/cm^3. The volume and mass of Hexid inside the total facility was calculated to be 50 cm^3 and 0.051 kg respectively. The time taken t_{hx}, for the Hexid solution to complete 1 cycle through the facility at a flow rate of 10.8 cm^3/s was 4.6 seconds. The increase in temperature of the Hexid solution after 1 complete cycle was calculated to be 3.36 °C using equation 4.10, where ΔQ is 140 W (the total heat load in the test facility).

The maximum heat that can be absorbed by the coolant Q_{Hex} *(W)*, for a given coolant temperature T_{Hex} (°C), can be approximated using the expression:

$$Q_{Hex}(W) = 7T_{Hex} + 300 \, . \tag{4.11}$$

The expression is a valid approximation between the ranges -25 °C > T_{Hex} < +25 °C. By using equation 4.11, it can be calculated that at a coolant temperature of 15 °C, the maximum heat load that can be absorbed is ~ 400 W. T_{Hex} was set to the dew point of water (typically 15 °C in the laboratory) to prevent water condensing on the coolant pipes, as electrical wiring was widespread across the test facility.

By re-arranging equation 4.10, the maximum increase in temperature (ΔT) of the Hexid was calculated to be ~ 10 °C, where ΔQ represents the maximum allowable heat load (400 W) at 15 °C. Since the increase of temperature of the Hexid was only 3.36 °C (F_C = 10.8 cm^3/s), F_C was reduced allowing a larger increase in the temperature of the Hexid. Figure 4.8 shows the minimum flow rate required to ensure ΔT < 10 °C.

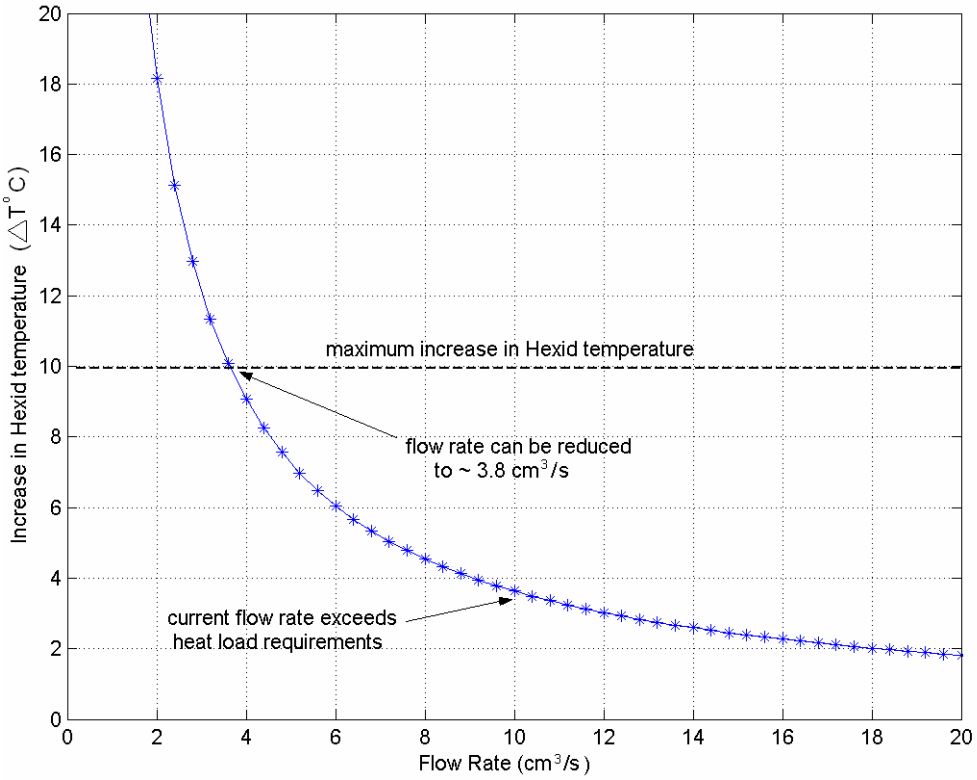

Figure 4.8: Minimum coolant flow rate required to dissipate 140 W

4.4 CCD-Array Portability

In order to determine the suitability of the CCD-Array as a portable instrument, an air leak test was performed to monitor the increase in pressure inside the CCD-Array, when unassisted by a vacuum pump. In order to isolate the CCD-Array from the vacuum pump, a valve was placed between the two, along with a gauge to monitor the increase in pressure inside the CCD-Array. Figure 4.9 shows the phase diagram of water with respect to temperature (°C) and pressure (mbars). The diagram also indicates the increase in pressure inside the CCD-array at given time after switching off the vacuum pump.

The results show that when operating at the coldest possible CCD temperature (-40 °C for CCD 2 and CCD 3 at full TEC power), the CCD-Array can only operate for 20 minutes, however, it is shown in Section 6.4, that the performance of the CCD30-11 is very similar at -10 °C when operating under AIMO. Therefore, the CCD-Array can be used remotely at -10 °C for 180 hours (> 7 days). Combined XRD/XRF data for typical samples is usually collected over a period of 3 hours. Assuming the CCDs are operated at -10 °C, the CCD-Array can analyse over 50 samples, before the danger of water vapour freezing on the CCDs and causing electrical damage.

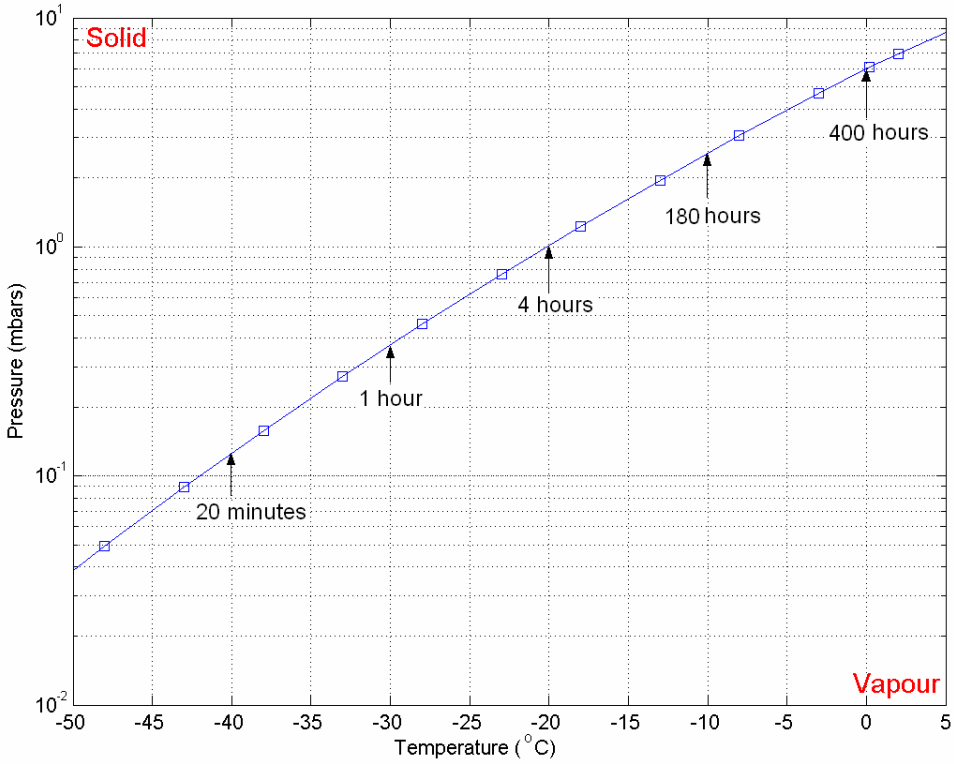

Figure 4.9: Phase diagram of water with respect to temperature and pressure. The times represent the maximum period over which the CCD-Array can be cooled at a given temperature

4.5 CCD-Array Angular Geometry

The performance of the CCD-Array as an XRD detector was dependant on 2 criteria. The CCD-Array was required to determine the exact position of diffracted X-rays and recognise these events as XRD data. The accuracy of determining peak positions was related to both the angular coverage and angular resolution. This section explains the designed geometry of the CCD-Array, outlining the calculations performed in the 2θ angular calibration of each of the CCDs.

4.5.1 CCD Angular Range

As previously mentioned, the CCDs were designed to lie along the curvature of a 120 mm circle, where the centre point was the point of sample irradiation. Since the CCDs were rectangular, the centre of each of the CCDs represented the point of tangency. Figure 4.10 shows the geometry of CCD 1 and CCD 2 in relation to the sample holder. The angle of each of the CCDs in relation to the sample was determined by the design of the Shapal ceramic. Since the distance between the CCDs and the sample holder was identical, all 4 CCDs covered the same angular range. This

can be understood by visualising CCD 1 in figure 4.10 being rotated around the 120 mm radius circle. The angular positioning of the CCD changes but the angular coverage (2θ) remains the same.

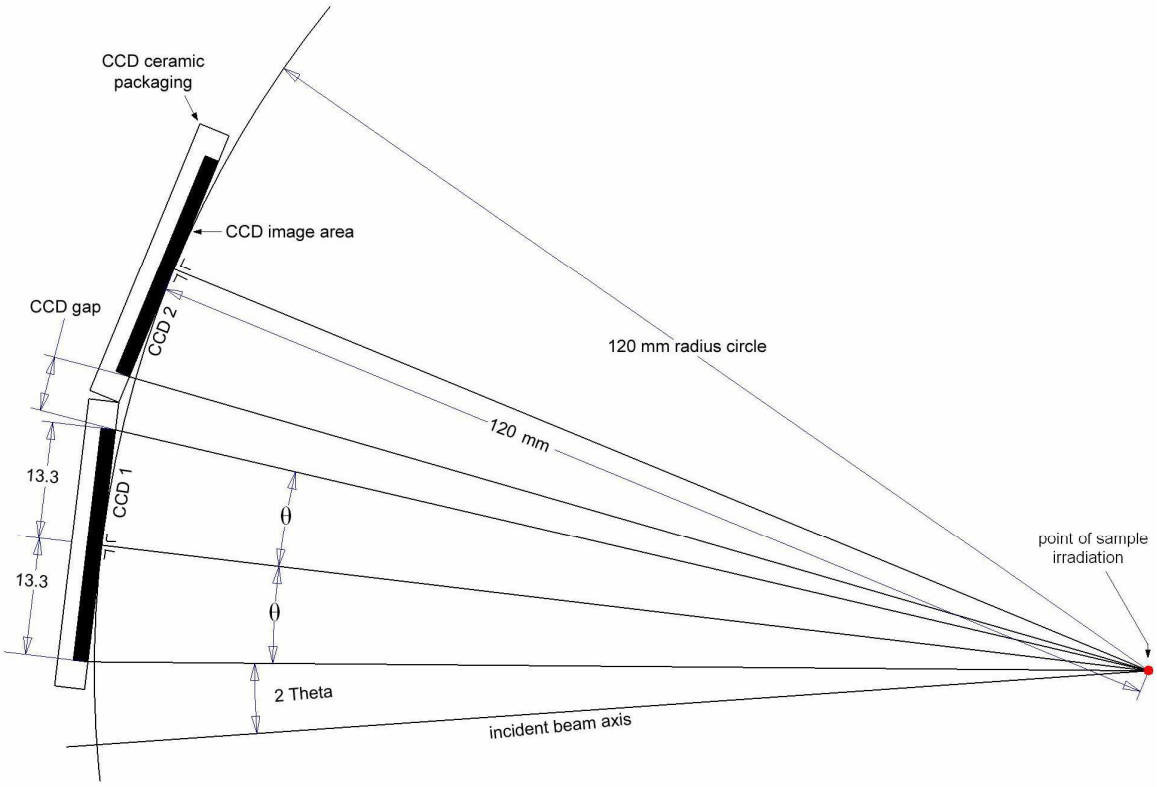

Figure 4.10: Geometry of CCD 1 and CCD 2 in relation to the sample holder (all dimensions in mm)

The length of the CCD30-11 was 32.89 mm with an imaging area of 26.6 mm. Figure 4.10 shows the centre of the imaging area forming a right angle with the sample holder at a distance of 120 mm. The angular coverage of θ can be expressed as:

$$\theta = \tan^{-1}\left(\frac{13.3}{120}mm\right). \tag{4.12}$$

The total angular coverage (2θ) of each of the 4 CCDs was therefore 12.65°. Since the CCD imaging area did not lie perfectly on the 120 mm circle due to their rectangular shape, this caused a variation in resolution across the CCD, which is shown in figure 4.11. The spatial resolution improved away from the centre of the CCDs, as pixels

toward the edges were further away from the sample (> 120 mm). However, this variation in spatial resolution was calculated to be 0.00015° and was not expected to cause any errors in qualitative analysis.

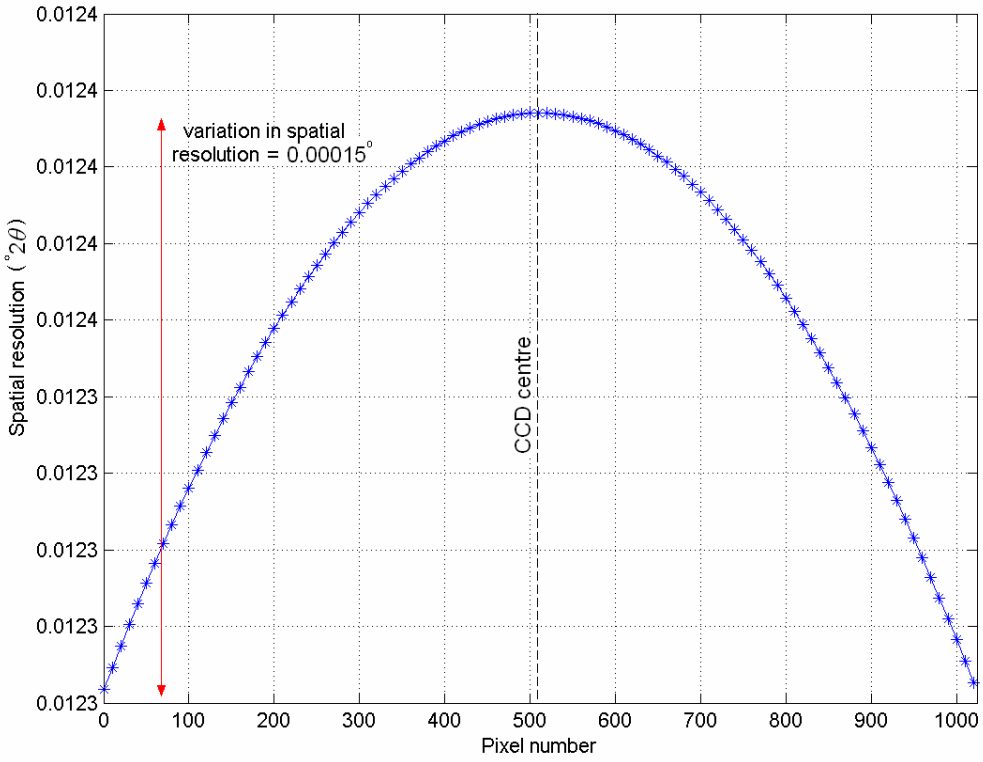

Figure 4.11: Variation in spatial resolution across each CCD 30-11

With the angular coverage of the CCDs calculated, the next stage was to determine the angular position of each of the CCDs, along with the position of the CCD gaps. These gaps represented the distance between the active CCD imaging areas.

4.5.2 Angular Position

For the CCDs to satisfy the 120 mm geometry with the sample holder, the CCD-Array was tilted at the correct angle (*B*) and lifted to the correct height (*C*), as shown in figure 4.12. The height of the base determined the lower and upper angular coverage limits of the CCD-Array. The angle of the inclination block was determined as follows. The angle required by CCD 1 to cover an angular range beginning at ~ 4.5° 2θ was 83.20°. The angle between CCD 1 and bottom of the CCD-Array was 66.30°. The angle of the inclination block, B, was therefore 30.50° (180° - (83.2° + 66.30°)). The height of the CCD-Array holder (C) was constrained by the height of the sample holder (184.5 mm) and was determined to be 65.57 mm. The distance between the

CCD-Array and sample holder was adjustable through the pivot screws indicated in figure 4.12.

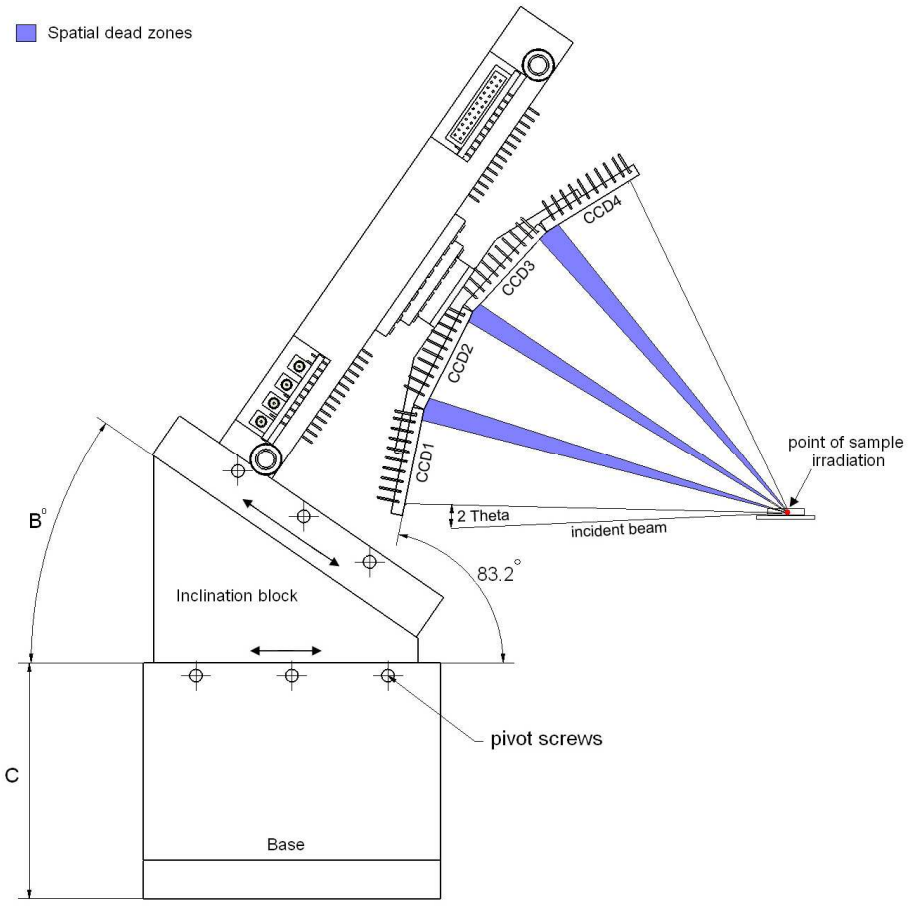

Figure 4.12: Geometry of entire CCD-Array assembly in relation to sample holder

Based on the geometrical calculations, the CCD-Array coverage ranged from 4.48° − 63.95° with 3 gaps in angular coverage. The angular coverage of each gap was 2.96°. The exact angular position of each CCD and CCD gap is listed in table 4.5.

	CCD1	Gap1	CCD2	Gap2	CCD3	Gap3	CCD4
Bottom Position (°2 θ)	4.48	17.14	20.09	32.74	35.69	48.35	51.30
Top Position (°2 θ)	17.13	20.08	32.73	35.68	48.34	51.29	63.95

Table 4.5: Angular coverage of CCD-Array active area and gaps

The presence of 3 gaps in angular coverage can cause peak loss in XRD experiments. The detector designed for this thesis was built as a prototype instrument. In Section 7.2, improvements to the CCD-Array design are presented, which includes a very large reduction in angular 'dead zones'. The main improvement is that the CCD

ceramic packaging in the 2nd generation instrument will be laser cut to allow the imaging areas on each of the CCDs to almost touch one another. This will reduce the angular coverage of the gaps from 2.96° to ~ 0.2°. Since the standard width (± 3 standard deviations) of diffraction peaks under normal operating conditions is greater than 0.2°, the complete loss of diffraction peaks due to gaps in angular coverage will be eliminated. For this reason, if an XRD peak was located in one of the gaps, the CCD-Array was simply moved along the curvature of the 120 mm measuring circle to bring the XRD peak into coverage. The effect of gaps in angular coverage is not discussed in this thesis, as this was an only an issue with the prototype instrument.

4.5.3 Spatial Resolution

The CCD30-11 consisted of 1040 (columns) × 256 (rows) pixels. The 256 pixels (6.7 mm) determined the fraction of the diffraction ring collected by the CCDs. The spatial resolution of the detector was defined by the number of pixels intercepting the 12.65° angular coverage. This was represented by the 1040 pixels in the vertical direction that included 16 over-scan pixels. The spatial resolution was therefore approximately 0.012° (12.65°/1024).

With the benefit of CCD binning, faster readout times could be achieved at the expense of spatial resolution. Table 4.6 lists the readout times and spatial resolution of different CCD binning modes. The total readout times include a 1 s CCD exposure time at a readout speed of 165 kHz per pixel.

Binning Mode	Pixels (v)	Pixels (h)	Spatial Resolution (°)	Readout Time (s)
1 × 1	1024	256	0.012	2.6
2 × 2	512	128	0.024	1.4
4 × 4	256	64	0.049	1.2
8 × 8	128	32	0.099	1.1

Table 4.6: Readout time and spatial resolution of different CCD binning modes

For XRD experiments with less resolution requirements, CCD binning has various advantages. Data collection times are greatly reduced when collecting a large number of exposures. For example, collecting 2000 exposures of 1 s each can be achieved in 1 hour and 26 minutes in full resolution mode. With 2 × 2 binning the total data collection time is reduced to approximately 46 minutes.

4.6 Confirmation of CCD-Array Spatial Geometry Using NIST SRMs

This section investigates the accuracy of the designed geometry using NIST SRMs. Using SRMs, any inaccuracies in the designed geometry, which may have occurred during assembly of the CCD-Array could be identified. The intensities of peaks across all 4 CCDs were also investigated in order to determine any varying QE problems. A variation in QE across a CCD would cause errors in calculating the relative intensities of diffraction rings.

4.6.1 Spatial Calibration – SRM 660a/SRM 675

In order to perform accurate XRD analysis and exploit the high spatial resolution of the CCD-Array, it was essential to confirm the accuracy of the designed 2θ geometry. For the spatial calibration of the detector, SRM 660a (lanthanum hexaboride powder) was used. This powder consisted of peaks starting from 21°, which allowed the calibration of CCDs 2 − 4. CCD 1, which covers an angular range from 4.48° to 17.13°, was calibrated using a separate low angle SRM 675, known as fluorophlogopite mica powder. Figure 4.13 shows the XRD patterns collected from both powders. The CCD was exposed for 1 s and 1500 exposures were collected.

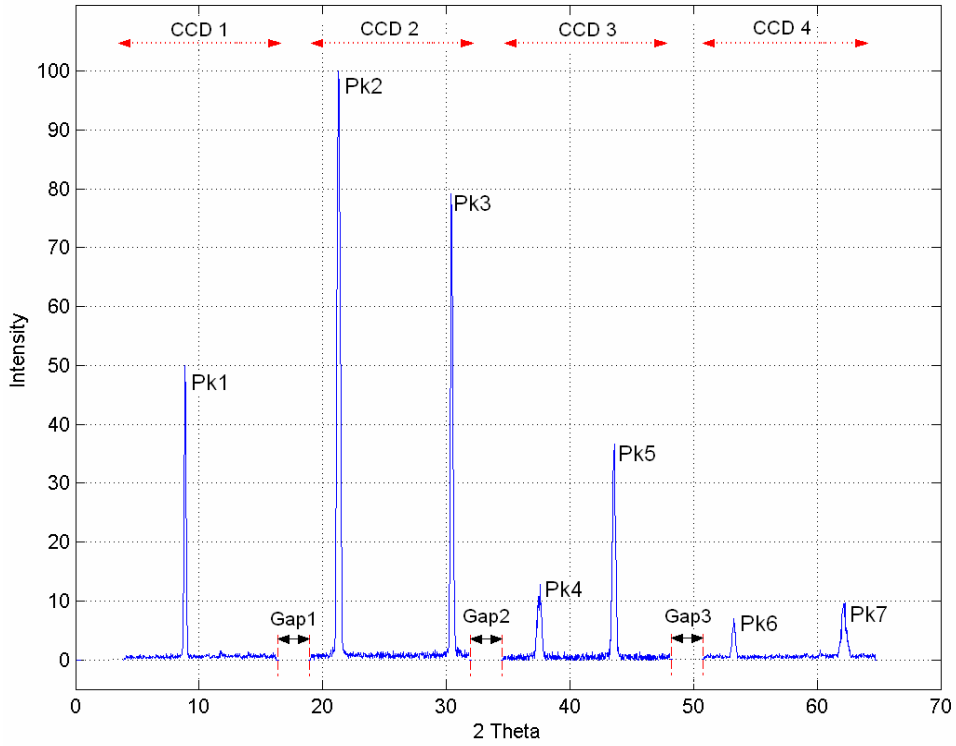

Figure 4.13: Spatial calibration of CCD-Array using SRM 660a and SRM 675

The initial XRD pattern, without altering the geometry contained errors of ~ 0.07° and was approximately 5 − 6 pixels misaligned. Using the pivot screws, the geometry was aligned as best as possible with SRM 660a and SRM 675. The errors on all 7 peaks were then calculated and are shown in table 4.7. The peak positions were calculated by fitting the experimental peaks with Gaussians models, and refining the position of the mean to find the best least squared fit.

Peak	CCD	SRM	2θ NIST (°)	2θ CCD-Array (°)	Error (°)
Pk1	1	675	8.8530	8.8612	-0.008
Pk2	2	660a	21.3578	21.3614	-0.004
Pk3	2	660a	30.3847	30.3968	-0.012
Pk4	3	660a	37.4417	37.4382	0.003
Pk5	3	660a	43.5064	43.4954	0.011
Pk6	4	660a	53.9886	53.9786	0.010
Pk7	4	660a	63.2183	63.2291	-0.011

Table 4.7: Summary of CCD-Array spatial calibration errors using NIST SRMs

The largest recorded error was 0.012°, located on CCD 2. This represents a misalignment of approximately 1 pixel. These minor inaccuracies can be attributed to gluing and manufacturing imperfections. The magnitude of these errors was not expected to influence qualitative XRD analysis, therefore no offsets were implemented during the post-processing stage.

4.6.2 Intensity Calibration - SRM 674b

For quantitative analysis, the intensity of XRD peaks is the crucial parameter. It was therefore essential to ensure that the QE response of each of the CCDs was identical (identical QEs were expected since all CCDs were CCD30-11s with an identical resistivity, biased to the same potential). This was investigated by collecting diffraction data from NIST SRM 674b.

Various factors can affect the intensity of an observed diffraction ring, the most important of which is sample quality. The sample quality can severely affect the measured line intensity through processes such as preferred orientation and absorption. The key feature of the SRM 674b set is that it eliminates these effects, which ensures any intensity discrepancies can be attributed to instrumental errors.

This will highlight any intensity errors across the CCD-Array and isolate problematic CCDs. The 4 powders contained within the SRM 674b set are zinc oxide (ZnO), titanium dioxide (TiO_2), chromium (III) oxide (Cr_2O_3) and ceric oxide (CeO_2). XRD patterns from all 4 samples were collected using the CCD-Array and scaled to 100 according to the intensity of the largest peak.

Since some peaks were located in between CCD gaps and no peaks were present on CCD 1, for certain samples the CCD-Array was moved along the curvature of the 120 mm measuring circle to detect specific peaks. This was achieved by increasing the height and angle of the CCD-Array base and inclination block respectively, with the use of angled blocks. The intensity errors were calculated by fitting the observed peaks with Gaussian models and comparing the peak height intensity with the expected peak heights. A minimum of 10,000 counts was detected in each peak resulting in counting errors of 2%, at a 95% confidence level. The average error (%) was calculated for each CCD using all 4 SRMs and is listed in table 4.8.

SRM	CCD1 error (± %)	CCD2 error (± %)	CCD3 error (± %)	CCD4 error (± %)
ZnO	8.43	4.20	9.92	16.12
TiO2	6.75	1.30	8.00	13.39
Cr2O3	6.84	0.45	6.77	15.60
CeO2	6.23	2.83	8.62	16.86
Average Error	7.06	2.20	8.33	15.49

Table 4.8: Summary of intensity calibration errors using NIST SRM 674b

CCD 4 displayed the largest errors with an average intensity error of ± 15.49%. These errors were then taken into account during post-processing of the XRD data and XRD patterns from the 4 SRMs were collected again. Figure 4.14 shows the reduction in intensity errors after the calibration from $45 - 63.95°$ 2θ.

As can be seen from figure 4.14, a much better agreement was reached between the observed and expected intensities after the introduction of the error offsets. Average errors on CCD 4 were reduced from 15.49% to 2.47%. The 3 other CCDs showed similar improvements and maximum intensity errors due to instrumental effects were determined to be 3.2%.

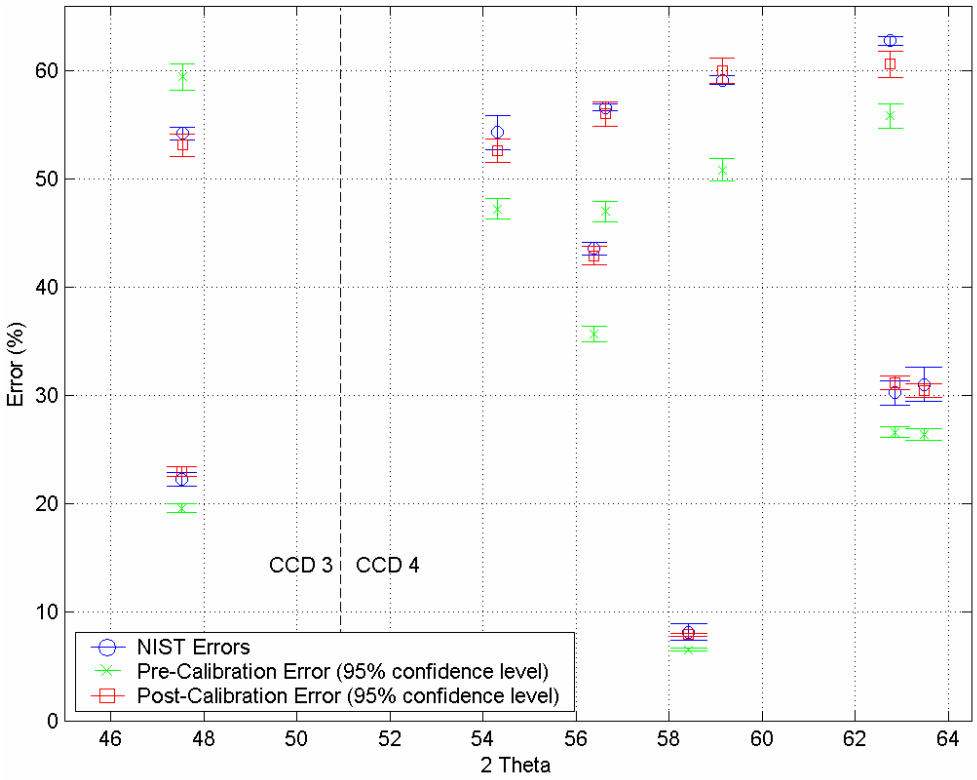

Figure 4.14: XRD intensity errors before and after calibration from 45 − 63.95° 2θ

4.7 The Test Facility

A purpose built test facility was created for testing the CCD-Array. Figure 4.15 shows an image of the test facility with all major components labelled 1 − 8.

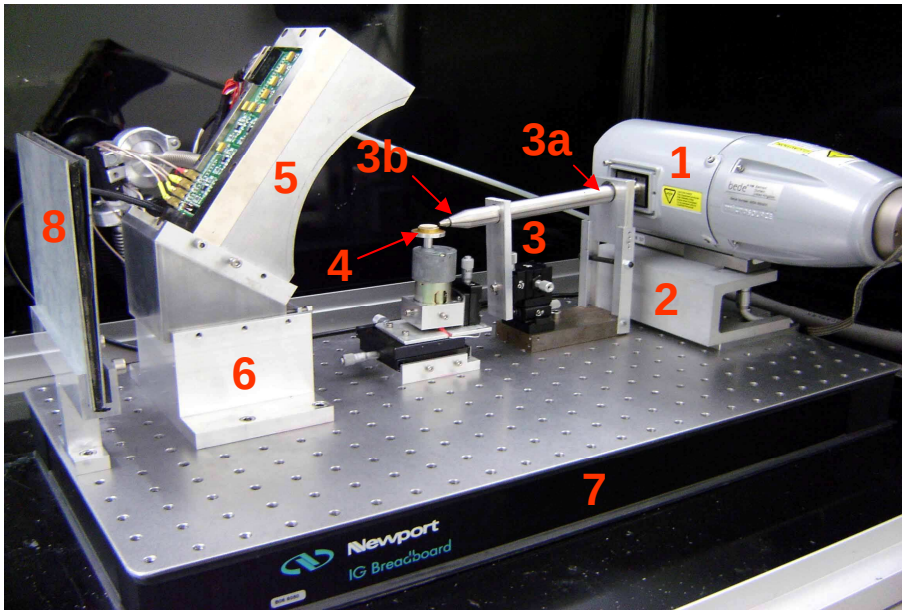

Figure 4.15: Image of the test facility including CCD-Array

The equipment shown in figure 4.15 was enclosed inside a radiation safety enclosure that is not shown, but is represented as feature 9. The test facility was designed to operate in the following manner. The Bede micro-source (1) produced a very small (~ 1 mm) beam of focussed X-rays that contained both continuous and characteristic Cu X-rays. A stainless steel X-ray collimator performed X-ray monochromation (3a) through a 15 µm Ni filter and collimated (3b) the direct X-ray beam to less than 150 µm. Samples were ground into very fine powders (less than 10 µm) and spread across the entire sample holder surface (4). A beam of collimated low divergent X-rays irradiated the sample at an incident angle of 4°. Diffracted and fluoresced X-rays were collected by the CCD-Array (5) which was operated in single photon counting mode. The CCD-Array holder (6) was designed to allow the CCD-Array to form a precise geometry with the sample holder. An X-ray beam stop (8) prevented the direct X-ray beam from escaping through the X-ray enclosure. The X-ray safety enclosure (9) contained sliding doors with magnetic interlocks, which prevented the X-ray shutter from opening whilst the doors were open. Sliding doors allowed easy access to the equipment for changing samples and positing the CCD-Array. When a single sheet of Mylar was used as an X-ray window, the equipment was covered using a lightproof box made from Al. An explanation of the individual components of the test facility is now described.

- **Bede Micro-source (1)**

The Bede micro-source consists of a conventional X-ray tube coupled with a polycapillary focusing optic. Electrons were generated within the X-ray head though thermionic emission and an electron gun accelerated the electrons towards a Cu anode. An electronically controlled shutter prohibited the emission of X-rays through the optic. The shutter consisted of a 3 mm piece of tungsten, which was powered using a 12 V solenoid and controlled using software or the X-ray controller head. When the shutter was opened, a rectangular 5 mm hole moved into position in front of the Cu anode and allowed the generated X-rays to be collected and emitted by the optic.

- **Bede Micro-source Holder (2)**

The holder for the Bede micro-source was manufactured from 10 mm thick aluminium to support the weight of the X-ray head (~ 8 kg). The micro-source was

bolted to the holder using two 6 mm bolts. The holder was designed with a 4° angle of incidence (86° from the optics table) that enabled a reflective geometry for XRD experiments.

- **Stainless Steel Collimator (3)**

In order to optimise the angular resolution of the XRD experiments, a very small focussed beam of X-rays was used to irradiate the sample. The direct output from the Bede micro-source was a 1 mm circular beam of continuous X-rays with 2 strong Cu Kα and Cu Kβ characteristic X-rays. The aim of the monochromation process was to isolate the strongest characteristic emission in the spectrum (Cu Kα X-rays). The collimation stage reduced the 1 mm beam of the Bede micro-source to a small spot (less than 150 µm in diameter).

- **Collimation (3a)**

A 25 mm square sheet of 0.1 mm thick tungsten was used for the collimation process. Circular discs with a 2 mm diameter were laser cut from the W sheet by Micrometrics ltd. Pinholes were cut centrally into the discs with various diameters (50, 80, 100, and 150 µm). Figure 4.16 (a) shows a scanning electron microscope (SEM) image of an 80 µm pinhole in the tungsten disc.

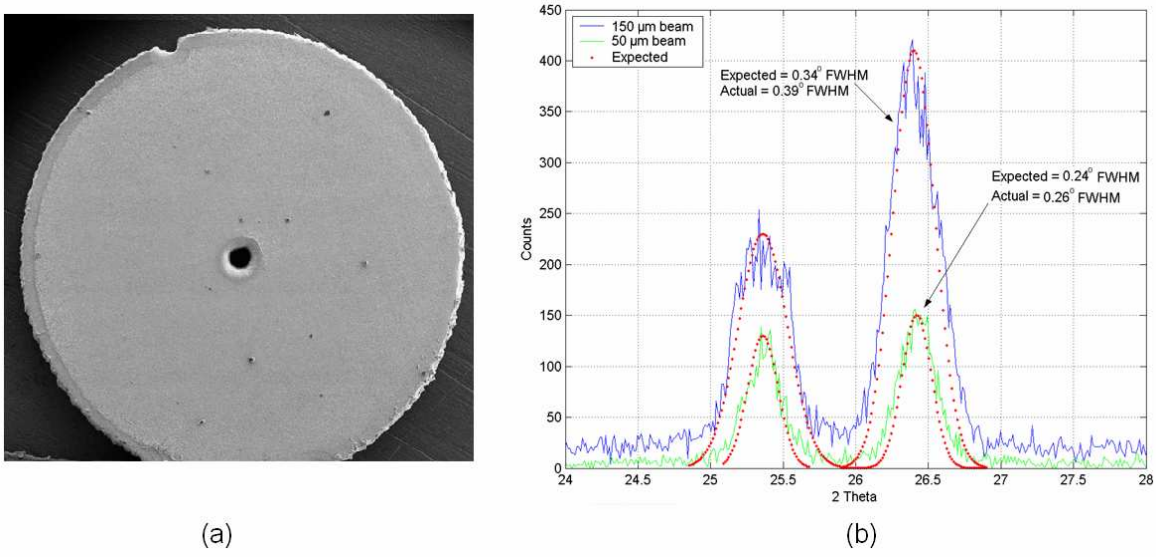

Figure 4.16 (a): SEM image of 2 mm wide tungsten disc with an 80 µm pinhole and the (b) comparison of a 50 µm and 150 µm incident beam on the FWHM and intensity of 2 $CaCO_3$ XRD peaks

Larger pinholes transmit a higher flux of X-rays onto the sample but cause a decrease in the angular resolution of diffraction peaks. For XRD applications with high resolution requirements, smaller pinholes were used (e.g. 50, 80 µm) at the expense of X-ray flux. Consequently, such experiments require longer total exposure times to achieve similar SNR as larger pinholes. Figure 4.16 (b) shows a comparison of a 50 µm and 150 µm incident beam on the intensity and resolution of 2 XRD peaks. The expected resolutions of the peaks are also shown, which were calculated using equation 2.14.

Notches were laser cut into the outer circumference of the discs to identify the different sizes. The tungsten sheets were placed at the front of the collimator using specially designed copper holders. A 0.5 mm hole was drilled through the copper holder to allow transmission of the main beam. Two copper holders were inserted into the collimator in the locations labelled 3a and 3b in figure 4.15. Figure 4.17 shows the dimensions of the copper holder.

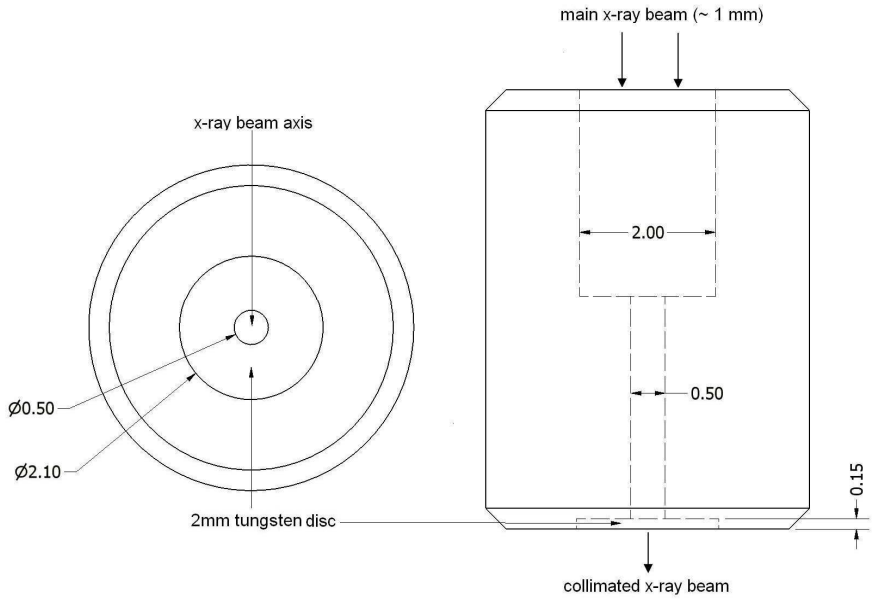

Figure 4.17: Schematic of Cu holders inserted into collimator to provide monochromation and collimation (all dimensions in mm)

Figure 4.17 shows the 150 µm deep recessed circular hole (2 mm wide) which was designed to allow gluing of tungsten/Ni discs. The copper holders used for collimation were placed at the front of the collimator to minimise divergence of the main beam prior to sample irradiation.

- **Monochromation (3b)**

Circular discs were also cut out of a 15 µm thick Ni sheet and glued into the recessed holes in the copper holder. The Bede micro-source produced characteristic Cu Kα (8047 eV) and Cu Kβ (8904 eV) X-rays. The Ni filter was used to reduce the Cu Kβ to Cu Kα ratio. Figure 4.18 shows the transmission of X-rays from 6 – 10 keV through the 15 µm Ni filter. The location of the K absorption edge of Ni is located between the Cu Kα and Cu Kβ energies at 8107 eV, causing a large drop in transmission of X-rays greater than 8107 eV. Using equation 3.21, the transmission of the 2 characteristic X-rays through the filter was calculated as:

$$\frac{I_x}{I_o}(CuK\alpha) = e^{-(49.2)\times(8.92)\times(0.0015)} = 0.52 \tag{4.13}$$

$$\frac{I_x}{I_o}(CuK\beta) = e^{-(286)\times(8.92)\times(0.0015)} = 0.02 \tag{4.14}$$

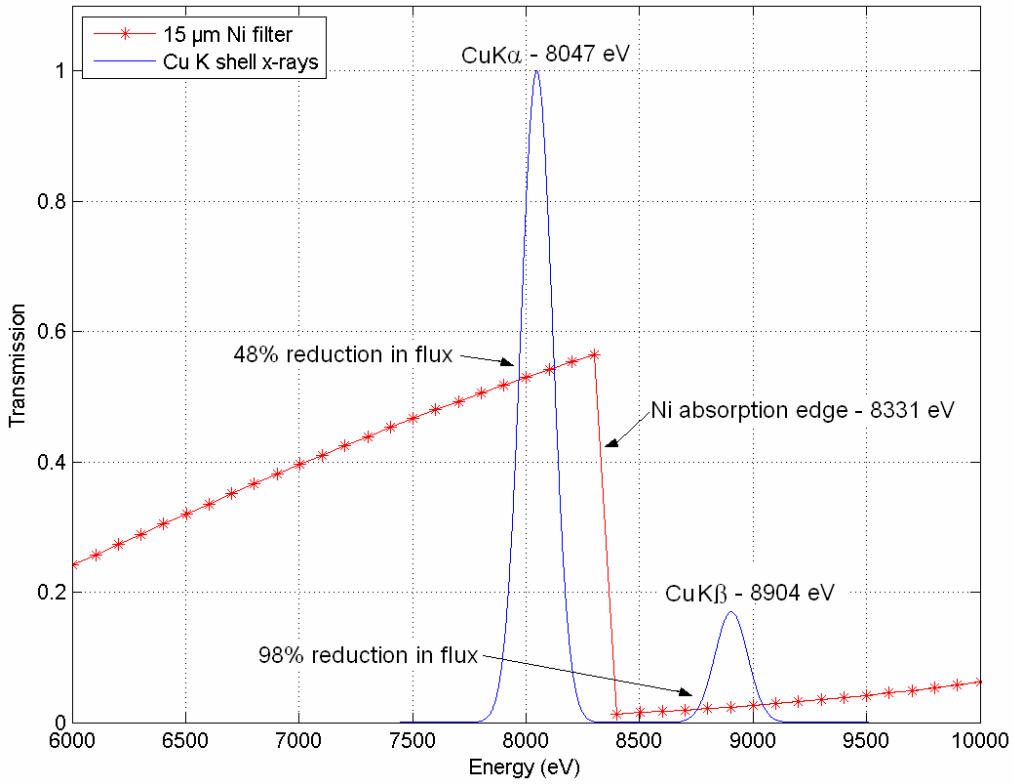

Figure 4.18: Transmission of X-rays from 6 – 10 keV through a 15 µm Ni filter

Since the CCD30-11 can perform single photon counting (easily distinguishing Cu Kα and Cu Kβ X-ray peaks), XRD analysis can also be performed without the use of a Ni filter. By focusing the raw spectrum produced by the optic onto the sample, both Cu Kα and Cu Kβ X-rays will be diffracted. The 2θ position of the diffracted Cu Kα and Cu Kβ X-rays will differ however, based on equation 1.1. For samples with many peaks, overlapping of Cu Kα and Cu Kβ XRD peaks is inevitable. If the diffraction efficiency of the sample is low, the probability of the 2 characteristic X-rays interacting is also low (probability will increase with binning). The advantage of this technique is that the incident flux of Cu Kα X-rays is not reduced by almost 50%, therefore approximately double the amount of diffracted photons are generated from the sample. However, samples with a high diffraction efficiency and a large number of peaks, will cause some interference between the characteristic Kα and Kβ peaks (e.g. a pixel containing a Cu Kα photon may also detect a Cu Kβ photon, or a Cu Kβ photon may be detected in a neighbouring pixel thereby preventing detection of the Cu Kα X-ray as an isolated XRD event). Generally, when using a laboratory X-ray source with high flux (as used in this project), monochromation is used to practically eliminate diffracted Kβ X-rays. Where less X-ray flux is available (such as a radioactive X-ray source), it is more beneficial to operate the CCD is photon counting mode to discriminate the intended Kα X-rays and reject Kβ X-rays.

- **Powder Sample Holder (4)**

The powder samples were placed on top of a 13.6 mm diameter zero background mount (ZBM), which was glued to a sample holder. The ZBM eliminated background scattering from the sample holder when analysing samples with a small linear attenuation coefficient (e.g. organics). Samples were grinded using a mortar and pestle to $1 - 10\ \mu m$ grains. The sample holder was designed on top of a d.c. motor (20 r.p.m.) which allowed sample rotation during data collection to reduce preferred orientation. The sample holder was fixed to the breadboard through an XYZ translator, which allowed easy calibration of the sample with the incident beam. The geometry of the sample irradiation process has been discussed in section 2.1.

- **Optics Table (7)**

The optics table contained a pitch of 25 mm to allow components of the test facility to be easily translated.

- **Lead Beam Stop (8)**

The lead beam stop consisted of 2.5 mm of lead (Pb) enclosed between two 2 mm thick steel plates. The beam stop attenuated the main beam to acceptable background levels.

- **Radiation Safety Enclosure (9)**

The equipment shown in figure 4.15 was contained inside a radiation safety enclosure with magnetic interlocking doors. The interlocking doors prevented the possibility of X-ray emission whilst doors were open. Sliding transparent doors allowed easy and safe access to the test facility for changing samples and pinholes. The doors were equivalent to 2.3 mm of Pb, ensuring any scattered X-rays from the source would be contained within the enclosure.

4.8 Experimental Arrangement

Figure 4.19 shows the experimental arrangement of the test facility.

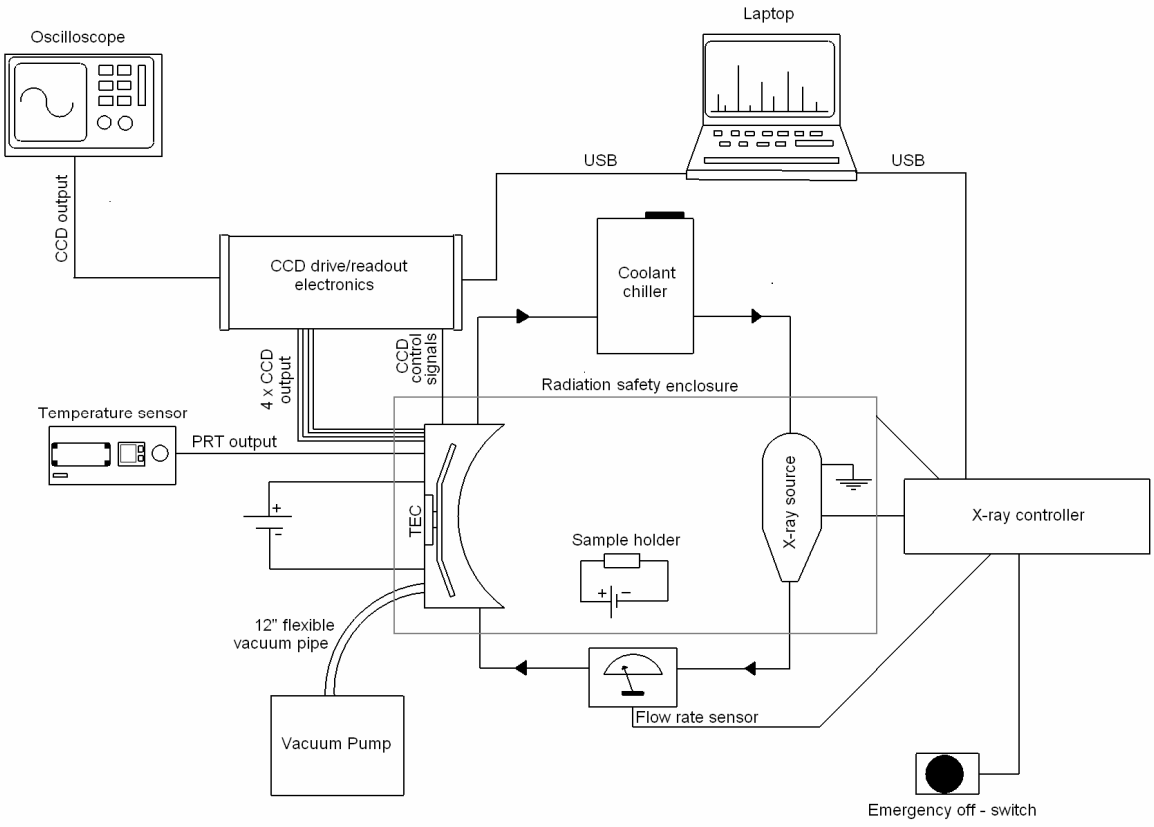

Figure 4.19: Experimental arrangement of test facility

The CCDs were controlled using 3rd party CCD drive and readout electronics (XCAM ltd.). An oscilloscope was used to confirm valid CCD biasing, clock waveforms and CCD outputs. Each of the 4 CCD outputs were readout individually and the resulting images were displayed on a laptop via a high-speed USB interface. Outputs from the PRTs were connected to a temperature sensor. The TEC and motorised sample holder were powered using a D.C. power supply. A 12-inch vacuum pipe connected the CCD-Array to a vacuum pump, which maintained a pressure of ~ 10^{-3} mbar inside the CCD-Array during cooling. A water chiller provided cooling to both the CCD-Array and the X-ray source at a flow rate of approximately 650 mL/min. A flow rate meter ensured a minimum flow rate of 300 mL/min passed through the X-ray head. If the flow rate dropped below this threshold, a signal was sent to the X-ray controller to suppress the generation of X-rays. The emission of X-rays was also controlled by the magnetic door interlocks of the radiation safety enclosure. An emergency footswitch allowed users to immediately place the X-ray system in standby in case of emergency. The operation of the X-ray source was controlled using software.

4.9 Experimental Alignment

The alignment of the system was performed in several individual stages. The sequence of alignment steps are summarised below:

micro-source → X-ray optic → collimator → pinhole → sample → detector

The first 3 stages in the alignment procedure involved imaging the X-ray beam from the micro-source using a dental CCD (e2v's CCD38-10). The CCD was fixed to the optics breadboard and centrally aligned with the micro-source optic. The first step was the alignment between the X-ray shutter within the micro-source and the X-ray optic. This involved adjusting the XYZ position of the optic in relation to the X-ray shutter. The position of the optic was varied until the maximum intensity was seen in the beam. The next stage was to align the collimator with the X-ray optic. Any pinholes were removed from the collimator during this process. The collimator was centrally aligned with the optic and tilted 4° (initially by eye) to allow the focused ~ 1 mm beam to travel through the collimator. This resulting beam was imaged by the dental CCD. The angle and position of the collimator was adjusted using XYZ translation stages (1 µm sensitivity) until the X-ray beam was centralised in the ~ 5 mm

collimator outlet. Next, the dental CCD image was analysed and the pixel location of peak intensity was noted. This was always approximately in the centre of the X-ray beam as the energy distribution resembled a 3-dimensional Gaussian shape. With the pixel location of peak intensity noted, the required pinhole was placed into the collimator using the copper holder. The position of the collimator was adjusted until the noted pixel location (of maximum intensity) was centralised in the pinhole. This ensured the beam produced from the collimation process contained the maximum possible flux. The penultimate stage in the alignment process involved aligning the pinhole with the powder sample. This was achieved with the use of very bright light emitting diode (LED). The LED was placed between the X-ray optic and collimator which allowed the intense beam of light to pass the through the pinhole and illuminate the powder grains. The sample holder was adjusted using XYZ translation stages until the incident beam was centralised in sample holder. The final stage of alignment was between the axis of the X-ray beam and the centre of the CCDs. This alignment procedure was completed during post processing of the CCD images through the use software. Once the alignment procedure was completed, samples were simply interchanged and the facility remained entirely aligned and calibrated.

4.10 Discussion

This chapter has described the design and characterisation of the CCD-Array. The CCD-Array was designed to collect combined XRD/XRF data from powdered rocks samples. A large 12 cm distance between the sample and detector allowed very high spatial resolution of 0.012° and the use of 4 CCDs provided large angular coverage from 4.48° − 63.95° 2θ. The detector was designed for portability with the use of a single TEC for CCD cooling and on-board CCD headboard electronics. Calculations have been outlined which determined that only 2.5 µm of Mylar was required to sustain the stress (~ 10^5 Pa) induced from creating a pressure of ~ 10^{-3} mbars inside the CCD-Array. The actual thickness used (20 µm), exceeds this requirement by a factor of 8 due to the high risk of CCD damage post window failure.

Thermal studies were performed on the CCD-Array outlining the ability of the TEC to cool the CCDs with heat loads of ~ 4.5 W. Calculations, measurements and thermal simulations revealed that operating the CCDs within a vacuum as opposed to N_2, resulted in a reduced heat load on the cold side of the TEC. Additional heat loads in

the form of conduction from electrical wiring and heat dissipation from the CCDs, further reduced the TECs cooling performance. The largest heat load in the CCD-Array was generated from the 0.52 mm thick electrical wiring. This was one of the major design flaws with the CCD-Array, as such thick wiring was not required for electrical purposes. The maximum current drawn by the CCD30-11 during operation was by V_{od}, in the range of 5 − 10 mA. A current of 5 − 10 mA can be achieved with 0.05 mm wiring. Approximately 29 wires allowed the transfer of heat from the copper base to the CCDs during operation. Figure 4.20 shows the reduction in heat transfer achieved with smaller diameter wiring.

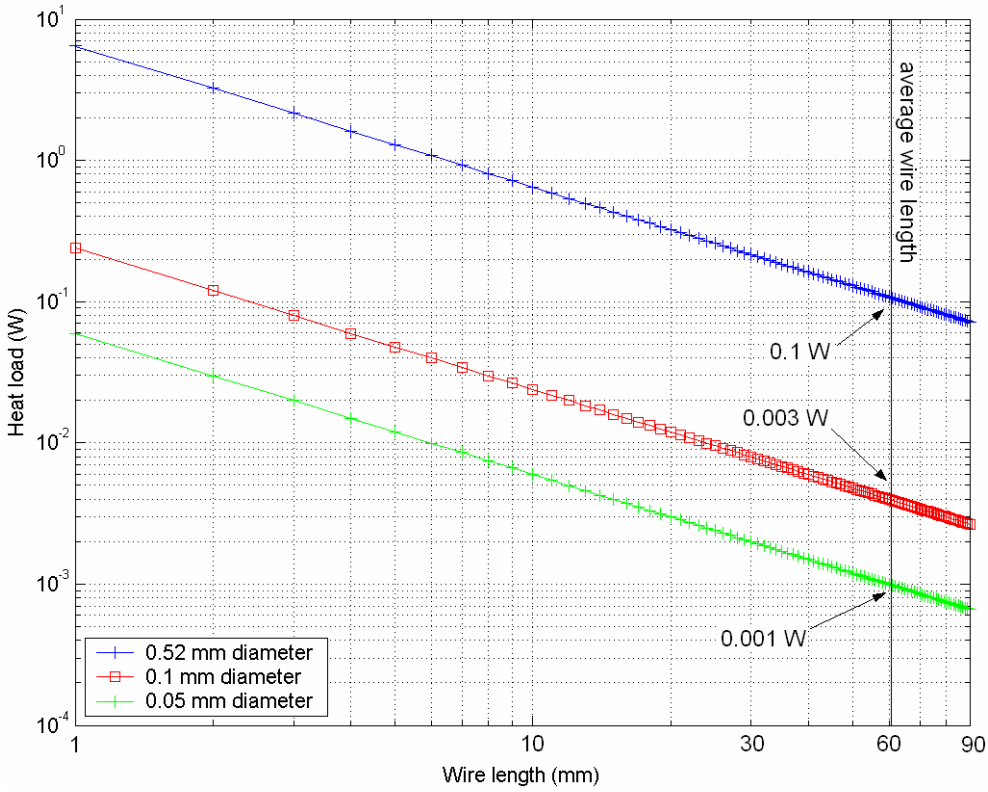

Figure 4.20: Reduced conductive heat load from thinner electrical wiring

The total heat load on the CCDs from the electrical wiring in the current configuration was ~ 2.9 W (29 wires × 0.104 W). By using 0.05 mm thick wiring, this total heat load can be reduced to ~ 0.029 W. This represents a significant decrease in Q_{cnd}. With Q_c reduced to 1.6 W, T_c would be approximately -62 °C as opposed to -45 °C. Figure 4.21 shows the performance of the TEC (T_c vs. Q_c) with the use of 0.05 mm wiring

(dashed red line) along with other heat loads which have been described in Section 4.3.

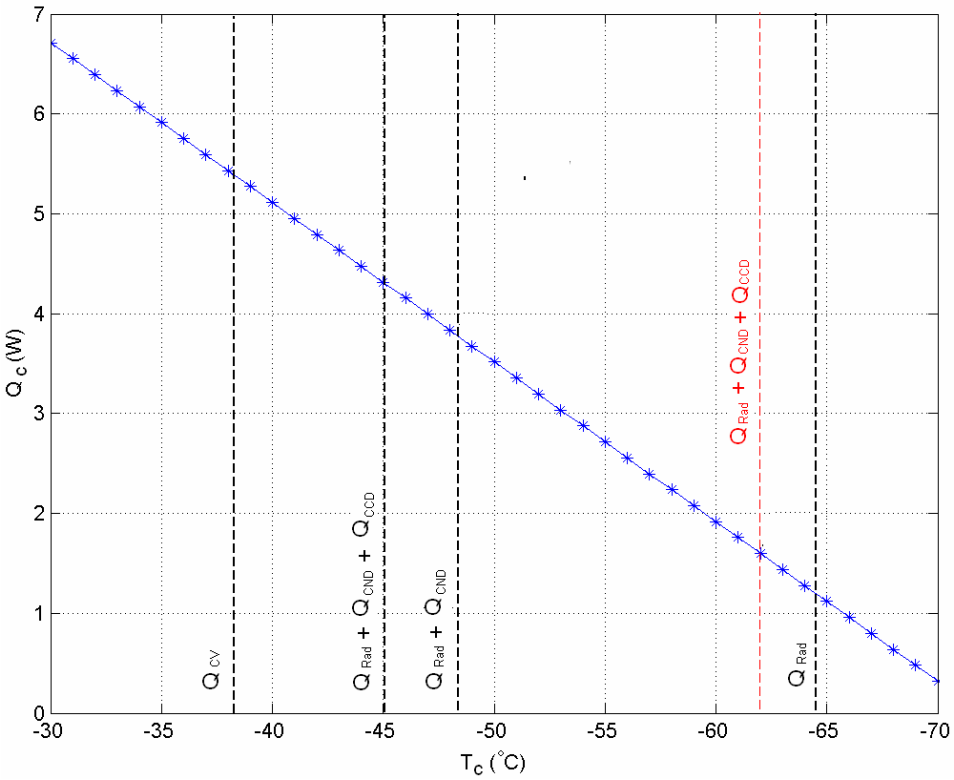

Figure 4.21: T_c vs. Q_c performance of TEC with different heat loads

Explanation of the CCD-Array's geometry with respect to the sample holder has also been discussed in this chapter. The calibration of each CCD in the spatial domain has been calculated and these calculations have been confirmed with the use of SRMs from NIST. Minor inaccuracies in the spatial calibration of the detector have been identified to be approximately 1 pixel (0.012°). Intensity errors have also been identified and corrected with maximum instrumental errors in peak intensity expected to be less than 3.2% (assuming at least 10,000 diffracted counts). The test facility designed for testing the CCD-Array has also been discussed with particular emphasis on the monochromation and collimation process. The next chapter describes the process of collecting, analysing and modelling XRPD/XRF data using CCDs.

Chapter 5 : Data Collection, Analysis and Modelling

5.1 Introduction

The key feature in the collection of combined XRD/XRF data is the ability of the CCD to collect isolated X-rays, or X-rays contained within a single pixel. The major factor dictating the amount of isolated events detected by a CCD is the depletion depth. Depletion depth is dependant on the biasing conditions of the CCD, but more importantly on the resistivity of the p-type epitaxial region. The initial section of this chapter aims to confirm the resistivity of the CCD30-11 devices that make up the CCD-Array. CCDs are very popular detectors for XRF analysis, but the use of CCDs for XRD analysis is still a relatively new technique (last decade). Therefore, the focus of this chapter is based on XRD data collection, analysis and modelling. Different data collection techniques are highlighted, including methods of reducing noise in XRD patterns. An investigation is also carried out to determine the best CCD architecture for collecting XRD data, namely frame transfer or full frame. The final section of this chapter is concerned with the modelling of XRD data using CCDs. The model allows users to calculate optimised CCD exposure times, total incident X-ray events, background noise, event statistics and CCD binning effects. The operation of the model is explained and agreement between the simulated and experimental data is highlighted.

5.2 CCD30-11 Depletion Depth Measurements

5.2.1 X-ray Events in CCD Detectors

Once a positive voltage is applied to the surface electrode, a depletion region forms underneath the SiO_2 layer with a finite depth. If X-rays interact in the CCD depletion region, the resulting charge cloud is quickly swept away by the strong electric field to the nearest potential well. These X-ray events are usually confined to a single pixel and are known as isolated or single pixel events. X-rays that ionise underneath the depletion layer where no electric field is present, diffuse into neighbouring pixels and cause split events. Figure 5.1 (a) shows the 3-dimensional Gaussian distribution of electrons contained within the charge cloud. The digitised value of each pixel is determined by calculating the fraction of the charge cloud in each pixel, as shown in figure 5.1 (b).

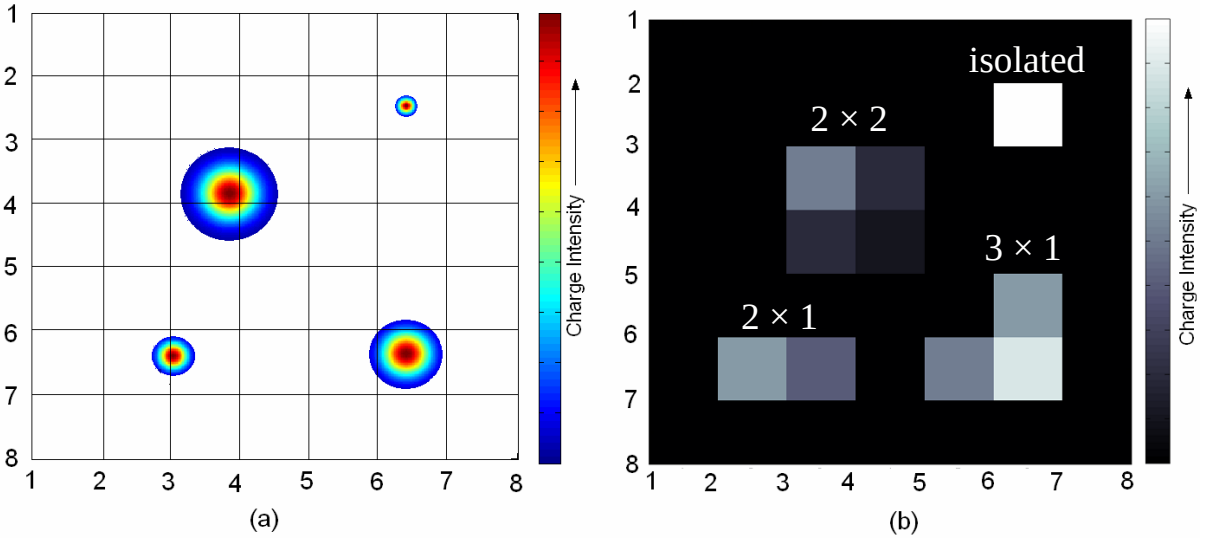

Figure 5.1 (a): Charge clouds produced at different X-ray ionisation depths and (b) corresponding digitised pixel values

To identify distinct X-ray energies, only isolated events are used in the data collection stage. The calibration of the X-ray spectrum is expressed as:

$$Cal(eV / ADC) = \frac{E_{x-ray}}{\pi_{x-ray} - \pi_{noise}}, \tag{5.1}$$

where $\pi_{x\text{-}ray}$ is the mean digitised value of the X-ray peak, π_{noise} is the digitised value of the noise mean and $E_{x\text{-}ray}$ is the energy of the X-ray peak in eV. The number of electrons per digitised value can be calculated by dividing *Cal* by ω, which represents the average amount of energy (eV) needed to create a single electron hole pair in Si. This value is temperature dependant and is approximately 3.74 at -100 °C and 3.67 at +25 °C [Groom 2004].

The presence of isolated events in the CCD image is determined as follows. The mean position of the noise peak π_{noise}, is identified and accurately fitted using a Gaussian distribution. The noise threshold is set to any events in the image that are $3 \times \sigma_{noise}$ greater than π_{noise}, where σ_{noise} represents the standard deviation of the noise peak. A pixel with an intensity greater than the noise threshold ($\pi_{noise} + 3\sigma_{noise}$) is considered as an 'event'. Isolated events must have an energy greater than the noise threshold, with 4 neighbouring pixels below the noise threshold (see figure 5.23).

X-ray ionisation in Si causes the formation of an electron-hole cloud, the size of which is based on the energy of the incoming X-ray and the absorption depth, *z*. A simulation was designed to determine the ratio of isolated to split events over $(26\ \mu m)^2$ pixels, with respect to increasing electron-hole cloud diameter. The simulation involved randomly distributing 1×10^5 photons over a 5 × 5 pixel imaging area (25 pixels) for each electron-hole cloud diameter. The events considered were isolated events, 2 × 2 and 2 × 1 split events. The results of the simulation are shown in figure 5.2.

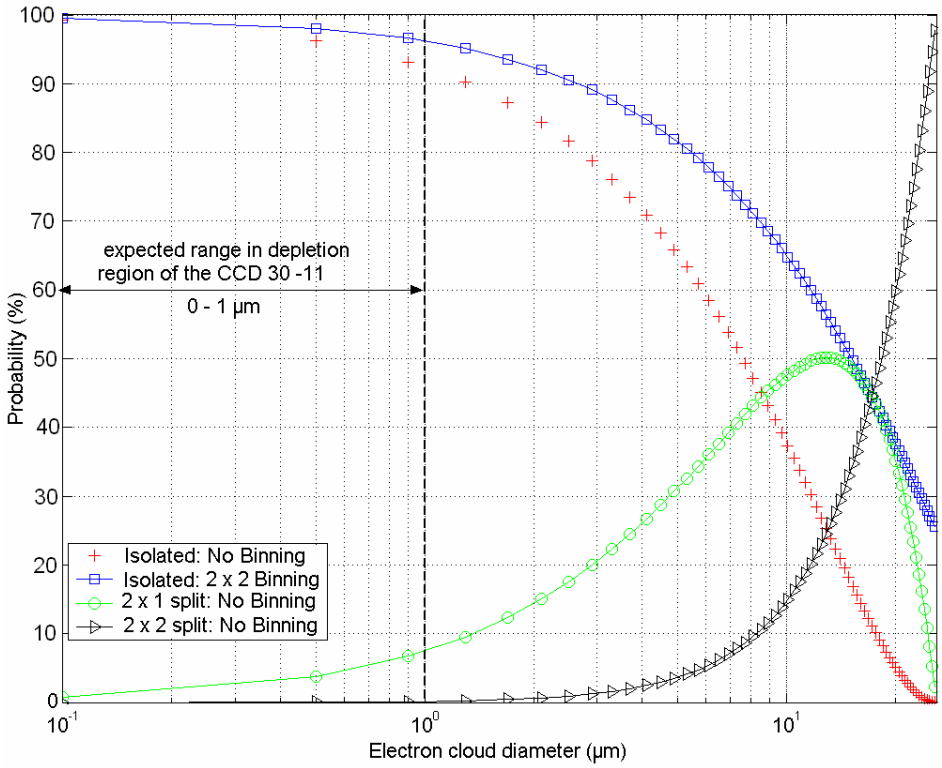

Figure 5.2: Simulation revealing the ratio of isolated to split events with increasing electron-hole cloud diameter over $(26\ \mu m)^2$ pixels

As can be seen from figure 5.2, the number of isolated events decreases with increasing cloud diameter until the cloud diameter reaches the size of the pixel and no isolated events can occur. It is important to note that photons collected within the depletion region of the CCD have very small cloud diameters (< 1 μm) which will result in a very high percentage of isolated events. Photons absorbed underneath the CCD depletion layer will form much larger electron-hole clouds due to diffusion and result in a much lower percentage of isolated events. The probability of 2 × 1 split events decreases when the electron-hole cloud diameter reaches half the pixel size.

2 × 2 split events become dominant at electron-hole cloud diameters greater than approximately half the pixel size.

By 2 × 2 binning the CCD image, an increase in the isolated event efficiency occurs, since the pixel area is quadrupled whilst the size of the charge cloud remains the same. Split events such as those seen in figure 5.1 (b) are summed to reform the original X-ray event. Binning causes an increase in the SNR as each pixel now contains 4 times as much signal intensity, whilst the readout noise remains the same, however each pixel also contains 4 times as much dark current.

5.2.2 Depletion Depth Measurement – X-ray spread events

The AIMO FI CCD30-11 manufactured by e2v is normally fabricated on 100 Ω.cm p-type Si with a 25 µm epitaxial layer. However, in recent years deep depletion AIMO CCD30-11 devices have also been fabricated on 1000 Ω.cm p-type Si with a 50 µm epitaxial region [Pool 2005]. The CCD30-11 devices used in building the CCD-Array were expected to be 100 Ω.cm as opposed to the 1000 Ω.cm resistivity, but measurements were required for confirmation.

Depletion depth measurements were made using X-ray spread event analysis. The size of the electron-hole cloud formed by a particular X-ray is dependant on its energy and the interaction depth within the Si. By determining the size of the electron-hole cloud formed by X-rays of different energies and simulating these events over a given pixel area, the ratio of isolated to split events for a given X-ray energy can be calculated. By measuring the ratio of isolated to split events in the experimental data and comparing to the simulated results, depletion depth estimates can be made.

5.2.2.1 Isolated Events in the Epitaxial Region

Figure 3.10 shows the small electron-hole cloud formed by X-rays in the depletion region in comparison to the pixel size $(26\ \mu m)^2$, for a 100 Ω.cm and 1000 Ω.cm device. It can be assumed that all events detected in the depletion region of the CCD result in single pixel events. Since the electron-hole cloud radius of X-rays detected in the depletion region is much smaller than the pixel size, this is a fair assumption. However, since some X-rays will statistically ionise in between pixel boundaries, such events although detected in the depletion region, can form split events. The formation of split events in the field free region is much more likely as the charge

cloud will diffuse before reaching the potential well of the CCD. Figure 5.3 highlights this effect as the number of isolated events immediately decays when X-rays begin to ionise in the field free region.

The transmission of monochromatic X-rays through Si is shown for 3 elements in figure 5.3. The diagram shows the depletion boundaries for 100 Ω.cm and 1000 Ω.cm devices biased at a 12 V gate voltage and 0 V substrate voltage. The resulting depletion depth of each of the devices was calculated to be 12 µm and 33 µm respectively, using equation 3.11.

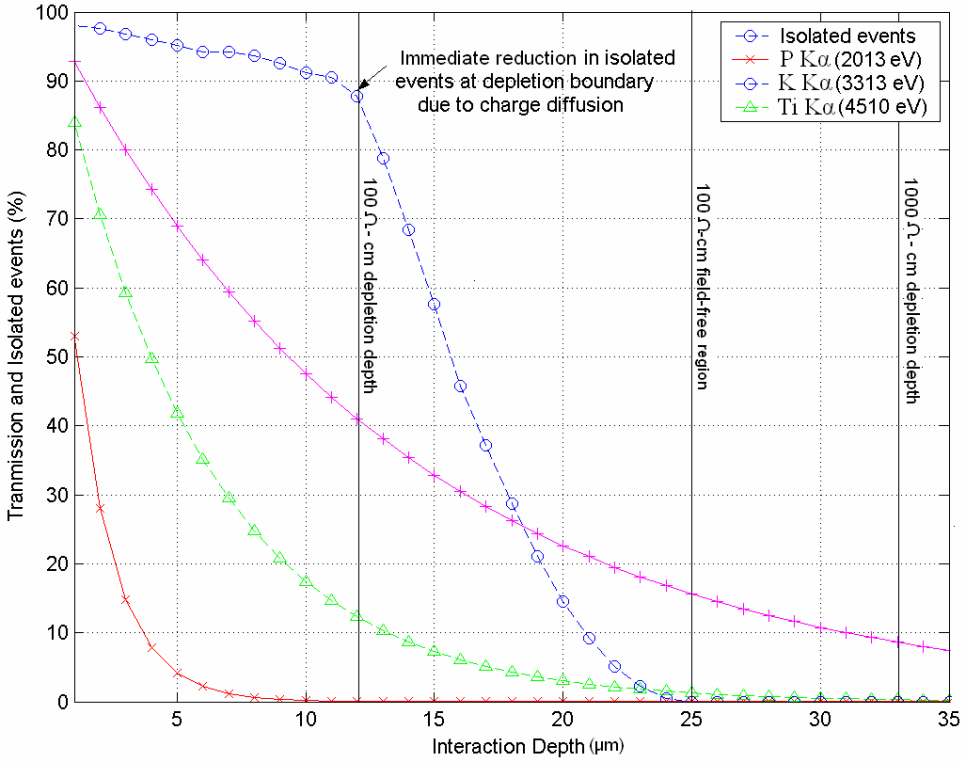

Figure 5.3: Transmission of P Kα, K Kα and Ti Kα X-rays in a 12 µm and 33 µm depleted CCD

The simulation begins by generating an interaction at depth *z*, based on the transmission plot shown in figure 5.3, with a random location within the pixel. An initial cloud radius forms at the depth of interaction R_i, the size of which can be calculated using equation 3.27. When the X-ray ionises in the depletion region ($z < Z_d$), the size of the charge cloud reaching the n-type buried channel is a combination of the initial charge cloud and subsequent spreading in the depletion region (equation 3.30). If the X-ray interacts in the field free region ($Z_d > z < Z_{ffr}$), the

charge cloud diffuses until it reaches the depletion boundary. The extent of the charge cloud in the field free region (FFR) is calculated using equation 3.31 and must also include additional spreading in the depletion region (equation 3.32). Since X-rays > 4.5 keV were not used for depletion depth measurements, interactions in the substrate are ignored. Charge clouds formed in this region produce events that are not confined to 2 × 1 or 2 × 2 split events, but form larger split events and are very difficult to detect experimentally. Charge from the electron-hole cloud is also lost due to recombination in the substrate, therefore these events cannot be summed to reform the original X-ray energy. Once the size of the charge cloud reaching the potential well for a given interaction depth has been calculated, the software calculates the fraction of the charge cloud in each pixel and determines whether the event is an isolated or spit event.

The results of the simulation are labelled as 'isolated events' in figure 5.3. Since the spreading of the charge cloud in the depletion and FFR is not related to the X-ray energy, the 'isolated events' curve is a very good approximation for all X-rays from 0.1 – 10 keV. The value of R_i (which is dependant on the X-ray energy) has little influence on the curve. The number of isolated events produced by an X-ray of energy *E*, is the number of X-rays absorbed in the epitaxial region multiplied by the 'isolated events' curve. As *E* increases, fewer X-rays are absorbed within the epitaxial region and the number of isolated events decreases. The results from the simulation are shown in table 5.1 for 8 different elements ranging from 2 − 4.5 keV.

Element	eV	Epitaxial (simulated) %	Depletion (simulated)%	Depletion (predicted) %
P Kα	2013	98.57	98.5337	99.9513
S Kα	2307	97.94	97.6328	99.56
Cl Kα	2622	96.822	95.54	97.99
Ar Kα	2957	94.5764	91.3299	94.1918
K Kα	3313	90.4947	84.6834	87.68
Ca Kα	3691	84.2859	75.89	78.94
Sc Kα	4090	76.32	66.1761	69
Ti Kα	4510	67.3821	56.4335	58.99

Table 5.1: Summary of simulated results calculating the percentage of isolated events for various characteristic Kα photons ranging from 2 − 4.5 keV

As predicted, the number of isolated events actually produced in the depletion region are very similar to the number of events absorbed in the depletion region (listed as

'Depletion (predicted)' in table 5.1). Table 5.1 also outlines the total number of isolated events detected in the epitaxial region. Depletion depth measurements were made by comparing the simulated data to experimental data. Experimental data was collected by detecting the Kα X-ray emissions of the elements listed in table 5.1. The percentage of isolated to split events was then calculated for each element and compared to the simulated data. The X-ray flux was reduced to ensure X-ray events were sparsely populated across the CCD (X-rays source flux was reduced according to samples fluorescence yield to allow ~ 50 total events/s). Results are shown in figure 5.4.

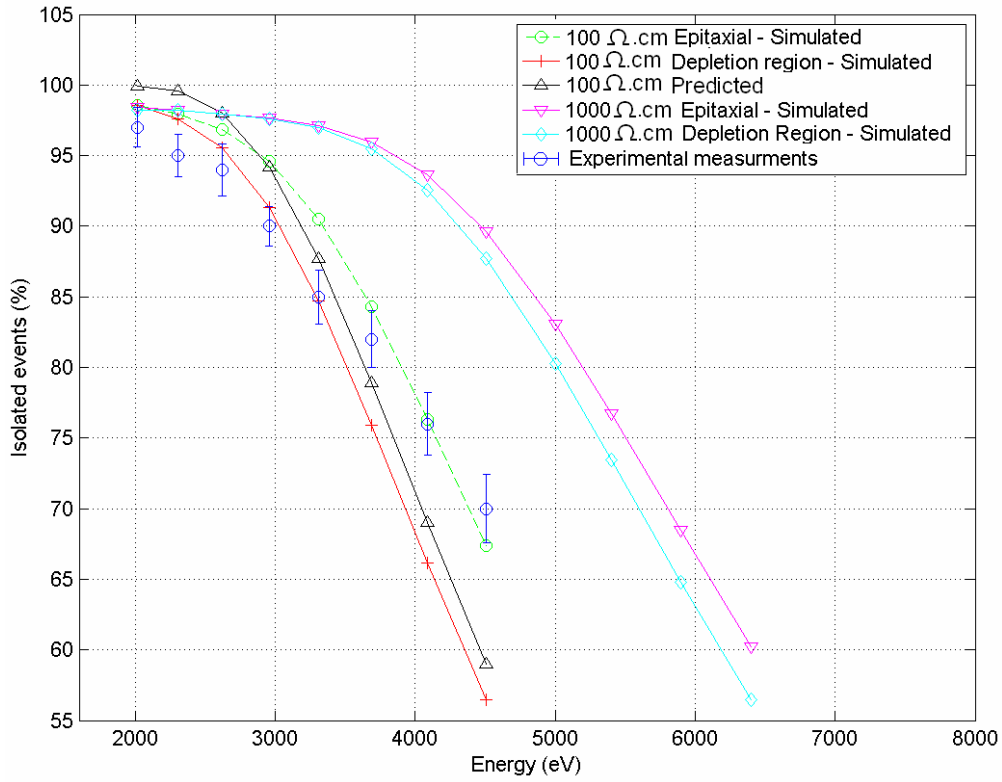

Figure 5.4: Comparison between simulated and experimental evaluation of depletion depth using X-ray spread events for 100 and 1000 Ω.cm devices

It is evident that the experimental evaluation of the depletion depth provides a good match to the 100 Ω.cm resistivity. The measurements aim to highlight the agreement between the experimental data and the total isolated events in the epitaxial region (green curve), as this represents the most accurate representation of the isolated events formed inside the CCD. The errors seen in the experimental data were expected to arise from difficulties in processing experimental CCD images for isolated and split events. The errors between 2 − 3.5 keV appear to underestimate the depletion depth.

Since lower energy elements have a low fluorescence yield, the X-ray source was operated at full power to deliver an appreciable flux of X-rays. Events in the CCD image were therefore dominated with elastically scattered Cu Kα photons, which caused some interference in detecting the intended X-ray events. For additional confirmation, another technique of determining the resistivity of the devices was performed by using a much simpler method, which is presented in the next section.

5.2.3 Depletion Depth Measurement – CCD30-11 vs. CCD42-10

Additional depletion depth measurements were made by using e2v's CCD42-10, which were FI, NIMO and deep depletion (1000 Ω.cm Si) devices. Since the resistivity of these devices was known, QE measurements could be compared between the CCD30-11 and CCD42-10 devices. As stated in equation 3.11, the depletion depth can be calculated using the expression:

$$x_p = \sqrt{\frac{2\varepsilon_{SI}(V_{G-avg} - V_{SS})}{qN_a}}, \tag{5.2}$$

where $V_{G\text{-}avg}$ is the average applied voltage to each pixel [Murray 2007] [Burt 2006]. Figure 5.5 shows the region of each $(26\ \mu m)^2$ pixel of the CCD30-11.

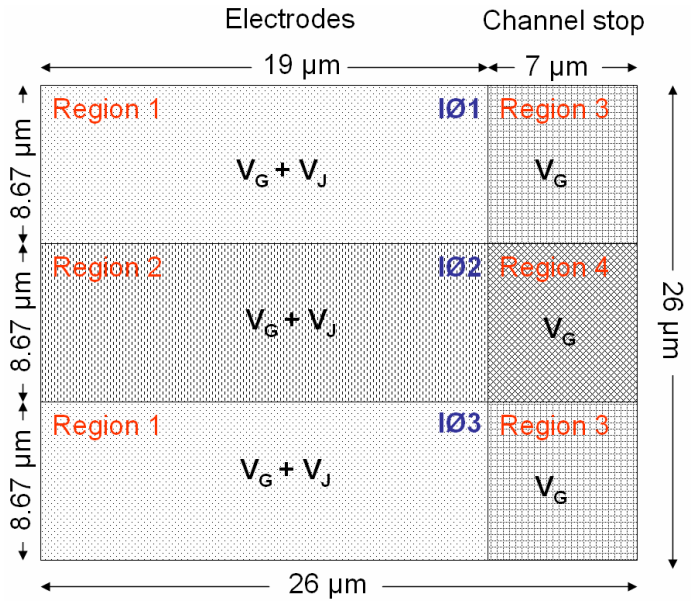

Figure 5.5: Average voltage applied to a single pixel in CCD30-11

Assuming the pixel is biased so that *Iø1* and *Iø3* are barrier phases, the only regions experiencing the presence of the positive gate voltage are Region 2 and Region 4. Located beneath Region 1 and 2 is the np junction which has a potential of ~ 11 V for the e2v devices discussed here. This also contributes to the voltage applied to each pixel. The channel stop regions (Regions 3, 4) do not experience additional potential, as no n-type material exists underneath the p^+ channel stops. Equation 5.3 represents the average voltage applied to the top surface of a single pixel during integration, the constants representing the fraction of the pixel area each region covers.

$$\underbrace{0.48(0V+11V)}_{\textit{Region 1}}+\underbrace{0.24(12V+11V)}_{\textit{Region 2}}+\underbrace{0.18(0V)}_{\textit{Region 3}}+\underbrace{0.09(12V)}_{\textit{Region 4}} \qquad (5.3)$$

For a 12 V gate voltage applied to *Iø2*, the average applied voltage to the top surface of the pixel is 11.88 V. The depletion depth was determined by comparing the transmission of Cu Kα X-rays in the CCD30-11 to that in the CCD42-10. With a gate voltage of 12 V and substrate voltage of 7 V, the depletion depth of the CCD42-10 was calculated to be ~ 22 µm. The percentage of Cu Kα photons absorbed within 22 µm of Si is 29%. Given that the CCD30-11 is a standard 100 Ω.cm device, the absorption of Cu Kα X-rays in the depletion region will be ~ 12% when biased under the same voltages. This is an increase by a factor of 2.4, which means for every 100 photons that are detected in the CCD30-11, ~ 240 will be detected in the CCD42-10. If the CCD30-11 was in fact deep depletion, the detection efficiency of Cu Kα photons would be very similar to the CCD42-10.

CCD 2 was exposed to a ZnO diffraction ring located at 31.7° *2θ* for a total of 1000 frames (1 s exposure each). The average number of events detected within the ring was calculated to be 49.88 Cu Kα photons/s. The CCD30-11 was replaced with the CCD42-10 (with an identical geometry in relation to the sample) and data was collected for a similar exposure time. The CCD42-10 image area was 2 × 2 binned to simulate $(27\ \mu m)^2$ pixels, which is a close approximation to the $(26\ \mu m)^2$ pixels of the CCD30-11. The average number of X-rays was calculated to be 137 Cu Kα counts/s. This represents an increase by a factor of ~ 2.56, which is acceptably close to the predicted value of 2.4. This confirms the resistivity of the CCD30-11 devices to be 100 Ω.cm.

5.3 Combined XRD/XRF Data Collection

This section discusses the process of collecting combined XRD/XRF data using CCDs. The overall aim of the process is to obtain a histogram (XRF) containing the elemental/chemical data and a 2θ vs. intensity plot (XRD) which can be used to determine mineralogy.

5.3.1 Single Photon Counting

The use of the single photon counting technique for collecting combined XRD/XRF data using CCDs has been well documented [Reyes-Mena et al. 2000]. The ability of the CCD to resolve the energy of incident X-rays (typical FWHM energy resolution of ~ 130 eV at 5898 eV) as well as determine the exact interacting position of X-rays (typical spatial resolution of 13 − 26 μm), makes it an ideal detector for XRF and XRD respectively. Operating a CCD in single photon counting mode involves integrating the CCD for short periods (0.1 − 2.0 s) and taking multiple exposures to increase the SNR. Exposing the CCD for a short time ensures the CCD is not flooded with X-ray events, thereby aiding the process of detecting single pixel events. By adjusting the X-ray source flux with respect to the sample's diffraction/fluorescence yield, a target of 250 − 500 events/s is achieved across the CCD in full imaging mode (256 × 1040 pixels). If the charge is confined to a single pixel, the software can determine the energy of the incident X-ray and once the resulting image has been generated, the exact pixel location of the isolated event. Once all the exposures are taken, split events from each frame are eliminated and all the frames are combined to form a histogram that contains isolated events only. Figure 5.6 shows the XRF spectrum collected from sodium chloride (NaCl) powder using the single photon counting technique. The data was collected under normal operating conditions for a total of 1000 exposures.

The energy resolution of an XRF peak is limited by the readout noise, fano factor and dark current. Assuming the first two parameters are fixed, exposing the CCD for short periods is ideal since this minimises the dark current generation, thereby improving the energy resolution. XRD data is extracted from the raw data through a process known as energy discrimination, which is now discussed.

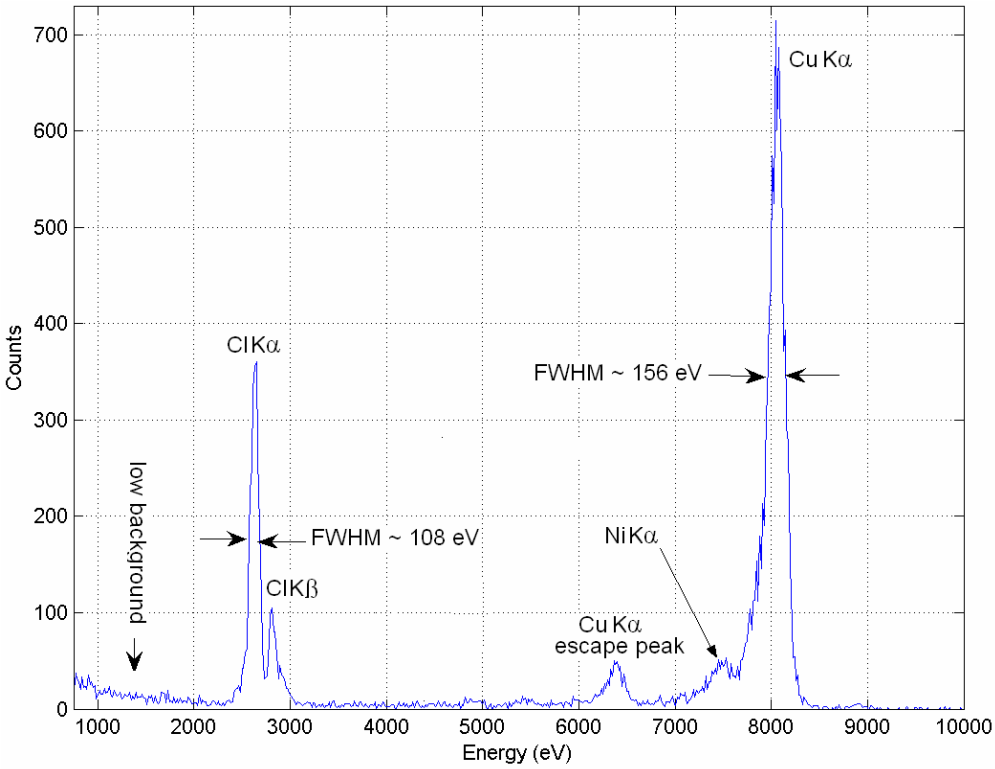

Figure 5.6: XRF spectrum of NaCl collected using the single photon counting technique

5.3.2 Energy Discrimination

The Bede micro-source produces a 93% monochromatic beam of Cu Kα X-rays when operated at 40 kV, 2 mA and using a 15 µm Ni filter. When diffraction occurs in the sample, the entire incident spectrum is diffracted, which is predominantly Cu Kα X-rays. When a histogram is generated of all X-rays incident upon the detector, a strong Cu Kα X-ray peak is present. These Cu Kα events represent X-rays that were diffracted from the sample and collected by the CCD. Cu Kα X-rays are also detected by the CCD through elastic scattering, which causes the background noise in the XRD pattern. A Gaussian fit is applied to the Cu Kα peak and events within 3 standard deviations of the mean are registered as diffraction data (99.7% of all Cu Kα events). In order to extract the XRD information from the CCD image, only isolated Cu Kα X-rays are collected in each CCD frame. This process is known as energy discrimination. Energy discrimination is applied to each CCD exposure and all exposures are accumulated. The resulting image contains single or multiple isolated Cu Kα X-rays. Figure 5.7 (a) shows the combined XRD/XRF data of peridotite collected using CCD 2. Events in the image are all the isolated X-rays detected in the

2000 exposures, regardless of energy. Figure 5.7 (b) shows the energy discriminated data, containing only isolated Cu Kα events and the removal of unwanted XRF data.

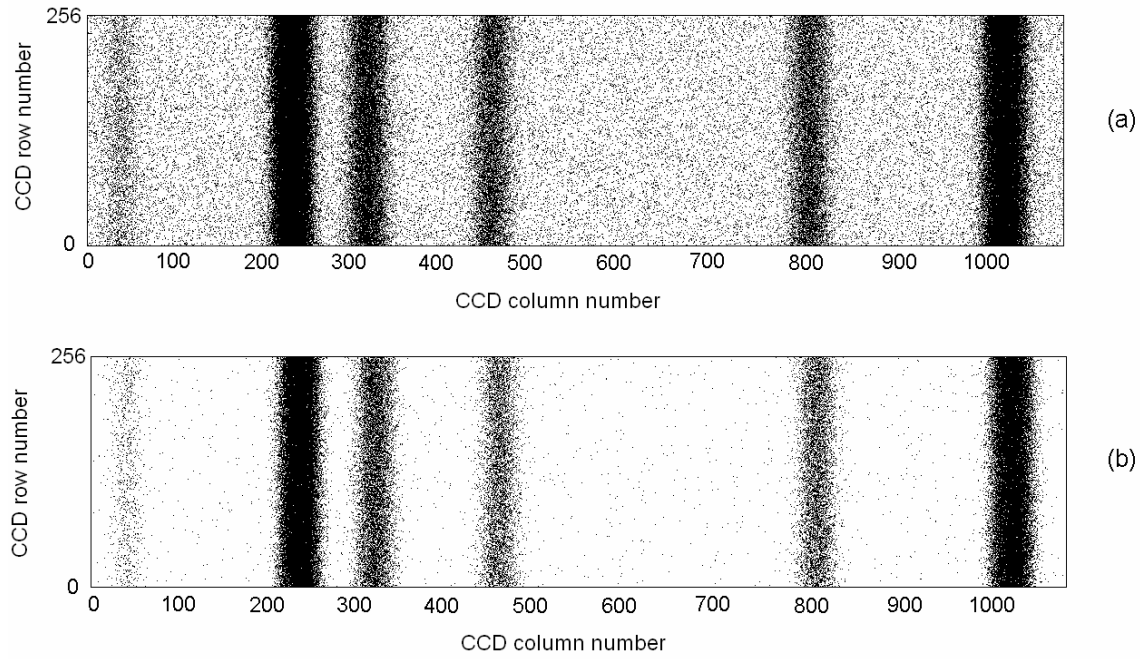

Figure 5.7 (a) Raw peridotite data containing all isolated events (XRD/XRF data) and (b) energy discriminated image (XRD data only)

5.3.3 XRD Software Processing

Once the energy discrimination technique is applied to all CCDs, software was used to extract the 2θ vs. intensity plot. The initial stage in the software process begins by placing each of the CCDs in ascending order of 2θ angle (CCD 1 − CCD 4). The software then constructs an array representing an angular coverage from 4.48° to 63.95°, which contains the 4 CCD images and gaps between CCD imaging areas. The geometry described in Section 4.5 was used to determine the 2θ coverage of each of the CCDs.

5.3.4 Beam Alignment and Radial Integration

The next stage of the software process involved determining and correcting any errors involved in the experimental alignment. Under ideal circumstances, the collimated beam was located on the same axis as the centre of the CCDs (pixel 128) on the CCD-Array. This ideal alignment was difficult to achieve, therefore inaccuracies in the alignment were calculated and corrected during post-processing of the diffraction data. The 2θ vs. intensity plot was generated by radially integrating the array

constructed by the software. Figure 5.8 shows the radial integration of the 4 CCDs and the resulting intensity distribution as a function of 2θ scattering angle. In order to perform the alignment, the array was radially integrated and the FWHM of the rings was calculated. The beam position was then refined until the highest angular resolution was achieved. The position where the highest angular resolution was achieved represented the axis of the X-ray beam from the collimator. Under the normal experimental arrangement the beam centre was usually found to be within ± 0.3 mm (11 − 12 pixels) from the centre of the CCD.

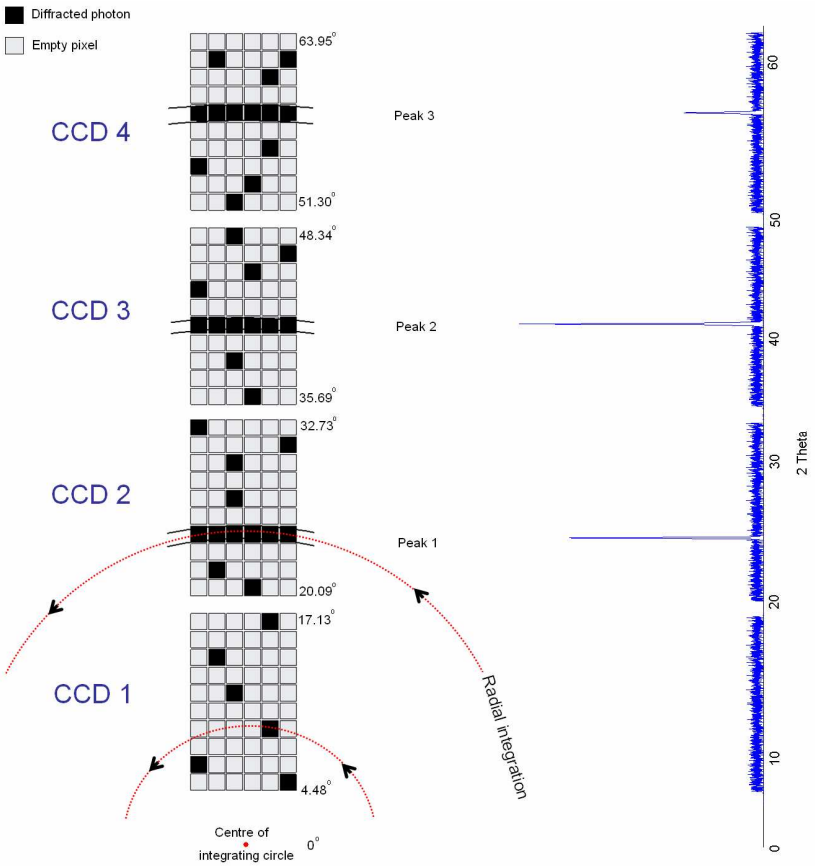

Figure 5.8: Radial integration of 4 CCDs revealing intensity distribution as a function of 2θ scattering angle

Figure 5.9 shows the radial integration of NaCl powder. In order to perform qualitative analysis, the positions of the 3 largest peaks are recorded and matched to a database, such as the ICDD PDFs (JCPDS file 5-628). A successful solution was found for the NaCl diffraction pattern shown in figure 5.9.

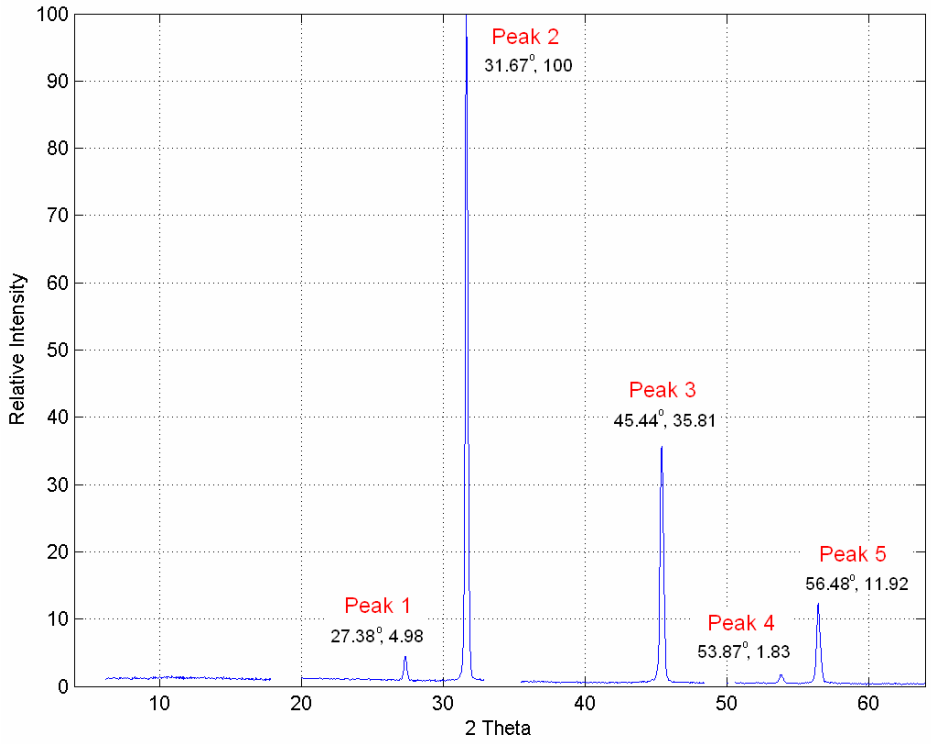

Figure 5.9: 2θ vs. intensity plot of NaCl generated by radial integration

5.4 XRD Noise Sources

This section describes the main sources of noise in XRD patterns and examines the impact of these noise sources in relation to the CCD-Array. Noise removal techniques are also investigated.

XRD patterns experience the presence of various noise sources. Incomplete monochromation of the X-ray beam used for irradiation of the powder sample is one of the major sources of noise. In order to identify diffracted X-rays incident on the detector, the ratio of Kα characteristic X-rays to non Kα X-rays (continuous and other characteristic X-rays) should be maximised. It has been shown in Section 3.15 that with the use of an XOS polycapillary optic and a 15 µm Ni filter, the Bede micro-source produces a spectrum which is composed of a 93% beam of Cu Kα X-rays, therefore noise induced from incomplete monochromation was negligible.

Another source of noise in XRD patterns is that generated by the detector. The main constituents of noise in CCDs comprises of readout noise (signal amplification and electronics) and leakage current (thermal). In Section 6.4.1, it is shown that CCD noise has negligible effect on the quality of the XRD pattern (assuming the CCD

noise < 30 e^- r.m.s). All XRD patterns detected by the CCD are accompanied by XRF data, which is separated by the energy discrimination process. Clearly, detectors that cannot distinguish XRD from XRF data experience XRF as an additional noise source. This results in a non-linear scattering profile and reduction in SNR (see figure 3.19). By using CCD detectors, this source of noise can also be eliminated. The main sources of noise in XRD patterns are either greatly reduced or almost completely eliminated with relation to the CCD-Array. The dominant noise source in relation to the CCD-Array originates from elastic scattering of Cu Kα X-rays. These X-rays are scattered from various locations in the test facility such as the sample holder, air and the aluminium front plate. The energy of these collisions is conserved (i.e the wavelength of the emitted photon is identical to the incident photon) and detected by the CCD as Cu Kα X-rays. These X-rays cannot be separated from the XRD data during the energy discrimination stage and constitute as noise in the diffraction pattern. The next section describes 2 methods of reducing the noise sources in XRD patterns.

5.4.1 XRD Noise Reduction Techniques

Figure 5.10 shows an XRD pattern collected from $CaCO_3$ using CCD 3. The spectrum has been energy discriminated, therefore all events are either single or multiple isolated Cu Kα events. The data was collected under normal operating conditions for a total of 4500 exposures. The image consists of 7 diffraction rings and the remaining areas represent the background. The strongest peak, ‘Ring 1’ and weakest peak, ‘Ring 2’ are used as examples.

The difference between background events and XRD data is evident from figure 5.10. For example, Ring 1 contains events confined to a small region of the imaging area (~ 1×10^4 pixels) whereas background events are scattered across the entire CCD imaging area (2.6×10^5 pixels). Background events are sparsely populated across the CCD and do not form large clusters like XRD events. This is shown in figure 5.10, where Λ_D is the average pixel intensity of XRD events per unit area, and Λ_B represents the average pixel intensity of background events per unit area. Since $\Lambda_D >> \Lambda_B$, XRD rings contain multiple isolated events in comparison to background noise for a given exposure period.

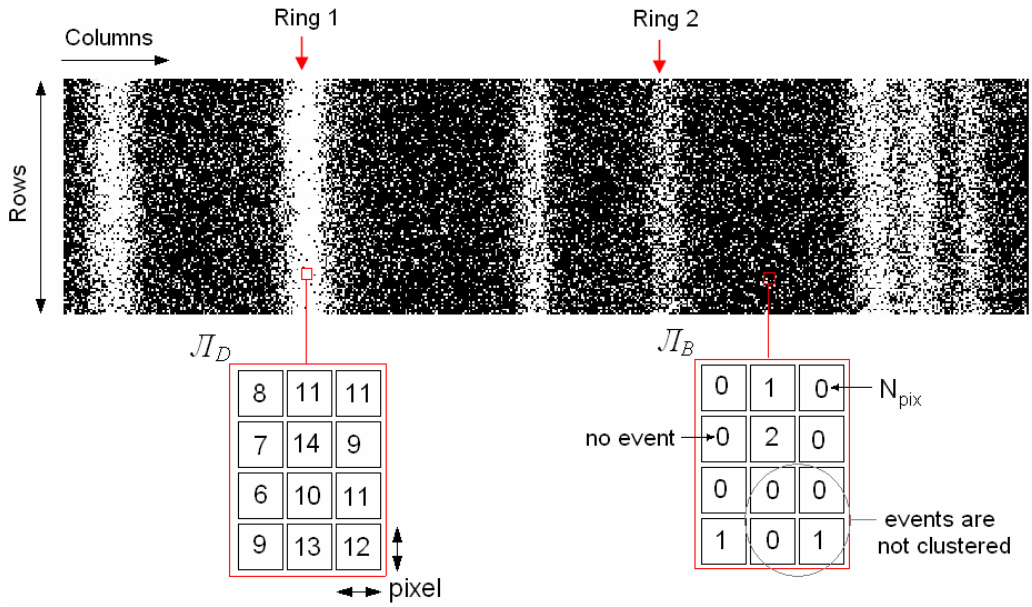

Figure 5.10: Energy discriminated CCD image of $CaCO_3$. The CCD image contains 7 XRD rings and background noise in the form of elastic scattering

Multiple isolated events represent pixels that have a value N_{pix}, greater than 1 (where N_{pix} is the number of isolated events detected within the given pixel over the total exposure period). Figures 5.11 and 5.12 show the variation of isolated Cu Kα events contained within the background and Ring 1/Ring 2 over 4500 exposures respectively.

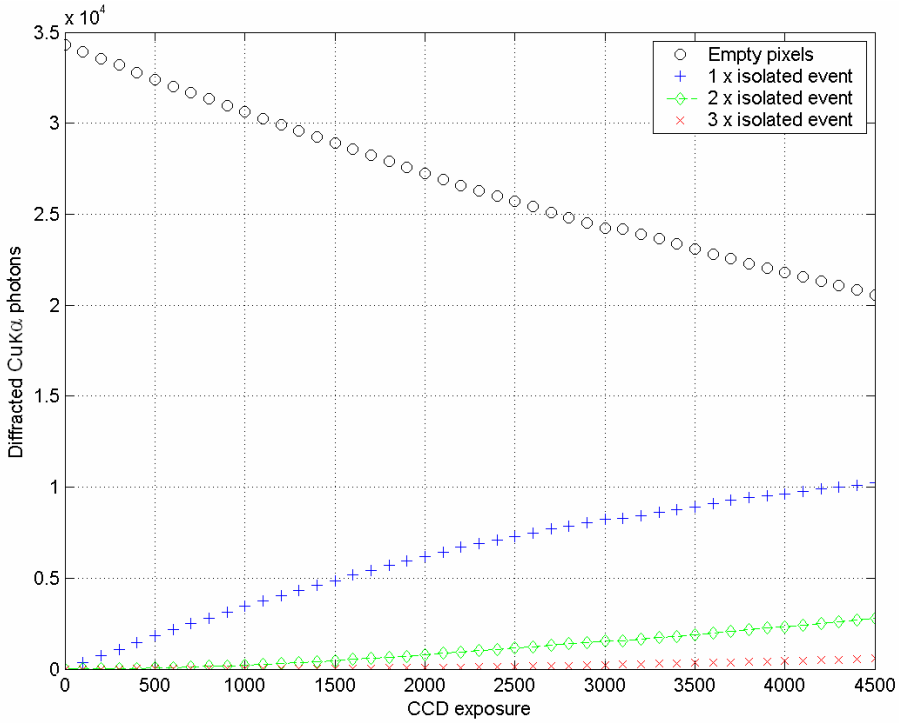

Figure 5.11: Variation in background noise events over 4500 CCD exposures

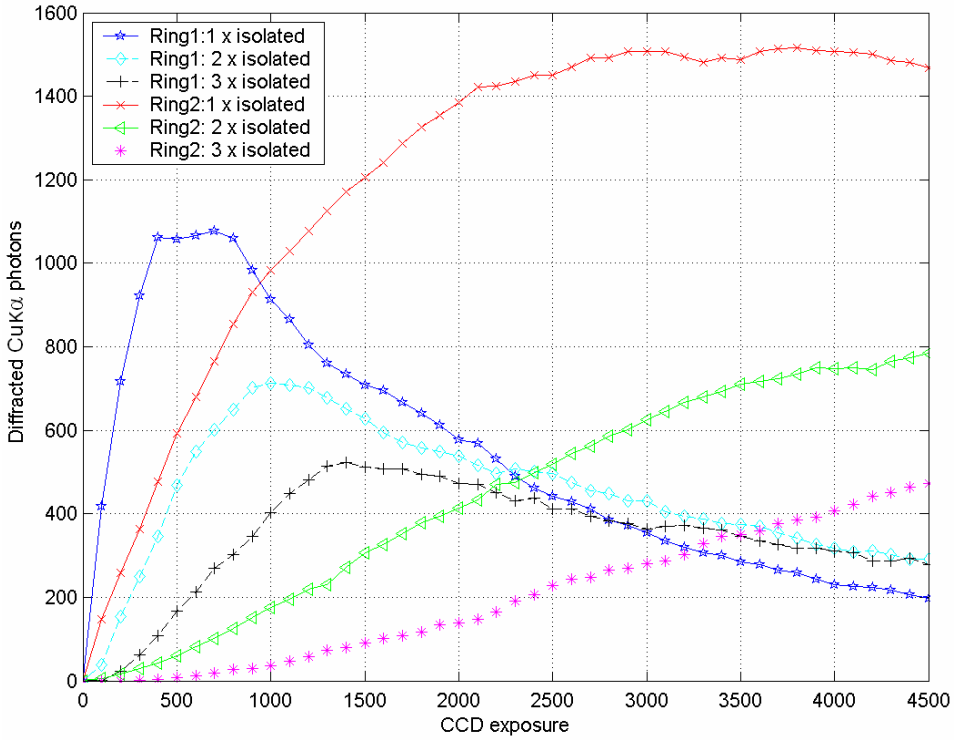

Figure 5.12: Variation in isolated XRD events in Ring 1 and Ring 2

As shown in figure 5.12, the single isolated events peak at approximately 800 and 3000 exposures for Ring 1 and Ring 2 respectively. Even after 4500 exposures, the single isolated events in the background noise have not peaked. In fact, at the end of the exposures, 60% of the background pixels are still empty. The next section discusses techniques to reduce the background noise, based on these observations.

5.4.1.1 Neighbouring Pixel Elimination (NPE)

As the number of CCD exposures increases, the density of background events also increases. One method of eliminating background events involves searching neighbouring pixels for similar background events. If the 8 neighbouring pixels contain no events, the original background event is eliminated [Cornaby et al. 2000]. Since almost all events within a diffraction ring contain a neighbouring event (assuming the CCD has been integrated for multiple exposures), no signal data is lost in the process.

5.4.1.2 Single Pixel Elimination (SPE)

After many exposures, another significant difference between the signal and background data can be exploited. The amount of single isolated X-ray events

contained within a diffraction ring is greatly reduced. The data contained within a diffraction ring contains multiple isolated X-ray events as seen in figure 5.12, whereas the background is still dominated by single isolated events. The single pixel elimination (SPE) technique, simply removes all single isolated events from the XRD image. This removes large amounts of background noise and very small amounts of diffraction data. The success of this technique depends on the number of counts in the weakest diffraction ring. Figure 5.13 (a) and (b) demonstrate the application of the SPE technique on Ring 1 after 1000 and 4000 exposures respectively.

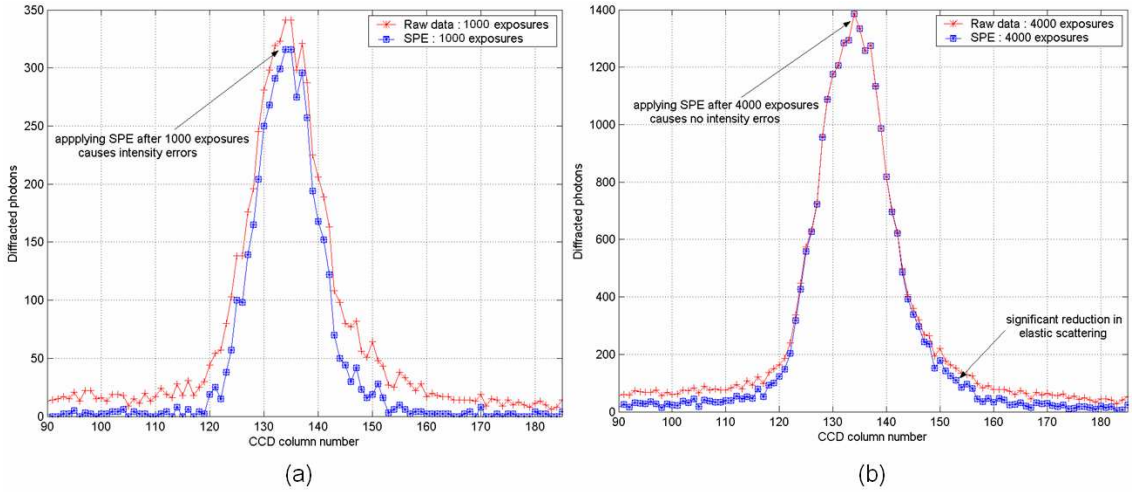

Figure 5.13: Application of the SPE technique after (a) 1000 and (b) 4000 exposures

As can be seen from figure 5.13 (a), the diffraction ring still contains single isolated events (37%). By applying the SPE technique, events are not only extracted from the background region as intended, but also from the signal data region. However, after 4000 exposures the diffraction ring is now dominated with multiple isolated events and applying the SPE technique only removes data from the tails of the Gaussian shaped diffraction peak. This does not cause any errors in determining the 2θ position, intensity or FWHM (°) of the peak. The mean level of the background noise has been reduced from 44 to 14 Cu Kα photons, thereby increasing the SNR of the diffraction pattern. This example emphasises that a large number of exposures must be taken before SPE can be applied efficiently. Figure 5.14 compares the SPE and NPE technique being applied to the CCD image shown in figure 5.10, after 1000, 2500 and 4000 exposures respectively.

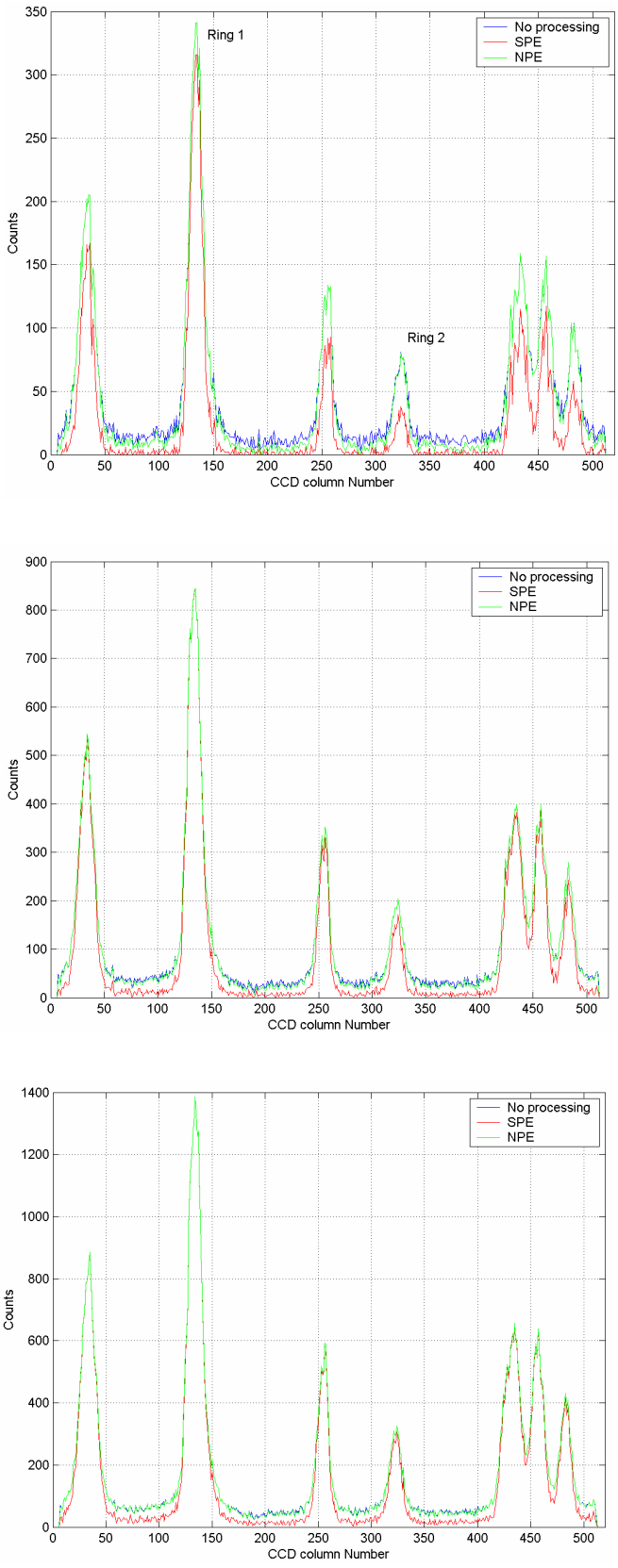

Figure 5.14: Comparison of the SPE and NPE techniques after (a) 1000 (b) 2500 and (c) 4000 CCD exposures

The NPE technique shows a much better response for shorter exposure periods. Even with short exposure periods, the probability of losing signal data with the NPE technique is very low. The SPE technique shows a very poor response at shorter exposures with errors of 51.2% in Ring 2 after 1000 exposures. After 4000 exposures, the intensity errors have been reduced to < 1% and the background has been reduced from an average of 43.45 to 14.27 Cu Kα photons. Since the density of background events is very high after 4000 exposures, the NPE technique has only reduced the background by 2.52 Cu Kα photons. Table 5.2 summarises the results shown in figure 5.14.

	Raw	Raw	NPE	NPE	SPE	SPE
Exposures	1000	4000	1000	4000	1000	4000
Error Ring1 (%)	0.00	0.00	0.00	0.00	7.10	< 0.05
Error Ring2 (%)	0.00	0.00	0.00	0.00	51.20	< 0.05
Background (Cu Kα counts)	10.48	43.45	4.86	40.93	1.21	14.27
Background error (Cu Kα counts)	3.82	8.18	1.85	8.27	1.10	5.33
SNR	91.76	168.89	192.51	167.4	N/A	264.7

Table 5.2: Summary of results comparing NPE and SPE techniques (SNR was calculated using equation 5.18)

5.5 Image Smearing Effects with XRPD

5.5.1 Frame Transfer

The CCD30-11 is a full frame device without a shutter and therefore experiences image smearing. As each column is sequentially amplified, the signal in the image section awaiting readout collects more X-rays. During readout, *Iø2* is held at a positive potential to hold the signal data. Since a positive gate voltage is applied to this electrode, a depletion region forms underneath *Iø2*, similar to the integration period. This results in incoming X-rays generating signal data that is collected in the potential well of *Iø2*, which already contains signal data from the integration period. The resulting image is therefore corrupted by 'smear'. The time taken to readout a full frame CCD T_{Ro}, can be expressed as:

$$T_{Ro} = \left(f_S^{-1} \times N_R \times N_C\right) + \left(N_R \times f_P^{-1}\right), \tag{5.4}$$

where f_S^{-1} is the time taken to readout one pixel of the serial register and f_P^{-1} is the time taken to transfer one column in the serial register. The readout of a full frame

device is carried out sequentially, where the first bracketed term in equation 5.4 is followed by the second bracketed term and repeated N_R times.

Figure 5.15 shows the effect of image smear on a NaCl diffraction ring. The CCD-Array was moved 25 mm off axis to accentuate the smearing effect (i.e. moved 25 mm in parallel with the incident X-ray beam). The exposure time of each frame is shown above the relevant image and the 'ratio' represents the ratio of integration to readout time.

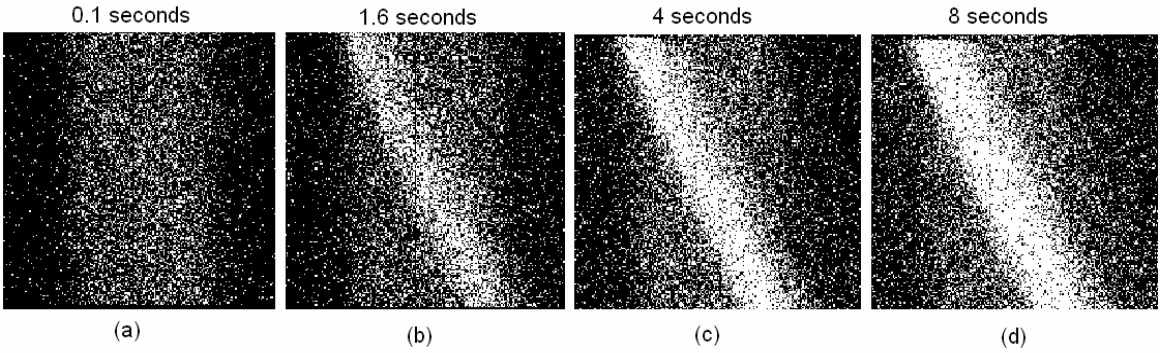

Figure 5.15: Effect of image smearing with increased integration time (readout time = 1.6 seconds). Figure 5.15 (a) ratio = 1:16 (b) ratio = 1:1 (c) ratio = 2.5:1 (d) ratio = 5:1

The data shown in figure 5.15 represents a total of 400 exposures. The CCD was operated without binning (256 × 1040 pixels) with each pixel in the serial register readout at ~ 165 kHz (~ 6 µsec). The parallel transfer speed for each pixel was ~ 75 kHz (~ 13.3 µsec). Using equation 5.4, the total readout time was calculated to be approximately 1.617 seconds. The amount of smear experienced is identical for all images, therefore as the exposure time is increased, the ratio of signal data to smear is increased.

Figure 5.16 shows the radial integration of the 1.6 s, 4 s and 8 s exposures shown in figure 5.15. Although the amount of smearing is identical, a minor increase in intensity in the smear regions is noticed with increasing exposure time. This is caused by an increase in elastic scattering because the smear region gathers more background Cu Kα events as the exposure time increases, but the amount of smearing is consistent for a fixed readout time.

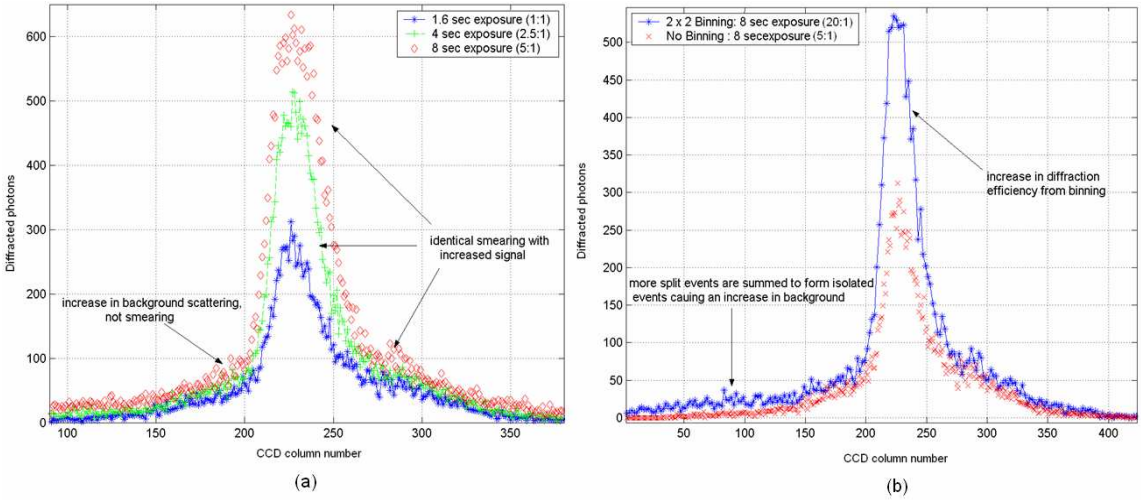

Figure 5.16: Effect of image smearing with (a) increased integration time and (b) CCD binning

For a full frame device, the amount of smearing generated in the image is related to the ratio of exposure time to readout time. For combined XRD/XRF applications, simply increasing the ratio of exposure to readout time can have detrimental effects for certain XRF applications. Increasing the exposure time causes an increase in leakage current, the extent of which depends on the operating mode of the device (AIMO vs. NIMO). Regardless of operating mode, increased integration times will cause a decrease in the energy resolution (FWHM) of X-ray peaks. This is a disadvantage to XRF applications where certain experiments require the highest possible energy resolution achievable by the detector. This is one of the drawbacks of using full frame devices (without shutters) for combined XRD/XRF applications. However, better performance can be achieved with on-chip binning. Figure 5.16 (b) shows a comparison of an 8 s integration time without binning and 2 × 2 binning. With 2 × 2 binning the readout time of the device is reduced by a factor of 4. The ratio of exposure time (8 s) to readout time increases from 5:1, to 20:1. Operating the CCD with pixel binning however, causes a larger increase in dark current for a given exposure time in comparison to full imaging mode. A loss in spatial resolution is also experienced but few XRD experiments are limited by the CCD resolution.

Image smear can be reduced in full frame devices but at the cost of energy and spatial resolution. The solution to reducing smear to acceptable levels and maintaining the integrity of energy and spatial resolution is to use full frame CCDs with electronic/mechanical shutters, or to operate the full frame device in pseudo frame

transfer mode. The next section explores this device process by simulating a frame transfer device using the full frame CCD30-11.

5.5.2 Full Frame vs. Frame Transfer

Figure 5.17 shows the geometry of the XRPD ring in relation to the CCD for the images shown in figure 5.15. To simulate a frame transfer device, a 1 mm thick sheet of stainless steel was glued over the lower half rows of the CCD imaging area (closest to the serial register). The only smear experienced in frame transfer CCDs occurs during the transfer of signal data from the image to store section. Assuming the device contains 256 pixels in the image and store region, the amount of smear time would be reduced from 1.617 s (full frame) to 3.4 ms with a parallel transfer speed of 75 kHz per pixel. Using the frame transfer architecture allows the impact of smearing to be practically eliminated.

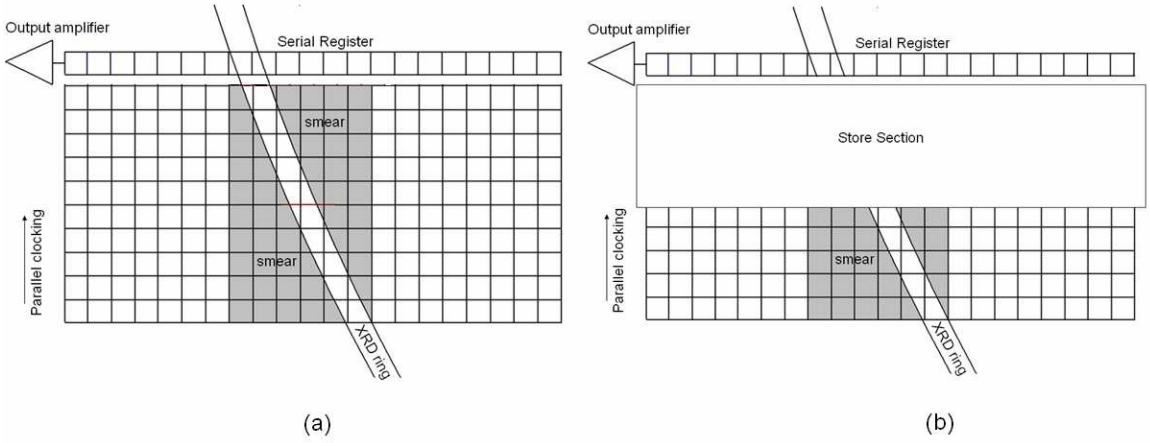

Figure 5.17: Architecture of a (a) full frame device in comparison to (b) frame transfer device. The grey shading represents the smearing caused from the additional integration of the diffraction ring during readout

Under frame transfer operation, the CCD was sequenced to perform 128 parallel transfers, to move the image into the store section and then begin readout. This would prevent any smear from taking place during the readout of the device as the signal data would be shielded from the XRPD ring. An exposure time of 8 s was used and 400 exposures were collected. The comparison to a full frame exposure of 8 s × 400 exposures is shown in figure 5.18. Only half of the image area was analysed in full frame mode, since the pseudo frame transfer imaging area was ~ 128 pixels.

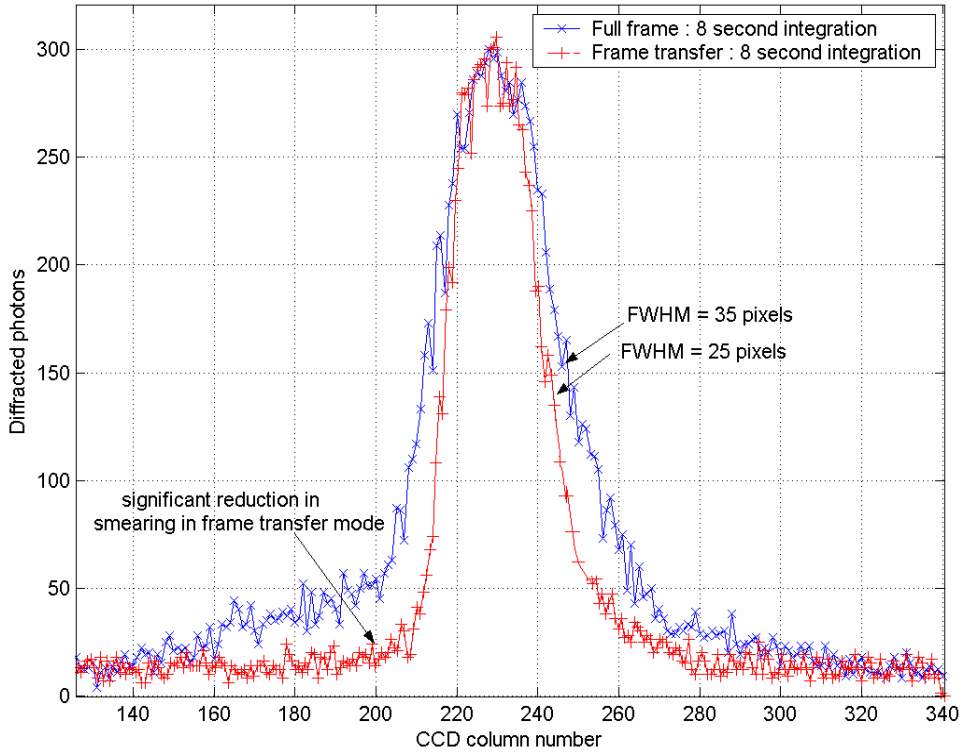

Figure 5.18: Comparison of an 8 s exposure using full frame and pseudo frame transfer architecture

The data shown in figure 5.18 shows a reduction in smearing using the pseudo frame transfer method. The FWHM has improved by 10 pixels (~ 0.12°). Using the CCD in frame transfer mode allows much shorter exposure times, which is essential for collecting combined XRD/XRF data.

5.5.3 Smearing with the CCD-Array

The fraction of the diffraction ring captured by the CCDs was limited by the width of the CCD imaging area (6.7 mm). Very small fractions of the diffraction rings were actually collected by the CCD-Array, which is why the rings seen in figure 5.10 resemble straight lines as opposed to curved rings. The effect of this is noticed at higher angles. For example, a diffraction ring located at the bottom of CCD 3 (~ 35°) will have a radius of approximately 106 mm. The percentage of the ring captured by the CCD is only 6.2%. The curvature of the rings is more noticeable at lower angles (< 10° 2θ), however low angle diffraction peaks are uncommon. Since the XRD data was orientated in a straight line and the smear also occurred in a straight line, the

smear simply added to the signal data. When low angle peaks were present, larger integration times were necessary to avoid smearing. However, since the majority of samples did not contain low angle peaks, the effect of image smear with the CCD-Array was negligible.

5.6 XRPD Modelling

This section describes the results from a modelling program designed to simulate the collection of XRPD data with CCD detectors. The overall aim of the modelling program is to allow users to understand the performance and limitations of CCDs in collecting XRPD data. The model also allows users to optimise CCD parameters in order to maximise the performance of the experiment for a given application. The motivations for the modelling program are summarised below:

Total X-ray events: Combined XRD/XRF data collection involves detecting isolated X-ray events and rejecting split events. For example, the strongest ZnO diffraction ring contains ~ 327 photon/s, localised across 28 × 256 pixels. Due to this high congestion of diffracted X-rays, it is impossible to analyse the ratio of isolated to split events in the diffraction ring from the experimental CCD images. Instead, the model is used to simulate the diffraction process and comparisons to experimental data are made in order to determine the total number of X-rays contained within the diffraction ring, as opposed to simply isolated events.

Optimisation of CCD exposure time: For XRF analysis the noise is a crucial factor in providing the best energy resolution possible. Since XRD analysis involves the processing of an image, the noise is not a performance limitation. Experiments that only involve XRD analysis can make use of longer integration times to collect more data at the expense of increased dark current. The model can be used to optimise the CCD integration time in order to collect the maximum number of isolated events based on diffraction efficiency. As more and more X-rays are collected inside the diffraction ring, a point is reached where the ring becomes too ‘crowded’ and split events begin to interfere with the recognition of isolated events. The efficiency of the CCD in detecting isolated events therefore begins to decay. The model is used to calculate the optimum integration time for each exposure based on the samples diffraction efficiency.

Pixel event statistics: The number of single isolated events peaks after a certain number of exposures and multiple isolated events become dominant. The modelling program can be used to understand the event statistics not just for a single exposure, but from exposure to exposure.

CCD Binning for XRD applications: Another benefit with using CCDs for XRD applications is the use of on-chip binning. Pixel binning (e.g. 2 × 2 binning) can increase single photon counting efficiency as 2 × 1 and 2 × 2 split events are summed to form single pixel events. Binning also greatly reduces the readout time of the device (e.g. in 2 × 2 binning mode the readout time is reduced from 1.6 s to 0.4 s). By modelling the effect of CCD binning in collecting XRD data, it is shown how binning can improve the data collection process.

Background noise: The background noise in an XRD pattern can easily be modelled by randomly scattering Cu Kα photons across the CCD image area. By simulating the noise, the amount of CCD exposures required to reduce the error in the noise and resolve low intensity diffraction peaks can be predicted.

5.6.1 Cu Kα X-ray Interactions in the CCD30-11

During XRD analysis the only X-ray energy of interest is the strong characteristic Cu Kα X-rays (8047 eV) produced by the Bede micro-source. This section investigates the ability of the CCD30-11 to detect these photons and how these interactions can be modelled by computer simulations. The probability that an X-ray of energy *E*, will interact at a depth *z*, is given by:

$$P(Z) = P(0)\exp\left(-\frac{z}{\lambda_z}\right), \tag{5.5}$$

where λ_Z is the linear attenuation coefficient for an X-ray with energy *E* in Si. The depletion depth of the CCD30-11 under standard biasing conditions is approximately 12 µm. The transmission of Cu Kα (8047eV) X-rays in Si is shown in figure 5.19. The probability of producing an isolated X-ray event at a given depth into the Si is also shown, which has been calculated by the simulations described in Section 5.2.

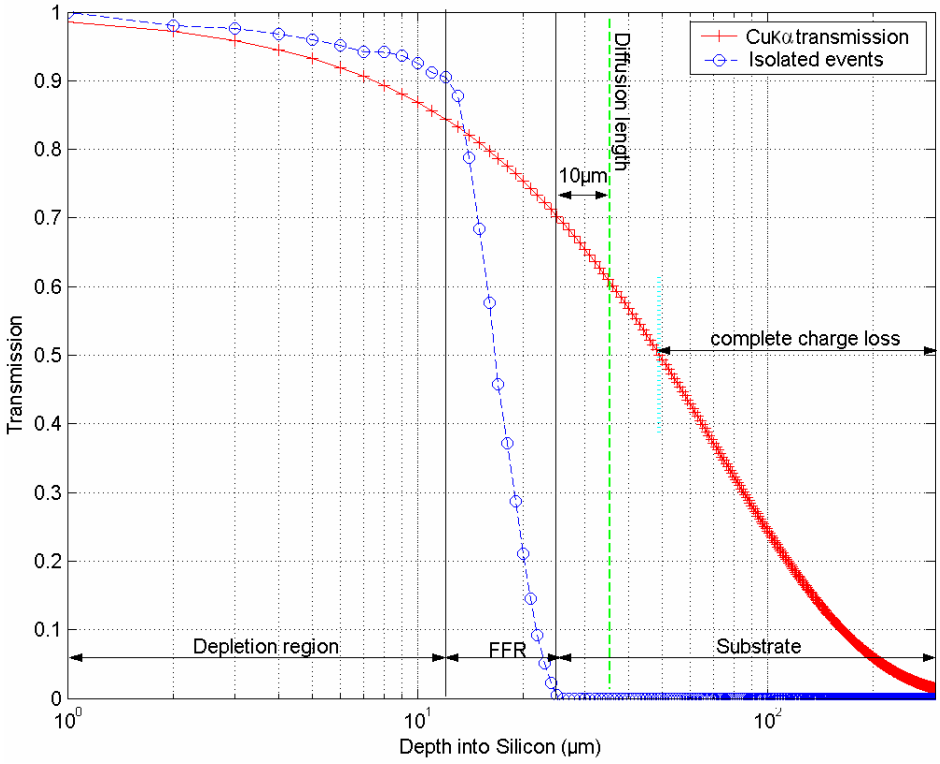

Figure 5.19: Transmission of Cu Kα X-rays through the CCD30-11

Only ~ 16% of Cu Kα X-rays are absorbed within the CCD's depletion region and ~ 30% are detected within the epitaxial region. Approximately 70% of the events are absorbed in the substrate region, which will result in charge diffusion and charge loss. Assuming an X-ray has been absorbed in the field free region at a depth *z*, the amount of charge reaching the depletion layer boundary Q_{ffr}, can be expressed as [Holland 1990]:

$$Q_{ffr} = Q_{total}\left[\frac{\exp\left(\frac{Z_{ffr}-z}{L_{ffr}}\right)+\exp\left(\frac{-Z_{ffr}-z}{L_{ffr}}\right)}{\exp\left(\frac{Z_{ffr}}{L_{ffr}}\right)+\exp\left(-\frac{Z_{ffr}}{L_{ffr}}\right)}\right], \tag{5.6}$$

where L_{ffr} represents the diffusion length in the field free region. The diffusion length is the length at which 68% of the charge carriers have recombined. The diffusion length, L_n, can be calculated using the expression [Sparkes 1994]:

$$L_n = \sqrt{D_n \tau_e}\ , \tag{5.7}$$

where τ_e is the recombination lifetime of the electron (s) and D_n is the diffusion coefficient. For a p-type doping concentration (N_a) of 1.25×10^{14} cm^{-3}, τ_e is approximately 0.0003 seconds [Tyagi & Overstraeten 1983]. The value of D_n depends on the electron mobility which is 1500 cm^2 V^{-1} s^{-1} for a doping concentration of 1.25×10^{14} cm^{-3}. Using equation 5.7, the diffusion length in the field free region of the CCD30-11 was calculated to be ~ 1000 µm. Since $L_{ffr} >> Z_{ffr}$, charge loss in the field free region can be ignored. Assuming the X-ray has been absorbed in the substrate, the amount of charge reaching the epitaxial layer boundary can be expressed as:

$$Q_{Total} = Q_o \exp\left(-\frac{z}{L_{sub}}\right). \tag{5.8}$$

Due to an increase in doping (p^+), the diffusion length in the substrate L_{sub}, reduces to ~ 10 µm (N_a = 1.25×10^{18} cm^{-3}), which occurs at a depth of 35 µm into the Si ($Z_d + Z_{ffr} + L_{sub}$). Therefore, over 99% of the charge reaching the potential well is lost when X-rays interact at a depth greater than ~ 50 µm in the Si. Since ~ 50% of the Cu Kα X-rays interact at a depth greater than 50 µm, 50% of the Cu Kα incident X-rays will be lost due to recombination. If an X-ray interacts at a depth > 50 µm, the software does not process the event. X-rays which interact at $Z_{ffr} > z < 50$ µm will form split events and experience charge loss. Unlike split events that occur in the epitaxial region, these events cannot be summed to reform the original X-ray energy. The 1σ cloud radius of X-rays absorbed in the substrate, r_{sub}, can be calculated using the expression [Holland 1990]:

$$r_{sub} = \frac{L_{sub}}{2.2}\sqrt{1-\left(\frac{z}{L_{sub}}\right)^2}\ . \tag{5.9}$$

The size of the charge cloud reaching the n-type buried channel includes additional spreading in the field free and depletion region and can be expressed as:

$$R = \sqrt{R_i^{\,2} + R_d^{\,2} + R_{ffr}^{\,2} + R_{sub}^{\,2}}\ . \tag{5.10}$$

The result is that out of the total Cu Kα X-rays incident on the detector surface, 30% of these events will interact in the epitaxial region and 70% will interact in the

substrate. Out of the 30% of X-rays that ionise in the epitaxial layer, ~ 20% will form isolated events. Out of the 70% of X-rays that ionise in the substrate, ~ 20% will form split events with charge loss and 50% will be completely lost due to recombination. It should be noted that the substrate region is purposely very highly doped to ensure photo-generated charge is greatly reduced when X-rays interact in this region. The substrate is therefore a 'dead region' and the performance of the device is based on the epitaxial layer. The interaction of Cu Kα X-rays in the CCD30-11 is simulated exactly as described in Section 5.2, with the additional introduction of charge loss in the substrate. To summarise, 20% of the Cu Kα X-rays will form isolated events, 10% will form split events without charge loss, 20% will form split events with charge loss and 50% will be lost to recombination. The overall performance of the CCD30-11 in detecting isolated Cu Kα X-rays is poor, since the epitaxial region is small (25 µm).

5.6.2 Peak Shapes and Counting Statistics

The profile of 2 $CaCO_3$ XRD peaks is shown in figure 5.20 (a). The diffraction rings have been accurately modelled using Gaussian peak shapes, therefore the peak mean, FWHM and amplitude can be accurately extracted from the fit. The parallel beams produced by the XOS optic result in very symmetrical diffraction peaks, leading to high quality fits with Gaussian models.

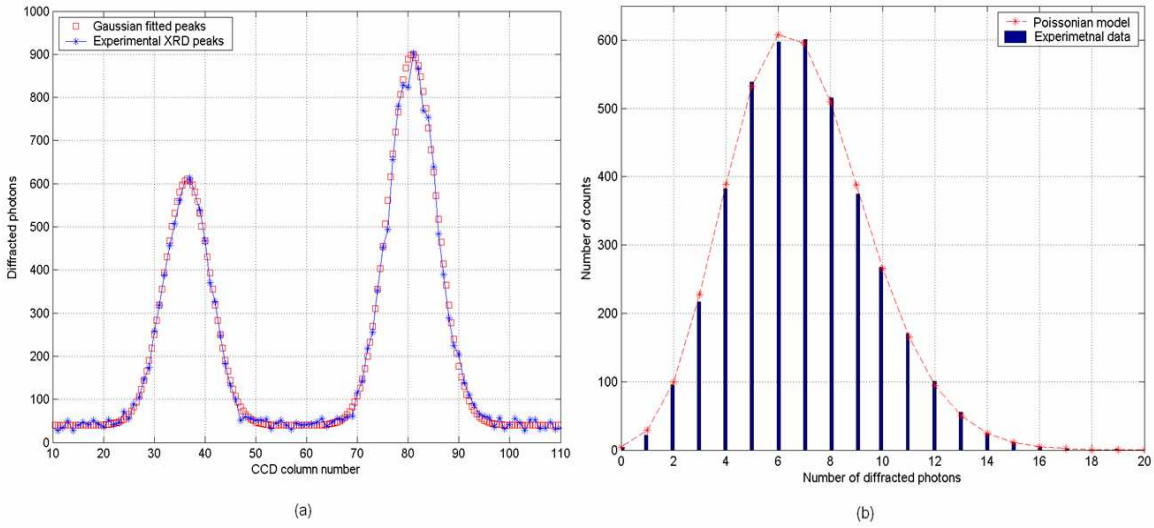

Figure 5.20: (a) XRD rings of $CaCO_3$ fitted using Gaussian peak shapes and (b) the number of diffracted events detected in 1 s exposures, over the period of 1 hour

Figure 5.20 (b) shows the number of events collected in 1 s exposures, over the period of one hour for the $CaCO_3$ peak located at CCD column number 37 in figure 5.20 (a). The mean number of events collected by the detector was 6.86 Cu Kα photons /s with an error of 2.6 Cu Kα photons/s. The number of diffracted photons collected in a given time interval can be accurately modelled using a Poissonian distribution, with an error given by the square root of the mean number of counts.

5.6.3 Model Operation

This section describes the operation of the modelling program used for simulating XPRD data using CCDs. A model of the strongest peak in ZnO (101 reflection) is used as an example throughout this section. The ZnO XRD data was collected under standard operating conditions with R_{sd} = 30 mm. The initial stage involves fitting the ZnO peak with a Gaussian function as shown in figure 5.20 (a). The 3 parameters extracted from the fit are the 2θ location of the peak (36.25°), the FWHM of the peak (0.13°) and the most important parameter, the integrated intensity of the peak (27.88 Cu Kα photons/s). This represents the number of isolated Cu Kα events collected per second. The main input parameters required for the simulation are listed in table 5.3.

Parameter	Explanation
Peak mean	2θ diffraction location
P_I	Number of isolated diffraction events/exposure
Peak FWHM	FWHM of XRD peak
X-ray energy	Energy of diffracted X-rays
λ_E	Linear attenuation coefficient of incident X-rays in Si
CCD binning mode / pixel size	Binning mode of CCD and pixel size
N_{Exp}	Total number of exposures to simulate
N_{bck}	Total number of background events/s
I_d	CCD dark current
σ_{RN}	CCD readout noise
Z_d	Depletion depth
Z_{ffr}	Field free region depth
Z_{sub}	Substrate region depth
L_{sub}	Diffusion length in substrate
N_a	p channel doping concentration

Table 5.3: Summary of the main input parameters required for simulation

Since the detectors are tiled along the measuring circle, the parallel beams diffracted from the sample are detected orthogonally by the CCDs. The simulation therefore assumes all diffracted X-rays are detected at an angle of 90°. The model begins by distributing Cu Kα photons in a Gaussian distribution in the horizontal direction and

randomly in the vertical direction, as shown in (figure 5.21 (a)). The number of diffracted photons simulated in each exposure is calculated from a Poissonian distribution with a mean P_{I+S+Cl}, where P_{I+S+Cl} is the total number of diffracted photons incident over the diffraction ring in each exposure. Figure 5.21 (b) shows the different types of electron-hole clouds formed by the Cu Kα photons interacting at different depths in the Si. During each exposure, N_{bck} X-rays are randomly scattered across the entire CCD imaging area. Once the diffracted/background X-ray positions have been simulated, the program determines the fraction of charge in each pixel. Each pixel is also assigned a dark current and readout noise value selected from a Poissonian distribution with mean I_d and Gaussian distribution with an error σ_{RN} respectively. A digitised image is then generated (figure 5.21 (c)) and the single photon counting technique is applied by rejecting split events from each exposure. The simulation is run for N_{Exp} exposures and the energy discriminated images are combined. The final image generated is an array of numbers representing the number of isolated diffracted photons collected in each pixel over N_{Exp} exposures. Figure 5.21 shows 3 screenshots of the program simulating the ZnO diffraction ring.

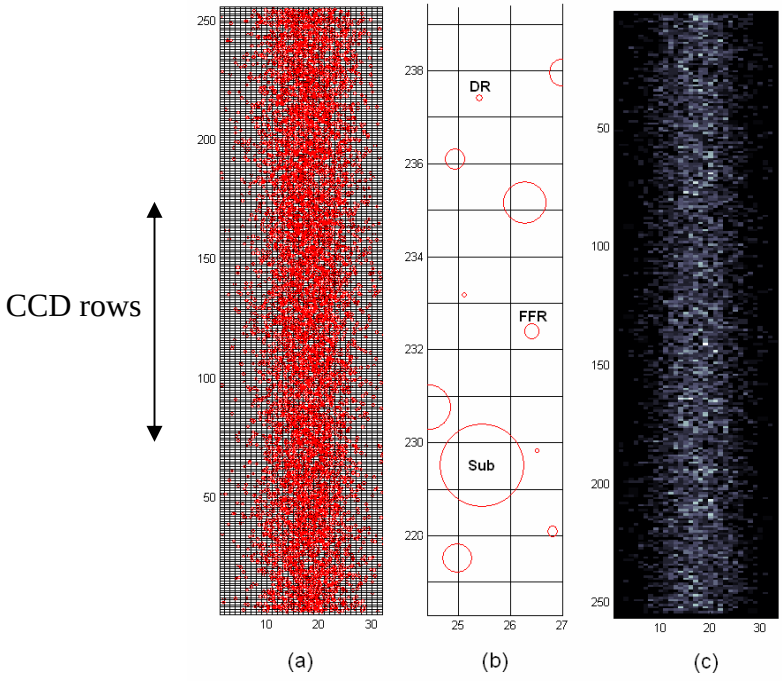

Figure 5.21: (a) Distribution of simulated photons inside diffraction ring of ZnO (b) electron-hole clouds being produced at different interaction depths (DR= depletion region, FFR = field free region, Sub = substrate) and (c) digitised image of the diffraction ring

5.6.4 Chi-Squared Goodness of Fit

In order to determine the quality of fit between the simulated and experimental data, a chi-squared (χ^2) goodness of fit test was used. The χ^2 test can be used to determine if sets of data are 'statistically significant', at a certain significance level, α_{sig}, also known as the confidence level (1 - α_{sig}). For example, if the data sets are found to be statistically significance when α_{sig} is 0.05, this means there is only a 5% chance the agreement occurred by chance. The χ^2 value can be calculated using the expression:

$$\chi^2 = \sum_{i=1}^{N_x} \frac{(Obs_i - Exp_i)^2}{Exp_i}, \tag{5.11}$$

where Obs_i is the experimental observation at data point i, Exp_i is the simulated value at data point i, and N_x is the number of samples tested. The agreement between the data sets is found to statistically significant when the χ^2 value is less than the critical Chi value, χ_{crit}. The χ_{crit} value can be determined from the Chi-squared distribution table based on α_{sig} and the degrees of freedom (*dof*). The *dof* can be calculated using the expression:

$$dof = N_x - p_{rm} - 1, \tag{5.12}$$

where P_{rm} is the number of parameters used to generate the simulated model (e.g. P_{rm} is 3 for a Gaussian distribution). The next section presents results from the modelling program and highlights the agreement between the simulated and experimental data for the ZnO powder sample.

5.6.5 Simulation Results

5.6.5.1 Total Events – Splits + Isolated

The ZnO peak (101 reflection) consisted of 27.88 isolated counts per exposure (1 s each) within a 28 pixels wide (± 3 standard deviations) diffraction ring. The total number of X-rays distributed over the diffraction ring per second is denoted by P_{I+S+Cl}, which represents the isolated events (P_I), split events (P_S) and events lost to recombination (P_{Cl}). Since 50% of these events are lost to recombination, P_{I+S} represents the number of detected events (isolated and split). After P_{I+S+Cl} photons are

distributed across the diffraction ring, the total number of isolated events within the ring P_I, is calculated. The total number of events can be expressed as:

$$P_{I+S+Cl} = P_I \times T_{ml} \,, \tag{5.13}$$

where T_{ml} is the multiplication factor and from the discussion presented in Section 5.6.1, was expected to be ~ 5. Therefore, if P_I was 27.88 Cu Kα photons/s, P_{I+S+CL} was expected to be ~ 139. The simulation distributed 139 photons across the ZnO diffraction ring each exposure. The simulation was repeated for 500 exposures in full imaging mode (256 × 1040 pixels). All input parameters used in the simulation were derived from the process involved in collecting the experimental ZnO data. Figure 5.22 shows the results from the simulation.

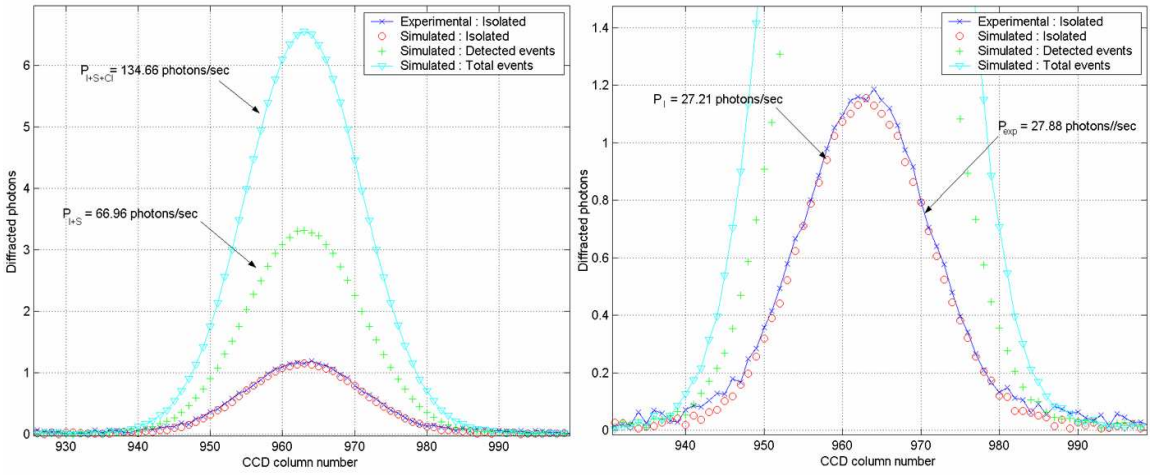

Figure 5.22: Simulation of ZnO diffraction ring revealing the total number of incident X-rays on the detector surface

The best fit to the experimental data was found at P_{I+S+Cl} = 134.66 Cu Kα photons/s, resulting in a multiplication factor of ~ 4.94. The number of isolated events P_I, generated through the simulation was 27.21 Cu Kα photons/s, which is in very good agreement with the observed data. Figure 5.22 also shows the number of detected events P_{I+S}, which is ~ 50% of P_{I+S+Cl}.

5.6.5.2 Optimisation of CCD Integration Time

As the exposure time is increased, the diffraction ring becomes congested with events and the detection of isolated X-rays begins to decay. The rate of this decay is dependant on the diffraction efficiency of the sample and the number of pixels the

ring occupies. Figure 5.23 highlights the effect of increased exposure time in collecting single pixel events. A single pixel event contains a value greater than the noise threshold with 4 neighbouring pixels having a charge less than the noise threshold. This is shown by blue spots in figure 5.23 (a). When the pixels are congested with events, as shown in figure 5.23 (b), the probability of producing an isolated event decreases. For XRD applications, the CCD exposure time can be increased to find the optimum time at which isolated events within the ring are at a maximum. This section aims to calculate this point through simulations and make comparisons to experimental data.

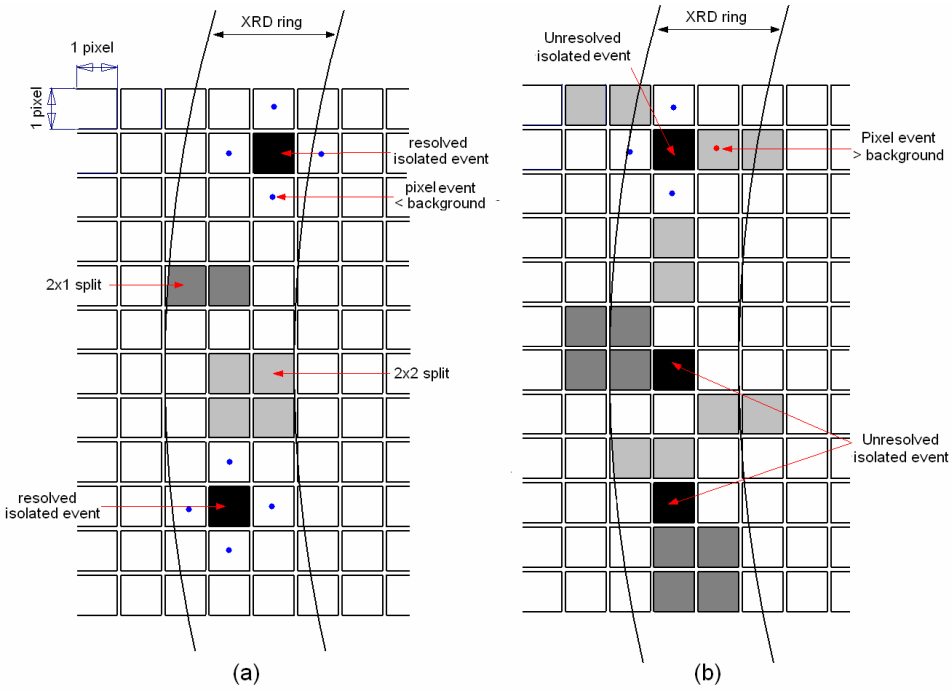

Figure 5.23: (a) Sparsely populated events inside diffraction ring and (b) congestion of events resulting in unresolved isolated events

Figure 5.23 (b) shows the difference between 'unresolved' and 'resolved' isolated events. An unresolved isolated event occurs when the pixel's charge is confined to a single pixel but the neighbouring pixels also contain charge above the noise threshold, usually due to overcrowding of events. An unresolved isolated event is therefore not detected by the energy discrimination process and is lost. A 'resolved' isolated event represents an event that has been successfully detected as an isolated event, as the neighbouring pixels have a charge less than the background threshold. The relationship between 'unresolved' and 'resolved' isolated events is simulated and presented in Section 5.6.5.5.

The ZnO ring was located across 0.33°, which results in a total of 7,168 available pixels (256 × 28 pixels). Since approximately 9 pixels are required to detect an isolated event, the maximum number of isolated events that can be detected is ~ 800. However, since the majority of events within the ring will form split events, the maximum number of isolated events was expected to be much lower than 800. According to the simulation, ~ 135 Cu Kα photons are incident on the CCD per second, as calculated in the previous section. The model distributes 135 photons/s over the diffraction ring, calculates P_I (already calculated to be approximately 27.21) and increments the CCD exposure time. During a CCD exposure of 2 s, 270 Cu Kα photons (135 counts/s × 2 s) are distributed across the ring and P_I is re-calculated. It is important to remember that 50% of the incident photons are lost to recombination, therefore only ~ 68 (135/2) events are produced in each exposure. The aim of the experiment was to determine the optimum CCD exposure time that produced the maximum number of isolated events. Figure 5.24 shows the results of the simulation.

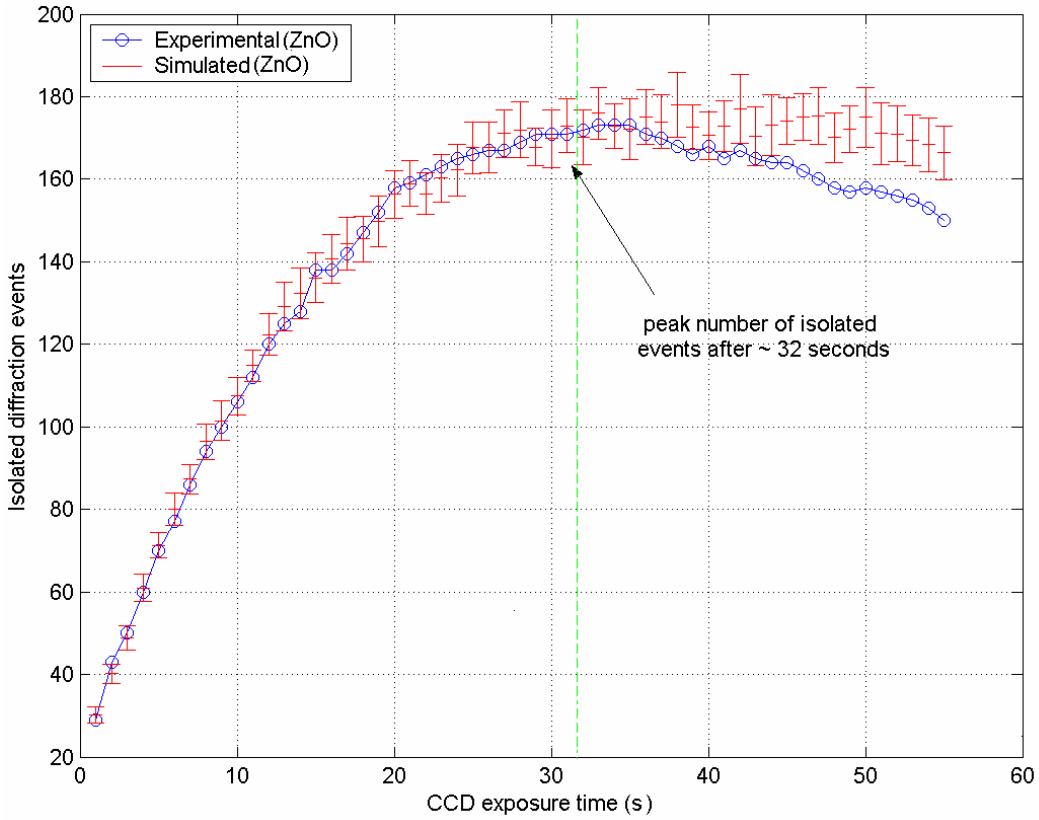

Figure 5.24: Variation in isolated events in ZnO diffraction ring with increasing CCD exposure time – experimental vs. simulated

After ~ 32 seconds of exposure time, the number of isolated events inside the ring peaks and a total of 2,176 events (68 photons/s × 32) have saturated the available 7,168 pixels. The number of isolated events then begins to decay as overcrowding of events becomes dominant. The simulation is in good agreement with the experimental data for exposure times < 34 seconds, with a confidence level of 97.1%, determined with the χ^2 test. Figure 5.25 shows a possible reason for the disagreement for exposure times > 34 seconds.

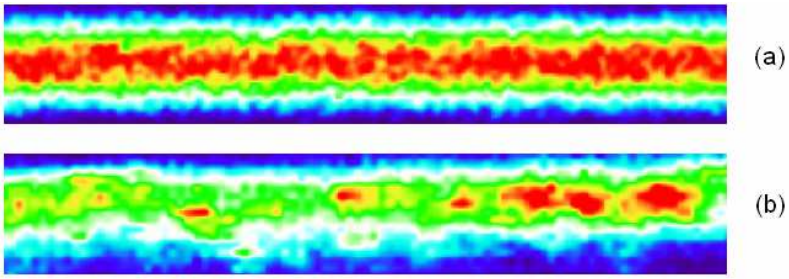

Figure 5.25: (a) Simulated image of ZnO diffraction ring with even distribution and (b) experimental image of ZnO peak displaying some preferred orientation

Figure 5.25 (a) and (b) show the simulated and experimental images of the ZnO diffraction ring respectively. The contrast of these images has been adjusted to enhance the regions of maximum intensity. Due to preferred orientation in powder samples, the distribution of photons in the experimental images is more like that seen in figure 5.25 (b). Since some grains in the ZnO powder sample are more orientated than others, particular regions of the diffraction ring experience a higher flux of diffracted X-rays. These regions become saturated with events (reducing the number of detected isolated events) whilst other regions receive a much lower flux of diffracted events. This is a possible reason for the disagreement between the model and experimental data, as the model assumes a perfectly Gaussian distribution of events inside the ring. However, the model still accurately predicts the point at which the isolated events peak. Using the model, the optimised exposure time for any sample can be calculated prior to data collection. Figure 5.26 shows the results of modelling samples with varying diffraction efficiencies over a 0.33° wide (± 3 standard deviations) XRD ring.

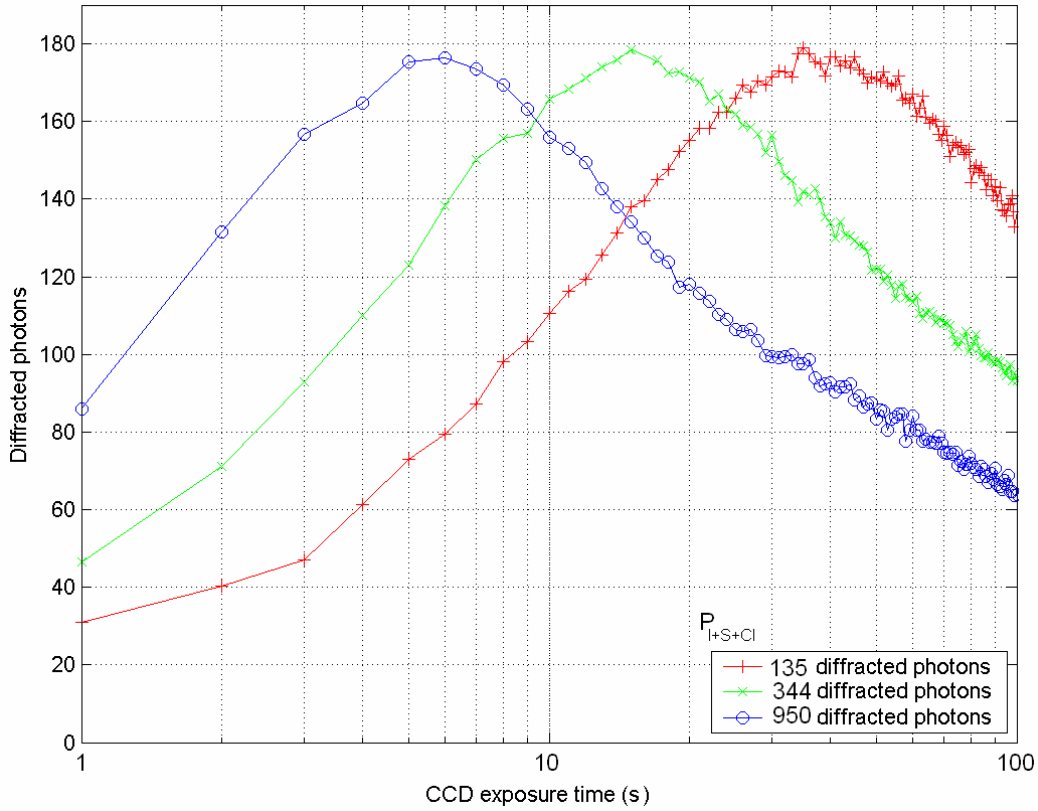

Figure 5.26: Diffraction efficiency vs. optimum CCD integration time over a 0.33° wide diffraction ring

The simulation clearly illustrates that as the diffraction efficiency increases, the CCD must be integrated for shorter periods because the higher flux of X-rays causes more interference with detecting isolated events. The model can be used to estimate the optimum time (τ_{opt}) to integrate the CCD in order to collect the maximum number of single pixel events for a given diffraction efficiency (P_{I+S+Cl}). For a 0.33° wide diffraction ring (± 3 standard deviations), τ_{opt} can be expressed as:

$$\tau_{opt} = 4137.8\left((P_{I+S+Cl})^{-0.9935}\right). \tag{5.14}$$

5.6.5.3 XRD Pixel Events

The previous section has discussed the detection of isolated events in a single CCD exposure. This section describes the variation in pixel events from exposure to exposure. During the energy discrimination of each exposure, each pixel (where an isolated Cu Kα photon is detected) is incremented by one. In the example of ZnO, this is applied to all 1000 exposures yielding an image where each pixel contains N

events. The modelling of post energy discriminated exposures is relatively simple compared to the simulation shown in figure 5.24. Out of the 7,168 available pixels in the ZnO ring, ~ 27 of these pixels are incremented by 1 each second (the number of events detected in each exposure has a Poissonian distribution with an error given by equation 2.15). As the exposures are increased, the probability of an event being detected in a previously filled pixel increases. Approximately 68% of the events are localised within 1 standard deviation of the mean, therefore multiple isolated events are more likely to occur in these regions. Figure 5.27 shows the progression of multiple single pixel events in the ZnO ring over 1000 exposures. The simulation shows a very good agreement to the experimental data, with an average confidence level of 95.6%, determined using the χ^2 test.

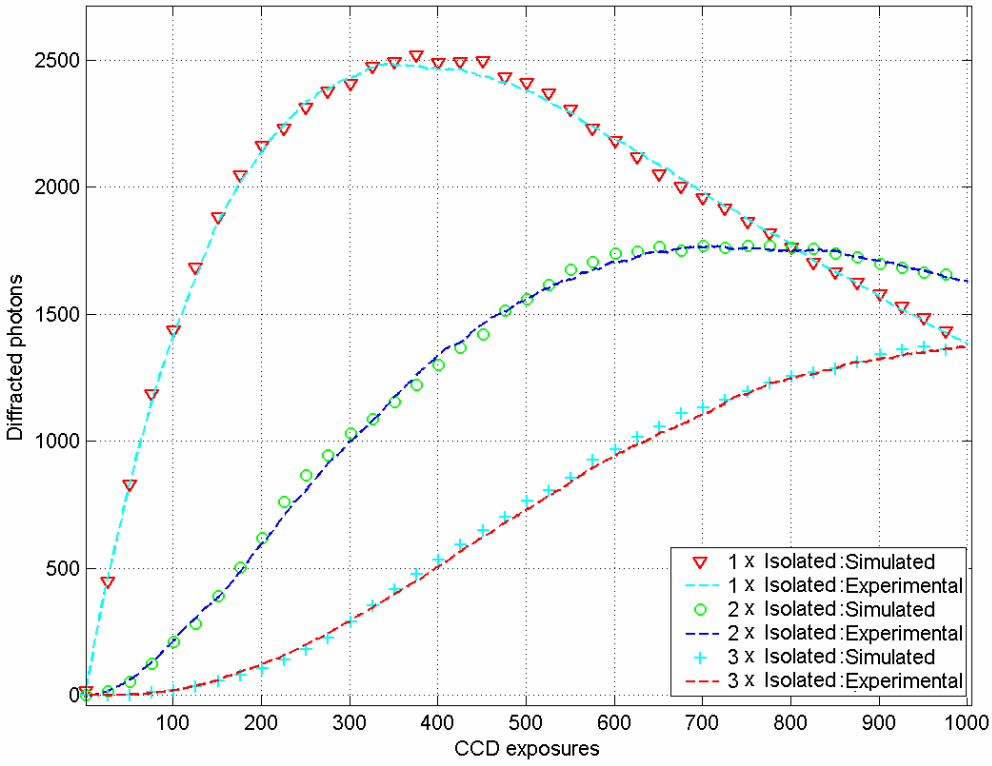

Figure 5.27: Progression of multiple single pixel events in a ZnO XRD peak (101 reflection) over 1000 exposures – experimental vs. simulated

5.6.5.4 CCD Binning Effects

Binning a CCD image involves summing numerous pixels, which results in an increase in isolated events but causes a loss in spatial resolution. For example, 2 × 2

binning of the CCD image quadruples the size of each pixel whilst maintaining the size of the charge cloud generated by each X-ray photon. Split events that are noticed without binning are now summed to form single pixel events. Although binning causes an increase in single pixel events, the number of available pixels is greatly reduced. In the ZnO example, the number of available pixels within the diffraction ring reduces from 7,168 in full imaging mode to 1,792 pixels in 2 × 2 binning mode.

Figure 5.28 (a) and (b) show the results from a simulation comparing the isolated event efficiency for a normal and 2 × 2 binned CCD image for a total of 68 and 386 detected events (P_{I+S}) per second respectively. The simulation with 68 detected photons represents the ZnO peak used in previous examples and is distributed over a 0.33° wide diffraction ring. The benefit of binning is evident from figure 5.28 (a), as an increase of ~ 11 isolated Cu Kα photons is seen in 2 × 2 binning mode. The ratio of resolved to unresolved isolated events is similar, as events are sparsely populated across the CCD and congestion of events is limited. With 386 detected events, binning becomes a disadvantage as overcrowding of events begins to interfere with the detection of single pixel events. The ratio of resolved to unresolved isolated events is also seen to decrease due to this effect.

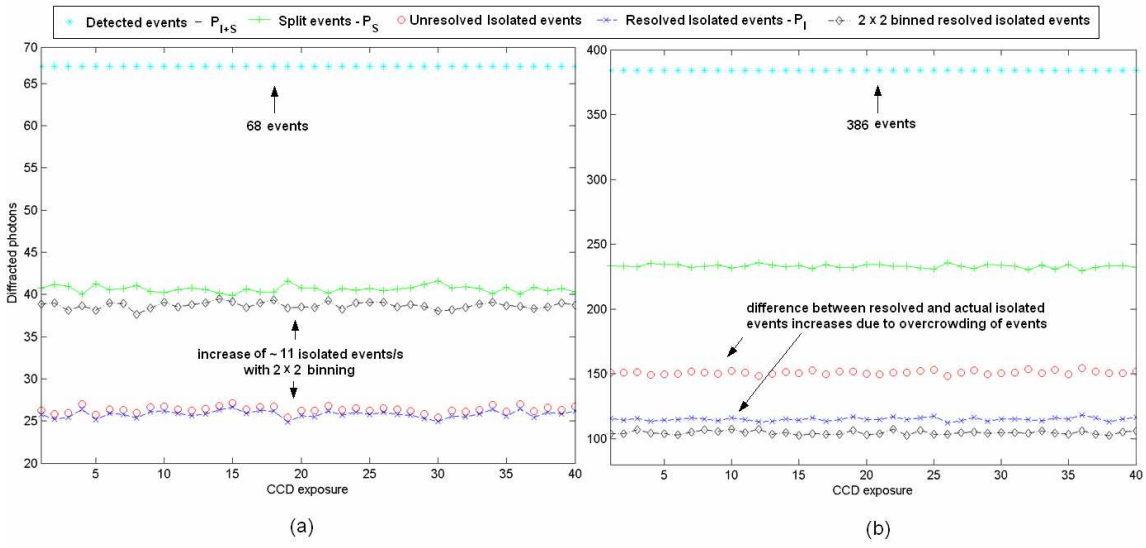

Figure 5.28: Comparison of isolated event efficiency for 1 × 1 and 2 × 2 binned images with (a) 68 and (b) 386 detected events

The majority of samples used in testing the CCD-Array produce less than ~ 250 detected events per second. The simulations highlight the fact that it is more

beneficial to operate the CCD in 2 × 2 binning mode as opposed to full imaging mode for the majority of applications. The readout time of the device is reduced from 1.6 to 0.4 seconds and more single pixel events are detected. The reduction in spatial resolution is irrelevant as the width of diffraction peaks in PB geometry is much greater than the spatial resolution of the CCD. The increase in dark current in binning mode is also irrelevant for reasons discussed in the next chapter.

5.6.5.5 XRD Background Noise

The simulation of XRD background noise involves the random scattering of Cu Kα photons across the CCD image area. For the majority of samples used for testing the CCD-Array, scattered background events (B_I) range from 5 − 75 events/s. This represents single pixel events therefore the total number of background events (B_{I+S+Cl}) incident on the detector surface is usually 25 − 375. Since the scattering of these background events is random, the mean noise level in the diffraction pattern (π_{xrd}) can be expressed as:

$$\pi_{xrd} = \frac{B_I}{N_c}, \tag{5.15}$$

where N_c is the number of columns in the CCD image (which depends on the CCD binning mode). For the ZnO example, the mean background level in the diffraction pattern was found to be 0.054 Cu Kα photons/s. The data was collected without binning (N_c = 1024), therefore re-arranging equation 5.15, the number of isolated Cu Kα background events incident on the CCD per second was calculated to be ~ 55.

The modelling program can be used to understand the error associated with the background noise with respect to increasing CCD exposures. Figure 5.29 shows π_{xrd} and the variation in the associated error σ_{xrd}, with increasing CCD exposures. The characteristics of the background noise are not influenced by any diffraction peaks. As stated in equation 5.15, π_{xrd} is dependant on B_I and N_c, whereas σ_{xrd} is determined by the number of CCD exposures. Many minerals and rocks contain diffraction peaks with very low intensities that are comparable to the mean level of the background noise. If σ_{xrd} is too high, such peaks are lost within the background noise and cannot be detected.

It is important at this stage to clarify the software process used in detecting an XRD peak. The aim of the peak-finding algorithm is to find any statistically significant events from the background noise, which has a Gaussian distribution with a mean π_{xrd} and standard deviation σ_{xrd}. This is performed using a 'Z test', which determines if the difference between an event and the noise mean is large enough to be statistically significant. The Z_{score} is determined using the expression:

$$Z_{score} = \frac{\pi_{event} - \pi_{xrd}}{\sigma_{xrd}}, \tag{5.16}$$

where π_{event} is the value of the event in question. The Z_{score} is then compared to a Z table, which contains the percent of area under the curve between π_{event} and π_{xrd}. Since XRD peaks are above the mean level of the noise, a one-tailed test is performed. For a significance level, α_{sig}, of 0.05, the Z_{score} must be greater than 1.64. The software calculates the Z_{score} of each count in the XRD pattern, then checks to see if N_{cnt} pixels are above α_{sig}. Since the standard width of XRD peak is ~ 40 – 50 pixels, N_{cnt} was pre-set to 15 pixels, although this was an adjustable parameter.

Consider a single exposure with the parameters given in table 5.4.

Parameter	Value	Units
N_{diff}	1	*counts/s*
B_I	55	*counts/s*
N_C	1024	*pixels*
π_{xrd}	0.05	*counts/s*
P_{xrd}	0.12	*counts/s*
α_{sig}	95	*%*
Z_{crit}	1.64	
N_{cnt}	15	*pixels*

Table 5.4: Summary of parameters used in simulation

For the parameters given in table 5.4, the software can be used to calculate how many CCD exposures are required to resolve the XRD peak, P_{xrd} (P_{xrd} has 1 diffracted photon/s). Figure 5.29 shows π_{xrd} and the reduction in σ_{xrd} with increasing exposure time for the parameters listed in table 5.4.

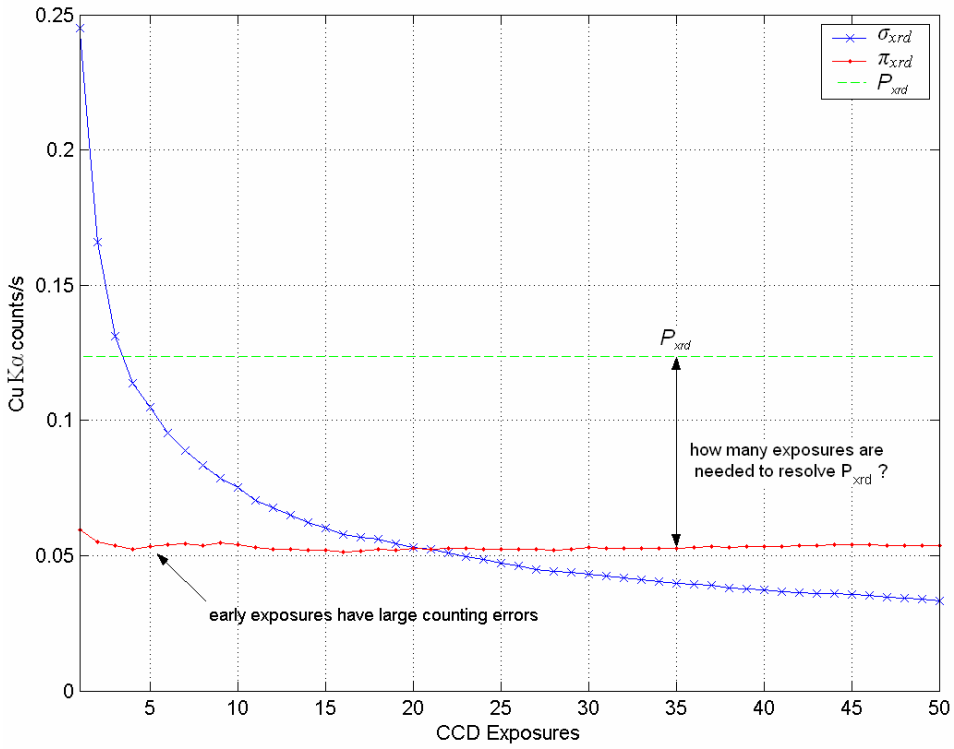

Figure 5.29: Variation of σ_{xrd} with respect to CCD exposures for the parameters listed in table 5.4

Figure 5.30 (a) and (b) show the effect of σ_{xrd} in detecting P_{xrd}, after 100 and 650 exposures respectively. After 650 CCD exposures, N_{cnt} pixels (located between pixel numbers 492 and 508) exceed a Z_{score} of 1.64, therefore these pixels are registered as containing statistically significant data (i.e. an XRD peak), at a 95% confidence level.

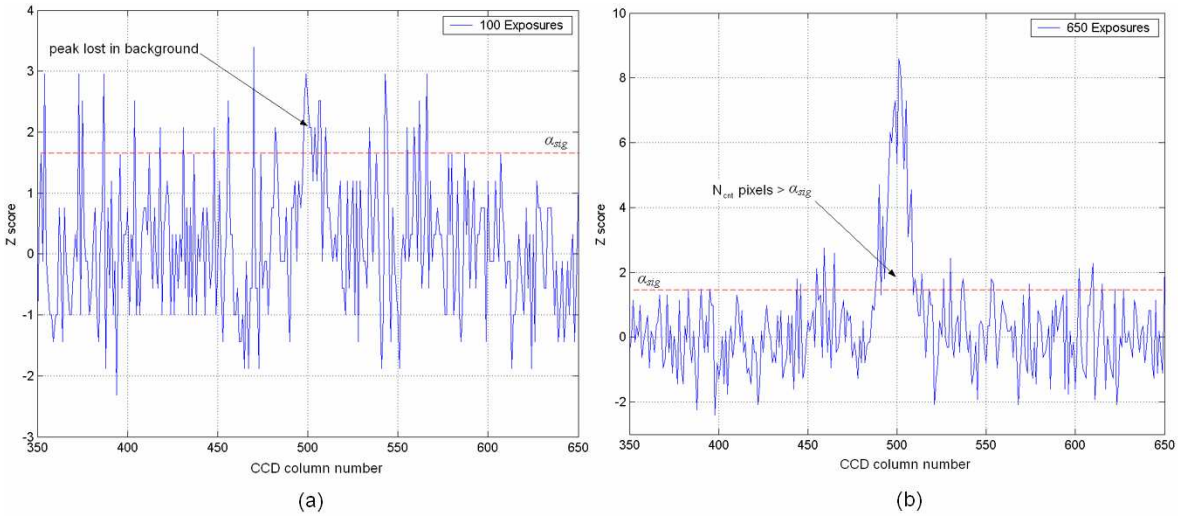

Figure 5.30: Simulated XRD pattern containing 55 background events and 1 diffracted photon after (a) 100 CCD exposures and (b) 650 CCD exposures.

If the number of background events is known prior to data collection, the modelling program can be used to calculate the minimum number of exposures required to resolve very low intensity peaks. The SNR of the diffraction pattern can be expressed as:

$$SNR_{xrd} = \frac{P_{xrd} - \pi_{xrd}}{\sigma_{xrd}}, \tag{5.17}$$

where P_{xrd} is the peak height of the XRD peak.

5.7 Discussion

This chapter has investigated the data collection and analysis of the XRPD technique using CCD detectors. The ability of the CCD30-11 to collect isolated X-ray events has been determined by depletion depth measurements, which conclude that the depletion region extends 12 µm into the Si epitaxial layer under standard biasing. Techniques in collecting combined XRD/XRF data have been highlighted and results have been presented. The different noise sources present in XRD patterns have been explained. A method of reducing elastic scattering noise in XRD patterns (SPE) has been presented and compared to existing techniques [Cornaby et al. 2000]. For shorter exposures, it was found that NPE was more effective at removing noise, with an improvement in SNR of ~ 100. For longer exposures, SPE was more productive at removing noise with a SNR of ~ 265 in comparison to ~ 167 for the NPE technique. The disadvantages of using full frame CCDs for XRD applications have been discussed and the advantages of using frame transfer devices have been highlighted. The final section of this chapter presented results from a novel modelling program designed to simulate the collection of XRPD data using CCD detectors. The model can be used to optimise the performance of the detector for different XRPD applications. Agreement between the model and experimental data has also been highlighted.

Chapter 6 : Operational Performance and Applications of the CCD-Array

6.1 Introduction

This chapter describes the operational performance of the CCD-Array. The initial section of this chapter examines the transmission of X-rays through the current test facility. All attenuation factors are calculated and the low energy detection limit of the CCD-Array is determined. The performance of the CCD30-11 in detecting soft X-rays is investigated by generating a response matrix. Different sample preparation issues experienced during testing of the CCD-Array are highlighted and the temperature and power required by the instrument to perform combined XRD/XRF analysis is presented. The use of the CCD-Array in different applications is discussed and optimisation of the geometry is suggested.

6.2 X-ray Transmission and Detection

The flux produced by the Bede micro-source with respect to tube voltage and current, has been calibrated in Chapter 2. At the standard operating power of 80 W (40 kV, 2 mA), the micro-source produced a flux of ~ 3×10^6 counts/s within a 150 µm spot. By knowing the flux incident on the sample and determining the attenuation factors of signal X-rays (characteristic and diffracted), it was possible to estimate the detection efficiency of X-rays ranging from 0.1 − 10 keV in the described experimental arrangement, with particular interest in the low energy response. The path of X-rays from the point of production in the Bede micro-source to detection by the CCD can be summarised as follows:

1. Continuous and characteristic Cu X-rays generated by Bede micro-source.

2. X-ray polycapillary optic greatly attenuates X-rays > 10 keV and focuses X-rays into a 1 mm low divergent beam (~ 0.2° FWHM).

3. A 15 µm Ni filter at the optic output, results in a 93% monochromatic beam of Cu Kα X-rays.

4. X-ray flux is reduced by 180 mm of air between optic and sample.

5. Incident X-rays are partly/fully absorbed in sample.
6. X-rays diffracted/fluoresced from sample based on sample's efficiency.
7. Signal X-rays attempting to escape the sample are partly/fully absorbed.
8. Flux of signal X-rays is reduced by 108 mm of air between sample and detector.
9. Signal X-rays are attenuated by 20/40 µm Mylar X-ray window.
10. Signal X-rays from 0.1 − 10 keV are detected based on the CCD's QE.

6.2.1 Sample Absorption

The signal X-rays produced by the incident radiation will be attenuated as they travel through the sample. The absorption of signal X-rays depends on the linear attenuation coefficient and thickness of the sample, T_{sp}. In the reflective XRD geometry, the attenuation of signal X-rays depends on the interaction depth. Photons emitted from the top surface of the sample experience little or no attenuation. The top surface of the sample also represents the maximum intensity of the irradiating beam. This is one of the major advantages of the reflective XRD geometry in comparison to the transmission geometry, since a high flux of characteristic X-rays can be generated on the detector side of the sample. X-rays that are emitted from inside the sample (as shown in figure 6.1) cannot escape if the emission depth is too high. E_d represents the maximum emission depth of a photon of a given energy and can be calculated based on the linear attenuation coefficient of the sample.

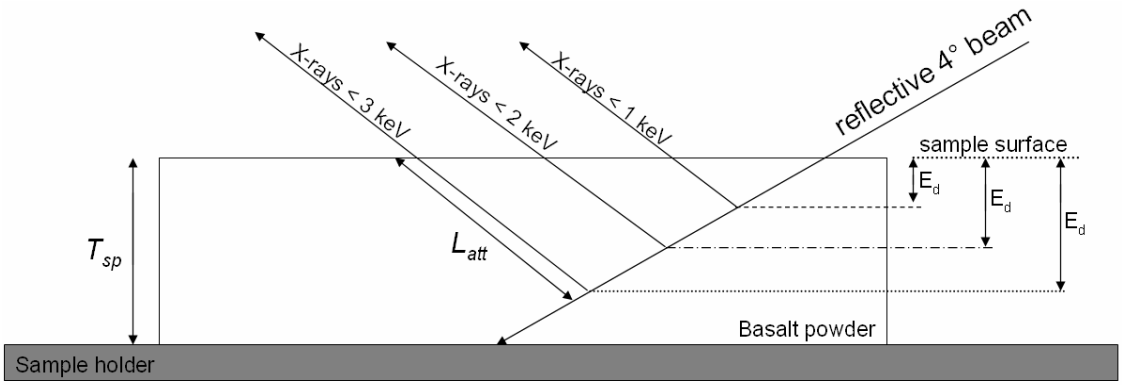

Figure 6.1: Maximum emission depth of signal X-rays in a basalt powder

The most common igneous rock found in Earths crust, basalt, is used as an example in this section. Igneous rocks are composed of approximately 9 primary oxides, which are Al_2O_3, CaO, Fe_2O_3, K_2O, MgO, Na_2O, P_2O_5, SiO_2 and TiO_2. By knowing the fractional weight of each of these oxides in the sample W_i, and the mass attenuation coefficients of the oxides [Henke et al. 1993], the overall mass attenuation coefficient can be calculated using the expression:

$$\frac{\mu}{p} = \sum_i W_i \left(\frac{\mu}{p} \right)_i . \tag{6.1}$$

Using equation 3.21, the transmission of X-rays from 0.1 − 10 keV can be calculated based on the thickness of the basalt sample and the density (typically 3 g/cm^3 for basalt). Complete attenuation of the signal X-rays L_{att}, was represented as the amount of sample required to reduce the intensity by 99.9%. For a 1 keV, 2 keV and 3 keV photon, L_{att} was calculated to be 6 µm, 15 µm and 45 µm respectively. The value of E_d is also dependant on the angle of emission θ, as shown in Figure 6.2.

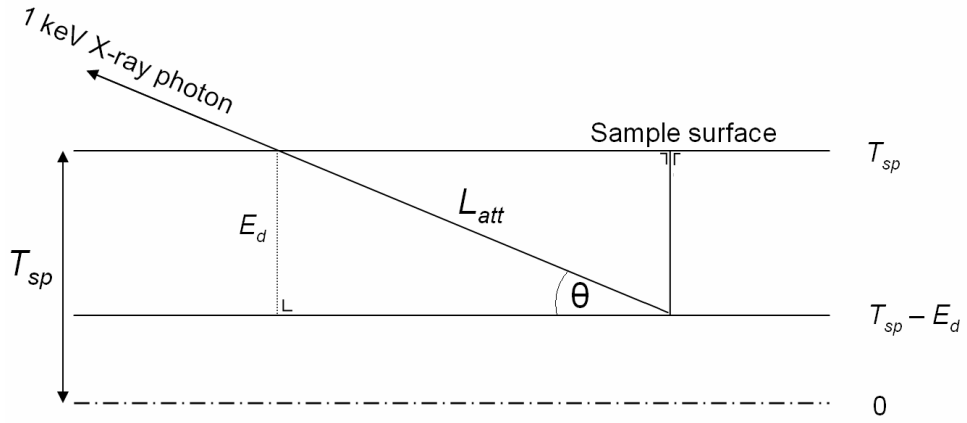

Figure 6.2: Maximum emission depth of a 1 keV X-ray photon in basalt

As discussed in Section 3.16.2, signal X-rays that are emitted at lower angles must travel longer path lengths to escape the sample resulting in increased attenuation. The value of E_d can be calculated using the expression:

$$E_d = \sin(\theta) \times L_{att} . \tag{6.2}$$

For the example in figure 6.2, the maximum emission depth of a 1 keV photon in basalt, emitted at an angle of 30°, was calculated to be 3 µm. Similarly, for a 3 keV photon, E_d was calculated to be 22.5 µm. Based on equation 6.2, as the emission angle decreases, E_d also decreases. Assuming the detector is active across an average angle of 20°, the maximum depth at which a 2 keV photon can be detected is ~ 5 µm. Increasing T_{sp} > 5 µm, will not change the number of detected 2 keV photons.

The thickness of the sample determines the attenuation of the incident radiation, as well as the attenuation of signal X-rays. Primary characteristic X-rays can cause secondary fluorescence of other atoms, thereby reducing the intensity of the primary radiation and increasing the intensity of secondary radiation. For example, an Fe Kα photon generated at a depth of 10 µm, may encounter a Ca atom at a depth of 2 µm when attempting to escape the sample. Since the energy of the Fe Kα photon (6403 eV) is greater than the K shell binding energy of Ca (4038 eV), a Ca Kα X-ray may be produced by the interaction (16.3% probability). This must be considered when performing quantitative XRF analysis through 'matrix corrections', where the 'matrix' represents the various elements in the sample. However, this does not influence the maximum emission depth at which X-rays can be generated. The next section takes into account the remaining absorption factors of signal X-rays prior to detection, in order to determine the low energy X-ray response of the CCD-Array.

6.2.2 Low Energy X-ray Response of the CCD-Array

Without the path between the sample and detector in a vacuum, the detection of low energy elements in air is difficult to achieve. A 108 mm distance between the sample and CCD-Array provides very high spatial resolution for XRD applications (0.012°), but results in severe attenuation of low energy X-rays for XRF applications. The attenuation of signal X-rays in the test facility prior to detection by the CCD is now discussed.

The main composition of air contains N (78%), O (21%), Ar (0.934%) and CO_2 (0.033%). Using equation 6.1 the overall mass attenuation coefficient for air was calculated and using equation 3.21, the transmission of soft X-rays through 108 mm of air was determined, as shown in figure 6.3. This figure also shows the fluorescence yield [Krause 1979] and the remaining absorption factors of signal X-rays, prior to detection (5 µm thick basalt sample, 20 µm Mylar X-ray window and the CCD's QE).

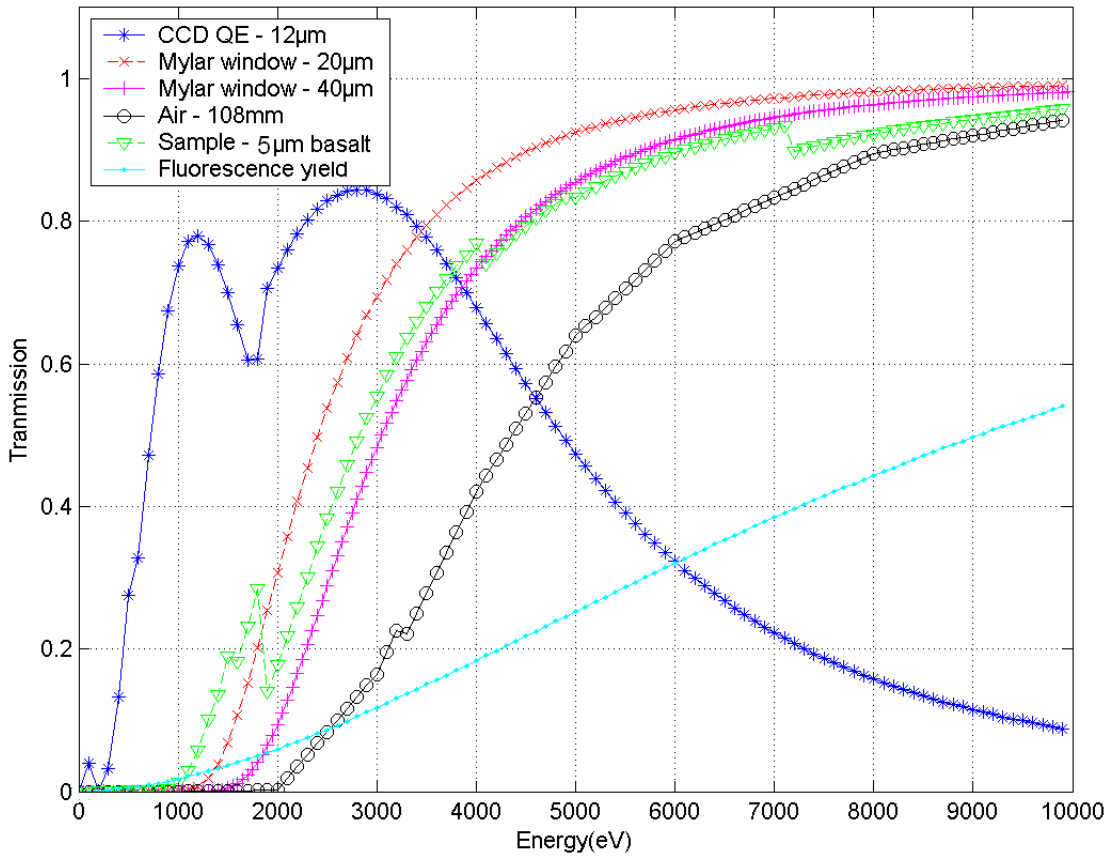

Figure 6.3: Attenuation of signal X-rays from 0.1 − 10 keV prior to detection

The transmission of X-rays through the sample was estimated using 5 µm of basalt powder. Based on figure 6.3, the low energy detection limit was expected to be between 1 − 2 keV. Since the maximum emission depth of a 1 keV and 2 keV photon in basalt is 3 µm and 7.5 µm respectively, attenuation through 5 µm is a reasonable approximation for the sample absorption. Basalt was an ideal sample to test since it contains 4 elements with characteristic Kα emissions in this energy range (Na, Mg, Al, Si).

Figure 6.4 shows the overall transmission of X-rays from 0.1 − 10 keV under standard operating conditions for a 20 µm and 40 µm X-ray window thickness. Figure 6.4 also shows the resulting increase in transmission when the air gap between sample and detector is eliminated, with and without a 20 µm Mylar X-ray window. All transmission curves include the K shell fluorescence yield for elements with Kα emission from 0.1 − 10 keV.

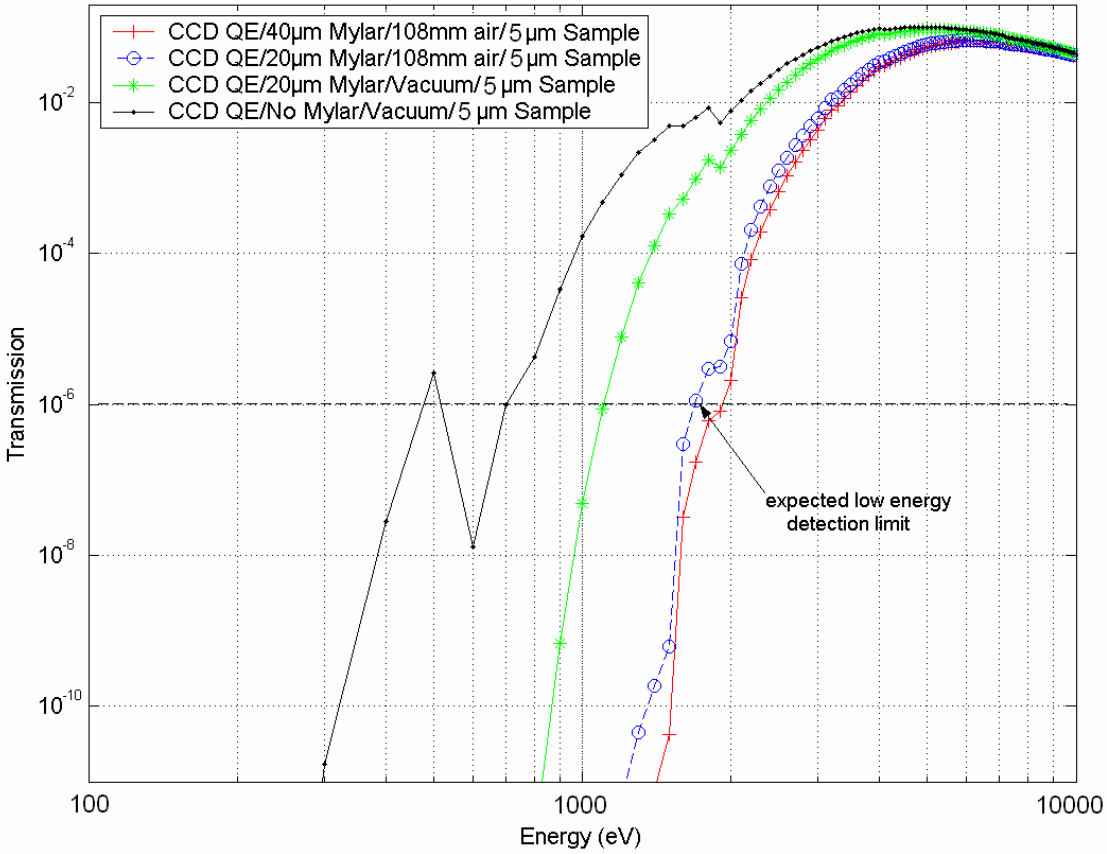

Figure 6.4: Transmission of X-rays from 0.1 − 10 keV from sample to detector

The low energy detection limit is related to the number of exposures accumulated. For typical samples, 10^2 − 10^3 exposures (1 s) are acquired by the CCD. The Bede micro-source produced ~ 3 × 10^6 counts/s in a 150 µm spot, although this was expected to be 1 order of magnitude lower than the actual flux produced [Gibson & Gibson 2002]. As an initial estimate, it was assumed that the low energy detection limit was ~ 1 keV, which corresponds to Na Kα X-rays (1041 eV). It is highly unlikely that 3 × 10^6 X-rays/s will interact with a Na atom in the basalt sample and result in the emission of characteristic Na Kα photons. In order to estimate the low energy detection limit, the number of incident X-rays that are available to excite the Na atom per second must be approximated. A crude approximation was made that 1% of the incident photons (~ 3 × 10^4 counts/s) interacted with the Na atoms (or Mg, Al, or Si atoms). If 1000 exposures are collected, ~ 3 × 10^7 X-rays will have interacted with the Na atoms (all incident X-rays have sufficient energy to dislodge K shell electrons with a binding energy < 2 keV (see figure 3.16)). To collect a minimum of

100 photons in 1000 exposures, the transmission cannot be less than ~ 1×10^{-6}, which is located at ~ 1.7 keV (Si Kα), as indicated in figure 6.4. This is the estimated low energy detection limit based on a collection time of 1000 exposures (1 s each) and an approximation that 1% of the incident photons interact with the Si atoms and all resulting Si Kα emissions (~ 4.7%) are detected based on the CCDs solid angle.

In order to determine the low energy detection limit, data was collected from a basalt powder under the same experimental conditions used in the calculations (20 µm Mylar X-ray window, 108 mm air gap, 12 µm CCD depletion depth, 150 µm spot size, 80 W X-ray source operating power and 1000 exposures). The resulting spectrum is shown in figure 6.5.

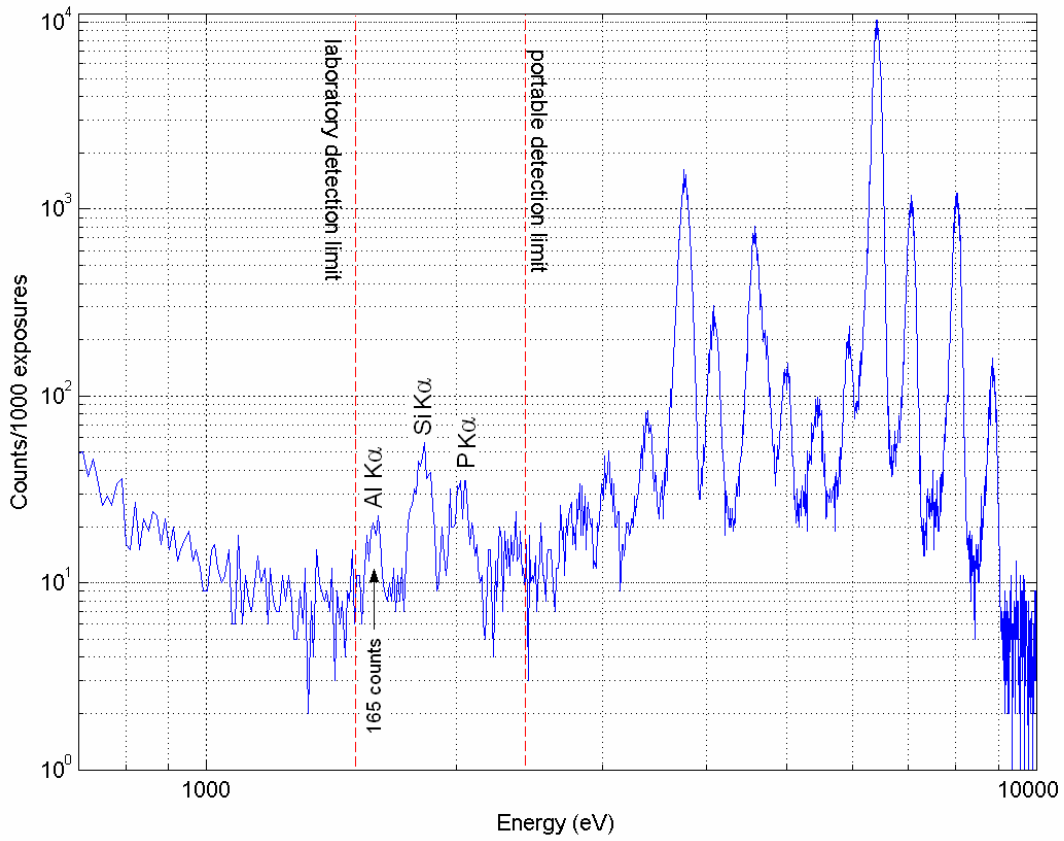

Figure 6.5: XRF spectrum of basalt highlighting the low energy detection limit under normal operating mode to be Al Kα (1487 eV)

As shown in figure 6.5, the lowest energy detected by the CCD-Array was ~ 1.5 keV (Al Kα), which was lower than expected (1.7 keV). In the laboratory arrangement, the

high absorption of X-rays in air is counteracted by the high flux produced by the Bede micro-source. For a portable X-ray source, the flux would be ~ 2 − 3 orders of magnitude lower than the Bede micro-source, thereby degrading the low energy detection limit to ~ 2.5 keV, as indicated in figure 6.5. Improvements to the low energy detection limit in the 2nd generation CCD-Array are discussed in Section 7.2.

6.2.3 CCD30-11 Response Matrix

The final stage in the X-ray transmission process is the detection of signal photons ranging from 0.1 − 10 keV by the CCD30-11. The response of the CCD30-11 to X-rays of different energies can be determined using a response matrix. The response matrix is a 2-dimensional image that represents the probability of generating a digitised value for a given X-ray energy. The response matrix was generated using Monte-Carlo simulations, which involved simulating 1×10^4 incident photons from 0.1 − 10 keV, in 1 eV steps. The process of determining the digitised value of a given X-ray photon was calculated as follows.

The simulation calculated the transmission of the incoming X-ray photon through the dead layer of the CCD, which consists of 0.835 µm of SiO_2, 0.085 µm of Si_3N_4 and 0.3 µm of polysilicon for the CCD30-11. The fraction of events absorbed in the CCD's depletion region was calculated using equation 3.25. Based on the absorption depth and X-ray energy, the size of the charge cloud reaching the buried channel was calculated. If the charge cloud was spread across multiple pixels the fraction of the charge cloud in each pixel was calculated. The fraction of energy assigned to the given pixel was determined by summing across a 3-dimensional Gaussian mesh, which represented the distribution of the charge cloud. If the X-ray interacted in the CCD substrate, the charge loss through recombination was also calculated. Each pixel was also assigned a dark current value, which was selected from a Poissonian distribution with a mean I_d, and readout noise value, which was selected from a Gaussian distribution with an error, σ_{RN}. The photon shot noise was also added to each X-ray photon, which depends on the X-ray energy and CCD operating temperature (equation 3.16). The simulated response matrix of the CCD30-11 is shown in figure 6.6 from 0.1 − 10 keV.

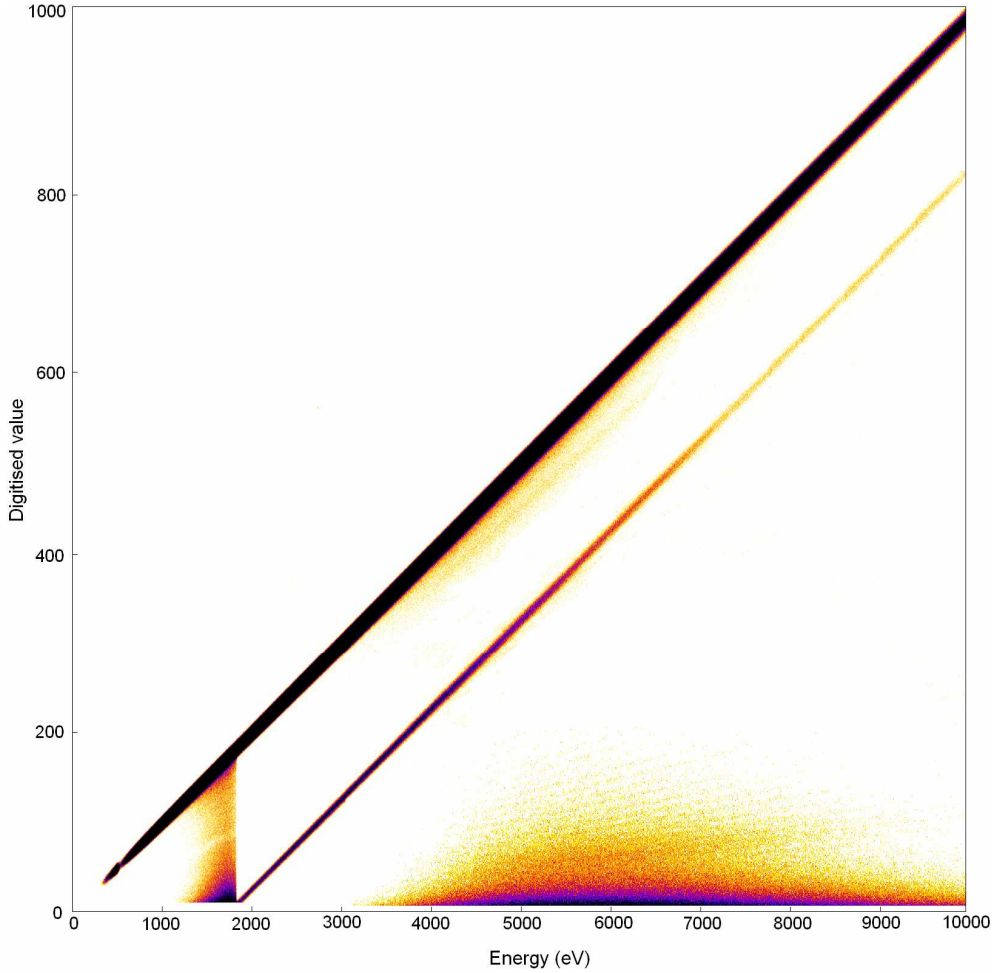

Figure 6.6: Response matrix of the CCD30-11 (Cal = 10 eV/ADC, pixel size = $(26\ \mu m)^2$, noise threshold = 14 (ADC), Z_d = 12 µm, Z_{ffr} = 8 µm, Z_{sub} = 300 µm, σ_{RN} = 7.4 e^- r.m.s, I_d = 1 e^- p/p/s, input photons = 1×10^4/eV, CCD operating temperature = -40 °C, ω = 3.7)

The x-axis represents the energy of the detected X-ray photon and the y-axis represents the digitised value of the photon. The image has been displayed in log scale to show the low intensity split events, located above the noise threshold. The main diagonal line in figure 6.6 represents the Kα X-ray peak, the FWHM of which is given by equation 3.24. The secondary line is located 1740 eV below the main X-ray peak and represents the Si escape peak.

By summing across the y-axis of the response matrix, the Gaussian profile of the main X-ray peak can be generated, along with the profile of split events. Figure 6.7 (a) highlights the agreement between the expected and simulated spectrum of a

radioactive Fe^{55} source. Figure 6.7 (b) emphasises the agreement between a simulated and experimental Ca Kα X-ray peak (3691 eV).

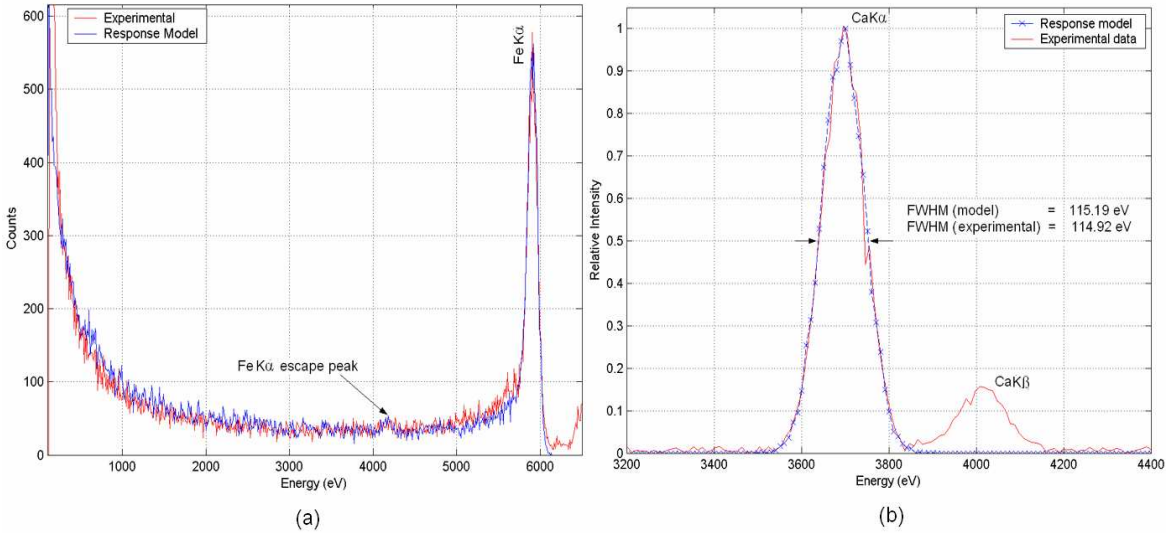

Figure 6.7: (a) Comparison between experimental data and response model for an Fe^{55} spectrum, which contains both isolated and split events. Figure 6.7 (b) Comparison between experimental data and response model for a Ca Kα X-ray peak (FWHM errors < 0.3 %)

By summing across the x-axis of the response matrix, the QE of the CCD can be calculated. Figure 6.8 shows a comparison of the expected QE (calculated using equation 3.25) of the CCD30-11 and the QE generated through the response matrix. The 'Expected DR QE – 12 µm' calculates the transmission of X-rays through the dead layer of the CCD and assumes all X-rays that are absorbed within the CCD's 12 µm depletion region result in isolated events. The 'Expected EPI QE – 25 µm' represents the total events (splits and isolated) detected in the 25 µm region. The 'Response model DR QE – 12 µm' takes into account the loss of events through escape peaks and events that are detected in the depletion region but still form split events. This response model depicts a more accurate representation of the isolated events detected in the CCD's depletion region. The 'Response model EPI QE – 25 µm' also takes into account the isolated events that are detected in the CCD's field free region, therefore this QE curve portrays the most accurate representation of the total isolated events collected within the CCD30-11.

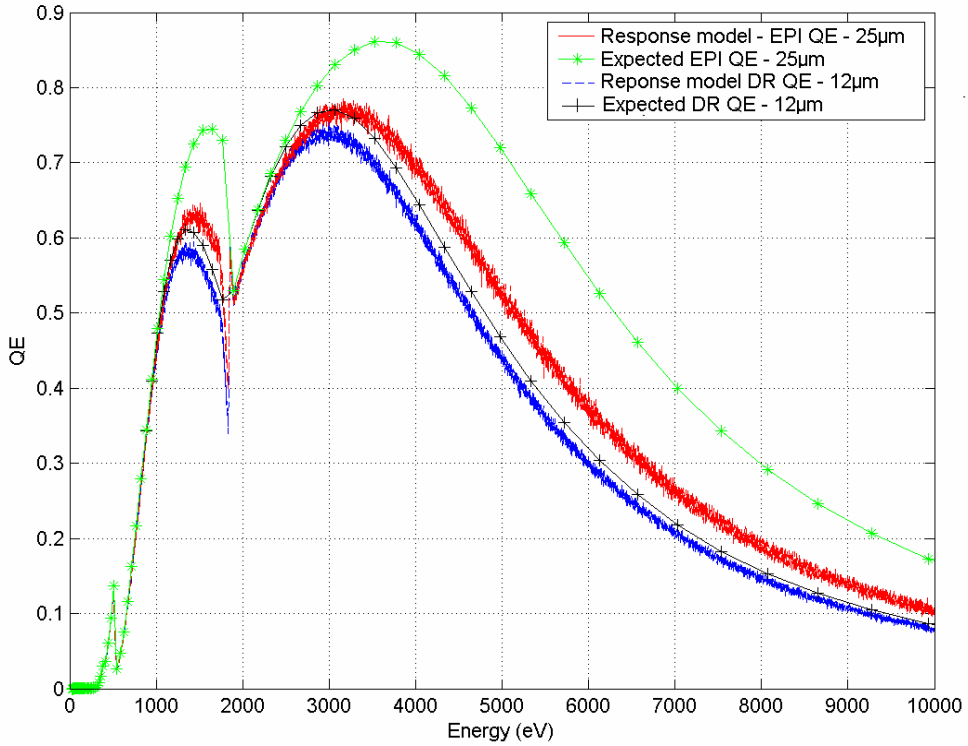

Figure 6.8: QE generated though response matrix compared with predicted QE for the depletion (12 µm) and epitaxial region (25 µm) of the CCD30-11

6.3 Sample Preparation Requirements

This section presents the major sample preparation issues experienced with the CCD-Array during testing and highlights the benefits of the PB geometry.

6.3.1 Sample Thickness

All X-rays have a maximum emission depth at which they can be emitted from the sample. It has been shown in Section 6.2.1 that a 1 keV X-ray cannot escape a sample of basalt at depths greater than 3 µm, assuming an emission angle of 30°. Therefore, increasing the thickness of the sample greater than 3 µm will not increase the amount of 1 keV X-rays collected by the detector. Figure 6.9 shows the XRF spectrum of andesite collected using 10 mg (~ 230 µm thick), 50 mg (~ 980 µm thick) and 100 mg (~ 1800 µm thick) samples with a 150 µm incident beam. After 50 mg of andesite powder was exposed to the incident beam, the maximum emission depth of the Si Kα X-rays had been reached. Doubling the thickness of the powder does not cause an increase in the number of Si Kα counts/s. An increase in Ca Kα X-rays was noticed however, since the maximum emission depth at 3691 eV had not been reached. Since the data was collected using CCD 3, emission angles were in the range

of 35 − 47° 2θ. Since higher energy photons are emitted from greater depths in the sample, an increase in Si Kα X-rays can occur due to secondary fluorescence when the sample thickness is increased, however, this was not noticed. For XRF analysis, the sample should be thick enough to absorb all of the incoming radiation, so that the incident X-rays only interact with the sample and not the sample holder. This will maximise the emission of characteristic photons.

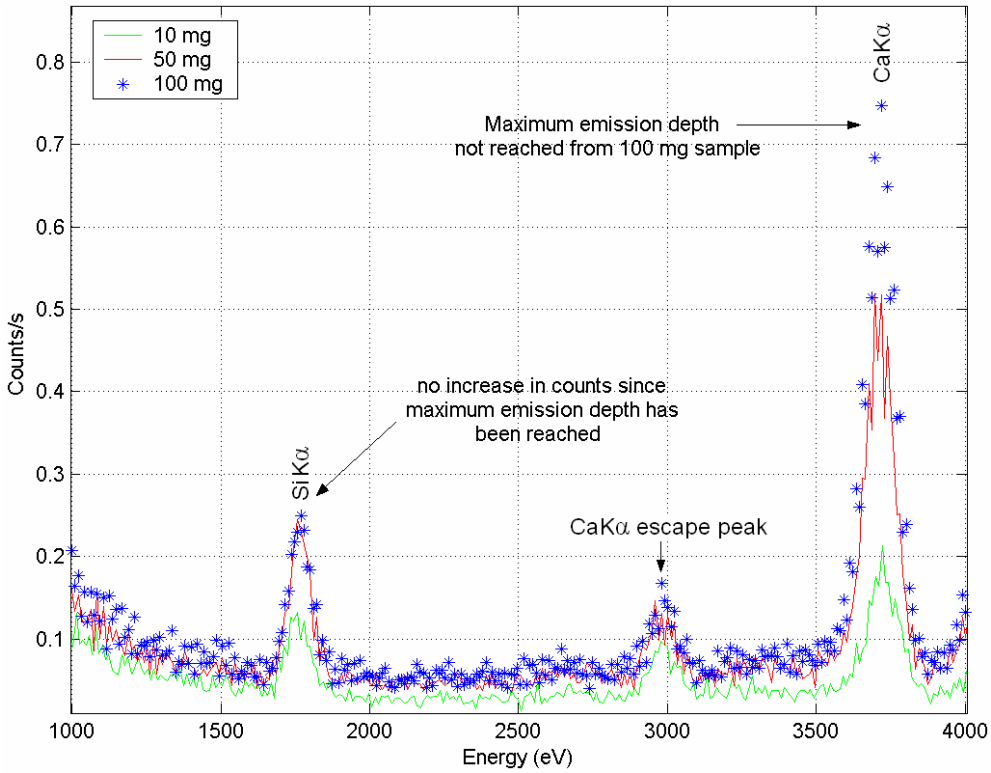

Figure 6.9: Effect of sample thickness on XRF spectrum

Sample preparation is crucial for accurate XRD analysis. Three main sources of errors exist in the BB_3 parafocusing geometry, which are flat specimen error, sample displacement error and sample transparency error [Jenkins & Snyder 1996]. Flat specimen error occurs because samples are typically flat and form a tangent to the focusing circle, as opposed to lying along its curvature. Sample displacement error occurs when the sample height is above the centre of the measuring circle. Sample transparency occurs because the sample has a small linear attenuation coefficient and the incoming radiation is not full absorbed by the sample at higher angles of incidence, thereby causing intensity variations of diffracted X-rays as well as asymmetrical peak shapes. These errors lead to deviations in 2θ peak positions as well as asymmetrical peak shapes. Although parafocusing geometries can achieve very

high resolution with the use of receiving slits, high precision sample alignment is required as well as very careful sample preparation.

Parallel beam diffraction eliminates some of the common sample related errors found in parafocusing geometries [Cao et al. 2002]. With the use of parallel beams, diffracted X-rays are focused, therefore the geometry is not bound to any focusing circles. This allows less precision sample alignment and also allows variation of the sample to detector distance. Flat specimen errors are eliminated since the sample is no longer required to conform to the curvature of a focusing circle. Sample transparency errors are eliminated since the angle of incidence does not vary. Thin samples can also be used since scattering from the sample holder is eliminated with the use of a ZBM. Sample displacement errors can be eliminated when performing parallel beam diffraction with a linear detector, but cannot be eliminated when using an area detector (such as an array of CCDs).

For XRD analysis, the sample should be completely opaque to the incoming X-ray beam. This represents a sample thickness that absorbs 99.9% of the incoming beam intensity. It is important to note that a 4° incident angle means that the majority of the incident beam is attenuated very close to the sample surface (especially for inorganics), therefore the only small amounts of powder are usually required in the reflective XRD geometry to make a sample opaque. For a known sample, the thickness can be calculated prior to analysis. For example, the thickness of $CaCO_3$ needed to attenuate 99.9% of Cu Kα radiation can be calculated to be 380 µm. Since the incident beam irradiates the sample at a 4° incident angle, the actual thickness required to make the sample completely opaque is 26 µm. Data was collected from a transparent $CaCO_3$ sample (< 26 µm thickness) and an opaque $CaCO_3$ sample (> 26 µm). The aim of the analysis was to highlight the symmetry of the peaks and show that the PB geometry was insensitive to the peak asymmetry caused by sample transparency in the parafocusing geometry [Misture & Hailer 2000]. Figure 6.10 shows the resulting XRPD patterns of $CaCO_3$ using a sample thickness < 26 µm (10 mg) and >> 26 µm (70 mg). The 70 mg sample shows an increase in diffraction intensity since greater depths of the powder are available for diffraction. The background scattering is also seen to decrease, since elastically scattered X-rays are more highly absorbed within the thicker sample. Sample displacement errors were

calculated to be 0.037° 2θ and the transparent sample provided symmetrical peak shapes as shown by the Gaussian fitted peaks. The data highlights, that with the use of parallel beams and a fixed angle of incidence, the main sample related issues from parafocusing geometries can be eliminated, apart from sample displacement.

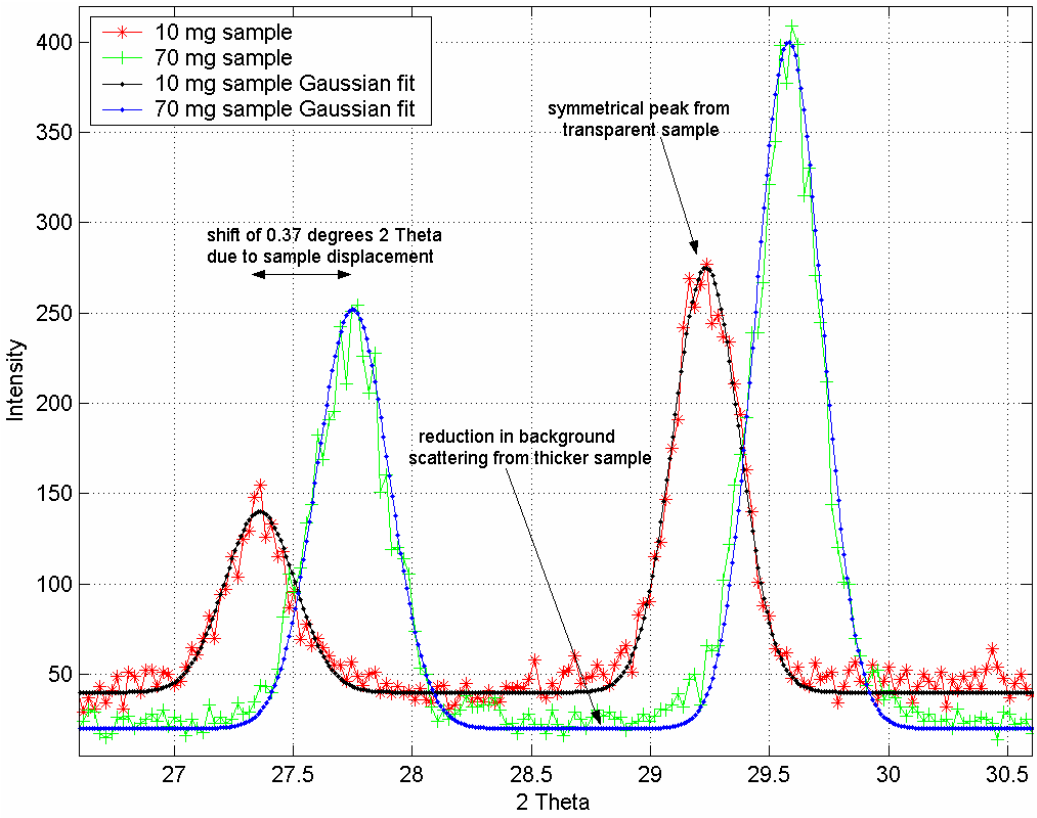

Figure 6.10: Effect of sample transparency/displacement on 2 $CaCO_3$ XRPD peaks

6.3.2 Grain Size

For a portable instrument used for in-situ analysis, samples obtained from manual grinding and drilling of rocks is expected. Powder grains should be reduced to < 10 µm to produce all possible reflections in the sample. Larger grains cause peak broadening and a reduction in the number of orientations available for Bragg's law to be satisfied. The impact of grain size and homogeneity on the XRD pattern was determined by collecting diffraction patterns from different basalt samples with different characteristics. The first sample consisted of untreated raw particles that were collected by drilling a basalt rock. Figure 6.11 shows an image of a large grain from the first sample against a 75 µm mesh. The average particle diameter in the first

sample was ~ 80 µm, with a maximum size of ~ 300 µm as shown in figure 6.11. This sample was very inhomogeneous in terms of grain size.

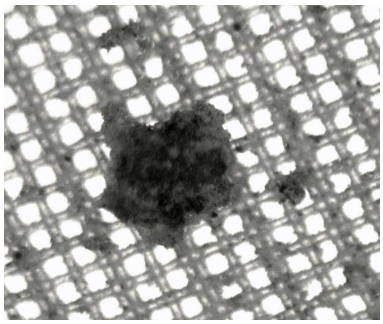

Figure 6.11: A 300 µm diameter particle against a 75 µm mesh

The second sample was sieved through a 75 µm mesh to remove large grains. The third sample was produced by grinding the second sample using a mortar and pestle and was used as the reference pattern. XRD patterns were collected from all samples in order to determine the quality of the pattern produced. The resulting XRD patterns for the 3 samples are shown in figure 6.12. The samples were rotated during data collection to reduce the effects of preferred orientation.

The XRD pattern produced from sample 1 was much better than expected as all major peaks could be identified. However, the SNR was much poorer than the XRD pattern obtained from the meshed and ground samples, since larger grains result in less crystallographic planes presented to the incident beam. This causes less diffraction to take place, resulting in larger intensity errors from Poissonian statistics. The result is a 'spotty' diffraction ring as opposed to a continuous ring. The poor SNR has also caused the loss of a peak located at ~ 32.3° 2θ. The diffraction pattern produced by sample 2 (figure 6.12 (b)) represents a much more homogenous sample resulting in an improved SNR and no peak loss.

Sample 3 has reduced particles sizes to < 10 µm and represents the most ideal sample with the largest number of available orientations presented to the incident beam. For qualitative analysis, further grinding of sample 1 may not be necessary since the major peaks are identifiable (includes other CCDs). For accurate quantitative analysis however, the quality of the diffraction pattern should be improved by grinding and sieving.

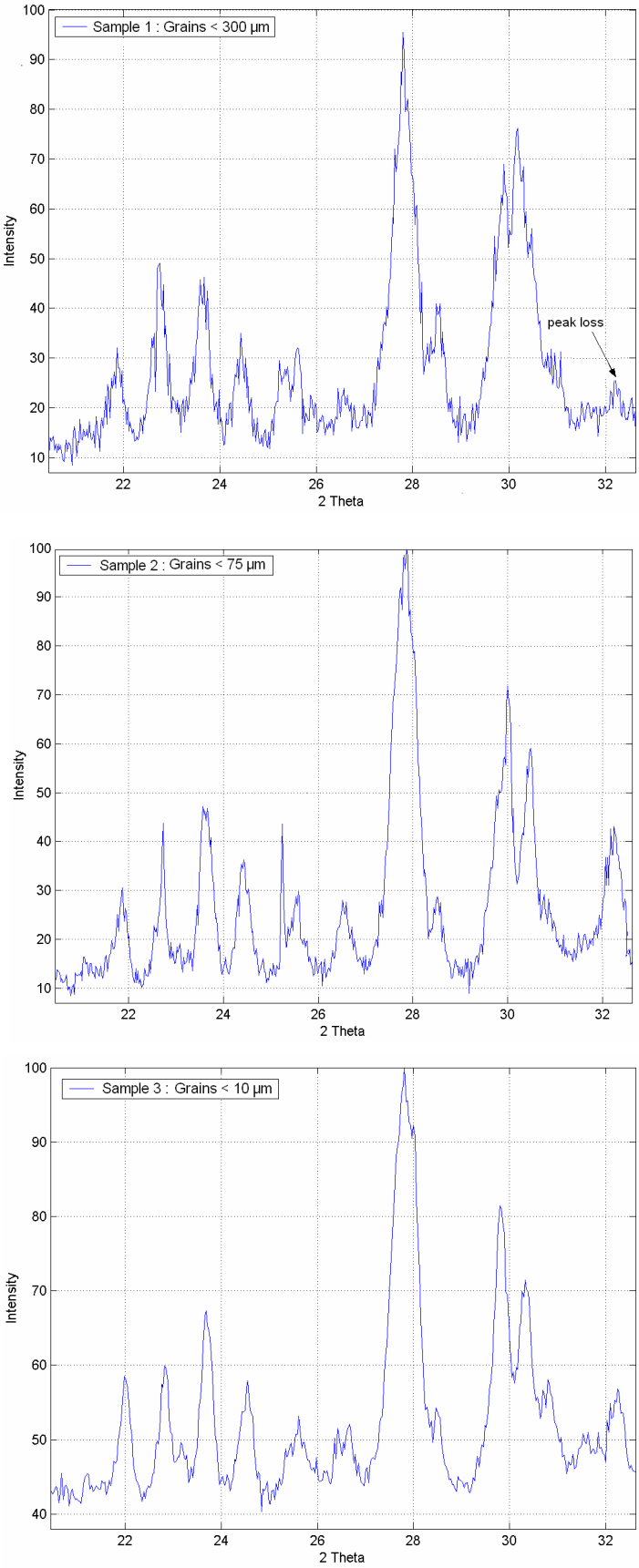

Figure 6.12: XRD pattern of (a) sample 3 (reference sample) (b) sample 2 (sieved through 75 µm mesh) and (c) sample 1 (raw drill particles)

6.3.3 Preferred Orientation

The theoretical definition of a perfect sample for powder diffraction experiments is one that exhibits an infinite amount of randomly orientated crystals. With all possible crystal orientations presented to the incident beam, all diffraction rings are recorded in the 2-dimensional CCD image. Achieving the ideal sample however is a very difficult task. The most common problem from poor sample preparation is preferred orientation [Pecharsky & Zavalij 2005].

Figure 6.13 (a) shows diffraction rings collected from an andesite powder. The density of X-ray photons inside the ring is very inconsistent. Instead of an even distribution, sharp peaks are noticed which are highlighted with red circles. This is caused by large crystals in the powder that have not been adequately ground to small enough particles (< 10 µm). These crystals cause single crystal diffraction which form sharp peaks inside the diffraction ring. Preferred orientation results in severe intensity errors in peaks, which will cause problems in both qualitative and quantitative analysis. In order to reduce the effect of preferred orientation, rotation can be used to bring other planes into diffracting positions and a more even intensity distribution is achieved across the diffraction ring, as shown in figure 6.13 (b). A major advantage of using 2D area detectors for XRPD in comparison to tradiational point detectors is that preferred orientation can be viewed and analysed using an image, which is also useful for texture analysis..

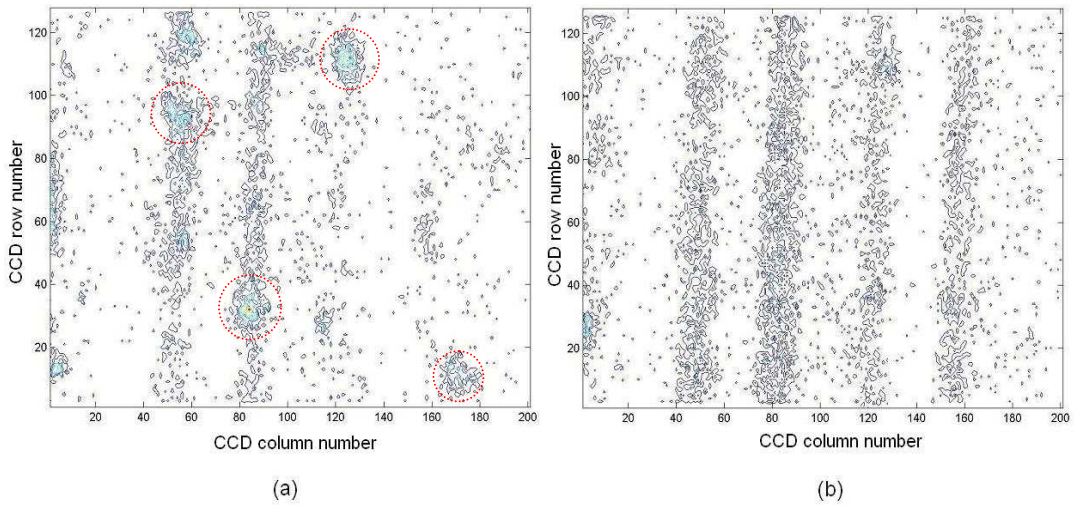

Figure 6.13: (a) Poorly prepared andesite powder displaying severe preferred orientation. Figure 6.13 (b) Sample rotation has presented more crystal orientations to the incident beam and reduced preferred orientation

In a reflective XRD geometry, the sample must be rotated perfectly level in relation to the horizontal axis. Figure 6.14 shows the effect of non-level sample rotation on 3 $CaCO_3$ XRD peaks. When the sample holder is not rotated about the horizontal axis, the surface area of the sample irradiated increases. Since the width of the diffracted beam is determined by the amount of irradiated sample, peak broadening occurs. Since the 3 peaks shown in figure 6.14 are in close proximity, peak broadening has resulted in loss of peak resolution. To achieve the best possible diffracted beam resolution, considerable effort should be made to ensure the sample holder is rotated perfectly on its axis.

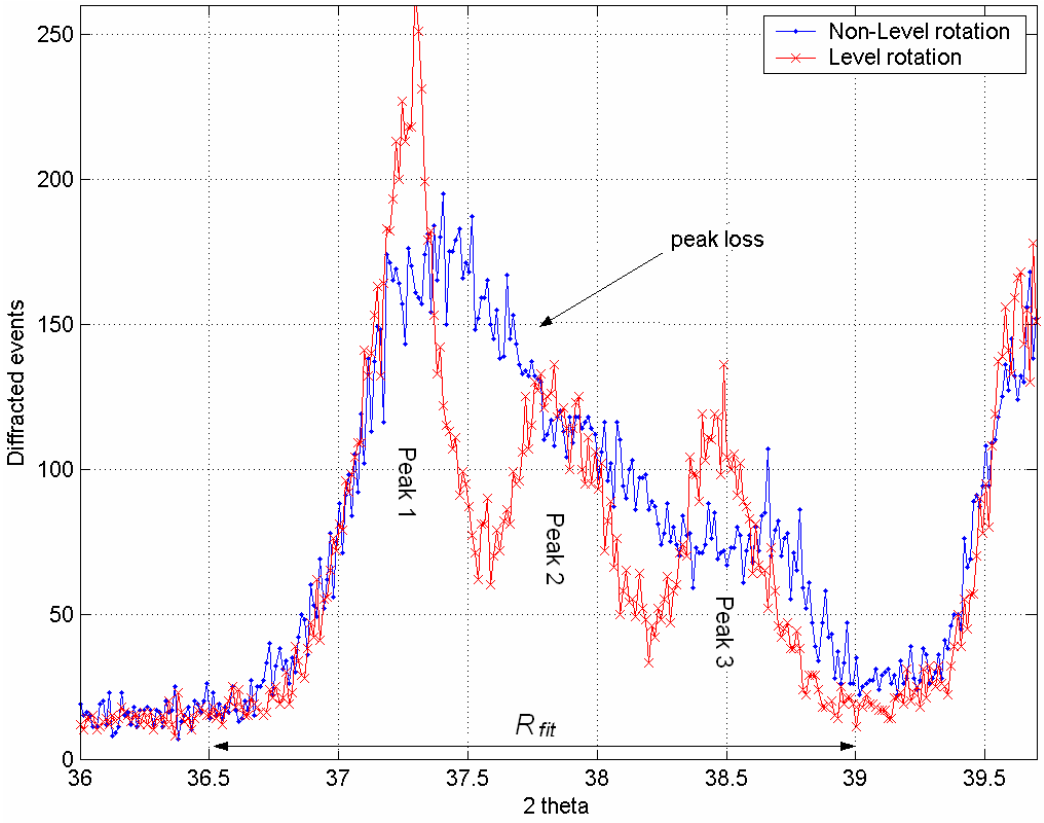

Figure 6.14: Non-level sample rotation causing peak loss

If the diffraction pattern collected from the level sample was not available, how could the analyst identify the peaks located in region, R_{fit}? XRD peaks can still be extracted from R_{fit} by means of Gaussian peak fitting and statistical significance testing. Since R_{fit} is 170 pixels wide and the standard width of XRD peaks is ~ 50 pixels, it can be expected that a maximum of 3 peaks exist within R_{fit} (assuming no peak overlapping). If statistically significant results are not achieved using 1, 2 or 3 Gaussian peaks, peak

overlapping may be assumed and R_{fit} is fitted with multiple peaks (> 3). Assuming no peak overlapping, the data located within R_{fit} is fitted with 1, 2 and 3 Gaussian peaks and the statistical significance of each fit is tested. During each fit, the parameters of each peak are refined (2θ position, FWHM and amplitude) and a least squares test is applied to find the best agreement with the experimental data. Once the best parameters for each peak are found, the statistical significance of the fit is tested. An 'F' test was used to calculate the statistical significance of the Gaussian fitted peaks to the observed XRD pattern. By using a significance level, α_{sig}, of 0.01 and calculating the degrees of freedom to be 1 and 320, the critical F value F_{crit}, was found to be 6.8. To accept the hypothesis H_o, that there is no significant difference between the fitted and observed XRD pattern, the calculated F statistics F_{calc}, must have a value < F_{crit}. Table 6.1 shows the best-fit parameters for the 1, 2 and 3 Gaussian fitted peaks.

Parameter	1 peak	2 peaks	3 peaks
Peak 1 mean (º 2θ)	37.49	37.35	37.393
Peak 1 FWHM (º 2θ)	1.55	0.66	0.65
Peak 1 amplitude (peak height)	130	100	160
Peak 2 mean (º 2θ)	-	37.9	38.02
Peak 2 FWHM (º 2θ)	-	1.56	0.61
Peak 2 amplitude (peak height)	-	78	78
Peak 3 mean (º 2θ)	-	-	38.65
Peak 3 FWHM (º 2θ)	-	-	0.54
Peak 3 amplitude (peak height)	-	-	57
α_{sig}	1%	1%	1%
F_{crit}	6.8	6.8	6.8
F_{calc}	46.34	15.83	6.66
Accept H_o ($F_{calc} < F_{crit}$)	No	No	Yes

Table 6.1: Best-fit parameters for 1, 2 and 3 Gaussian fitted peaks to the observed XRD pattern

Table 6.1 shows the agreement between the observed data and the fitted XRD pattern with 3 Gaussian peaks (as predicted by the spectrum collected with the level sample). Since $F_{calc} < F_{crit}$ with $\alpha_{sig} = 0.01$, H_o can be accepted with 99% confidence. Based on the discussions that are presented in Section 6.4.2, the confidence intervals concerning the peak mean, FWHM and intensity were calculated and are summarised in table 6.2.

Parameter	Peak 1	Peak2	Peak3
Peak mean position (2θ)	37.39	38.02	38.65
Mean confidence interval (º 2θ)	< ± 0.01	< ± 0.01	< ± 0.01
Peak FWHM (º 2θ)	0.65	0.61	0.54
FWHM confidence interval (º 2θ)	< ± 0.01	< ± 0.01	< ± 0.01
Peak Integrated Intensity (counts)	7284	4694	3720
Intensity confidence interval (%)	± 2.3	± 2.86	± 3.21

Table 6.2: Summary of extracted Gaussian parameters with confidence intervals (all confidence intervals are at a 95% confidence level)

Figure 6.15 shows the resulting fit using 3 Gaussian peaks with the parameters listed in table 6.2 and the confidence intervals for the intensity.

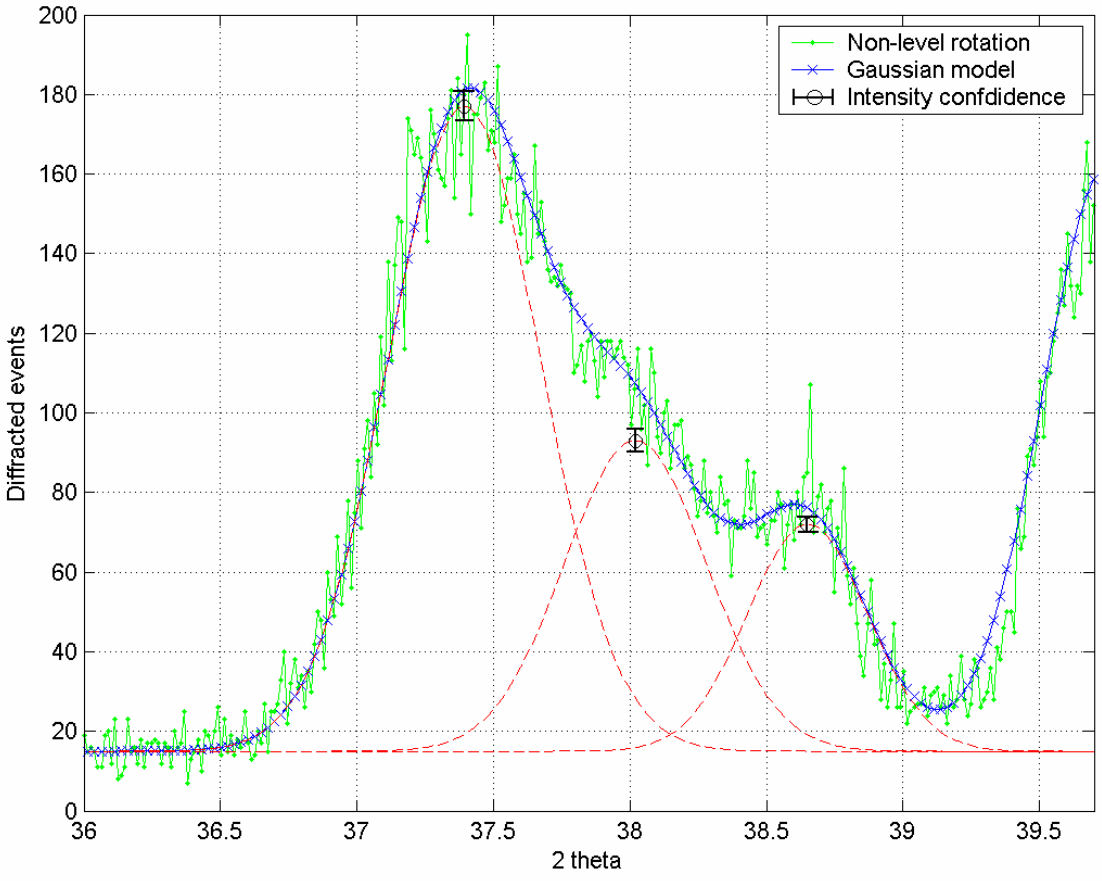

Figure 6.15: Optimum fit of 3 Gaussian peaks with observed data between the region R_{fit}. An F test confirmed the statistical significance of the fit with a 99% confidence level

6.4 Thermal and Power Requirements of the CCD-Array

In order to determine the suitability of the CCD-Array as a portable instrument, a study was carried out to determine the thermal and power requirements of the detector to perform accurate combined XRD/XRF analysis. The main source of power consumption in the detector was the TEC, which was used to cool the CCDs to reduce dark current. The effect of CCD temperature on XRD and XRF spectra are now discussed and the confidence in measurements based on the SNR is calculated.

6.4.1 XRD

The analysis of XRD data is simplified by the fact that the image contains events of a single energy, 8047 eV. A histogram of isolated events collected over all the exposures reveals a strong Cu Kα X-ray peak, which represents the diffracted X-rays from the sample. The intensity of the XRD peaks will always contain errors from Poissonian statistics, which is discussed later in this section. This section determines the influence of CCD noise on the intensity of XRD peaks and determines if the CCDs can perform XRD analysis at warm temperatures (+20 °C).

The effect of increasing the temperature of the CCD is an increase in the FWHM of the Cu Kα peak due to an increase in dark current. This causes a reduction in the SNR of the Cu Kα peak. During the energy discrimination process, the Cu Kα peak is fitted using a Gaussian model and the 3 degrees of freedom (peak position, FWHM and intensity) are refined using the χ^2 test, and the optimum parameters are determined. The accuracy of the fit is related to the SNR of the peak, therefore at higher CCD temperatures, the 3 parameters are determined with less confidence. Once the peak is fitted, all events within 3σ (where σ is the standard deviation) of the mean are registered as diffraction events. If the X-ray peak is perfectly Gaussian without any noise contribution, then 99.7% of events will be within ± 3σ of the mean. However, since the Cu Kα peak will contain noise contributions from the dark current and readout noise, the percentage of events detected will vary based on the SNR.

A simulation was developed to calculate the errors involved in determining the percentage of events detected within 3σ of the mean, for an operating temperature of -40 °C (I_d = 1 e^- p/p/s) and +20 °C (I_d = 600 e^- p/p/s). Poissonian errors from the random arrival of diffracted events were also included in the simulation. Diffracted

events were simulated and the resulting Cu Kα peaks were fitted using Gaussian models and the best-fit parameters were determined using the χ^2 test. Using the calculated mean and standard deviation, the number of events within ± 3σ of the mean were calculated and compared to the known number of diffracted events. The percentage of detected events was then computed for the 2 operating temperatures and the results are shown in figure 6.16.

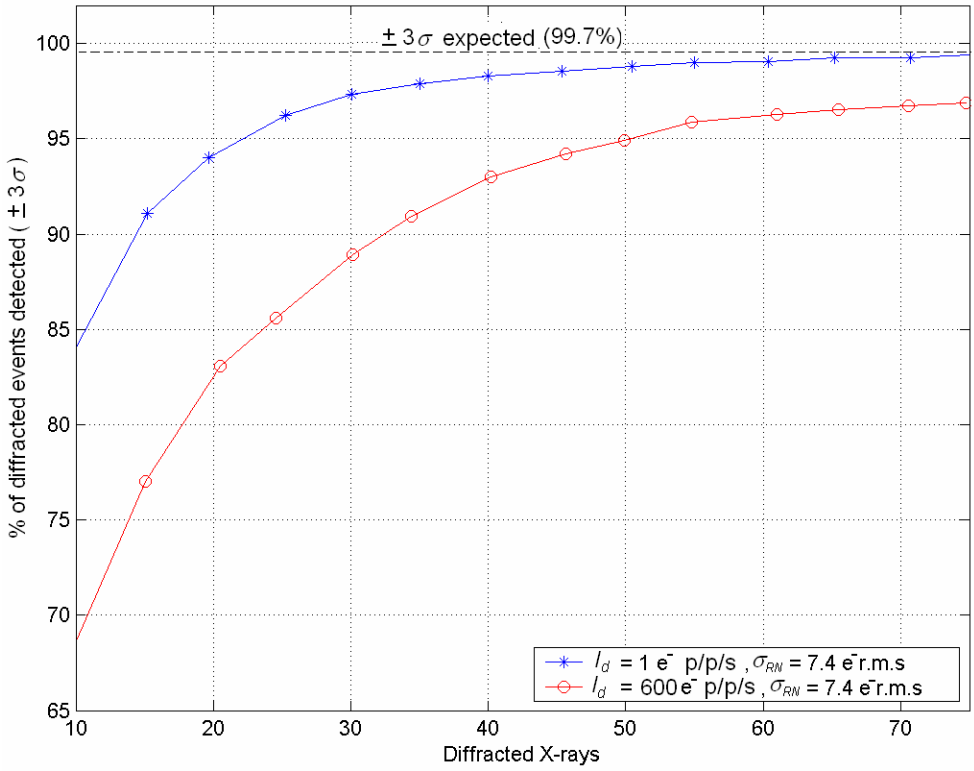

Figure 6.16: The percentage of diffracted events detected within 3 standard deviations of the mean based on the CCD noise

When operating at -40 °C, the accuracy of the Gaussian peak fitting allows more diffracted events to be detected in comparison to operating at +20 °C, but this has no influence on the XRD pattern on a single CCD image. At +20 °C, less XRD events are detected, but the intensity of each of the diffraction rings remains correlated. If 99.7% of events are detected, 0.3% of the intensity of each of the peaks is reduced. Similarly, if 68% of events are detected, 32% of the intensity of each of the peaks is reduced. Therefore, operating the CCD at +20 °C does not cause any errors in the diffraction pattern. However, since less diffracted events are detected, the Poissonian

errors on the XRD peaks are larger at warmer CCD temperatures, but this can be compensated for by increasing the number of exposures. For example, if 1000 diffracted events are detected at -40 °C, 99.707% of events are detected (~ 998). If 1000 X-rays are detected at +20 °C, 99.108% of events are detected (~ 992). Approximately 6 extra events are detected from operating the CCD at -40 °C, which improves the errors on the counting statistics by 0.01 diffracted events. From these results, it is clear that if a single CCD is used, the CCD can perform XRD analysis at any operating temperature. This is true when the CCD30-11s are operated with a system noise < 30 e^- r.m.s. When the CCD noise exceeds 30 e^- r.m.s, the Cu Kα and Cu Kβ peaks overlap at the 3σ level, which begins to cause interference in the energy discrimination process. However, even at room temperature, when the CCDs were operated using AIMO, the CCD noise was less than 30 e^- r.m.s, therefore Cu Kβ X-rays did not interfere with the energy discrimination of Cu Kα events. Figure 6.17 shows a comparison of the XRD pattern of SiO_2 collected using CCD 2 at -40 °C and +20 °C. The intensity scale is relative to the largest peak.

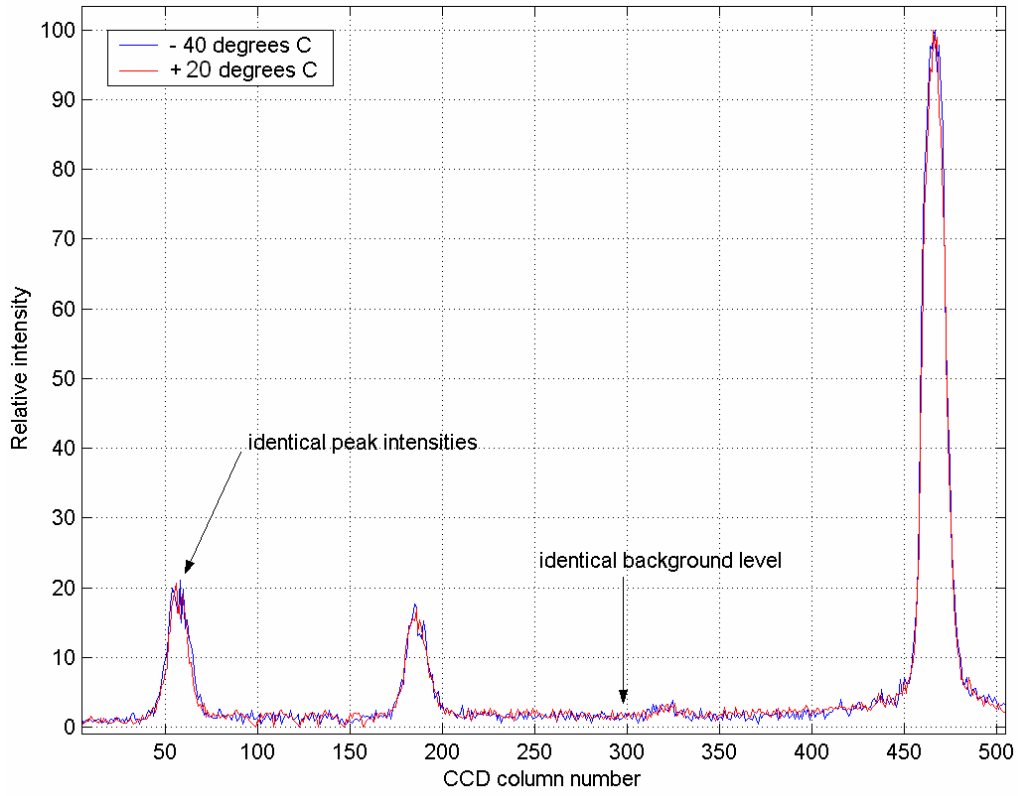

Figure 6.17: Relative 2θ vs. intensity patterns of SiO_2 at -40 °C and +20 °C revealing identical XRD patterns

As seen in figure 6.17, the XRD patterns at both operating temperatures are identical. This highlights a major advantage of using CCDs for XRD analysis, as the CCDs can collect accurate XRD data at room temperature, without the need for cooling.

When using multiple CCDs, variations in dark current will result in peak intensity errors. At +20 °C, the variation in temperature between CCD 1 & CCD 4 and CCD 2 & CCD 3 was 0.1 °C. In AIMO, this caused a variation in dark current of ~ 6 e^- p/p/s. Assuming 1000 events were detected, the intensity errors were calculated to be < 0.03 diffracted events, which is negligible. Errors from using multiple CCDs can also be caused by the number of events detected by each CCD. For example, consider two peaks with a ratio of 5:1, located on CCD 1 and CCD 2 respectively (both CCDs are operating with a dark current of 600 e^- p/p/s and a readout noise of 7.4 e^- r.m.s). As shown in figure 6.16, if 50 events are collected on CCD 1, 95% of the events (47.5) will be detected by the energy discrimination process. If 10 events are collected by CCD 2, 68% will be detected, which is ~ 6.8. The actual ratio of the peaks will be determined as 6.98:1, as opposed to 5:1. Therefore, it is crucial when operating at warmer CCD temperatures to increase the number of exposures collected. If 2000 diffracted X-rays were collected by CCD 1 and 400 diffracted X-rays collected by CCD 2, the ratio would be determined as 5.03:1. For samples with a low diffraction efficiency, operating the CCD at warmer temperatures may not be practical. However, for the majority of samples used in testing the CCD-Array, operating the CCDs at +20 °C resulted in negligible errors in the XRD patterns. Since CCD cooling was unnecessary for XRD applications, the cooling required for combined XRD/XRF applications was entirely dependant on XRF requirements.

Although XRD analysis can be performed without CCD cooling, the confidence in determining the peak mean, FWHM and intensity is based on the SNR of the XRD peak. XRD peaks are the accumulation of diffracted X-rays over a given time, in a given area of the CCD. The intensity of the XRD peak is therefore affected by counting errors or Poissonian errors. The error associated with the number of diffracted counts per exposure, is the square root of the mean number of counts, $N_{diff}^{0.5}$. For example, if 100 X-rays are collected in an exposure, 68% of the events will be spread across $N_{diff} \pm N_{diff}^{0.5}$ (100 ± 10) and the resulting error will be 10%. If a

1% error is required, at a 68% confidence level, the number of exposures must be increased to 1×10^4 counts. The SNR of the XRD peak is given by the expression:

$$SNR_{XRD-peak} = \frac{N_{diff}}{\sqrt{N_{diff}}} = \sqrt{N_{diff}} \tag{6.3}$$

As shown in equation 6.3, the error and SNR of the XRD peak are the same. The confidence interval defines the uncertainty in a parameter, at a given confidence level (usually 95%). The confidence intervals for the XRD peak 2θ mean position, FWHM and intensity were calculated using the χ^2 test. A CCD exposure was simulated (background events and a single XRD peak) and the 2θ vs. intensity pattern was generated through radial integration. The XRD peak was fitted using a Gaussian model and the 3 parameters of the model were refined to achieve the best χ^2 fit. The values of N_{diff} and N_{bck} were derived from typical exposures and the peak FWHM R_{PB}, was calculated using equation 2.14, for a 2θ diffraction angle of 50°. The variables used in the simulation are listed in table 6.3.

Parameter	Value	Units
N_{diff}	50	counts/s
N_{bck}	30	counts/s
N_R	256	pixels
N_C	1024	pixels
R_{PB}	15	pixels
dof	21	
χ_{crit}	32.6	
N_{exp}	1 - 500	exposures

Table 6.3: Variables used in the simulation to determine the confidence intervals of the peak mean, FWHM and intensity

Statistically significant fits (i.e. $\chi^2 < \chi_{crit}$) were noticed for exposures > 30. By fixing the position of 2 parameters (e.g. intensity and FWHM), the mean was varied and the region within the 95% confidence level was recorded. This region represented the confidence interval for the mean at a 95% confidence level. The CCD exposures were increased to improve the SNR of the peak and the process was repeated. The confidence intervals for the FWHM of the peak were also calculated by fixing the position of the two unused parameters and recording the regions were $\chi^2 < \chi_{crit}$. The confidence intervals for the intensity were calculated using equation 6.4. Figure 6.18 shows the results of the simulations.

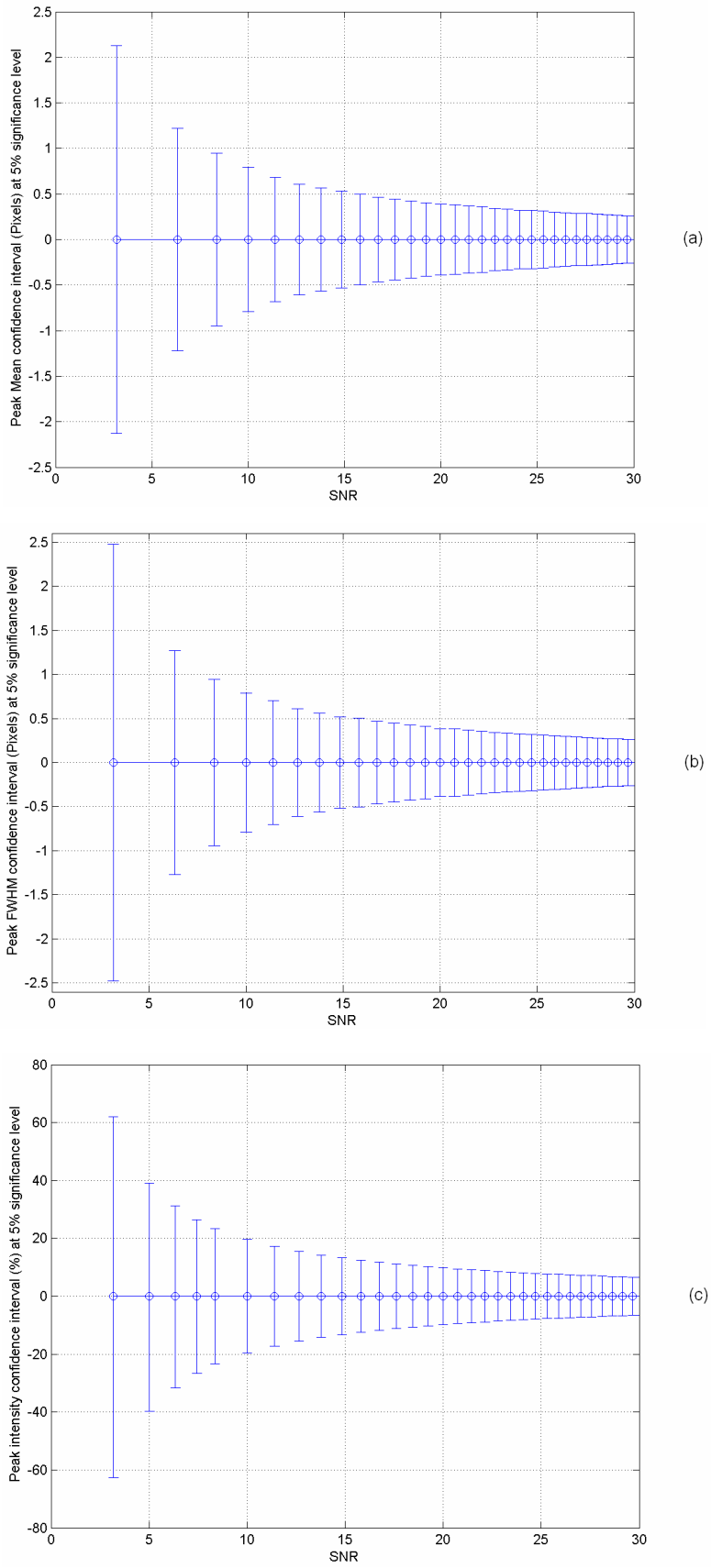

Figure 6.18: (a) Peak mean confidence interval (pixels), (b) peak FWHM confidence interval (pixels) and (c) peak intensity confidence interval (%)

Figure 6.18 (a) and (b) highlight how insensitive the peak mean and FWHM are to Poissonian noise, as the confidence intervals are within ± 1 pixel, even at a SNR of 8 (~ 60 exposures). Since the SNR of XRD peaks used for analysis are much greater than 8, errors on the peak mean position and FWHM from Poissonian noise can be completely ignored.

The peak intensity is more greatly affected by Poissonian noise with errors of 10% at a SNR of 20 (this mean that 95% of the diffracted events are within ± 10% of N_{diff}). The number of diffracted events required to achieve a certain confidence interval *CI*, at a given confidence level, Z_{val}, can be calculated using the expression:

$$N_{diff} = \left(\frac{Z_{val}}{CI} \right)^2 \tag{6.4}$$

For a 68%, 95% and 99% confidence level, Z_{val} is 1, 1.96 and 2.59 respectively. To achieve an intensity confidence interval of ± 3% at a confidence level of 95%, ~ 4,300 diffracted X-rays must be collected. To achieve a confidence interval of ± 1% on the intensity, at a similar confidence level, ~ 38,400 diffracted X-rays must be collected. The confidence required is determined by the requirements of the application. For example, quantitative analysis may require intensity accuracies of ± 1% since the intensities are related to the concentration of the different phases in the sample. Qualitative analysis may be performed with a confidence interval of ± 10%, since the strongest peaks in the diffraction pattern simply need to be identified.

6.4.2 XRF

The energy resolution of a CCD is limited by 3 factors, which are the readout noise, dark current and photon shot noise. Since the dark current and photon shot noise have a Poissonian distribution where the error is described as the square root of the mean number of counts, equation 3.18 can be re-written as:

$$\sigma_{Total} = \sqrt{{\sigma_{RN}}^2 + I_d + \frac{FE}{w}} \,. \tag{6.5}$$

Equation 6.5 highlights that the main contribution to the degradation of the energy resolution is the readout noise. With the use of an Fe^{55} X-ray source, the readout noise of all 4 devices was calculated by measuring the serial over-scan pixels on the CCD

image. The noise contribution from this region of the CCD contains zero signal data but includes the noise induced from reading out the device. The lowest readout noise was 6.4 e^- r.m.s. from CCD 3. The average readout noise from all 4 CCDs was calculated to be ~ 7.4 e^- r.m.s. at a readout frequency of 165 kHz per pixel.

The dark current performance of the devices was related to the operating mode. NIMO (V_G = 12 V and V_{SS} = 0 V) provides a depletion depth of ~ 12 µm and AIMO (V_G = 0 V and V_{SS} = 7 V) provides a depletion depth of 6 µm. AIMO greatly reduces dark current generation from the surface of the device which is the main contributor to the leakage current. Figure 6.19 shows the average dark current and CCD system noise measurements for AIMO and NIMO, as a function of temperature for the 4 CCD30-11 devices.

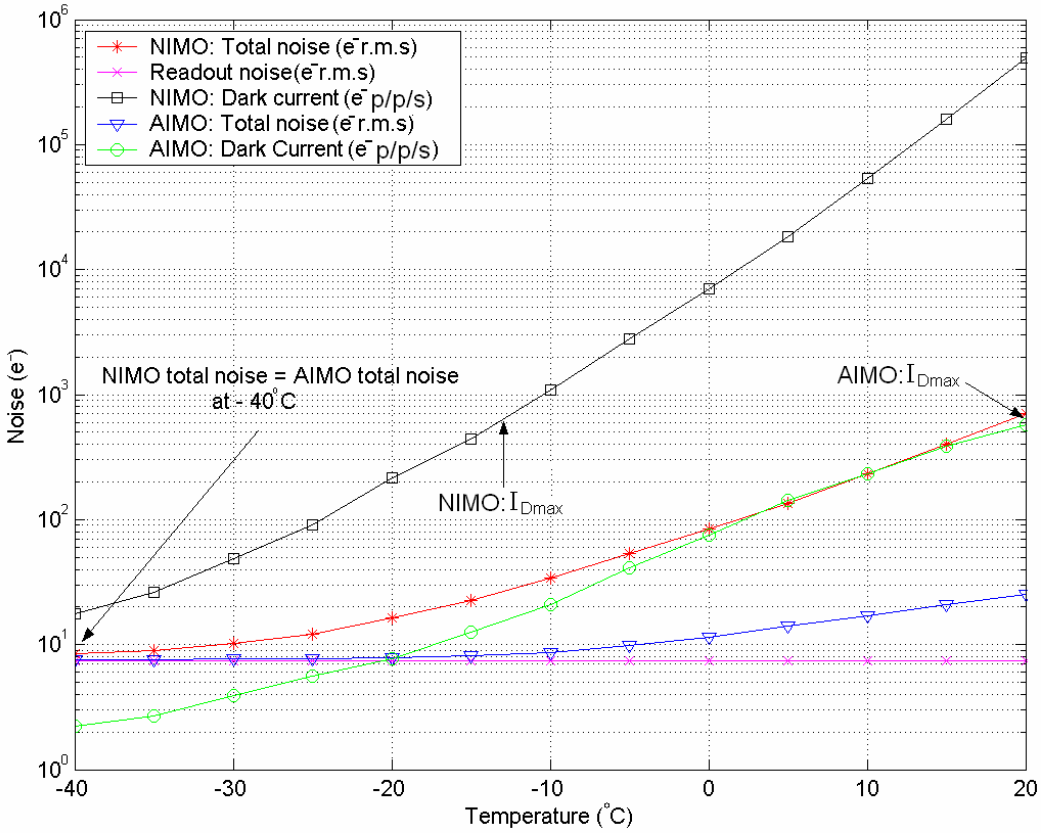

Figure 6.19: Average noise values for the 4 CCD30-11s in AIMO and NIMO

The most commonly found element in rocks on Earth is O, which has a Kα X-ray emission at 532 eV. The detection of this element is very difficult to achieve by any

XRF instrument due to a very low transmission through materials combined with a very low fluorescence yield (0.006). All other major elements found in rocks range from 1 − 10 keV. The CCD-Array should therefore be able to uniquely identify all Kα characteristic photons in this range. Since the separation in eV between Kα emissions is shorter at lower Z elements, the energy resolution requirements would be based on Kα X-rays in the region of 1 − 2 keV.

The energy resolution required to distinguish X-rays from 1 − 2 keV was calculated through computer simulations. The Kβ emissions were ignored due to very low fluorescence yield [Krause 1979]. Since Kα emissions in this range also have a very low fluorescence yield (0.02 − 0.047), a crude approximation was made that ~ 1 photon of each of the 4 elements was incident on the CCD per second. In each CCD exposure, the number of electrons generated by each of the 4 Kα photons was determined using equation 3.15. The noise contribution was determined using equation 6.5, where the readout noise and photon shot noise were fixed and the dark current was varied. The dark current was gradually increased to find I_{Dmax}, which represented the maximum dark current that would allow the detection of elements from 1 − 2 keV. I_{Dmax} was determined when two peaks overlapped at approximately half the peak height.

The SNR of each peak was calculated using the expression:

$$SNR_{XRF-peak} = \frac{counts}{\sqrt{\sigma_{RN}{}^2 + I_D + \frac{FE}{\omega}}} \tag{6.6}$$

For a fixed number of counts, readout noise and dark current, the SNR decreases with increasing X-ray energy, since the statistical uncertainty in the number of electron-hole pairs produced increases.

Figure 6.20 shows the simulated results for a 10 minute, 2 hour and 10 hour total exposure period. Signal data collected from the readout process and the CCDs CTI was ignored. After the histogram for a given exposure time was generated, Gaussian peaks were fitted to the 4 X-ray peaks and the statistical significance of the fit was determined using the χ^2 test.

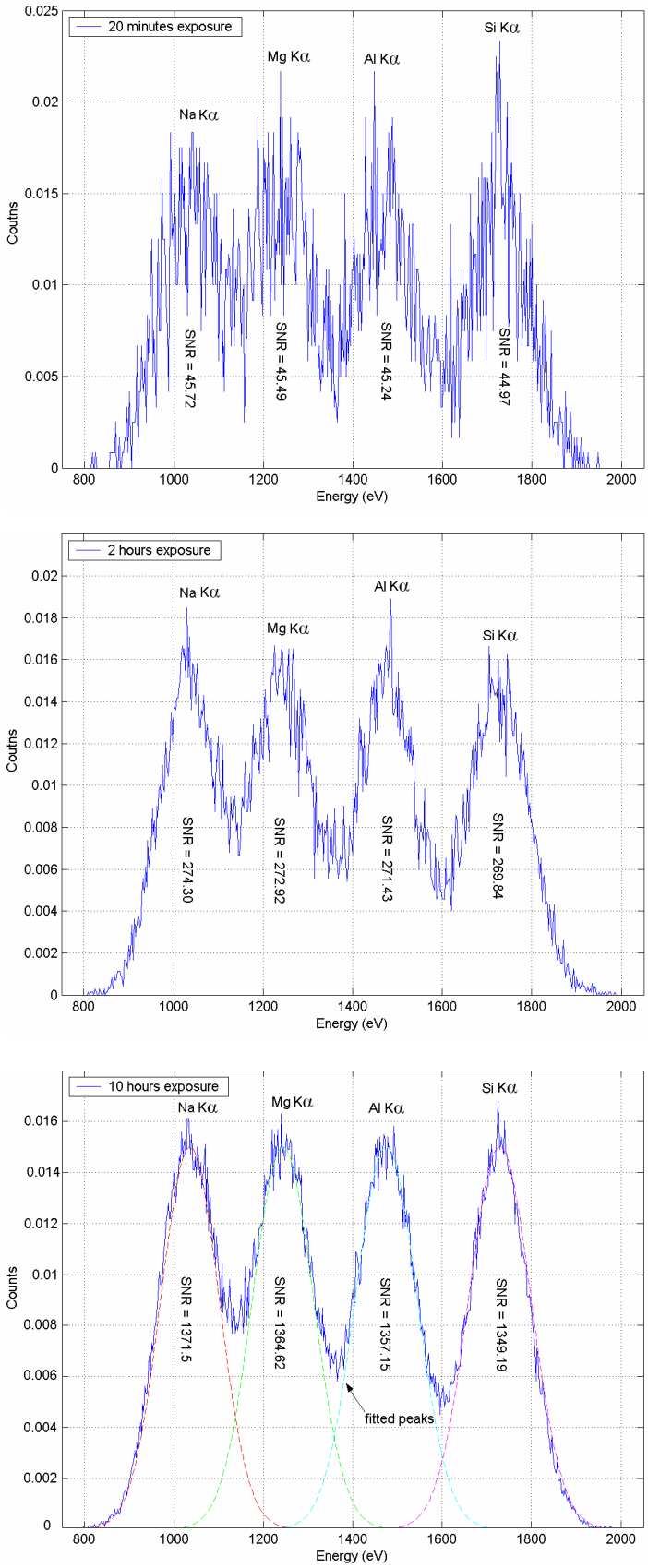

Figure 6.20: Simulated XRF spectrum from 1 − 2 keV with 600 e^- p/p/s dark current for exposures of (a) 20 minutes (b) 2 hours and (c) 10 hours

By increasing I_d and monitoring the effect on the FWHM of the X-ray peaks, it was found that X-rays from 1 − 2 keV could be identified with a maximum dark current of ~ 600 e^- p/p/s (I_{Dmax}). The overall noise includes the average readout noise of 7.4 e^- r.m.s. for all 4 CCDs, resulting in a total CCD noise of ~ 25.5 e^- r.m.s. By increasing the exposures and thereby the SNR, a higher confidence level can be achieved between the observed and expected spectra. The number of exposures required is dependant on the confidence intervals required for the 3 parameters of the fitted Gaussian peaks.

Figure 6.19 outlines the temperature required to operate at I_{Dmax} for AIMO and NIMO. AIMO allows the CCD to operate at +20 °C, which has 3 significant benefits. Firstly, at +20 °C the CCDs are not required to be inside a vacuum. However, when operating at atmospheric pressure the CCDs should always be operated above the dew point of water (typically +15 °C in the laboratory environment) to prevent water vapour in the air condensing on the CCDs. Secondly, power consumption from the TEC is practically eliminated since the CCDs are close to room temperature (+23 °C). Finally, the front lid of the CCD-Array can be removed to increase the transmission of X-rays (this assumes the CCD-Array is inside a lightproof box and the CCDs are covered with a thin material to prevent contamination). Although the CCD-Array can detect Kα emissions from 1 − 10 keV at +20 °C when operating in AIMO, by increasing the CCD noise, longer exposure times are required to achieve a given SNR. The confidence intervals for the 3 parameters of the XRF peak based on the SNR are now discussed.

Through the technique described in the previous section, the confidence intervals for the XRF peak mean position, FWHM and intensity were determined using the χ^2 test. The XRF peak of Mn Kα (5898 eV) was simulated and the number of photons was increased to improve the SNR. The confidence intervals for the 3 parameters were calculated at a 95% confidence level. The results of the simulations are shown in figure 6.21.

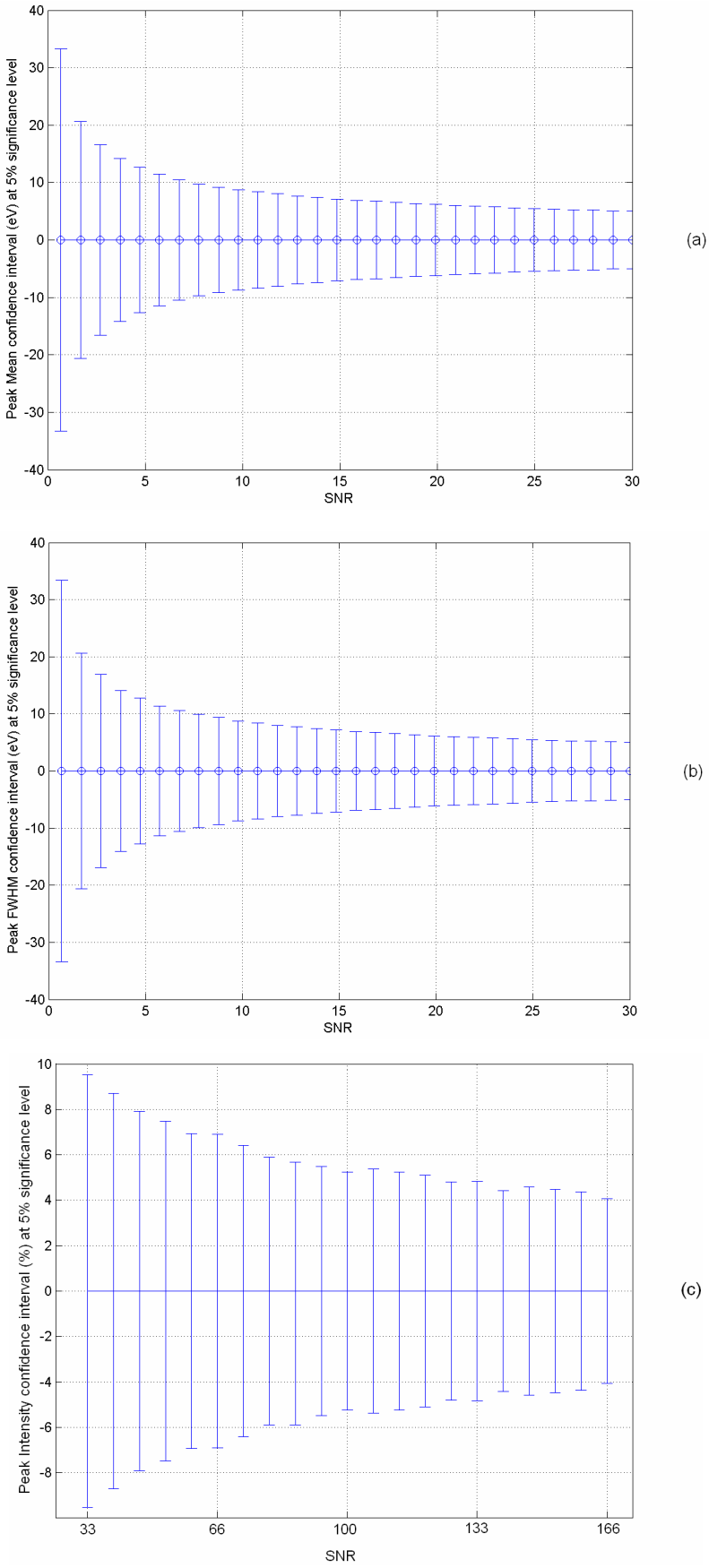

Figure 6.21: (a) Confidence intervals for the peak (a) mean position in eV, (b) FWHM in eV and (c) integrated intensity (%) at a 95% confidence level

To achieve a confidence interval of ± 1 eV on the peak mean position and FWHM, a SNR of ~ 500 is required. The separation between Kα peaks between 1 − 2 keV is ~ 200 − 250 eV. The separation between neighbouring Kα peaks increases at higher energies (e.g. separation is 591 eV between the Cu Kα and Zn Kα). Therefore a confidence interval of ± 10 eV will allow accurate qualitative analysis when analysing Kα emissions in the 1 − 10 keV range. This level of confidence requires a SNR of 8.8, which is 115 Mn Kα photons. Equation 6.6 can be re-arranged in terms of the number of counts required by an X-ray of energy E, to achieve a given SNR (e.g. 152 Cu Kα photons are required to achieve a SNR of 8.8). This level of accuracy assumes that only Kα emissions between 1 − 10 keV are detected by the CCD. If L series radiation is also detected from elements with an atomic number > 40, higher accuracy is required due to the proximity of different peaks. For example, a Promethim (Pm) $L\alpha_1$ photon contains an energy of 5431 eV which is similar to the energy of a Cr Kα photon at 5414 eV. A confidence interval of ± 10 eV would not be sufficient to distinguish the two peaks and accuracies of ~ ± 5 eV would be more suitable.

It is important to note that when XRF is performed with higher CCD noise, the time required to reach a given confidence interval increases, since the SNR increases at a slower rate. For example, the confidence interval for determining the mean of an Fe^{55} X-ray peak can be determined by dividing the standard deviation of the peak by the square root of the number of counts. Therefore, with a CCD noise of 25.5 e^- r.m.s (I_d = 600 e^- p/p/s), a 9.2 eV confidence interval is achieved after ~ 500 Mn Kα photons have been detected, whereas a confidence interval of 5 eV is achieved with a similar number of counts if the CCD noise is 7.4 e^- r.m.s (I_d = 1 e^- p/p/s). If XRF analysis is performed at warm temperatures, longer exposure times are required to achieve a given confidence interval for the mean, FWHM and intensity.

6.4.3 Combined XRD/XRF Analysis of Basalt at + 20 °C Operating Temperature

Based on the discussions presented in the previous section, combined XRD/XRF data was collected from a basalt powder at an operating temperature of +20 °C. The aim of the experiment was to ensure no characteristic or diffracted X-rays were lost from the XRF or XRD data respectively. The XRF spectrum taken at +20 °C was compared to a spectrum collected at -40 °C and the XRD pattern was compared to a reference

pattern, courtesy of the Natural History Museum (NHM). Figures 6.22 and 6.23 show the XRF and XRD data collected at +20 °C operating temperature.

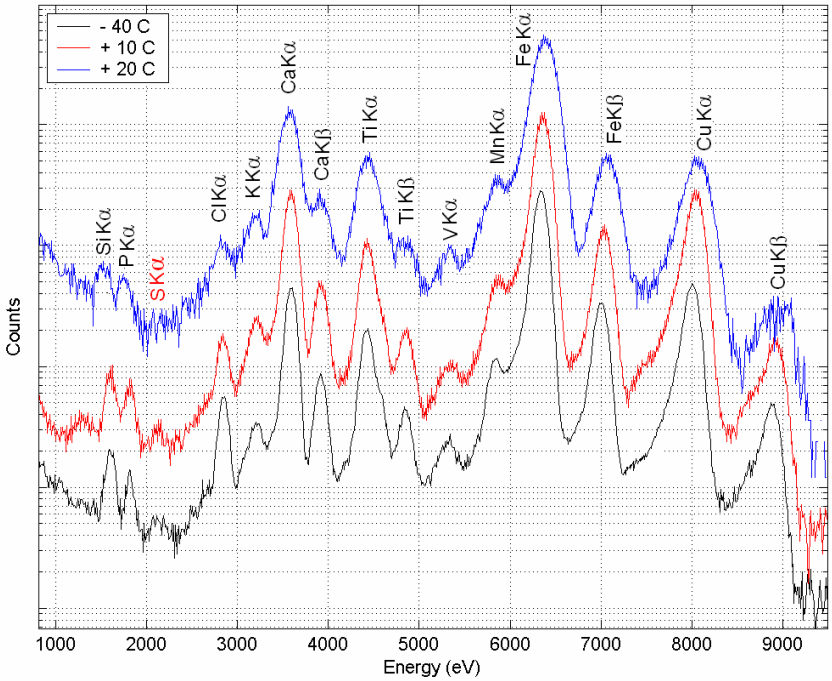

Figure 6.22: XRF spectra of basalt collected at -40, +10 and +20 °C (2000 exposures)

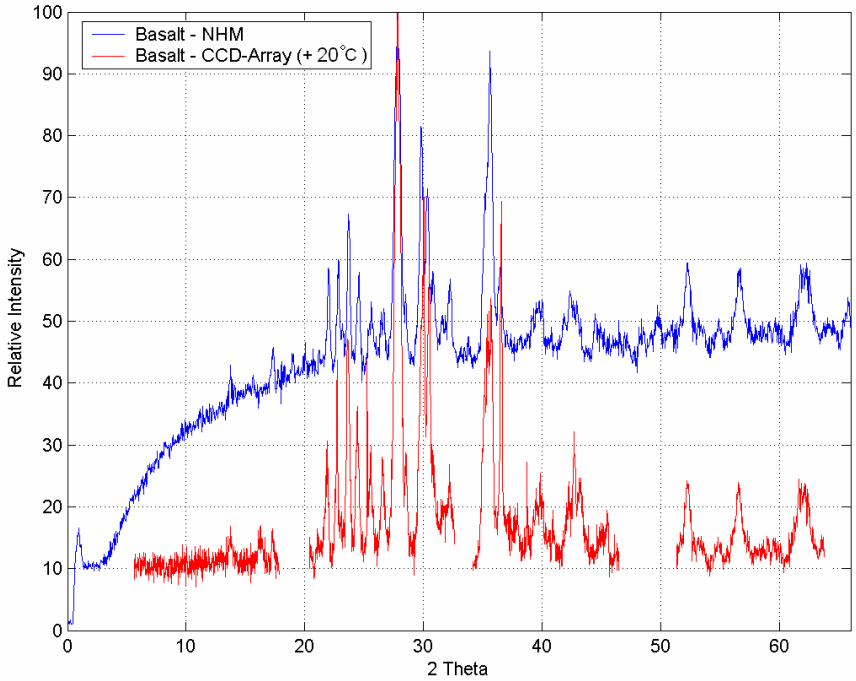

Figure 6.23: XRD pattern of basalt taken at + 20 °C compared with a reference pattern (2000 exposures)

The XRF spectra shown in figure 6.22 show an obvious decrease in energy resolution at +20 °C. Only one major X-ray peak is lost from the spectrum at +20 °C, which is S Kα (2308 eV). Due to the increase in noise at +20 °C, the SNR of the S Kα X-ray peak is very low. Larger exposure times would be required to allow detection of the S Kα X-ray peak. However, all other Kα emissions were identifiable.

The XRD pattern shown in figure 6.23 displays a very good agreement with the reference pattern. All major peaks were identifiable with maximum errors of 0.016° 2θ, which includes the 3 largest peaks required for qualitative analysis. At +20 °C, the XRD pattern provided a successful qualitative solution of basalt, which was confirmed with the elemental data provided by the XRF spectrum.

6.5 Applications of the CCD-Array – Mars

This section presents possible applications of the CCD-Array. The need for a combined XRD/XRF instrument for in-situ X-ray spectroscopy on Mars has been well documented [Blake 2000]. The ability of the CCD-Array to meet the science requirements of such an instrument are discussed and improvements to the current geometry are suggested.

As discussed in Chapter 2, the geometry most suited to portability with the lowest power consumption, is the use of the BB_2 geometry with a radioactive X-ray source. Although in development [Oxford Instruments 2009], no miniature X-ray tubes with polycapillary collimating optics are currently available (miniature tubes with X-ray focusing optics are widely available). The flux produced by miniature X-ray tubes such as the Mini-X are only a factor of 7 − 8 times higher than that produced by a radioactive source, which does not justify the increased power consumption (~ 4 W) and instrument volume (additional 45 cm^3 for the Mini-X, not including additional power supply and control electronics) for application on Mars. It is expected that a radioactive source used in conjunction with the CCD-Array will provide the most suitable option for a payload instrument on Mars. However, the use of the PB geometry is also discussed.

6.5.1 XRD

Over 30 Martian meteorites analysed on Earth and results returned from various in-situ spectrometers on Mars, have confirmed that the Martian surface is dominated

with igneous rocks and minerals such as olivine, peridotite and basalt. However, in 2005, the OMEGA instrument onboard the Mars Express found deposits of phyllosilicates in many regions of Mars [Poulet et al. 2005]. Phyllosilicates are a group of clay minerals that are of particular interest to future in-situ spectrometers on Mars since they indicate the process of water interaction. For both qualitative and quantitative analysis, it is crucial for the diffractometer to cover an angular range where the major peaks of clay minerals and igneous rocks can be detected. As shown in figure 3.19 (peridotite) and figure 6.23 (basalt), the major peaks in igneous rocks/minerals ranges from approximately 15 − 60° 2θ. Figure 6.24 shows the XRD pattern of 3 common phyllosilicate clay minerals, chlorite, smectite and illite.

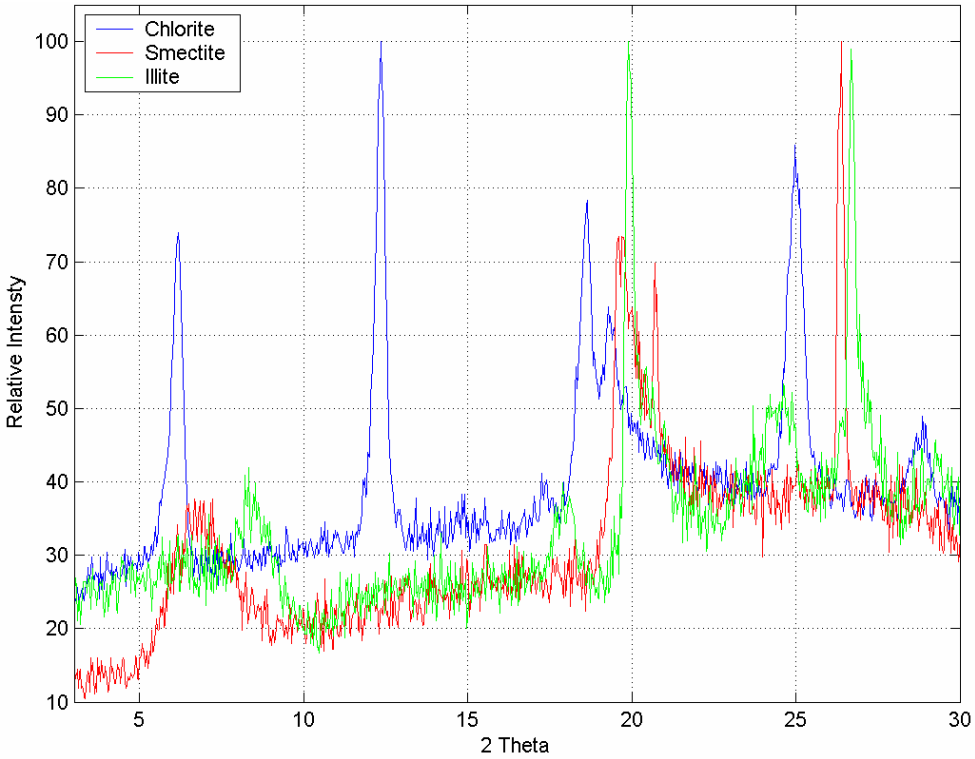

Figure 6.24: The major peak locations of some common Phyllosilicate minerals (data courtesy of the NHM)

It is obvious from figure 6.24, in order to identify the major peaks of clay minerals, low angle detection is crucial. The clay minerals in figure 6.24 with the largest d-spacings, smectite and chlorite, contain the lowest angle peaks ranging from 5 − 6°. The angular coverage achieved by the CCD-Array, which ranges from 4.48 − 64°, will allow the detection of all major peaks in phyllosilicates and igneous rocks

[Cuadros 2006]. The low background achieved by the CCD-Array at lower 2θ angles will also facilitate the detection of peaks in clay minerals.

Qualitative analysis involves identifying the overall phase of the sample (e.g basalt or smectite). The most common technique to perform qualitative analysis is to locate the 2θ positions of the 3 largest peaks in the sample and compare the results to reference patterns in a database, such as the ICDD PDFs. To perform accurate qualitative analysis, the detector must have adequate resolution to resolve the 3 largest peaks in the sample and must also be able to determine the peak positions with high accuracy. Figure 6.25 shows the resolution required to resolve 3 of the most intense peaks in some common Martian samples. For example, the marker located at 9.2° 2θ for chlorine, means a resolution of ~ 3° FWHM is required to resolve the peaks located to the left of the marker (6.175°) and the right of the marker (12.3°).

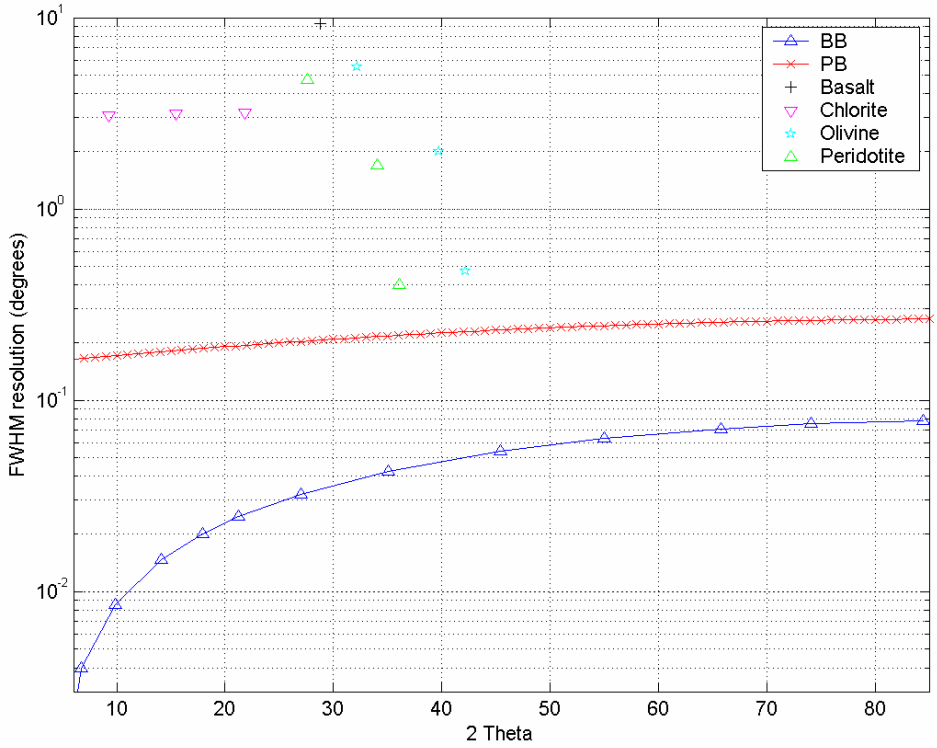

Figure 6.25: Resolution required to resolve the 3 largest peaks in some common Martian related samples (data courtesy of UCL and NHM). P_{ob} = 30µm

The calculations highlight that the resolution achieved by the current PB geometry easily meets the requirements for qualitative analysis. The increased resolution achieved using a radioactive Fe^{55} source in BB_2 geometry with a similar beam size is

also shown, since this is the expected operating mode on Mars. The other main consideration for qualitative analysis is how accurately the 2θ peak positions can be determined. As discussed in the previous section, the accuracy in determining the mean 2θ position of the XRD peaks is insensitive to SNR, therefore, the only limitation is the spatial calibration of the detector. The CCD-Array was calibrated using NIST SRMs (see section 4.6) and maximum errors of ~ 0.012° were recorded (~ 1 pixel). This value includes a 0.00015° error due to the non-linear resolution experienced by the CCD-Array because the CCDs are not curved along the measuring circle but lie on a tangent to it. However, an accuracy of 0.012° 2θ will easily allow accurate qualitative analysis of samples.

For accurate quantitative analysis, the detector must be able to resolve more peaks (~ 20 should be sufficient), determine the peak positions with high accuracy, and most importantly be able to determine the intensity of each peak with high accuracy. Figure 6.26 shows the resolution required to resolve 20 of the most intense peaks for some common Martian related samples.

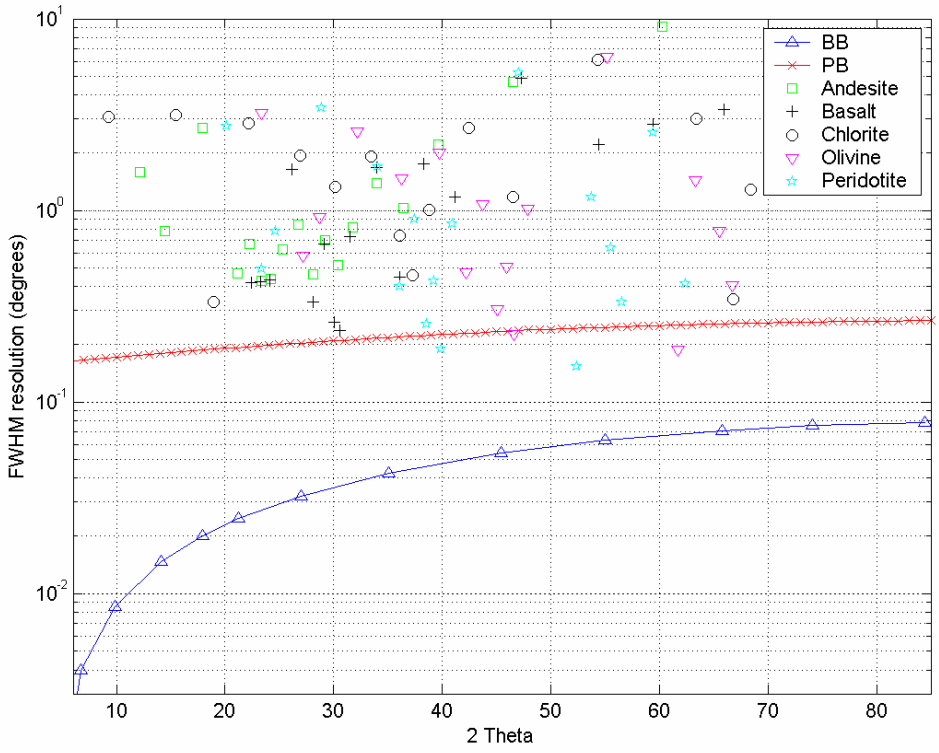

Figure 6.26: Resolution required to resolve the 20 largest peaks in some common Martian related samples (data courtesy of NHM). P_{ob} = 30 µm

Figure 6.26 highlights that the resolution achieved by the CCD-Array in PB geometry can allow the detection of over 95% of peaks in the samples listed. The resolution achieved in BB_2 geometry with a similar beam size (30 µm) allows the detection of all major peaks. The resolution requirements for both qualitative and quantitative XRD analysis on Mars have been documented to be ~ 0.26° FWHM, between the 2θ range of 5 − 55° [Sarrazin et al. 2005]. Assuming a radioactive Fe^{55} source is employed using the BB_2 geometry, this resolution can be achieved using a beam size of ~ 120 µm. This will increase the incident Mn Kα flux to ~ 1.7×10^3 counts/s and the total flux (Mn Kα and Mn Kβ) to 2.05×10^3 counts/s, at a distance of 40 mm. This is a significant increase in flux from using a 30 µm beam (total flux of 1.28×10^2 counts/s) and will greatly reduce data collection times. To provide a resolution of ~ 0.26° FWHM, the PB geometry is limited to very small spot sizes of 30 µm. A major improvement to the CCD-Array design is discussed in section 7.2, which allows much higher XRD resolution to be achieved. The 2nd generation CCD-Array will be able to meet the resolution requirements of a Martian diffractometer with beam sizes of 90 µm in PB geometry.

With the use of NIST SRMs, maximum intensity errors were calculated to be ~ 3.2% at a 95% confidence level, which includes SNR errors and energy discrimination errors. The minimum number of diffracted photons collected in each peak was ~ 10,000, which results in an intensity confidence interval of 2% at a 95% confidence level. Assuming 10,000 counts are detected, the CCD-Array can determine the intensity of diffracted peaks to within ± 3.2%. Careful sample preparation can reduce sample related intensity errors, which can also be accounted for in Rietveld refinement. This high level of accuracy in intensity measurements will allow precise quantitative analysis of XRD patterns on Mars.

Although high quality data is preferred, significant information can also be obtained from lower quality data. Consider the discussion in section 6.3.3, where peak broadening due to non-level sample rotation resulted in the loss of 3 XRD peaks. Through Gaussian peak fitting and statistical significance testing, the mean, FWHM and intensity of the peaks was determined, with a 99% confidence level. The confidence intervals at a 95% confidence level were also calculated. If the user simply wanted to confirm the sample was in fact $CaCO_3$, certain features of the 'corrupted'

XRD pattern ('non-level rotation') could be used for confirmation, such as the 2θ separation of the 3 peaks and the intensity ratios of the 3 peaks. The 'level rotation' data can be used as a reference pattern. In the reference pattern, the separation between Peak 1 − Peak 2, and Peak 2 − Peak 3 was determined to be 0.62° and 0.65° respectively (determined through Gaussian peak fitting). Using the results shown in table 6.2, the separation between the same 'corrupted' peaks was found to be 0.63° for both, with a confidence interval of < ± 0.01°. From the reference pattern, the intensity ratios between the 3 peaks were found to be 1:0.52:0.45 (scaled to Peak 1). From table 6.2, ratios for the same peaks were determined to be 1:0.48:0.35. The separation between the peak positions from the 'corrupted' data provides significant agreement with the reference pattern, with errors of only 0.02°. The intensity ratios display larger errors but still provide a high level of confidence. Through similar techniques, data that has been corrupted by poor sample preparation or experimental misalignment can still be used to yield crucial information. This may be particularly important on Mars where data collection times for payload instruments are limited and the ability to repeat measurements may not be possible.

6.5.2 XRF

The crucial energy range required for chemical analysis on Mars is between 1 − 10 keV. To maximise the number of isolated events collected, the CCD30-11 should be operated in NIMO (V_G = 12 V, V_{ss} = 0 V), to provide a depletion depth of ~ 12 µm and a QE of ~ 33% at 5898 eV. To increase the collection efficiency, deep depletion devices can also be used to increase the QE from 3 − 10 keV. Devices with a resistivity of 1000 Ω.cm, can provide depletion depths of ~ 33 µm under similar biasing and a QE of 65% at 5898 eV. Regardless of resistivity, the CCD30-11 provides sufficient QE over the required energy range (1 − 10 keV).

The detection of low energy elements by the CCD-Array in its current geometry is difficult due to excessive absorption by the 108 mm air gap between sample and detector. The low energy detection limit in the laboratory is ~ 1.5 keV, but this is due to the high flux produced by the Bede micro-source. Assuming the region between the sample and detector is at standard atmospheric pressure (1 bar), the reduced flux produced by a portable X-ray source will prevent the detection of elements < 2.5 keV. Since the average pressure on Mars is 5 − 7 mbar [Chamberlain et al. 1976], the high

absorption of signal X-rays in air is practically eliminated. The Mylar X-ray window can therefore be removed, as the CCD-Array can be operated at Martian atmospheric pressure. Figure 6.4 highlighted the effect of placing the sample to detector area inside a vacuum and removing the Mylar X-ray window. To prevent contamination by dust and other small particles, a very thin sheet of Mylar (~ 1 − 2 µm) would be required to protect the CCD imaging area. Therefore, the main limitation to the detection of X-rays from 0.1 − 10 keV on Mars, would be the CCD's QE and absorption by the sample. Assuming an average emission depth of 1.5 µm for a 1 keV photon in basalt, the number of incident photons (that interact with the target atom) required to detect a single 1 keV photon would be ~ 500. Assuming multiple exposures are collected, this will allow the detection of an appreciable number of 1 keV photons.

Figure 6.27 outlines the resolution achieved by the CCD-Array at different operating temperatures.

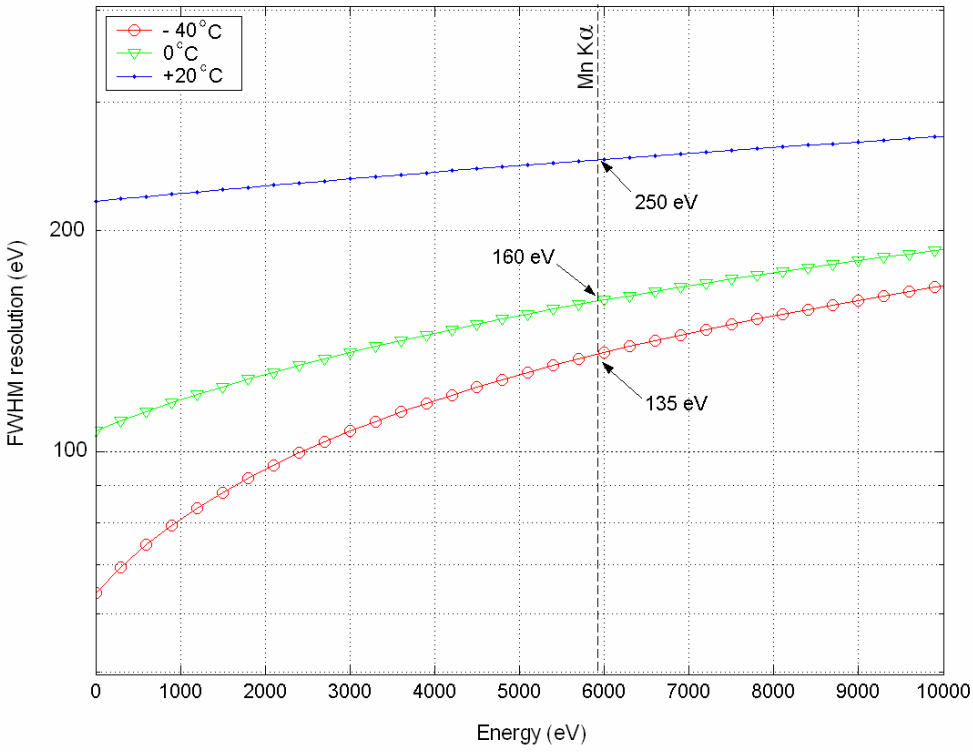

Figure 6.27: Variation in XRF FWHM at various operating temperatures using AIMO

At full TEC power, the CCD30-11s can reach an operating temperature of -40 °C, where the dark current is practically eliminated (~ 1 e^- p/p/s). Combined with an

average readout noise of 7.4 e^- r.m.s, FWHM resolutions of 135 eV at Mn Kα can be achieved. However, this resolution greatly exceeds the resolution required to identify the 22 elements in the 1 − 10 keV range by their Kα emissions. In Section 6.4.2, it was found that all Kα emissions from 1 − 10 keV could be identified with a CCD system noise of ~ 25.5 e^- r.m.s. With an average readout noise of 7.4 e^- r.m.s, this allows the CCD30-11 to operate with 600 e^- p/p/s dark current, which is at an operating temperature of +20 °C (in AIMO). The resolution achieved by the CCD-Array at +20 °C is shown in figure 6.27. At an operating temperature of 0 °C, the CCD-Array achieves similar resolution (160 eV at 5898 eV) to the MER APXS [Lechner et al. 2004]. At temperatures < 0 °C, the CCD-Array surpasses the XRF energy resolution performance achieved by any in-situ XRF instrument used on Mars to date. The CCD-Array can therefore provide versatility in performance based on the XRF resolution requirements.

The reduction in power consumption is crucial for a payload instrument on Mars. The main source of power consumption in the CCD-Array was the TEC, which provided cooling to the CCDs to reduce dark current. A detailed study was preformed on the CCD-Array to determine the required operating temperature of the CCD30-11 to perform combined XRD/XRF analysis, in an aim to reduce power consumption from the TEC. It was found that an increase in dark current had negligible effect on the XRD patterns, presuming a large number of exposures were collected. The operating temperature of the CCDs for combined XRD/XRF analysis was therefore entirely dependant on XRF requirements. Through simulations it was concluded that the CCDs could operate with an average dark current of 600 e^- p/p/s and detect all Kα X-ray emissions from 1 − 10 keV. The required temperature of the CCDs to operate with 600 e^- p/p/s dark current was dependant on the operating mode. If the CCDs operate using NIMO, they must be cooled to ~ -15 °C and require a total power consumption of ~ 4.5 W. However, if the CCDs are operated using AIMO, they can be used close to room temperature (+20 °C). This mode of operation reduces the depletion depth of the devices by ~ 6 µm, but the total power consumption of the CCD-Array is reduced to < 500 mW. Operating the CCDs in AIMO is an ideal mode of operation on Mars, since the power consumption of the instrument is greatly reduced. Assuming a radioactive source is used to provide flux, the only source of power consumption would be the CCDs and a small motor used to rotate the samples

during data collection, in order to reduce preferred orientation. It is expected the CCD-Array payload instrument could perform accurate XRD/XRF analysis consuming < 1 W of power when operated in this mode. Since this mode of operation reduces the SNR for a given number of X-ray counts, longer exposure times will be required to achieve a given confidence interval for the intensity, mean and FWHM.

The current CCD-Array geometry can meet the science requirements for both XRD and XRF on Mars. The XRD resolution achieved in BB_2 geometry allows a maximum beam size of ~ 120 µm, which produces a flux of ~ 1.7×10^3 Mn Kα counts/s. The data collection time required to reduce the XRD intensity errors to 1% (at a 68% confidence level) would be sample dependant, but is expected to be in the range of 5 − 10 hours. Due to the low absorption of X-rays in the Martian atmosphere, a radioactive source will allow detection of all X-rays from 1 − 10 keV.

6.6 Applications of the CCD-Array- Pharmaceuticals

The CCD-Array can also be applied to a broad range of markets for terrestrial use, one of which is the pharmaceuticals industry. This section discusses the requirements of XRPD and XRF instruments used in the pharmaceuticals industry and highlights possible uses of the CCD-Array.

Since power consumption is less crucial a consideration for terrestrial instruments, a low power miniature X-ray tube would be ideally suited for use with the CCD-Array. As shown in figure 6.10, unlike parafocusing geometries, the PB geometry with a fixed angle of incidence is insensitive to sample transparency. In the pharmaceuticals industry, samples are usually highly transparent (e.g organics), therefore an X-ray tube fitted with a polycapillary collimating optic would be ideal. The use of a miniature X-ray tube with X-ray optics would also greatly reduce data collection times for both XRD and XRF experiments. Therefore, for many applications, data can be collected in less than 1 hour, which is ideal for on-site analysis.

6.6.1 XRD

An important use of XRD in the pharmaceuticals sector is the determination of quantities of amorphous content within a crystalline substance. During pharmaceutical processes such as milling, the periodic structure of crystalline substances can be disrupted, resulting in the formation of amorphous areas. This can cause large

variations in the dissolution and bioavailability of a medication in the human body, therefore monitoring the change in crystalline substances is crucial during the pharmaceutical processing stage. A recent study was performed using Panalytical's X'pert Pro to determine the accuracy of the XRPD technique in determining the quantities of amorphous regions in a crystalline substance [Beckers et al. 2007]. Precise quantities (1%, 3%, 5%, 7% and 9%) of amorphous regions were added to 100 % crystalline lactose by lyophilization. The aim of the experiment was to perform XRPD on the samples, calculate the quantity of amorphous content by comparing the ratio of XRD peaks (from crystalline portion of the sample) to the background (from the amorphous region of the sample), and then compare the findings to the expected results. The CCD-Array's ability to perform this type of analysis on pharmaceuticals samples can be determined by comparing the detectors performance with the instrument used in the study. A performance comparison is summarised in table 6.4.

Parameter	Required	CCD-Array (PB)
Angular range (2θ)	10 - 35º	4.48 - 63.95º
Step size (2θ)	0.016º	0.012º
Diffracted beam resolution at 20º 2θ	~ 0.13º	~ 0.23º

Table 6.4: XRPD performance of an instrument used to determine the quantity of amorphous content in a crystalline sample in comparison to the CCD-Array (P_{ob} = 100 µm)

As shown in table 6.4, the angular range and spatial resolution offered by the CCD-Array can meet the requirements of such analysis, however, the overall resolution achieved by the CCD-Array in PB geometry is lower that that used in the experiment. The major reason for the lower resolution achieved by the CCD-Array in PB geometry is due to the low angle of incidence (4°). Since the area of interest starts at 10° 2θ, the angle of incidence can be increased to 10°, thereby increasing the resolution to ~ 0.17° at 20° 2θ (P_{ob} = 50 µm). This resolution is comparable to the resolution used in the study and provides sufficient resolution to perform the required analysis (modifications to the current CCD-Array design, which are discussed in Section 7.2, will vastly improve the detectors resolution performance).

Similar applications include determining the percentage crystallinity in amorphous substances [Sarsfield et al. 2006]. The analysis in this study was performed over a 2θ range from 12 − 22° with a step size of 0.04°. Again, the angular region of interest is

covered by the CCD-Array and the spatial resolution can be matched in 2 × 2 binning mode. The resolution of the diffraction peaks in the study was ~ 0.26° FWHM and this can be achieved by the CCD-Array in the PB geometry with beam sizes of 30 µm. Similarly, it is important to note a 12° incident angle could be used to vastly improve the diffracted beam resolution.

Other XRPD applications of the CCD-Array in the pharmaceuticals industry include polymorph screening and drug discovery. A recent study showed that 97% of crystalline samples from random off the shelf pharmaceutical samples could be identified using the ICDD PDFs [Fawcett et al. 2006]. With the use of the ICDD PDFs, the CCD-Array could be used on site to test for counterfeit drugs and medications.

XRPD is a highly utilised technique in the pharmaceuticals industry. Currently all XPRD analysis is performed on high resolution laboratory diffractometer such as Panalyticals X'pert Pro. These instruments usually operate in BB_3 geometry, achieving very high resolution. However, by increasing the angle of incidence, the CCD-Array can achieve much better resolution in PB geometry and in BB_2 geometry, can produce resolutions closer to laboratory diffractometers. The CCD-Array cannot match the resolution achieved by laboratory diffractometers but can still be utilised in many areas of the pharmaceuticals industry where resolution requirements are less critical. Since pharmaceuticals substances are highly transparent to X-rays, the use of parallel beams will also prevent asymmetrical peak broadening due to sample transparency [Cao et al. 2002]. To optimise the CCD-Array geometry for XRPD pharmaceutical applications, the angle of incidence should be increased to ~ 10°, which would greatly reduce the length of irradiated material and thereby greatly improve the diffracted beam resolution. The resolution achieved by the 2nd generation CCD-Array with a 10° angle of incidence is shown in figure 7.3.

6.6.2 XRF

The most obvious use of XRF analysis in the pharmaceuticals industry is testing for contamination of food and medicines. The CCD-Array could be used by organisations such as the Food and Drug Administration (FDA) to perform quality control on medications and food. For example, the CCD-Array could be taken on site to test for contaminants in multi-vitamin tablets. Figure 6.28 shows an XRF spectrum collected

from a multivitamin tablet with the CCD-Array. The multivitamin tablet was purposely contaminated with chlorine.

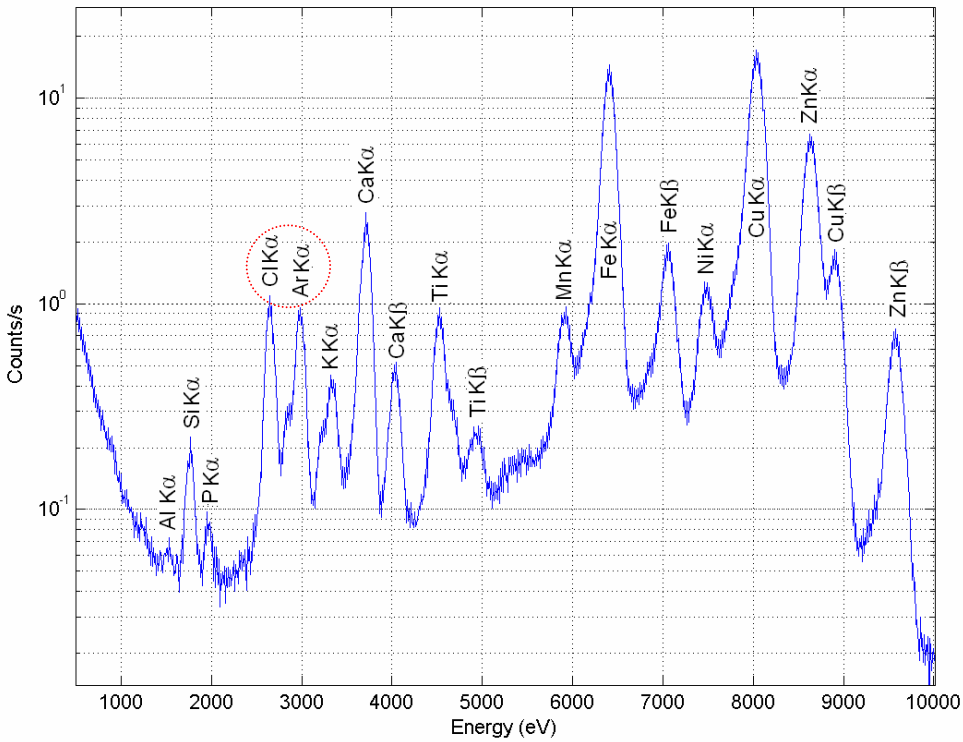

Figure 6.28: XRF spectrum of a multivitamin tablet contaminated with Cl. Data was collected for 30 minutes at 40 kV, 2 mA

The spectrum shows the presence of two unidentified elements from the multi-vitamin tablet, which are Cl Kα (2622 eV) and Ar Kα (2957 eV). As shown in figure 3.18, the background spectrum produced by the CCD-Array contains an Ar Kα peak due to the presence of Ar atoms in the air (~ 1%). The Cl peak can therefore be identified as a contaminant in the substance.

The range of elements required for analysis of pharmaceutical substances is far more diverse than that of the planetary sciences sector. The maximum X-ray energy detectable by the CCD30-11 is limited to ~ 15 keV (QE of 1%) in AIMO and 20 keV (QE of 1%) in NIMO. This is sufficient to allow the detection of all possible elements, since elements with an atomic number < 40 can be identified through K series radiation and elements with an atomic number > 40 can be identified through L series radiation (see figure 1.5). To allow this however, the excitation energy of the incident X-rays must be ~ 25 keV or greater. For example, a tube with a Cu anode

could be operated at 25 keV potential to excite all elements for XRF analysis, and provide a strong Cu Kα characteristic peak for XRD analysis. The low energy detection limit of the CCD-Array with a portable X-ray source is ~ 2.5 keV, which will not allow the detection of elements between 1 − 2 keV. Improvements to the 2nd generation CCD-Array will improve the low energy limit to ~ 1 keV (see section 7.2).

Unlike the planetary sciences sector, the XRF resolution required for pharmaceuticals analysis is high. This is because of peak overlapping between K series and L series radiation. One of the most popular XRF instruments utilised in the pharmaceuticals field is the 'Minipal Pharma', by Panalytical [Panalytical 2009]. This instrument uses a Si-pin detector that achieves a typical resolution of 145 keV at 5898 eV. Assuming a readout noise of 7.4 e^- r.m.s, a similar resolution can be achieved by the CCD-Array when operating with a dark current of 40 e^- p/p/s. This requires an operating temperature of ~ -8 °C in AIMO and a power consumption of ~ 2.5 W (CCD-Array only, not including X-ray source).

The CCD-Array can match the performance of benchtop XRF spectrometers such as the Minipal Phamra in terms of both elemental coverage and resolution. However, the main use of XRF in the pharmaceuticals industry is for quantitative analysis of contaminants, usually in the parts per million (ppm) range. For example, the Committee for Human Medicinal Products (CHMP) issue a guideline on the limits for residual catalyst in pharmaceutical processing [EMEA 2009]. Residual catalysts are used as reagents during pharmaceutical processing and are leftover in trace amounts (ppm) in the active pharmaceutical ingredient (API). XRF instruments can be used to detect the quantity of these elements (mostly transition elements) and ensure they are within the recommended guidelines. For example, the guideline for the amount of Cu residual catalysts in a 5 g sample is 500 ppm [EMEA 2009]. The quantity of powder samples used for XRF analysis are usually ~ 100 mg, therefore detection limits of ~ 10 ppm are required. To detect such low concentrations, high quality data and calibration is required. Although quantitative analysis has not currently been performed on CCD-Array XRF spectra, this technique can be performed very accurately with the use of the fundamental parameters technique and SRMs [Sprang 2000]. Typical accuracies range from 0.5 ppm − 100 ppm [Loubser & Verryn 2008]. Assuming the fundamental parameters technique is employed with the use of

SRMs, and SNR errors are greatly reduced through increased data collection times, it is expected that the CCD-Array will quantify the concentration of elements with similar accuracies. The CCD-Array can then be used to determine the quantities of contaminants in both food and medicines.

6.7 Discussion

This chapter has discussed the operational performance of the CCD-Array in the current laboratory environment. The transmission of signal X-rays from the sample to the detector has been determined and the detectors response in detecting these X-rays has been outlined using a response matrix. The most common sample preparation issues experienced with the CCD-Array in the reflective XRD geometry have been highlighted. It has been shown that the PB geometry relaxes sample preparation requirements and eliminates the common sample preparation issues experienced in parafocusing geometries. The power and operating temperature required by the CCD-Array to perform XRD/XRF analysis have been investigated. It has been shown that the CCD-Array can perform both XRD/XRF analysis at +20 °C, as long as a large number of exposures are collected to reduce SNR errors. Possible applications of the CCD-Array have been suggested and variations to the geometry to suit these applications have been recommended.

Chapter 7 : Conclusions and Future work

7.1 Conclusions

This chapter presents the main conclusion of this thesis and possible future work to be carried out.

The work carried out for this thesis involved the design and testing of a CCD array detector capable of simultaneously collecting XRD/XRF information from powder samples. A test facility was also designed to incorporate the detector for testing purposes. The work involved in this thesis provided an initial investigation into the eligibility of a CCD array detector for combined XRD/XRF analysis. CCDs are ideal detectors to be used for such applications due to their ability to discriminate X-ray energies with high resolution (XRF), as well as determine the position of detected X-rays with high spatial resolution (XRD).

The CCD-Array consisted of 4 CCDs (e2v's CCD30-11 FI, AIMO) tiled along a 120 mm measuring circle. The CCDs were bonded to a Shapal ceramic, which had a very high thermal conductivity (90 W/m K) and low thermal expansion (4.4×10^{-6} / °C). All 4 CCDs were cooled using a single 3-stage TEC, which was selected using Melcor's thermoelectric cooler selection software [Aztec 2005]. Each of the CCDs received sufficient cooling to reduce the dark current to ~ 1 e^- p/p/s with an average readout noise of ~ 7.4 e^- r.m.s. at 165 kHz readout speed. The CCDs were enclosed inside a vacuum using an aluminium chamber with a 20 µm thick Mylar X-ray window. The Mylar X-ray window was durable and allowed a high transmission of X-rays from 1 − 10 keV. Liquid cooling was incorporated into the copper base plate to absorb heat generated from the backside of the TEC during operation. Two environments for cooling were considered, which consisted of creating a vacuum inside the CCD-Array or filling the CCD-Array with N_2. Calculations performed prior to measurements indicated that the heat loads incident on the cold side of the TEC were much larger in the N_2 environment. The calculations were confirmed by both measurements and simulations. The CCD headboard was incorporated onto the backside of the copper base plate, which provided CCD bias and clock voltages, TEC power terminals and PRT outputs. A 12-inch flexible

vacuum pipe connected the CCD-Array to a vacuum pump, which maintained a pressure of ~ 3×10^{-3} mbar inside the CCD-Array during cooling.

The other main feature of the test facility was a high brightness X-ray micro-source manufactured by Bede Scientific Instruments. The main advantage of the micro-source was the coupling of an XOS polycapillary collimating optic. The optic focussed a highly divergent beam of X-rays into a low divergent beam (3.5 mrad FWHM) of collimated quasi-parallel X-rays. Using the micro-source greatly reduced data collection times and increased the efficiency of both XRD and XRF experiments. When used at 40 kV, it was found that the optic almost entirely eliminated the transmission of high energy bremsstrahlung photons (> 10 keV). A 15 µm Ni filter was also used to reduce Cu Kβ X-rays by 98% and lower energy bremsstrahlung X-rays. The resulting spectrum incident on the sample was a 93% monochromatic beam of Cu Kα X-rays, focused into a small collimated beam (< 150 µm). This was ideal for XRD applications since X-rays other than the main characteristic peak (Cu Kα) act as noise in the diffraction pattern.

In recent years, the advantages of using CCDs for the collection of XRPD data have been well documented [Reyes-Mena et al. 2000], but this is still a relatively new technique. Chapter 4 presented detailed studies concerning the collection, analysis and modelling of XRPD using CCDs. The data collection process involved integrating the CCD for very short periods. This ensured the image was not clustered with X-ray events, which is important to the process of identifying isolated X-ray events. The number of isolated events generated within the CCD is dependant on the depletion depth of the device. By using X-ray spread event analysis, the depletion depth of the CCD30-11 was confirmed to be 12 µm when biased at 12 V gate voltage and 0 V substrate voltage. A QE of 33% was achieved at Mn Kα (5898 eV) with a depletion depth of 12 µm. Single exposures ranged from 0.1 − 2 s with readout times of 1.6 s and 0.4 s for full imaging (256 × 1040) and 2 × 2 binning mode respectively. Multiple exposures were collected (100 − 10,000) to increase the SNR of both XRD and XRF data. Isolated events were determined by identifying events with an energy greater than the noise threshold, which was 3 standard deviations above the mean background noise. An ‘event’ was registered as a pixel containing a value greater than the noise threshold with 4 neighbouring pixels below the threshold. All isolated

events detected in the individual exposures were then accumulated to provide a histogram representing the combined XRD/XRF data.

When X-rays diffract from a sample, the entire incident spectrum is diffracted. Since the spectrum incident on the sample was almost entirely composed of Cu Kα X-rays (93%), all X-rays diffracted from the sample were detected as Cu Kα events. By applying the energy discrimination technique, XRD data was extracted from the raw CCD images, revealing the diffraction pattern. Cu Kα events were also elastically scattered from various parts of the test facility and detected as noise in the diffraction pattern (typically 5 − 75 isolated events/s). Methods to reduce XRD noise have been demonstrated in Section 5.4. Once the diffraction data was extracted, radial integration was preformed on the 4 CCD images to reveal the 2θ vs. intensity diffractogram. Prior to radial integration, alignment of the sample with the CCDs was performed. The position of the integrating circle (centre of the diffraction rings) was refined by ± 0.3 mm and radial integration was performed. The FWHM of the peaks was calculated and the position with the highest angular resolution represented the centre of the diffraction rings. Beam alignment ensured the maximum possible angular resolution was achieved and errors in sample to detector alignment were eliminated.

The performance of the CCD-Array as an X-ray spectroscopy device has also been investigated. The operational performance of the device has been highlighted in Chapter 6. The ability of the CCD30-11 to detect soft X-rays in the current laboratory arrangement has been discussed and the low energy detection limit was found to be ~ 1500 eV (Al Kα) using a collimated 150 µm beam. By increasing the diameter of the irradiating beam to ~ 1.5 mm, the low energy detection limit increased to 1254 eV (Mg Kα). As a portable instrument, the reduced flux from a miniature X-ray tube or radioactive source would degrade the low energy detection limit to ~ 2.5 keV. An investigation was carried out to determine the CCD operating temperature required to perform combined XRD/XRF analysis. It was found that XRD analysis could be performed at room temperature, as CCD noise had negligible effect on the XRD pattern. Since CCD system noise has no effect on XRD patterns, the operating temperature of the CCDs was therefore entirely dependant on XRF requirements. Through computer simulations it was found that operating the CCD with 600 e^- p/p/s

of dark current (+20 °C), allowed the detection of all Kα emissions from 1 − 10 keV. Accurate qualitative XRD/XRF analysis of basalt was performed by the CCD-Array at an operating temperature of + 20 °C in AIMO, with a power consumption of less than 400 mW.

7.2 Future Work

From the knowledge gained in testing the CCD-Array, 3 major improvements can be made concerning the design, 2 of which concern the XRD performance. Firstly, the resolution achieved by the CCD-Array is limited by the size of the diffracted beam from the sample, not by the spatial resolution of the detector. The first major improvement to the CCD-Array design will be the reduction in R_{sd}, which will result in higher XRD resolution since divergence of the diffracted beams is reduced. By reducing R_{sd} to 33 mm, only 2 CCDs are required as opposed to 4, which will also cover a larger 2θ angular range.

The second improvement to the design will be the reduction in angular gaps, currently located at 3 positions along the measuring circle with a range of 2.96° each. This will be achieved by laser cutting the ceramic packaging of the CCDs, allowing the imaging areas to almost touch one another.

The final improvement will be the low energy XRF response. For X-ray spectroscopy, the detection of elements from 1 − 2 keV is crucial, namely Na Kα (1041 eV), Mg Kα (1254 eV), Al Kα (1486 eV) and Si Kα (1740 eV). Detection of X-rays < 2 keV is difficult to achieve for portable detectors due to a low transmission in air and the X-ray window material. Figure 7.1 shows the geometry of the 2nd generation instrument in relation to the CCD-Array.

The CCD regions in figure 7.1 (coloured black) represent the imaging areas of the CCD30-11s (26.6 mm length). By using a 33 mm sample to detector distance, an angular coverage from 1.1° − 89.15° θ can be achieved. The laser cut ceramic packages result in a single gap in angular coverage of 0.2° (located from 45.05° − 45.25°). This assumes a 100 µm gap between the CCD imaging areas, which can be achieved by manual gluing.

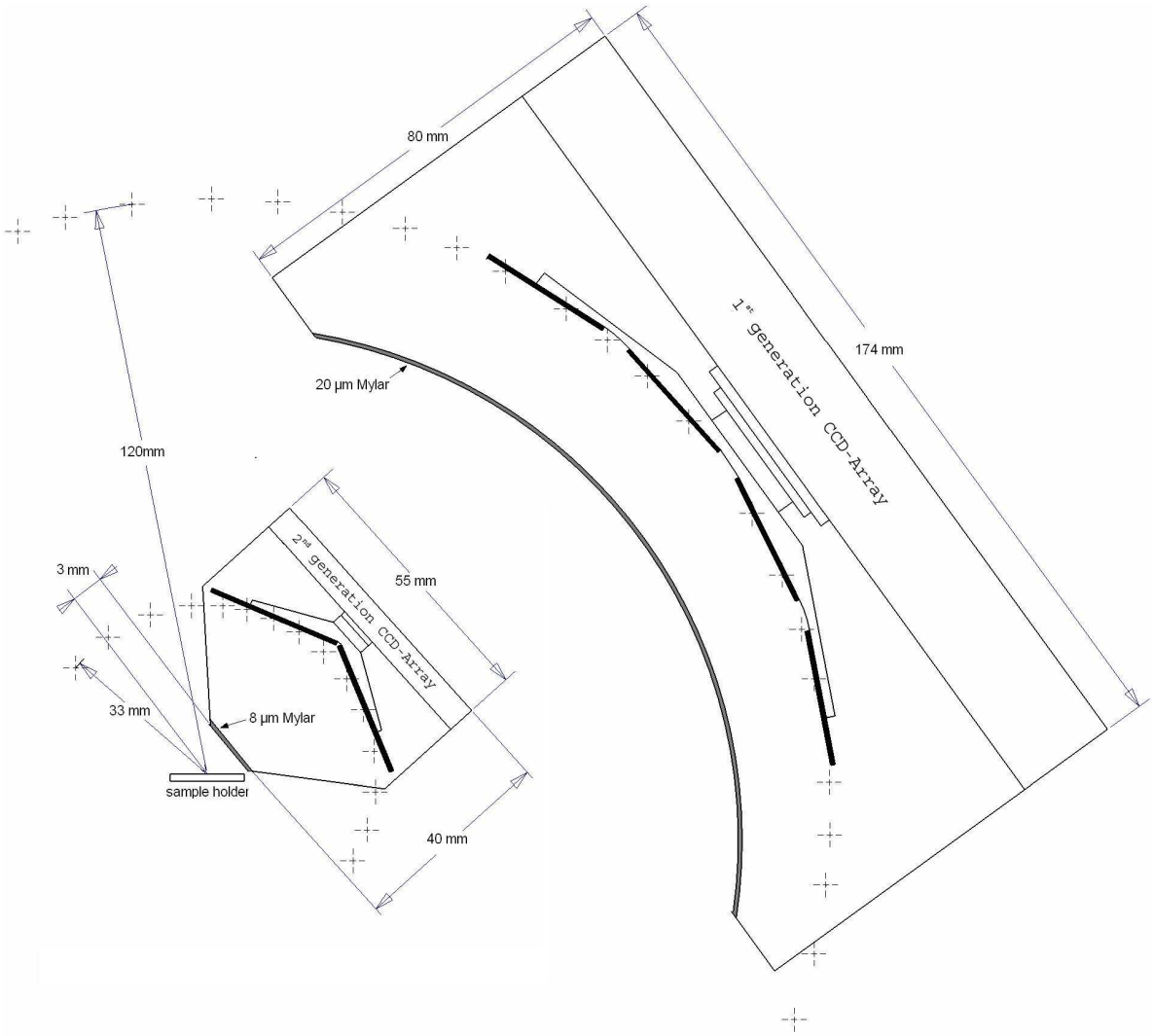

Figure 7.1: Geometry of improved 2nd generation CCD-Array. Both instrument use the CCD30-11 FI AIMO, with an imaging area length of 26.6 mm

As can be seen from figure 7.1, the 2nd generation instrument has a reduced instrument volume and extends the X-ray window to within ~ 3 mm of the sample. Assuming the CCD-Array is placed under vacuum, this geometry greatly improves the low energy X-ray response as shown in figure 7.2. The XRF response will also be improved with the use of an 8 µm Mylar X-ray window, however, this reduces the detectors opacity to light and requires the CCD-Array to be inside a lightproof container during data collection. As shown in figure 7.2, the 2nd generation CCD-Array allows the detection of X-rays between 1 − 2 keV, which was not possible with the 1st generation model. Figure 7.3 shows the improved XRD resolution achieved by the 2nd generation CCD-Array in PB geometry.

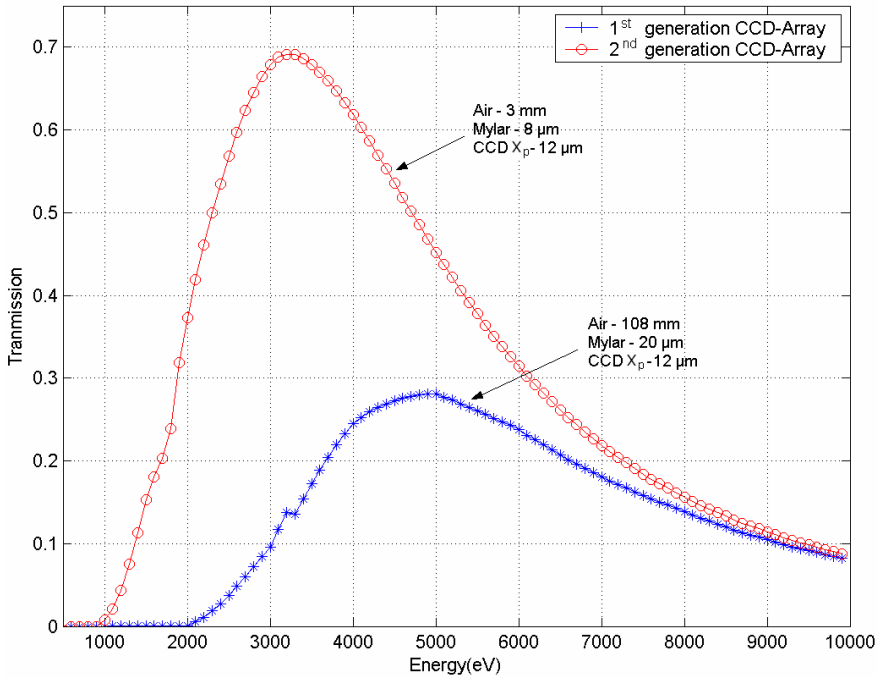

Figure 7.2: Improved overall QE of 2nd generation CCD-Array

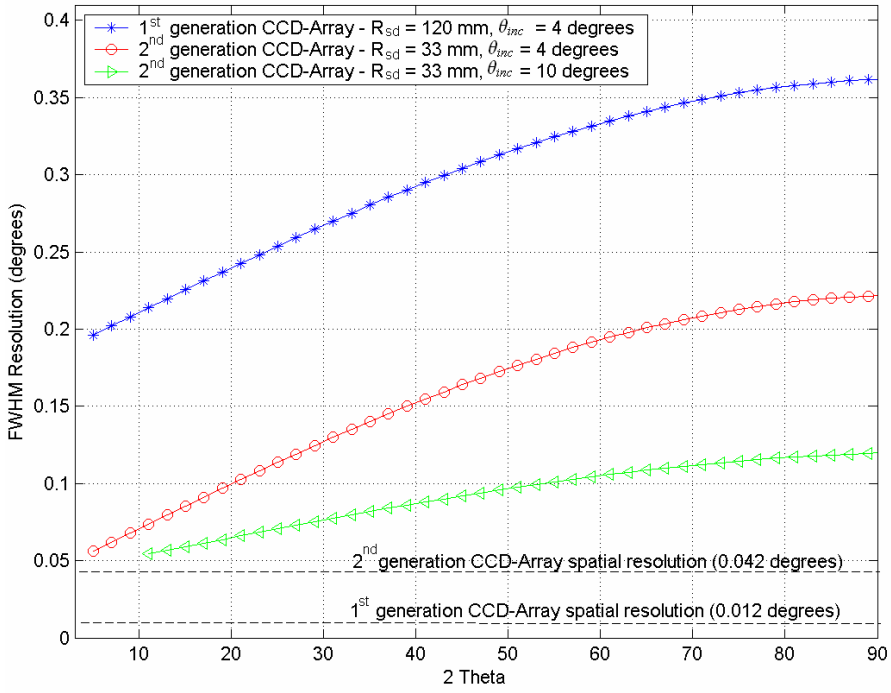

Figure 7.3: Improved XRD resolution achieved by the 2nd generation CCD-Array in PB geometry (P_{ob} = 50 µm). Resolutions do not include any broadening effects from the sample

By increasing the angle of incidence, a comparable resolution to laboratory instruments can be achieved. The new geometry provides a degraded spatial resolution of 0.042° in comparison to the 1st generation instrument (0.012°), but as

shown in figure 7.3, the size of the diffracted beams is still much larger than the spatial resolution of the detector. A consequence of reducing the radius of the measuring circle is the increase in distance between the CCD imaging area and the curvature of the measuring circle. This results in a larger variation in spatial resolution (see Section 4.5.1) from 0.00015° to 0.008° 2θ. This variation is still not expected to cause any errors in qualitative analysis, however, these errors could be easily corrected during post-processing. Table 7.1 summarises the advantages of the 2nd generation CCD-Array.

Parameter	**1st generation CCD-Array**	**2nd generation CCD-Array**	Units
Number of CCDs	4	2	
R_{sd}	120	33	*mm*
Spatial resolution	0.012	0.042	*º 2θ*
θ_{inc}	4	4	*º θ*
Angular coverage	4.48 - 63.95	5.1 - 93.15	*º 2θ*
Angular gaps	3 × 2.96º	1 × 0.2º	*2θ*
R_{PB} at 10º, 30º, 60º	0.21, 0.27, 0.33	0.07, 0.12, 0.19	*º2θ (FWHM)*
Instrument size	174 (H) × 80 (L) × 70 (W)	70 (H) × 50 (L) × 40 (W)	*mm*
XRF energy range	2,500 - 10,000	1,000 - 10,000	*eV*
Geometry	PB with fixed θ_{inc}	PB with fixed θ_{inc}	
X-ray window	20 µm Mylar	8 µm Mylar	

Table 7.1: Comparison of 1st generation and 2nd generation CCD-Array

The 2nd generation CCD-Array will use the deep depletion version of the CCD30-11, which has a resistivity of ~ 1500 Ω.cm. This will provide a larger depletion region, resulting in a higher number of single pixel events. The use of BI CCDs is unnecessary for the CCD-Array since the benefits in QE are at energies < 1 keV. The 2nd generation CCD-Array will be ideally suited to portability due to the decreased instrument volume and power consumption. The CCDs will be typically operated at -20 °C to reduce the dark current to < 1 e^- p/p/s. The CCDs can also perform combined XRD/XRF analysis at room temperature, however, this requires longer data collection times. Future work will also involve investigating alternative heat dissipating methods to liquid cooling. Fan assisted heat sinks may provide a more feasible option for portability. The 2nd generation CCD-Array greatly improves on the design of the 1st generation model and can be applied to many applications such as those discussed in section 6.5. and section 6.6. The type of X-ray source used in conjunction with the new CCD-Array will be application specific. Figure 7.4 shows the concept and geometry of the new CCD-Array.

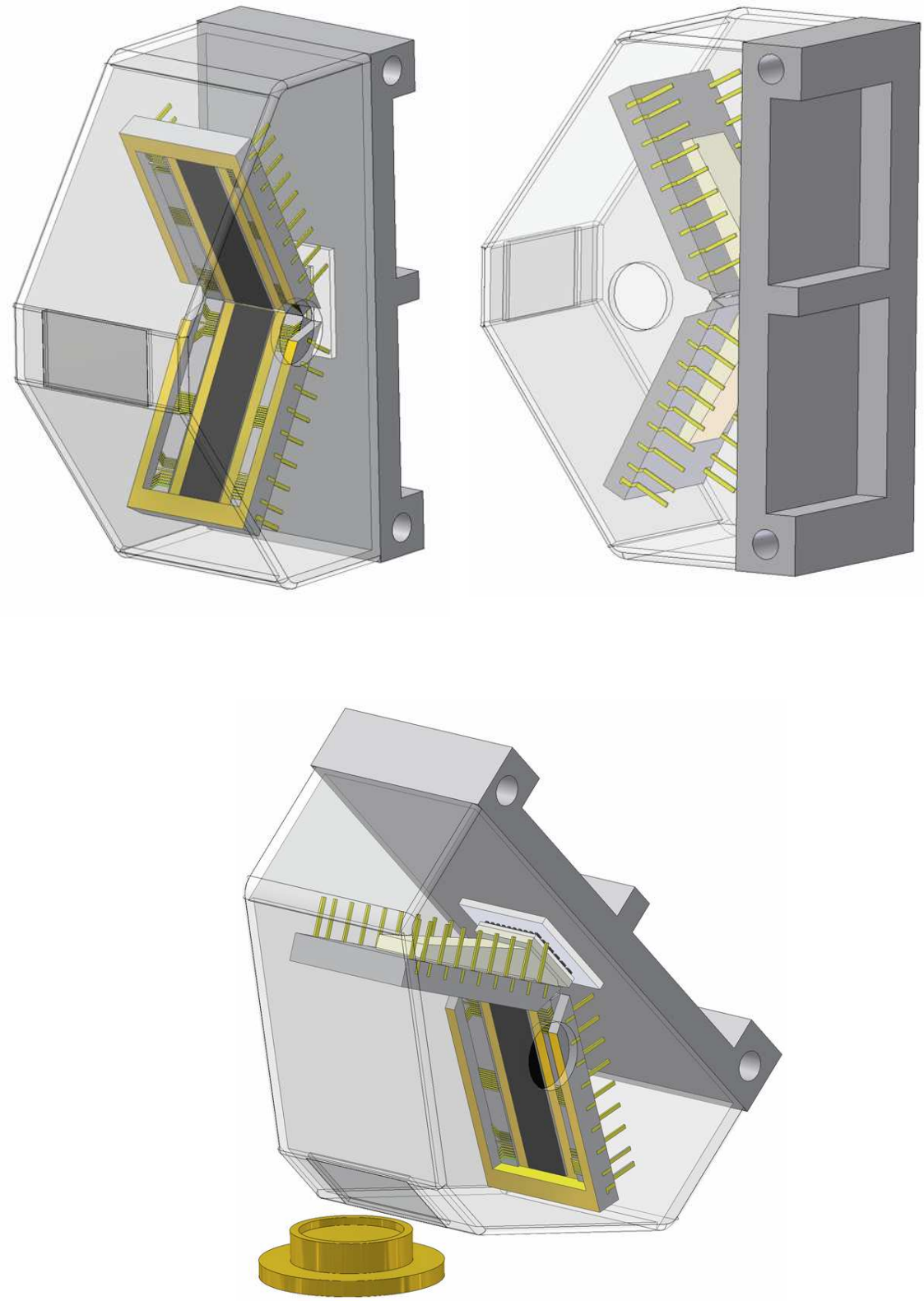

Figure 7.4: Illustration of the improved 2nd generation CCD-Array

The curvature of the imaged diffraction rings will be more pronounced in the 2nd generation instrument, therefore, unlike the 1st generation instrument, image smearing cannot be ignored. If full frames CCDs without shutters are used, longer integration times will be required to reduce errors from image smearing, but this will increase the dark current. CCD binning can also be applied to increase the ratio of integration to readout time, but the spatial resolution of the 2nd generation instrument should not be reduced further than 0.042°. Frame transfer CCDs may also be considered to eliminate errors from image smearing. The 2nd generation CCD-Array will also collect a larger fraction of the diffraction cones, thereby improving counting statistics for a given data collection time.

Future work will also involve performing quantitative analysis on both XRF spectra and XRD patterns. The intensity of an XRF peak for a given element is related to the concentration of the element in the sample. However, the intensity is affected by other elements in the sample due to secondary/tertiary fluorescence. This process can be modelled by software programs that perform 'matrix corrections', the 'matrix' in this case referring to the sample. By using SRMs, the experimental geometry can be calibrated to perform quantitative XRF analysis using the fundamental parameters technique [Sprang 2000].

Quantitative XRD analysis can be performed using techniques such as Rietveld refinement [Young 1993]. Software programs such as GSAS can be used to generate a synthetic version of the expected diffraction pattern [Larson & Von Dreele 1994]. The expected diffraction pattern is generated using sample, geometrical and instrumental parameters. The synthetic pattern is then refined using the different parameters (one of which is the scale factor that represents the weight of each phase in the sample) until the best agreement is found between the experimental and simulated data. Once the best fit is achieved, the scale factor reveals the weight of each phase in the sample and quantitative analysis can be performed [Gonzalez 2003].

Bibliography

Alig, R.C., Bloom, S. & Struck, C.W., 1980. Scattering by ionisation and phonon emission in semiconductors. Phys. Rev. B., Vol. 22, pp. 5565-82.

Amptek, 2008. Mini-X datasheet. Available at: http://www.amptek.com/minix.html [Accessed 5th October 2008].

Aztec, 2005. Meclcor Thermoelectric cooler selection Ver 2.2. Available at: ww.melcor.com\software [Accessed 8th March 2005].

Bearden, J.A., 1967. X-Ray Wavelengths. Review of Modern Physics, Vol. 39, pp. 86-99.

Beckers D. et al., 2007. Monitoring processing-induced crystallinity changes. Pharmaceutical Technology Europe, Vol. 19, Issue 11, pp. 38–41.

Bede Scientific Instruments, 2004. Bede micro-source: Installation, Maintenance and Operation Manual.

Beiser, A., 1995. Concepts of Modern Physics. 5th ed. New York: McGraw-Hill.

Bell, J.F. et al., 2004 Pancam Multispectral Imaging Results from the Opportunity Rover at Meridiani Planum. Science, Vol. 306, pp. 1703-1709.

Bertolini, G. & Coche, A., 1968. Semiconductor Detectors. Amsterdam: North-Holland Pub. Co.

Bish, D. et al., 1998. CHEMIN: A miniaturized CCD-based instrument for simultaneous XRD and XRF analysis. 47th Annual Denver X-ray Conference, pp. 55.

Bish, D.L. et al., 2007. Field XRD/XRF Mineral Analysis by the MSL CheMin Instrument. 38th Lunar and Planetary Science Conference, LPI Contribution No. 1338, p.1163.

Blake, D. F. et al., 1992. Design of an X-ray Diffraction/ X-ray Fluorescence Instrument for Planetary Applications. Proceedings of the Lunar and Planetary Science Conf. XXIII, pp. 117-118.

Blake, D.F., 2000. Remote X-ray Diffraction and X-ray Fluorescence analysis on planetary surfaces. Advances in X-ray Analysis, Vol. 43, pp. 487-496.

Boyle, W.S. & Smith, G.E., 1970. Charge Coupled Semiconductor Devices. Bell Syst. Tech. Jn., Vol. 49, pp. 587-93.

Bruijne, J.H.J. de., 2007. Gaia: how to map a billion stars with a billion pixels. Proceedings of the International Astronomical Union, Vol. 3, pp. 262-263.

Burt, D.J., 1991. CCD performance limitations: theory and practise. Nuclear Instruments and Methods in Physics Research Section A, Vol. 305, Issue 3, pp. 564-573.

Burt, D.J., 2006. Private communication.

Cao, W. et al., 2002. Quantitative determination of polymorphic composition in intact compacts by parallel-beam X-ray powder diffractometry. Jn. of Pharmaceutical and Biomedical Analysis, Vol. 30, pp. 1111-1119.

Castelli, C.M., 1991. The soft X-ray performance of CCD detectors. Ph. D. Thesis, University of Leicester.

Chamberlain, T.E. et al., 1976. Atmospheric measurements on Mars: the Viking Meteorology Experiment. American Meteorological Society, Bulletin, Vol. 57, pp. 1094–1104.

Chipera, S.J. et al., 2009. Real-Time XRD/XRF at a Mars-analog sulfate site in Leadville, Colorado, using a CheMin-heritage instrument. Lunar and Planetary Science Conference XL, LPI Contribution No. 1328.

Clark, B.C. et al., 1977. The Viking X-ray fluorescence experiment: analytical methods and early results. Jn. of Geophysical Research, Vol. 82, pp. 4577-4594.

Clark, B.C. et al., 1982. Chemical composition of Martian fines, Jn. of Geophysical Research, Vol. 87, pp. 10059-10067.

Cornaby, S., 2002. Simultaneous XRD/XRF with low power X-ray tubes. Advances in X-ray Analysis, Vol. 45, pp. 34 – 40.

Cornaby, S. et al., 2000. Using a Charged-Coupled Device (CCD) as an X-ray Single Photon Energy-Dispersive Detector. Jn. of X-ray Science and Technology, Vol. 9, pp. 1-13.

Cornaby, S. et al., 2001. An XRD/XRF Instrument for the Microanalysis of Rocks and Minerals. Measurement Science and Technology, Vol. 12, pp. 676-683.

Cressey, G., 2006. Private communication.

Cuadros, J., 2006. Private communication.

Cullity, B.D., 1978. Elements of X-Ray Diffraction. 2nd ed., Reading Massachusetts: Addison-Wesley Publishing Co.

e2v technologies, 2007. Datasheet: Full-Frame Spectroscopic & Scientific CCDs, CCD30-11, FI, AIMO. Available at: http://www.e2v.com/products/imaging-devices/space---scientific-imaging/datasheets [Accessed at: 17th January 2005].

EMEA, 2009. Guideline on the specification limits for residues of metal catalysts. Available at: http://www.emea.europa.eu/pdfs/human/swp/444600.pdf [Accessed 21st April 2009].

Fano, U., 1947. Ionization yield of radiations. II. The fluctuations of the number of ions. Physical Review, Vol. 72, pp. 26-29.

Fawcett, G.T. et al., 2006. Development in formulation analyses by powder diffraction analysis. Powder Diffraction, Vol. 21, Issue 2, pp. 105-110.

Fuggle, J.C. & Martensson, N., 1980. Core-Level Binding Energies in Metals. Jn. of Electron Spectroscopy and Related Phenomena, Vol. 21, pp. 275.

Gibson, D. & Gibson, W., 2002. Polycapillary optics: An enabling technology for new applications. Advances in X-ray Analysis, Vol 45, pp. 286-297.

Gonzalez, R.M., 2003. Analysis of geologic materials using Rietveld quantitative X-ray diffraction. Advances in X-ray Analysis, Vol. 46, pp. 204–209.

Grieken, R. & Markowicz, A., 2001. Handbook of X-ray spectrometry, 2nd ed., Routledge: CRC Press.

Groom, D., 2004. Temperature dependence of mean number of e-h pairs per eV of X-ray energy deposit. Available at: http://www-ccd.lbl.gov/w_Si.pdf [Accessed 3rd May 2007].

Hall, H., 1936. The theory of photoelectric absorption for X-rays and γ-rays. Review of Modern Physics, Vol. 8, pp. 358–397.

Harland, D. M., 2005. Water and the Search for Life on Mars. Glasgow: Springer-Verlag.

Henke, B.L., Gullikson, E.M. & Davis, J.C., 1993. X-ray interactions: photoabsorption, scattering, transmission, and reflection at E=50-30000 eV, Z=1-92. Atomic Data and Nuclear Data Tables, Vol. 54, pp. 181-342.

Holland, A. D., 1990. Radiation effects in CCD X-ray detectors. Ph. D. Thesis, University of Leicester.

Hopkinson, G. R. & Lumb, D.H., 1982. Noise reduction techniques in CCD image sensors. Jn. of Physics E: Scientific Instruments, Vol. 15, pp. 1215-1222.

Hopkinson, G.R., 1983. Charge Diffusion effects in CCD X-ray detectors I. Theory. Nuclear Instruments and Methods, Vol. 216, pp. 423 – 429.

Hubbell, J.H. & Seltzer, S.M., 1995. Tables of X-ray mass attenuation coefficients and mass energy adsorption coefficients 1 keV to 20 MeV for elements Z = 1 to 92 and 48 additional substances of dosimetric interest. National Institute of Standards and Technology, US Department of Commerce, Gaithersburg, MD 20899.

Intisar, A. et al., 2008. Development of a CCD Array detector for combined XRD/XRF applications. Proc. SPIE, Vol. 7021.

Janesick, J. R., 2001. Scientific Charge-Coupled Devices. The Society of Photo-Optical Instrumentation Engineers, Washington.: SPIE Press.

Jenkins, R. & Snyder L.R., 1996. Introduction to X-ray Powder Diffractometry, 2nd ed., New York:Wiley.

Jorden, P. et al., 2006. Commercialization of full depletion scientific CCDs. Proc. SPIE, Vol. 6276.

Jorden, P., Morris, D. & Pool, P., 2003. Technology of large focal planes of CCDs. Focal Planes for Space Telescopes, SPIE, Conference 5167, pp. 72-83.

Kargel, J. S., 2004. Mars: A Warmer, Wetter Planet – Climate Change on the Red Planet. UK: Springer- Verlag.

Kawai, J. & Ishii, H., 2005. Comparison between blackbody radiation and continuous X-ray spectra produced by electron deceleration. Radiation Physics and Chemistry, Vol. 75, Issue 11, pp. 1716-1718.

Kane, E.O., 1962. Theory of photoelectric emission from semiconductors. Physical review, Vol. 127, pp. 131–141.

Klein, C.A, 1968. Bandgap dependence and related features of radiation ionization energies in semiconductors. Jn. of Applied Physics, Vol. 39, pp. 2029–2038.

Krause, M. O., 1979. Atomic Radiative and Radiationless Yields for K and L Shells. Jn. of Physical and Chemical Reference Data, Vol. 8, Issue 2, pp. 307-327.

Krause, M. O. & Oliver, J. H., 1979. Natural Widths of Atomic K and L Levels, Ka X-Ray Lines and Several KLL Auger Lines. Jn. of Physical and Chemical Reference Data 8, pp. 329-338.

Larson, C.A. & Von Dreele, B.R., 1994. General Structure Analysis System (GSAS). Los Alamos National Laboratory Report LAUR, pp. 86-748.

Lechner, P., Pahlke, A. & Soltau, H., 2004. Novel High-Resolution Silicon Drift Detectors. X-Ray Spectrometry, Vol. 33, pp. 256-261.

Leonhardt, J.W. & Mapes, M., 1993. Design of large aperture, low mass vacuum windows. Proceedings of the 15th IEEE Particle Accelerator Conference, pp. 3882 – 3884.

Loubser, M. & Verryn, S., 2008. Combining XRF and XRD analyses and sample preparation to solve mineralogical problems. South African Journal of Geology, Vol. 111, pp. 229–238.

Lumb, D.H. et al., 1991. Charge coupled devices in X-rays astronomy. Experimental astronomy, Vol. 2, pp. 179–201.

Lumb, D.H. & Holland, A., 1998. X-ray imaging spectroscopy with EEV CCDs. X-ray instrumentation in astronomy II, pp. 116-122.

Marinangeli, L. et al., 2007. A European XRD/XRF instrument for the ExoMars mission. 38th Lunar and Planetary Science Conference (XXXVIII), LPI Contribution No. 1338, pp. 1322.

McDonald, C.A., 1996. Applications and Measurements of Polycapillary X-Ray Optics. Jn. of X-ray science and technology 6, pp. 32 – 47.

McFee, C., 2000. CCD Power Requirements of Solar – B. Available at: http://www.mssl.ucl.ac.uk/solar-b/docs/ccd/desnote/001pwrdis.pdf [Accessed 18th June 2008].

McKay, C. P., 1986. Exobiology and future Mars missions: The search for Mars' earliest biosphere. Advances in Space Research, Vol. 6, pp. 269-285.

Misture, S.T. & Hailer, M., 2000. Application of polycapillary optics for parallel beam powder diffraction. Advances in X-ray Analysis, Vol. 43, pp. 248-253.

Moseley, H. G. J., 1913. The high frequency spectra of the elements. Philosophical Magazine, Vol. 26, pp. 1024-1034.

Moseley, H. G. J., 1914. The high frequency spectra of the elements. Part II. Philosophical Magazine, Vol. 27, pp. 703-713.

Murray, N.J., 2007. Private communication.

Murray, N.J. et al., 2008. The X-ray performance of high resistivity (high-rho) scientific CCDs. Proc. SPIE, Vol. 7021.

Oxford Instruments, 2009. Private communication.

Padiyar, D.S. et al., 2000. Beam collimation using polycapillary X-ray optics for large area diffraction applications. Advances in X-ray Analysis, Vol. 43, pp. 254-259.

Panalytical, 2009. Trace element analysis of heavy metals in pharmaceutical materials. Available at: http://www.panalytical.com/index.cfm?pid=1215. [Accessed 23rd April 2009].

Pavlov, G. & Nousek, J., 1999. Charge diffusion in CCD X-ray detectors. Nuclear Instruments and Methods, Vol. 428, pp. 348–366.

Pecharsky, V. & Zavalij, P., 2005. Fundamentals of Powder Diffraction and Structural Characterization of Materials. New York: Springer.

Pool, P., 2005. Private communication.

Poulet, F. et al., 2005. Phyllosilicates on Mars and implications for early martian climate. Nature 438, pp. 623-627.

Precision Ceramics, 2007. Private communication.

Redus, R. H., Huber, A.C. & Pantazis, J.A., 2001. Improved thermoelectrically cooled X/γ-ray detectors and electronics. Nuclear Instruments and Methods, Vol. A458, pp. 214-219.

Reyes-Mena, A. et al., 2000. Using a CCD to Gather XRF and XRD Information Simultaneously. Advances in X-ray Analysis, Vol. 44, pp. 343–348.

Rieder, R.H., Wänke, T. & Economou, A.T., 1997. Determination of the chemical composition of Martian soils and rocks: The alpha proton X-ray spectrometer. Jn. of Geophysical Research, Vol. 102, issue E2, pp. 4027-4044.

Rieder, R. et al., 2003. The new Athena alpha particle X-ray spectrometer for the Mars Exploration Rovers. Journal of Geophysical Research, Vol. 108 (E12).

Ryan, R.D., 1973. Precision Measurements of the Ionization Energy and Its Temperature Variation in High Purity Silicon Radiation Detectors. IEEE Transactions on Nuclear Science, Vol. 20, Issue 1, pp. 473–480.

Sarrazin, P. et al., 2005. Field deployment of a portable X-ray diffraction/X-ray fluorescence instrument on Mars analog terrain. Powder Diffr., Vol. 20, Issue 2, pp. 128-133.

Sarsfield, A.B. et al., 2006. Powder X-ray diffraction detection of crystalline phases in amorphous pharmaceuticals. Advances in X-ray Analysis, Vol. 49, pp. 322-327.

Sparkes, J.J., 1994. Semiconductor Devices. 2nd ed., New York: Chapman and Hall, pp 81-82.

Sprang, A.H., 2000. Fundamental parameters method in XRF spectroscopy. Advances in X-ray Analysis, Vol. 42, pp. 1-10.

The Engineering Toolbox, 2005. Emissivity Coefficients of some common Materials. Available at: http://www.engineeringtoolbox.com/emissivity-coefficients-d_447.html [Accessed 12th May 2008].

Tyagi, M. S. & Overstraeten, R.V., 1983. Solid State Electronics 26, Vol. 6 pp. 577-598.

Yiming, Y. & Gibson, M.W., 2002. Polycapillary optics and X-ray analytical techniques. Advances in X-ray Analysis, Vol. 45, pp. 298 – 305.

Young, D.H., 1992. University Physics - Extended version with Modern Physics. 8th ed., Reading: Addison-Wesley.

Young, R.A., 1993. The Rietveld Method, Oxford: University Press.

Vaniman, D.T. et al., 2000. CCD-based XRD/XRF for Determining Environmental Mineralogy on Mars. Concepts and Approaches for Mars Exploration, LPI contribution No. 6138.

Varshni, Y.P., 1967. Temperature Dependence of the Energy Gap in Semiconductors. Physica 34, pp. 149-154.

Appendix A

Sample name	Form	Origin	Chemical formula/composition
Lanthanum hexaboride	SRM 660a	NIST	LaB_6
Fluorophlogopite mica	SRM 675	NIST	$KMg_3(AlSi_3O_{10})F_2$
Zinc oxide	SRM 674b	NIST	ZnO
Titanium dioxide	SRM 674b	NIST	TiO_2
Chromium (III) oxide	SRM 674b	NIST	Cr_2O_3
Ceric oxide	SRM 674b	NIST	CeO_2
Basalt	Rock	NHM	Olivine/Pyroxene/Feldspar/Quartz
Aragonite	Synthetic powder	UCL	$CaCO_3$
Peridotite	Rock	UCL	Olivine/Pyroxene
Andesite	Rock	NHM	Plagioclase/Pyroxene/Feldspars/Biotite/Magnetite/Quartz
Multivitamin tablet	Tablet	Brunel	Miscellaneous
Sodium chloride	Granuals	Brunel	NaCl
Quartz	Powder	NHM	SiO_2
Chlorite	Rock	NHM	$(Mg,Fe)_3(Si,Al)_4O_{10}(OH)_2{\cdot}(Mg,Fe)_3(OH)_6$
Smectite	Rock	NHM	$(Ca, Na, H)(Al, Mg, Fe, Zn)_2(Si, Al)_4O_{10}(OH)_2 - \times H_2O$
Illite	Rock	NHM	$(K, H)Al_2(Si, Al)_4O_{10}(OH)_2 - \times H_2O$
Olivine	Powder	UCL	$(Mg, Fe)_2SiO_4$

Table A: Sample reference (NHM = Natural History Museum, UCL = University College London, Brunel = Brunel University, NIST = National Institute of Standards and Technology)